Allegato N. ..1.. al punto
dell'ordine del giorno N. 12 bis

Università degli Studi di Perugia

Dipartimento di Ingegneria

Master Universitario di 2°livello

IN

Proprietà Intellettuale e Trasferimento Tecnologico

Regolamento didattico

ART. 1 - ISTITUZIONE

Ai sensi del vigente Regolamento di Ateneo dei corsi per master universitario e del D.M. n. 270/2004, presso il Dipartimento di Ingegneriadell'Università degli Studi di Perugia è istituito, per l'a.a. 2019/2020, il Master di 2° livello in «Proprietà Intellettuale e Trasferimento Tecnologico» in collaborazione con CIRIAF - Centro di Ricerca Interuniversitario sull'Inquinamento e l'Ambiente "Mauro Felli".
Il Master si inserisce nelle attività di formazione del dipartimento di Ingegneria ed è finalizzato alla preparazione di Manager del Trasferimento Tecnologico.Il Master prevede un periodo di tirocinio presso enti o aziende.

ART. 2 - OBIETTIVI FORMATIVI QUALIFICANTI

Il Master di 2°livello in «Proprietà Intellettuale e Trasferimento Tecnologico», di durata annuale, si articola in 70crediti formativi e si propone di fornire competenze specifiche ai laureati magistrali nell'ambito della proprietà intellettuale e del trasferimento tecnologico, definito internazionalmente come il processo che favorisce il successo della trasformazione dei risultati della ricerca in imprese.
In particolare il master è finalizzato a fornire le basi culturali necessarie per colmare il vuoto educativo che esiste in questo settore, in termini di conoscenza operativa dei processi e delle complessità della proprietà intellettuale, esperienza e comprensione di aree professionali e culture ampiamente diverse, capacità di "parlare la lingua" sia del mondo accademico che dell'impresae di sviluppare una vasta gamma di reti di contatti.
Il master ha quindi l'obiettivo di offrire un corso unico in Europa per la formazione della categoria professionale emergente dei Technology Transfer Managers (TTM).
Le conoscenze e le capacità teorico-pratiche, che saranno acquisite al termine del corso, prevedono l'approfondimento dei linguaggi della scienza e del business e delle basi economiche e giuridiche della proprietà intellettuale e del trasferimento tecnologico che permettano al TTM di comprendere l'ecosistema imprenditoriale circostante in modo da assorbire l'innovazione e fornire servizi ausiliari

L'importanza crescente del trasferimento tecnologico nella recente evoluzione universitaria ha fatto si che questo acquisisse un'importanza notevole in termini sia delle sfide che delle opportunità che presenta per lo sforzo costante degli inventori nel trovare soluzioni adeguate a vecchi e nuovi problemi per il progresso delle società.

La realtà contemporanea impone la necessità di disporre di Technology Transfer Managers, correttamente formati e soprattutto aggiornati, capaci di svolgere sempre al meglio la loro professione, sia in ambito pubblico (le università stesse hanno bisogno di competenze specifiche di proprietà intellettuale e trasferimento tecnologico), sia in ambito privato (gli inventori hanno bisogno di un "luogo sicuro" in cui discutere le condizioni per la rivelazione e divulgazione delle proprie idee; gli investitori hanno bisogno di informazione e rassicurazione in merito ai possibili rendimenti e agli scopi dei loro investimenti; le aziende, in particolare le PMI la cui flessibilità e spirito imprenditoriale sono fondamentali per lo sviluppo di nuove idee, necessitano di indicazioni chiare sulla ricerca e sviluppo da effettuare nonché una conoscenza approfondita dei potenziali nuovi clienti per i loro prodotti).
Ruolo chiave per la formazione dei discenti svolge il punto di vista dei potenziali reclutatori: il profilo versatile richiesto indica aspettative di fluidità tra le diverse aree in cui esercitano le proprie competenze e contribuiscono all'intero processo. Una qualifica professionale che prevede tirocini è adatta alle esigenze operative del ruolo del TTM, ponendo le basi per le relazioni di lavoro basate sull'alleanza e il lavoro di squadra.
Infine, la possibilità di svolgere un periodo di stage presso enti di produzione e promozione della ricerca, quali uffici del trasferimento tecnologico delle Università, agenzie inter-governative per la proprietà intellettuale e l'innovazione come EUIPO, EPO, WIPO,o grandi aziende tecnologiche e PMI che investono in innovazione garantisce una formazione completa per un professionista con qualifiche rispondenti alle esigenze delle aziende e degli enti che predispongano di un'unità altamente formata di trasferimento tecnologico.

ART. 3 - ACCESSO E DURATA DEL MASTER

Nel rispetto del vigente Regolamento d'Ateneo per i corsi per Master universitario e del D.M. n. 270/2004, il presente Master si configura come Master di 2°livello avrà durata annuale e si svolgerà nell'a.a. 2019/2020.L'accesso al Master è riservato in via prioritaria ai laureativecchio ordinamento/magistrale/specialistica in «Architettura e Ingegneria Edile-Architettura» (Classe LM04), «Biologia» (Classe LM06), «Biotecnologie Agrarie» (Classe LM07), «Biotecnologie Industriali» (Classe LM08), «Biotecnologie Mediche, Veterinarie e Farmaceutiche» (Classe LM09), «Farmacia e Farmacia Industriale» (Classe LM13), «Fisica» (Classe LM17),«Informatica» (Classe LM18),«Ingegneria Aerospaziale e Astronautica» (Classe LM20),«Ingegneria Biomedica» (Classe LM21),«Ingegneria Chimica» (Classe LM22),«Ingegneria Civile» (Classe LM23),«Ingegneria dei Sistemi Edilizi» (Classe LM24),«Ingegneria dell'Automazione» (Classe LM25),«Ingegneria della Sicurezza» (Classe LM26),«Ingegneria delle Telecomunicazioni» (Classe LM27),«Ingegneria Elettrica» (Classe LM28),«Ingegneria Elettronica» (Classe LM29),«Ingegneria Energetica e Nucleare» (Classe LM30),«Ingegneria Gestionale» (Classe LM31),«Ingegneria Informatica» (Classe LM32),«Ingegneria Meccanica» (Classe LM33),«Ingegneria Navale» (Classe LM34),«Ingegneria per l'Ambiente e il Territorio» (Classe LM35),«Matematica» (Classe LM40),«Medicina e Chirurgia» (Classe LM41),«Medicina Veterinaria» (Classe LM42),«Modellistica Matematico-Fisica per l'Ingegneria» (Classe LM44),«Odontoiatria e Protesi Dentaria» (Classe LM46),«Pianificazione Territoriale Urbanistica e Ambientale» (Classe LM48),«Scienza e Ingegneria dei Materiali» (Classe LM53),«Scienze Chimiche» (Classe LM54),«Scienze della Natura» (Classe LM60),«Sicurezza Informatica» (Classe LM66),«Scienze e Tecniche dello Sport» (Classe LM68),«Scienze e Tecnologie Agrarie» (Classe LM69),«Scienze e Tecnologie Alimentari» (Classe LM70),«Scienze e Tecnologie della Chimica Industriale» (Classe LM71),«Scienze e Tecnologie della Navigazione» (Classe LM72),«Scienze e Tecnologie Forestali ed Ambientali» (Classe LM73),«Scienze e Tecnologie Geologiche» (Classe LM74),«Scienze e Tecnologie per l'Ambiente e il Territorio» (Classe LM75),«Scienze Geofisiche» (Classe LM79),«Scienze per la Cooperazione allo Sviluppo» (Classe LM81),«Scienze Zootecniche e Tecnologie Animali» (Classe LM86),e affini.

Il Collegio dei docenti può ammettere, inoltre, possessori di lauree appartenenti ad altre classi, previa valutazione dei curriculum formativi, riconosciuti idonei sulla base delle modalità di ammissione.

Il Master è aperto anche ai possessori di altro titolo equipollente conseguito all'estero in discipline e tematiche attinenti, purché riconosciute idonee in base alla normativa vigente.

La quota d'iscrizione è pari ad € 6600, da erogare in tre rate:

- Prima rata pari a €2500 in fase di immatricolazione
- Seconda rata pari a €2500 entro 3 mesi dall'inizio del Corso
- Terza rata pari a €1600 entro 6 mesi dall'immatricolazione.

Per l'attivazione del Master sarà necessario il raggiungimento del numero minimo di 15 iscritti; il numero massimo sarà di 25partecipanti.

Il Collegio dei docenti procederà a nominare una Commissione al fine di procedere alla selezione volta a verificare il possesso da parte dei candidati delle conoscenze di base indispensabili per partecipare al corso. La selezione sarà per titoli e colloquio. Al colloquio saranno attribuiti 10 punti, ai titoli 10 punti.

I criteri di attribuzione dei punteggi per i titoli sono i seguenti:

- voto di laurea:
  fino a 102 = 2 punti
  da 103 a 109 = 3 punti
  110 = 4 punti
  110 e lode = 5 punti
- Pubblicazioni inerenti gli argomenti del Master: fino ad un massimo di 2 punti
- Specifiche esperienze professionali in ambiti inerenti al Master: fino ad unmassimo di 3 punti.

ART. 4 – ORGANI DEL MASTER

Organi del Master, ai sensi dell'art. 99 del Regolamento Generale d'Ateneo, sono il Collegio dei Docenti che definisce la programmazione delle attività didattiche e formative, provvede all'organizzazione e svolge ogni altra funzione inerente i fini istituzionali,il Direttore e il Consiglio direttivo.
Il Direttore è eletto dal Collegio dei docenti, a maggioranza assoluta dei suoi componenti, tra i professori del Collegio stesso. Il Direttore è nominato con provvedimento del Rettore, dura in carica per la durata del corso e comunque per non più di tre anni e può essere eletto consecutivamente una sola volta.
Il Collegio dei docenti è composto dai docenti responsabili delle aree disciplinari del Master universitario, è presieduto dal Direttore ed è nominato dal Rettore.
Il Consiglio direttivo è eletto dal Collegio dei docenti tra i propri membri, è presieduto dal Direttore,dura in carica per la durata del corso e comunque per non più di tre anni e può essere eletto consecutivamente una sola volta.
Il Consiglio Direttivo coadiuva il Direttore in merito alla programmazione didattica.

ART. 5 - ATTIVITÀ FORMATIVE E CREDITI CORRISPONDENTI

La durata del Corso per il conseguimento del titolo di Master è di1750 orecosì ripartite:600ore di lezione frontale -con possibilità di e-learning e videoconferenza interattiva - e assistita, 975 ore per studio individuale ed elaborato finale e175 ore per la partecipazione al periodo di tirocinio.
Al raggiungimento degli obiettivi e alla maturazione delle conoscenze e capacità operative e relazionali di cui all'art. 2, corrisponde il conseguimento di70 crediti formativi universitari.
In particolare, la ripartizione fra i crediti formativi è la seguente:
n. 60crediti formativi per attività didattica frontale, assistita/laboratoriale e studio individuale;
n. 3crediti formativi per l'elaborato e la prova finale;
n. 7crediti formativi per il tirocinio.
Le attività formative del corso di Master sono articolate in2 moduli, come da programma.
Non è previsto il riconoscimento di crediti per esami già sostenuti nei corsi di studio precedenti seguiti dagli iscritti.

PROGRAMMA DEL MASTER

Modulo	Insegnamento	SSD	ORE	CREDITI
1	Patents	IUS/04	**125**	**5**
1	Trademarks and designs	IUS/01	**125**	**5**
1	Plant varieties and geographical indications	AGR/01	**125**	**5**
1	Copyright, know-how, transfer and licensing of intellectual property rights Mod.1: Copyright (4 CFU) Mod.2: Know-how (1 CFU) Mod. 3: Transfer and Licensing (1 CFU)	IUS/04	**150**	**6**
1	IP systems and process of granting (EPO, EUIPO, WIPO) Mod.1: Intellectual property systems (3 CFU) Mod.2: Process of granting (1 CFU)	IUS/04	**100**	**4**
1	Digital innovation	INF/01	**100**	**4**
2	History and Anthropology of Innovation	SPS/09	**125**	**5**

2	Innovation finance and proof of concept	SECS-P/09	**125**	**5**
2	Business planning of a technology start up Mod. 1: Economics and management of scientific-technological innovation (1.5 CFU) Mod. 2: Market analysis tools (2 CFU) Mod. 3: Business planning of a technology start up (1.5 CFU)	SECS-P/08	**125**	**5**
2	Corporate finance for start ups	SECS-P/11	**125**	**5**
2	Sustainability as an innovation tool Topic 1: Sustainability indicators (1 CFU) Topic 2: Circular Economy Fundamentals (1 CFU)	ING-IND/11	**50**	**2**
2	Ethics and technology transfer Topic 1: Ethics (3 CFU) Topic 2: Communication for innovation and technology transfer (2 CFU)	M-FIL/06SPS/08	**125**	**5**
2	Innovation ecosystems	SECS-P/08	**100**	**4**
Stage	Tirocinio formativo		**175**	**7**
Prova finale	Tesi di master		**75**	**3**
TOTALE			**1750**	**70**

Al termine del corso, i candidati in regola con gli adempimenti formali e sostanziali (tasse, verifiche in itinere, frequenze, etc...) dovranno sostenere, di fronte ad una Commissionecomposta da almeno 7 membri,proposta dal Collegio docenti e nominata con decretorettorale,una prova finale così articolata:
Sviluppo della tesi di Master su argomenti interdisciplinari da concordare con i docenti del Master in forma di elaborato scritto e discussione della stessa tramite presentazione orale di fronte alla suddetta Commissione.

A coloro i quali supereranno l'esame finale sarà rilasciato il titolo di diploma universitario di Master di 2°livello in "Proprietà Intellettuale e Trasferimento Tecnologico" firmato dal Rettore dell'Università degli Studi di Perugia, e verranno attribuiti 70CFU.
I7 crediti formativi relativi al tirocinio ed i 3per la preparazione della tesi di Master potranno essere acquisiti, oltre che presso l'Università degli Studi di Perugia e le sedi consociate, anche pressoaltri enti pubblici e/o privati, ai sensi della Legge n. 196 del 24/6/1997 e del Decreto attuativo n. 142 del 25/3/1998.

ART. 6 - FREQUENZA

La frequenza di almeno il 75% delle attività d'aula, di laboratorio e di stage è obbligatoria ed il conseguimento dei crediti è subordinato alla verifica delle competenze acquisite oltre che delle frequenze. Le ore di assenza non sono cumulabili in un unico modulo.Coloro che non siano in regola con le frequenze o che non abbiano sostenuto la prova finale entro la data fissata dal Collegio dei docenti sono considerati decaduti.

ART. 7 - RISORSE E AMMINISTRAZIONE

L'attività didattica sarà svolta presso le strutture del CIRIAF e/o del Dipartimento di Ingegneriae/o di eventuali altre sedi individuate dal Collegio dei docenti del Master.
La gestione finanziaria e contabile, per tutte le pratiche amministrative relative alla retribuzione dei compensi e rimborsi dei docenti del Master nonché le procedure relative

alreclutamento dei docenti esterni secondo i regolamenti di Ateneo e gli atti relativi ai contratti di docenza, sarà affidata alla Segreteria Amministrativa del CIRIAF.
La funzione di tutor d'aula e di coordinamento, organizzazione e gestione del periodo di stage sarà affidata ad una unità di personale reclutata secondo le norme vigenti, per un numero di 1 tutor ogni 5 studenti.
La gestione della carriera degli iscritti al corso del Master è affidata all'Ufficio gestione Dottorati, Master e Corsi post lauream.Non è prevista l'erogazione di borse di studio.

UNIVERSITÀ DEGLI STUDI DI PERUGIA

PROGETTO DI CORSO

Anno Accademico 2019 / 2020

☒ **Master universitario: Proprietà Intellettuale e Trasferimento Tecnologico**

☐ **Corso di perf. di alta formazione :**

Denominazione del corso in lingua Inglese: Intellectual property and Technology Transfer

Livello	☐	*Primo*	☒	*Secondo*
Durata	*1750 ore*			
Totale C.F.U. rilasciati	*70*			
Titolo/Certificazione rilasciata	☒	*Diploma di Master*	☐	*Attestato di Frequenza*

Istituzione ☒ **Riedizione** ☐

Il progetto di riedizione di un Corso deve essere corredata da una relazione sulle attività svolte e sui risultati conseguiti, con particolare attenzione per i Master alla collocazione lavorativa di coloro che ne hanno conseguito il titolo finale (art. 15, co.3 del Regolamento in materia di corsi per master universitario e corsi di perfezionamento).

Dipartimento/i proponente/i: Dipartimento di Ingegneria, CIRIAF

Obiettivi formativi e finalità del corso, sbocchi professionali

Introduzione

Il trasferimento tecnologico è definito internazionalmente come il processo che favorisce il successo della trasformazione dei risultati della ricerca in imprese. Studiosi del settore considerano il trasferimento di tecnologia come "il movimento formale e informale di know-how, abilità, conoscenze tecniche o tecnologia da un ambiente organizzativo all'altro". Tuttavia, poiché il processo spesso si scontra con incentivi economici sfavorevoli e un'offerta inadeguata di servizi complementari per tradurre nuove idee in innovazioni tecnologiche economicamente valide, il suo coordinamento tra le varie parti interessate è una sfida. Il processo di trasferimento tecnologico richiede pertanto la disponibilità di risorse finanziarie e umane al livello adeguato.

Il trasferimento tecnologico è diventato centrale nella recente evoluzione universitaria e ha acquisito un'importanza notevole in termini sia delle sfide che delle opportunità che presenta per lo sforzo costante degli inventori nel trovare soluzioni adeguate a vecchi e nuovi problemi per il progresso delle società.

Esso è un processo nuovo e complesso che funziona in un arco di tempo non convenzionale e con un alto livello di incertezza. Un processo di trasferimento tecnologico di successo richiede un solido portafoglio di proprietà intellettuale, una unità del trasferimento tecnologico dedicata come punto di incontro di scienza e business, un team di Technology Transfer Managers (TTM) altamente qualificati che comprendono i linguaggi della scienza e business e un ecosistema imprenditoriale circostante in grado di assorbire l'innovazione e di fornire servizi ausiliari.

Il Master in Proprietà Intellettuale e Trasferimento Tecnologico dell'Università degli Studi di Perugia intende colmare il vuoto educativo che esiste in questo settore ed offrire un corso unico in Europa per la

formazione dei Technology Transfer Managers.

1. Obiettivi formativi

Essendo il TTM una categoria professionale emergente, le università stesse hanno bisogno di competenze specifiche di proprietà intellettuale e trasferimento tecnologico; gli inventori hanno bisogno di un "luogo sicuro" in cui discutere le condizioni per la rivelazione e divulgazione delle proprie idee; gli investitori hanno bisogno di informazione e rassicurazione in merito ai possibili rendimenti e agli scopi dei loro investimenti; le aziende, in particolare le PMI la cui flessibilità e spirito imprenditoriale sono fondamentali per lo sviluppo di nuove idee, necessitano di indicazioni chiare sulla ricerca e sviluppo da effettuare nonché una conoscenza approfondita dei potenziali nuovi clienti per i loro prodotti.

Molti dei problemi riguardano la comprensione e l'accettazione dei rischi inerenti, e questo implica la disponibilità di persone brillanti nella negoziazione dei rapporti fra tutte le parti interessate, il cui profilo comprende non solo una conoscenza operativa dei processi e delle complessità della proprietà intellettuale, ma anche esperienza e comprensione di aree professionali e culture ampiamente diverse, la capacità di "parlare la lingua" sia del mondo accademico che dell'impresa, e una vasta gamma di reti di contatti.

Chiaramente, ciò che viene delineato qui è una professione emergente, finora nebulosa, di Technology Transfer Manager. Tra le varie domande che sorgono intorno a questa professione emergente ci sono: quali qualifiche dovrebbero essere concepite per questi nuovi professionisti? e come sarebbe garantita una formazione continua al fine di consentire loro di stare al passo con le esigenze in rapida evoluzione del trasferimento tecnologico?

Al momento, le agenzie di trasferimento di tecnologia sono frammentate in modo diverso all'interno dei diversi segmenti del processo di trasferimento tecnologico e non esistono qualifiche standard per il ruolo dei TTM dedicati ad aiutare le innovazioni a fare il salto verso il mercato.

Il ruolo del trasferimento tecnologico differisce a seconda dei paesi, ma l'esperienza nello sviluppo e nel lancio del prodotto è fondamentale e internazionale. Ciò include la familiarità con gli aspetti normativi, inclusi quelli della proprietà intellettuale.

Un background scientifico è un vantaggio, ma anche esperienza in economia e finanza, in particolare nella modellazione dei cicli economici coinvolti nel processo di trasferimento tecnologico, risulta molto adatto. Il Master includerà poi cicli di lezione di etica dello sviluppo di nuove tecnologie in particolare quelle legate all'Intelligenza Artificiale.

2. Finalità del Master

Non solo il ruolo di un TTM è eccezionalmente esigente in termini di competenze e responsabilità, ma varierà anche con mercati diversi, "ecosistemi" dissimili e livelli di innovazione distinti.

Le PMI rappresentano il 99% di tutte le imprese dell'Unione europea (UE) e contribuiscono per il 57% al prodotto interno lordo (PIL) dell'UE. Tuttavia, gran parte del valore generato dalle PMI deriva da un piccolo numero di imprese ad alta crescita che sono spesso molto innovative.

Studi internazionali mostrano che le PMI che hanno almeno un brevetto hanno il 21% in più di probabilità di sperimentare un periodo di crescita e hanno il 10% in più di probabilità di diventare un'impresa ad alta crescita rispetto alle aziende senza diritti di proprietà intellettuale.

Gli studi rivelano anche che le probabilità che una PMI diventi un un'impresa ad alta crescita

aumentano del 33% se utilizzano "pacchetti" di proprietà intellettuale con marchi, brevetti e design invece di un'unica categoria di diritti.

Un buon TTM dovrà perciò comprendere e distinguere i diversi livelli di innovazione e i loro impatti sociali, economici e finanziari. Il primo livello è l'innovazione "sostenibile", in cui l'obiettivo è sostituire il vecchio con prodotti nuovi e migliori in modo che la domanda chiave per un TTM sia "questa innovazione può prolungare la crescita del fatturato esistente?". Le competenze richieste sono quindi relativamente semplici. Il secondo livello è l'innovazione "orientata all'efficienza", che essenzialmente cerca di produrre di più con meno. La domanda chiave qui è "questa innovazione migliora i margini di profitto?" Al terzo livello, "creazione di mercato innovativo", il lavoro di un TTM è molto più complesso. La domanda chiave è "l'innovazione risolve un problema ampio e complesso meglio delle soluzioni esistenti?" Si tratta di innovazioni di trasformazione, che genericamente generano rischi più elevati, ma hanno anche un impatto maggiore.

Inoltre, il ruolo del TTM è necessariamente interfunzionale: un TTM deve essere "conversante" piuttosto che "esperto" in diversi campi. Tuttavia, non solo hanno bisogno di "parlare la lingua" di diversi campi, ma devono anche farlo con sufficiente autorità, ad esempio per selezionare e respingere progetti, gestire i conflitti di interesse e giudicare il miglior momento di azioni e interazioni con attori diversi.

Questo porta alla questione della responsabilità per l'esito del progetto che è generalmente attribuito al ruolo di marketing, ma alcune responsabilità del TTM sono essenziali, perché il TTM è coinvolto nel processo dall'inizio alla fine. Nel settore in rapida evoluzione dell'innovazione tecnologica, ciò implica un continuo processo di apprendimento sul posto di lavoro per i TTM e una presa di responsabilità continua.

Il panorama in rapida evoluzione e molto diversificato dell'innovazione e del trasferimento tecnologico suggerisce che la formazione formale dovrebbe includere una forte componente di apprendistato. L'esperienza di coloro che sono attualmente coinvolti in trasferimento tecnologico, in ogni parte del mondo, suggerisce fortemente che i bisogni cruciali sono l'esperienza industriale o ingegneristica, una certa specializzazione in un determinato campo (acqua, ambiente, agro-biotecnologia, ecc.) stage formativi, sia in start-up, PMI o aziende più grandi.

Nel contesto attuale, sta diventando più importante che le competenze del lavoro siano codificate attraverso qualifiche e certificazioni formali. Ciò contribuisce ad attrarre il talento necessario oltreché a portare una misura di standardizzazione nella formazione offerta. Nel progettare l'attrazione degli studenti la formazione sarà studiata dal punto di vista dei potenziali reclutatori: il profilo versatile richiesto indica aspettative di fluidità tra le diverse aree in cui esercitano le proprie competenze e contribuiscono all'intero processo. Una qualifica professionale che prevede tirocini è adatta alle esigenze operative del ruolo del TTM, ponendo le basi per le relazioni di lavoro basate sull'alleanza e il lavoro di squadra.

3. Sbocchi professionali

Il trasferimento tecnologico riguarda le persone, dall'inventore di un'idea fino al cliente finale una volta che l'idea ha raggiunto il mercato. Molte idee nuove sorgono casualmente, senza particolare attenzione agli scopi finali; quindi è essenziale considerare ciò che si vuole raggiungere traducendo le innovazioni in prodotti e servizi commerciabili.

Per costruire legami più stretti con l'industria e facilitare la commercializzazione della ricerca, è essenziale che un'unità di trasferimento tecnologico recluti, ricompensi e mantenga i managers di

trasferimento tecnologico di alta qualità (TTM), nel lungo periodo. Lo staff deve essere di talento, altamente motivato, profondamente qualificato e ben informato in settori di attività molto diversi e in rapida evoluzione, ed essere anche in grado di mediare efficacemente tra scienza e imprese.

Gli sbocchi occupazionali sono pertanto molteplici e vanno dagli uffici del trasferimento tecnologico delle Università di tutto il mondo, alle agenzie inter-governative per la proprietà intellettuale e l'innovazione come EUIPO, EPO, WIPO, alle grandi aziende tecnologiche che investono in innovazione come Google, Amazon, Apple, alle PMI che vivono di innovazione come Menarini, fino agli uffici nazionali dei brevetti che sempre di più si occupano di sviluppo di nuove idee oltreché di deposito e protezione.

Progetto di articolazione delle attività formative

ATTIVITÀ FORMATIVA (Insegnamento, laboratorio, tirocinio, stage, esame finale)		**ORE** (1)			ENTE (4) ome e nome	**ATENEO E DIPARTIMENTO DI AFFERENZA SSD**
Denominazione con relativo settore scientifico disciplinare (2)	CFU	Didattica frontale (3)	Didattica laboratoriale (3)	Studio individuale/ stage/ tirocinio		
Modulo 1: INTELLECTUAL PROPERTY						
Patents (IUS/04)	5	40	10	75	Caforio Giuseppe	Università degli Studi di Perugia, Dipartimento di Giurisprudenza, CIRIAF IUS/04
Trademarks and designs (IUS/01)	5	40	10	75	Cianci Alberto Giulio	Università degli Studi di Perugia, Dipartimento di Scienze Politiche, CIRIAF IUS/01
Plant varieties and geographical indications (AGR/01)	5	40	10	75		Esperto esterno
Copyright, know-how, transfer and licensing of intellectual property rights (IUS/04) (IUS/04) Mod.1: Copyright (4 CFU) Mod.2: Know-how (1 CFU) Mod. 3: Transfer and Licensing (1 CFU)	6	48	12	90	Mod. 1-3: Schiuma Laura (50 ore) Mod. 2: Esperto esterno (10 ore)	Università degli Studi di Perugia, Dipartimento di Economia, CIRIAF IUS/04 Esperto esterno
IP systems and process of granting (EPO, EUIPO, WIPO) (IUS/04) Mod.1: Intellectual property systems (3 CFU) Mod.2: process of granting (1 CFU)	4	32	8	60		Esperto esterno
Digital innovation (INF/01)	4	32	8	60	Milani Alfredo	Università degli Studi di Perugia, Dipartimento di

						Matematica e Informatica, CIRIAF INF/01
Modulo 2: TECHNOLOGY TRANSFER						
History and Anthropology of Innovation (SPS/09)	5	40	10	75	Ullan de La Rosa Javier	University of Alicante, Dep. of Sociology II SPS/09
Innovation finance and proof of concept (SECS-P/09)	5	40	10	75		Esperto esterno
Business planning of a technology start up (SECS-P/08) Mod. 1: Economics and management of scientific-technological innovation (1.5 CFU) Mod. 2: Market analysis tools (2 CFU) Mod. 3: Business planning of a technology start up (1.5 CFU)	5	40	10	75	Ferrucci Luca (15 ore) Runfola Andrea (20 ore) Rizzi Francesco (15 ore)	Università degli Studi di Perugia, Dipartimento di Economia, CIRIAF SECS-P/08
Corporate finance for start ups (SECS-P/11)	5	40	10	75	Nadotti Loris Lino Maria (20 ore) Gallo Manuela (15 ore) Vannoni Valeria (15 ore)	Università degli Studi di Perugia, Dipartimento di Economia, CIRIAF SECS-P/11
Sustainability as an innovation tool (ING-IND/11) Mod. 1: Sustainability indicators (1 CFU) Mod. 2: Circular Economy Fundamentals (1 CFU)	2	16	4	30	Rossi Federico (10 ore) Castellani Beatrice (10 ore)	Università degli Studi di Perugia, Dipartimento di Ingegneria, CIRIAF ING-IND/11
Ethics and technology transfer Mod. 1: Ethics (SPS/09) (3 CFU) Mod. 2: Communication for innovation and technology transfer (SPS/08) (2CFU)	5	40	10	75	Flavia Marcacci (25 ore) Esperto Esterno (5 ore) Mazzoni Marco (20 ore)	Pontificia Università Lateranense Esperto Esterno Università degli Studi di Perugia, Dipartimento di Scienze Politiche, CIRIAF SPS/08
Innovation ecosystems (SECS-P/08)	4	32	8	60		Esperto esterno
		Totale ore: 480	Totale ore: 120	Totale ore: 900		
Stage/tirocinio (tirocinio formativo)	7	175				

Prova/e finale/i	3	75		
	Totale CFU: 70	Totale Ore: 1750		

(1) Ogni CFU corrisponde a 25 ore complessive di lavoro per lo studente. Il numero complessivo delle ore di ogni attività formativa va ripartito nelle colonne sottostanti.
(2) L'indicazione del settore scientifico-disciplinare è richiesto solo per gli insegnamenti e i laboratori disciplinari. In caso di insegnamento modulare inserire fra parentesi la parola "modulo" dopo la denominazione dell'insegnamento.
(3) Le ore di didattica laboratoriale devono essere sommate alle ore di didattica frontale per il calcolo delle percentuali previste dall'art.9 del Regolamento in materia di corsi per master universitario e corsi di perfezionamento.
(4)Se l'insegnamento è affidato ad un esperto di chiara fama riportare solo la dizione: "esperto esterno"

Il Collegio Docenti del Master provvederà a definire eventuali sostituzioni di docenti in caso di necessità.
Si richiede inoltre di poter andare in deroga a quanto deliberato dal Consiglio di Amministrazione nella seduta del 13 aprile 2016 con riferimento al costo orario dei docenti esterni. Il piano del Master consente infatti l'erogazione di una retribuzione oraria pari ad Euro 100.

	ORE DID.ASSISTITA (frontale+laboratoriale)	PERCENTUALE
Docenti Dip. proponente	330	55 % (*)
Docenti universitari (Dip. Proponente +altri dip.+altri atenei)	405	67 % (**)
Esperti chiara fama	195	33 %

(*)Tale percentuale deve essere superiore o uguale al 25%del totale di ore di didattica assistita.
(**)Tale percentuale deve essere superiore o uguale al 45%del totale di ore di didattica assistita.

☒	**Proposta di contratti per attività di laboratorio, tutorato o integrative con PTA e con personale esterno**

Sede/sedi di svolgimento delle attività (comprese quelle di tirocinio /stage): Attività di didattica presso il CIRIAF e altre sedi individuate dal Collegio dei Docenti del master. Tirocini da stabilire mediante accordi di collaborazione con enti e aziende.

Numero massimo di ammissibili	25

Numero minimo degli iscritti. In caso di mancato raggiungimento di tale numero, il Corso non può essere attivato	15

Numero di eventuali uditori ammissibili al corso (agli uditori sarà rilasciato solo un attestato di partecipazione)	0

Nominativi dei componenti il Collegio dei Docenti (art.8 Regolamento in materia di corsi per master universitario e corsi di perfezionamento)
Rossi Federico, Caforio Giuseppe, Cianci Alberto Giulio, Milani Alfredo, Ferrucci Luca, Nadotti Loris Lino Maria, Mazzoni Marco, Castellani Beatrice

Borse di Studio:

Eventuali enti e/o soggetti esterni disposti a collaborare a vario titolo	

Impegno delle aziende e delle strutture sanitarie ad autorizzare gli studenti allo svolgimento di tutte le attività cliniche, diagnostiche e strumentali, anche su pazienti, previste dal programma formativo del corso(*da compilare solo per corsi di master di area medica e sanitaria)*	☐	**Si**	☐	**No**

*

Centro di Spesa (Struttura cui è affidata la gestione amministrativa e finanziaria)	[ ] Dipartimento di _____ Delibera del _____ [X] Centro interdipartimentale __CIRIAF_____

PIANO FINANZIARIO		
numero minimo partecipanti	15	
Contributo pro-capite per l'iscrizione	6600	
RISORSE FINANZIARIE		
Ente finanziatore	*0*	*€ 0*
Quote di iscrizione - n.studenti *euro/studente		€ 99.000
TOTALE RISORSE		**€ 99.000**
COSTI DI GESTIONE		
Costi diretti		
docenza (100€/ora)	100	€ 60.000
es.materiale didattico 500 euro a studente		€ 7.500
tutor 3000 a tutor ogni 5 studenti	3	€ 9.000
altri costi (8 trasferte)		€ 7.650
Costi indiretti		
Quota Amministrazione centrale - 10% contribuzione studenti		€ 9.900
Quota Dipartimento - 5% contribuzione studenti		€ 4.950
TOTALE COSTI		**€ 99.000**

(*) Il Consiglio di Amministrazione nella seduta del 13/04/2016 ha stabilito che il trattamento economico c

lei docenti esterni per ciascuna ora di insegnamento sia di 35 euro, al lordo degli oneri di Ateneo.

PIANO FINANZIARIO		
numero massimo partecipanti	25	
Contributo pro-capite per l'iscrizione	6600	
RISORSE FINANZIARIE		
Ente finanziatore	*0*	*€ 0*
Quote di iscrizione - n.studenti *euro/studente		€ 165.000
TOTALE RISORSE	25	**€ 165.000**
COSTI DI GESTIONE		
Costi diretti		
docenza (100€/ora)		€ 60.000
es.materiale didattico 500 euro a studente		€ 12.500
tutor (3000 euro a tutor ogni 5 studenti)	5	€ 15.000
altri costi (8 trasferte)		€ 7.650
Costi indiretti		
Quota Amministrazione centrale - 10% contribuzione studenti		€ 16.500
Quota Dipartimento - 5% contribuzione studenti	5	€ 8.250
Quota CIRIAF - 27% contribuzione studenti		€ 45.100
TOTALE COSTI		**€ 165.000**

Allegato N. 1 al punto dell'ordine del giorno N. 14

Titolo del progetto:

"Analisi teorica e sperimentale della tecnologia Solid Oxide Cell sia per la generazione di potenza che per la produzione di syngas da fonte rinnovabile"

Relazione - IV anno di attività

Maggio 2018 – Aprile 2019

Giovanni Cinti Ph.D – RTDa tempo definito

Attività di Ricerca

L'attività di ricerca ha riguardato lo studio della tecnologia SOFC/SOE per la produzione di potenza e per la produzione via elettrolisi di combustibili gassosi quali idrogeno o miscele ad alto contenuto di idrogeno (syngas).

L'attività di questo anno ha portato a completamente lo studio dell'elettrolisi ad alta temperatura ed, in particolare, il ruolo dell'elettrodo ossigeno e dei gas utilizzati come sweep gas. In aggiunta significativo sforzo è stato dedicato al miglioramento della qualità dei test. Nuovi sealing a nuovi current collector sono stati testati sia per ciò che riguarda i materiali che le geometrie. Lo scopo, raggiunto, è stato quello di ottenere un aumento dell'OCV e della corrente massima ottenibile. Il nuovo standard di test permetterà le studio sistematico dei processi di elettrolisi e di fuel cell. In particolare, per poter valutare correttamente l'effetto del funzionamento SOFC e SOE, è stata perfezionata la tecnica di test di lunga durata. Questo ha richiesto la modifica dei materiali, in particolare i coating, l'aumento di affidabilità del banco prova e tecniche di analisi online, quali l'EIS, e soprattutto le tecniche di post test, quali l'analisi SEM, l'EDX e la XRD.

Nel dettaglio le specifiche attività sono state:

- Aggiornamento bibliografico dei temi di ricerca riguardanti SOFC e SOE;
- Progettazione campagna prove finalizzata all'analisi delle performance della cella e allo studio dell'effetto della composizione;
- Realizzazione dei test;
- Analisi dati e studio dei risultati;
- Pubblicazione dei risultati in conferenze e giornali scientifici;
- Supporto e chiusura delle rendicontazioni del progetti PON: "SMART GENERATION" e "FCLAB";
- Raccordo e coordinamento tra le attività del Dipartimento dell'Università degli Studi di Perugia e gli altri partner dei progetti PON;
- Partecipazione alla stesura e presentazione di progetti sottoposti a finanziamento a valere su fondi nazionali ed europei;
- Attività tecnica/sperimentale di laboratorio: utilizzo e progettazione di strumenti e tecniche per lo studio di sistemi celle a combustibile/elettrolizzatori ad alta temperatura;
- Supporto all'acquisto di strumenti e materiale di consumo necessari all'attività di ricerca;
- Partecipazione alle attività dell'associazione HYDROGEN EUROPE RESEARCH di cui il Dipartimento è membro, associazione che gestisce in partenariato con la Commissione e il raggruppamento degli industriali i fondi Comunitari destinati ad Idrogeno e celle a combustibile;
- Gestione di due progetti europei a valere sul fondo HORIZON2020: NET TOOLS e ELECTROU dei quali sono responsabile scientifico per l'Università degli Studi di Perugia;
- Scrittura, sottomissione e gestione, quale responsabile scientifico, del progetto TEZIO a valere sul bando della Fondazione Cassa di Risparmio di Perugia;
- Gestione del progetto Europeo "HySchools" a valere sul bando ERASMUS+;
- Partecipazione alla conferenze: NH_3 event Europe, Rotterdam June 6-7 2019; 13th European SOFC & SOE Forum 2018;
- Partecipazione al programma ERASMUS + for training presso DTU;

Pubblicazioni

Specificatamente alle attività di ricerca relative al progetto del contratto e relative al periodo di riferimento del presente report sono state pubblicati i seguenti lavori interamente riportati in allegato:

1. Barelli, L., Bidini, G., Cinti, G. "Air variation in SOE: Stack experimental study"(2018) International Journal of Hydrogen Energy, 43 (26), pp. 11655-11662. DOI: 10.1016/j.ijhydene.2018.01.070
2. Barelli, L.; Bidini, G.; Cinti, G. "Airflow Management in Solid Oxide Electrolyzer (SOE) Operation: Performance Analysis", ChemEngineering 2017, 1, 13
3. Barelli, L., Bidini, G., Cinti, G. "Steam as sweep gas in SOE oxygen electrode" (2018) Journal of Energy Storage, 20, pp. 190-195. DOI:10.1016/j.est.2018.09.009

In aggiunta grazie ad ulteriori collaborazioni sviluppate in questi anni e ad attività di ricerca svolte precedentemente sono stati pubblicati i seguenti lavori, anch'essi riportati in allegato:

1. Liso, V., Savoia, G., Araya, S.S., Cinti, G., Kær, S.K. "Modelling and experimental analysis of a polymer electrolyte membrane water electrolysis cell at different operating temperatures" (2018) Energies, 11 (12), art. no. 3273. DOI: 10.3390/en11123273
2. Barelli, L., Bidini, G., Cinti, G. "Steam vs. dry reformer: Experimental study on a solid oxide fuel cell short stack" (2018) Catalysts, 8 (12), art. no. 599. DOI: 10.3390/catal8120599
3. Cinti, G., Bidini, G., Hemmes, K. "Comparison of the solid oxide fuel cell system for micro CHP using natural gas with a system using a mixture of natural gas and hydrogen" (2019) Applied Energy, pp. 69-77. DOI: 10.1016/j.apenergy.2019.01.039

In stesura o in attesa di pubblicazione:

1. G. Cinti, L. Barelli, G. Bidini "The use of ammonia as a fuel for transport: integration with solid oxide fuel cells" sottomesso su *ATI Conference*;
2. L. Barelli, G. Bidini, G. Cinti "High temperature electrolysis using Molten Carbonate Electrolyzer" in stesura;

I risultati dell'attività di ricerca sono stati presentati in conferenze e meeting internazionali:

1. G. Cinti, " Degradation of SOFC cells when fueled with ammonia", NH3 event Europe, Rotterdam June 6-7 2019;
2. Cinti, G., Barelli, L., Bidini, G., Milewski J. "Modeling a molten carbonate electrolysis cell through reduced-order approach", 11th International Symposium on Molten Salts;
3. Cinti, G., Barelli, L., Bidini, G. "Study of STEAM as sweep gas in SOE oxygen electrode", 13th European SOFC & SOE Forum 2018;

Attività didattica integrativa

Sullo stesso tema delle attività di ricerca è stata realizzata l'attività di formazione ed affiancamento – didattica integrativa. In particolare:

- Supporto alle attività di formazione riguardanti lo sviluppo e l'utilizzo di sistemi di controllo per banchi prova di celle a combustibile;

- Formazione teorica sull'idrogeno e celle a combustibile, sulle problematiche dell'integrazione e sui componenti necessari al funzionamento corretto del sistema;
- Attività formative nell'ambito dell'Alternanza Scuola Lavoro;

ARTICLE IN PRESS

INTERNATIONAL JOURNAL OF HYDROGEN ENERGY XXX (2018) 1–8

Available online at www.sciencedirect.com

ScienceDirect

journal homepage: www.elsevier.com/locate/he

Air variation in SOE: Stack experimental study

*L. Barelli, G. Bidini, G. Cinti**

Department of Engineering, University of Perugia, Via G. Duranti 1/A4, Perugia 06125, Italy

ARTICLE INFO

Article history:
Received 22 September 2017
Received in revised form
27 December 2017
Accepted 13 January 2018
Available online xxx

Keywords:
SOE
Hydrogen production
Air variation
Energy storage

ABSTRACT

Solid oxide electrolyzer are the electrolysis technology that can achieve higher efficiency and power densities. This study aims to analyze the role of air when used as a sweep gas in the oxygen electrode of a SOE. Based on experimental activity on a SOE stack, both polarization and constant utilization tests were performed changing the air flow rate in the stack. Due to air reduction, oxygen concentration of off gasses was increased from 25% up to 50%. All experimental results indicated that, reducing air flow down to 9% of nominal value, the effect on performances is negligible and variation of voltage is maintained below 2%. Thermoneutral condition was achieved at 500 mA cm^{-2}. Advantages of air reduction in SOE operation stand in both capital and operation costs. System design is simplified, ancillary consumptions are reduced and, in view of oxygen as a by-product, high oxygen concentrated off gases are produced with lower energy request for possible O_2 separation.

Introduction

Solid Oxide Electrolyzer (SOE) has been recently presented as a high efficiency technology to produce hydrogen as a green energy carrier for energy storage [1,2]. The scheme of a SOE stack is reported in Fig. 1. The hydrogen electrode and oxygen electrode reactions are the followings:

$$H_2O + 2e^- \rightarrow H_2 + O^{2-} \quad \text{hydrogen electrode} \qquad \text{(i)}$$

$$O^{2-} \rightarrow \frac{1}{2}O_2 + 2e^- \quad \text{oxygen electrode} \qquad \text{(ii)}$$

The hydrogen electrode is fed with a mixture of steam and hydrogen. Hydrogen is usually in small concentration and is fed only to maintain a reductive atmosphere and protect the catalyst from the well-known problem of reoxidation [3]. Electrochemical reaction at the hydrogen electrode consists in the decomposition of steam and the production of hydrogen, while oxides are produced and brought via the electrolyte to the oxygen electrode. The gas exiting the hydrogen electrode is a mixture with high concentration of hydrogen and the amount of steam that did not react. At the oxygen electrode air is usually fed to collect and transport oxygen out of the device. The off gasses of oxygen electrode are a mixture of nitrogen and oxygen with concentration of oxygen higher than air (21%), depending on both electrolysis reaction rate and air flow rate.

Main studies concerning SOE operation are focused on the system integration to optimize benefits of the technology [4–7] or the optimization of operative conditions such as hydrogen electrode composition [8], operative temperature and reactant utilization [9–14]. Regarding the oxygen electrode the main effort was given to develop efficient materials [15–20], but very small attention has been focused on oxygen electrode gas operation. From the chemical point of view there is no real need of any gas flow in the oxygen side of a solid oxide electrolyte cell, since oxygen is a product and not a reactant. Gas is fluxed mainly as a sweep gas to collect oxygen and flow it out from the system. Due to low cost and wide

* *Corresponding author.*
E-mail address: giovanni.cinti@unipg.it (G. Cinti).
https://doi.org/10.1016/j.ijhydene.2018.01.070

Please cite this article in press as: Barelli L, et al., Air variation in SOE: Stack experimental study, International Journal of Hydrogen Energy (2018), https://doi.org/10.1016/j.ijhydene.2018.01.070

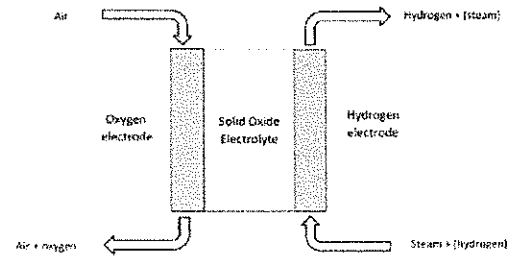

Fig. 1 – Scheme of a SOE stack.

availability, air is used as sweep gas. An additional reason for using air is the experience available derived from SOFC where, differently from SOE, air is necessary to supply oxygen, that is a reactant, to the cell.

Air flow plays a significant role in electrochemical equilibrium: in principle, the air flow reduces losses due to diffusion polarizations. In addition, oxygen concentration is reduced thanks to the effect of nitrogen dilution. This has a beneficial effect on the voltage because oxygen is a product of the reaction and Nernst losses increase with oxygen concentration. Obviously, air contains oxygen and therefore listed benefits are not maximized. In this sense, the utilization of pure nitrogen or of any oxygen free gas brings additional benefits, but it can be hardly compared to air in terms of availability and cost.

Different considerations arise, concerning oxygen concentration in the electrode, if the production of pure oxygen as SOE by-product is considered. In case of hydrogen and oxygen co-generation, an additional unit for O_2 separation is necessary and all available technologies benefit from a high oxygen concentration in the off gases.

Therefore, a trade-off must be found, considering also what discussed above in reference to the positive effect of low oxygen concentrations on the electrochemical equilibrium. Moreover, feeding air to the electrode under high flow rates has also drawbacks, mainly at system level. Before entering the stack, air must be heated to avoid thermal shock to the materials. The heat requirement can be easily recovered from electrode off gasses that have higher gas flow and higher temperature. At this regard it is remarked that: i) a higher gas flow is guaranteed by the oxygen flow rate coming from the hydrogen electrode side; ii) Off gasses outlet temperature can be considered the stack operative one, usually higher than the inlet value because final temperature increase is realized inside the stack. This latter aspect is extremely important because the heat necessary to increase air temperature is subtracted to the reaction and, thus, it influences SOE efficiency. The air flow variation has, therefore, an effect on the operative point of the system and on the its efficiency.

For what is in the knowledge of the authors, literature does not report any experience on the variation and the optimization of air flow in a SOE stack. In all stack tests reported in literature [13,20–24], air is used at the oxygen electrode and kept to a generic constant value, while varying hydrogen electrode conditions or stack operative temperature. No specific design of the oxygen electrode flow is also reported in Ref. [25] but, in this case, pure oxygen is used as sweep gas. In Ref. [26] oxygen electrode was fed with nitrogen, air and with no gas. The effect on OCV and on performances is highlighted but no variation of gas flows is performed nor any design indication is provided for the selected values. Also in Ref. [27] two different stacks were tested with no sweep gas or with a constant value of air flow rate.

In this study, we aim to answer the following questions:

- What is the effect of air flow reduction on SOE performances?
- What is the effect of air flow reduction on SOE thermal equilibrium?

An experimental campaign was designed and air study test was performed on a solid oxide short stack. Both polarization curves and long-term tests were performed changing the air flow rate fed to the stack.

Results show how reducing air flow down to 9% of nominal value, voltage variation is below 2%. The temperature variation at the oxygen electrode outlet confirms the slight decrease in stack efficiency when air flow rate is reduced.

SOE experimental characterization

Materials

The study is based on experimental activity. Tests were performed on a commercial SOFC short stack (supplied by SOLID Power) that was operated in electrolysis mode in a test rig which realizes gas supply, temperature control, current control and measurement of temperature and voltages. The short stack is composed of six planar anode supported cells. The cell is a sandwich of Ni/8YSZ anode, 8YSZ electrolyte, GDC barrier layer and LSCF cathode. Every cell has an active area of 80 cm^2. The stack operates in the range 650–800 °C. Each cell is monitored by means of voltage sensors, while no direct measurements of temperature can be realized in the stack. Four thermocouples are placed close to the stack in the four pipes: two entering and two exiting the stack (two thermocouples per electrode). Regarding gas supply, the hydrogen electrode is fed with a mixture of steam and hydrogen produced in a controlled evaporator mixer where water is evaporated and mixed with hydrogen. Both water and hydrogen are stored in external pressurized thanks and are controlled via a flow meter controller. In a similar way air is stored and fluxed into the oxygen electrode. Test rig and instrumentations are deeply described elsewhere [28].

Test campaign

The aim of the test campaign is to perform experimental studies of SOE operation varying the Air flow into the stack. Two different test types where designed: polarization curves and RU tests. The first type is the traditional polarization curve performed keeping constant gas flows and temperature,

Please cite this article in press as: Barelli L, et al., Air variation in SOE: Stack experimental study, International Journal of Hydrogen Energy (2018), https://doi.org/10.1016/j.ijhydene.2018.01.070

increasing current at constant step up to a defined value. The second test type is performed varying current in a specific range and changing, at the same time, gas flows so to keep constant the ration between current and gases. Such a test procedure is more similar to the real operation of the system where variation of gas flows is expected when current, and consequently power, needs to be changed. For the design of the test campaign several parameters where defined. Considering electrolysis reaction in SOE, hydrogen and oxygen produced in the operation can be calculated as follows (Eq. (iii) and Eq. (iv)):

$$n_{H2out} = \frac{I \cdot N}{2 \cdot F} \quad \text{(iii)}$$

$$n_{O2out} = \frac{I \cdot N}{4 \cdot F} \quad \text{(iv)}$$

where I is stack current, N is the number of cells, F is the Faraday constant and n_{H2out} and n_{O2out} are molar flows of hydrogen and oxygen respectively produced in the stack. Reactant utilization (RU) is the ration between the steam that reacts in the stack, same molar quantity of hydrogen produced, and the total steam fed at the inlet. RU parameter defined as follows (Eq. (v)):

$$RU = \frac{n_{H2out}}{n_{H_2O}} = \frac{I \cdot N}{2 \cdot F \cdot n_{H_2O}} \quad \text{(v)}$$

where n_{H2O} is the molar flow of inlet steam. Final concentration of oxygen (O_2) is the concentration at the oxygen electrode output evaluated according to the following equation (Eq. (vi)) derived from the relation between oxygen production and current.

$$O_2 = \frac{n_{O2out}}{n_{air} + n_{O2out}} = \frac{0.21 \cdot n_{air} + \frac{I \cdot N}{4 \cdot F}}{n_{air} + \frac{I \cdot N}{4 \cdot F}} \quad \text{(vi)}$$

in Eq. (vi) n_{air} represents the molar flow of air. Both RU and O_2 where used in defining the test campaign as indirect parameters for n_{air} and n_{H2O} calculation. Specifically, once a current density is selected, in our case 500 mA cm^{-2} (@500), is possible to calculate total current and following gas flows per each RU and O_2 parameter. Finally, the sweep gas parameter (S/O_2) can be calculated as the ration between molar air flow and oxygen produced by the reaction (Eq. (vii)):

$$S/O_2 = \frac{n_{air}}{n_{O2out}} = \frac{n_{air}}{\frac{I \cdot N}{4 \cdot F}} \quad \text{(vii)}$$

Also for sweep factor can be calculated at current density of 500 mA cm^{-2} (S/O_2@500). Six polarization curves where selected to be tested in the stack. Gas composition, indirect parameters and gas flows entering the stack are reported in Table 1. Operative temperature at 750 °C, hydrogen electrode composition H_2:H_2O 10:90 and RU@500 equal to 0.7 were kept constant for all curves. Operative temperature is considered the state of the art for SOFC and SOE. Gas composition is the hydrogen steam mixture that guarantees higher efficiencies [29], while RU@500 was fixed at 0.7 as a tradeoff between low values, that reduce concentration losses, and higher ones, preferable from the system point of view to reduce steam production and relative heat requirements. Finally, the six polarization curves differ for the air flow rate. In designing the campaign O_2@500 was chosen as the main parameter, varying from 25% to 50% at steps of 5%. Lower values of O_2 are difficult because require high values of air flow that could not be realized in the test rig. Oxygen concentration of 25% is already a very low value considering that there is a theoretical minimum of 21% due to oxygen concentration in air. Maximum value of 50% was considered as an acceptable value that reduces the risk of material degradation due to oxidant atmosphere.

Regarding the second part of the study, concerning the so-called RU tests, the campaign was designed as reported in Table 2.

Same parameters values were chosen for the RU test but, in this case, there is no need to indicate a specific current density for RU and O_2 parameters because gas values change at each current step to maintain constant RU and O_2 for all current density values. In each RU test current values were 10, 20, 30 and 40 A, corresponding to current density from 125 to 500 mA cm^{-2}.

Results

Polarization results are reported in Fig. 2. Each polarization point was kept for 1 min and reported values are the average in that period. In Fig. 2a, cell voltage values are reported as function of current density. In this figure and in all the following ones cell voltage is calculated as cell average between the six cells. Very small variation can be deduced from

Table 2 – RU test campaign design.

	Temp. [°C]	H_2 [%]	H_2O [%]	RU	O_2 %
RU1	750	0.1	0.9	0.7	25%
RU2	750	0.1	0.9	0.7	30%
RU3	750	0.1	0.9	0.7	35%
RU4	750	0.1	0.9	0.7	40%
RU5	750	0.1	0.9	0.7	45%
RU6	750	0.1	0.9	0.7	50%

Table 1 – Design of polarization curves.

	TEMP. °C	H_2 %	H_2O %	RU@500	O_2@500 %	S/O_2@500	H_2O g h^{-1}	H_2 nl h^{-1}	AIR nl h^{-1}
POL01	750	0.1	0.9	0.7	25%	18.75	115.13	15.93	940.67
POL02	750	0.1	0.9	0.7	30%	7.78	115.13	15.93	390.20
POL03	750	0.1	0.9	0.7	35%	4.64	115.13	15.93	232.93
POL04	750	0.1	0.9	0.7	40%	3.16	115.13	15.93	158.43
POL05	750	0.1	0.9	0.7	45%	2.29	115.13	15.93	114.97
POL06	750	0.1	0.9	0.7	50%	1.72	115.13	15.93	86.50

Please cite this article in press as: Barelli L, et al., Air variation in SOE: Stack experimental study, International Journal of Hydrogen Energy (2018), https://doi.org/10.1016/j.ijhydene.2018.01.070

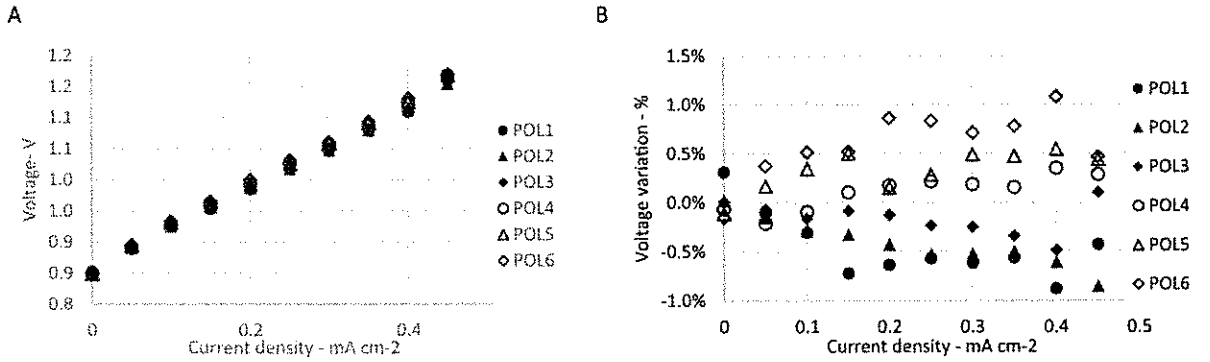

Fig. 2 – Results of polarization s test in terms of cell voltage and cell voltage variation as function of current density.

Table 3 – Polarization results in terms of OCV and ASR values.

	OCV – V	ASR – Ω cm^2
POL1	0.852	0.651
POL2	0.850	0.650
POL3	0.850	0.663
POL4	0.849	0.679
POL5	0.849	0.680
POL6	0.848	0.686

the graph and, with the aim of a deeper and more clear study, same values are reported in Fig. 2b, for each current density point, as variation between the measured values and the voltage averages of all compositions. The graph clearly shows that minimum variation was registered when changing air flow from POL1 to POL6. All variations stand below 1%. From Fig. 2b emerges that even such small variations have a trend related to gas compositions with a slight decrease in performances when going from POL1 to POL6. Air flow reduction has therefore a negative, but negligible, effect on performances.

The reason is that increasing air flow reduces losses due to diffusion polarizations. Moreover, oxygen concentration is reduced thanks to the effect of nitrogen dilution with corresponding lower Nernst losses.

This is evident also from the analysis of Area Specific Resistance (ASR) values obtained from polarization curves. Voltage variation with current density can be completely described by means of two parameters: cell open circuit voltage (OCV), equivalent to no current in drained from the stack, and curve slope obtained from data regression and usually called ASR. As evident in Table 3, the decrease in air flow rate causes a negligible OCV reduction and an increase in ASR. Variation of OCV is always lower than 0.3% with respect to the mean value of OCV relative to the six polarization curves; no effect is expected because there is no production of

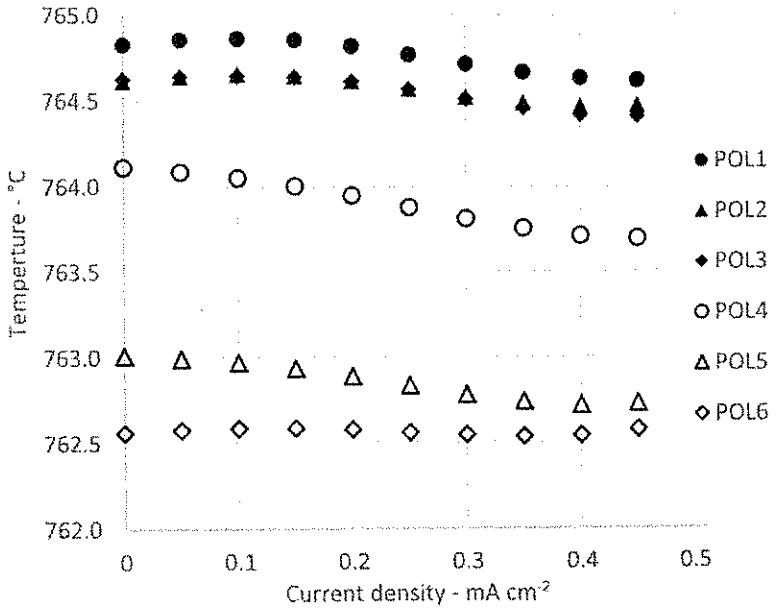

Fig. 3 – Variation of temperature of oxygen electrode as function of current density.

Please cite this article in press as: Barelli L, et al., Air variation in SOE: Stack experimental study, International Journal of Hydrogen Energy (2018), https://doi.org/10.1016/j.ijhydene.2018.01.070

oxygen at OCV and the same gas composition – pure air – is sent to the electrode. ASR variation, instead, achieves a maximum absolute deviation from the mean ASR value of 2.7%, related to the increase in losses at the oxygen electrode, of the same magnitude order of voltage deviations (Fig. 2b).

Therefore, a slight decrease in efficiency occurs at low air flow rates, compatible with lower stack temperature. What stated above is confirmed by the temperature variation measured at the oxygen electrode outlet which exhibits, as visible in Fig. 3, a monotonic decrease with air flow rate moving from POL1 to POL6.

Fig. 4 reports temperature difference between air electrode and hydrogen electrode. The decrease of air flow reduces, as expected, the temperature difference.

Finally, Fig. 5 shows the temperature trend at the oxygen electrode inlet as the result of the thermal balance at the cathodic regenerator. Specifically, nevertheless the temperature slightly lower at the regenerator inlet (electrode outlet visible in Fig. 3), reducing the air flow rate temperature increases at the stack inlet.

In the RU tests, each current condition was kept for 1 h before moving to the next step. Compared with the polarization curves, where each point is kept for only 1 min, temperature equilibrium is obtained and the stack reaches steady state condition. Values reported in following graphs are the average of samples taken during a 5 min period ending, to avoid possible border effect, 2 min before the new current condition. Fig. 6 reports values of RU tests as

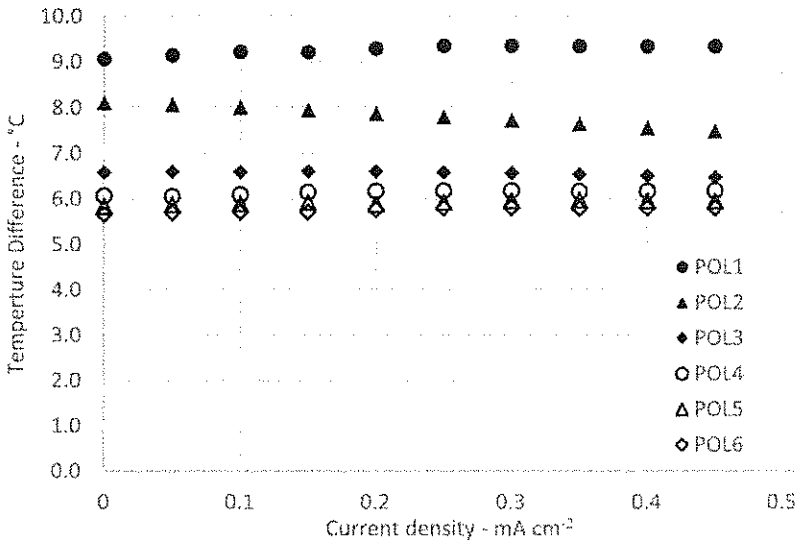

Fig. 4 – Temperature difference as function of current density.

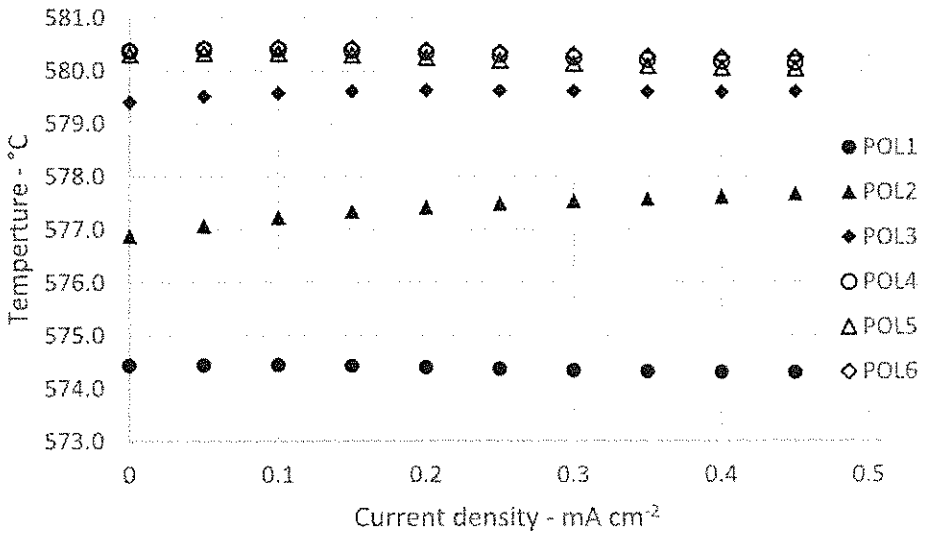

Fig. 5 – Temperature at oxygen electrode inlet.

Please cite this article in press as: Barelli L, et al., Air variation in SOE. Stack experimental study, International Journal of Hydrogen Energy (2018), https://doi.org/10.1016/j.ijhydene.2018.01.070

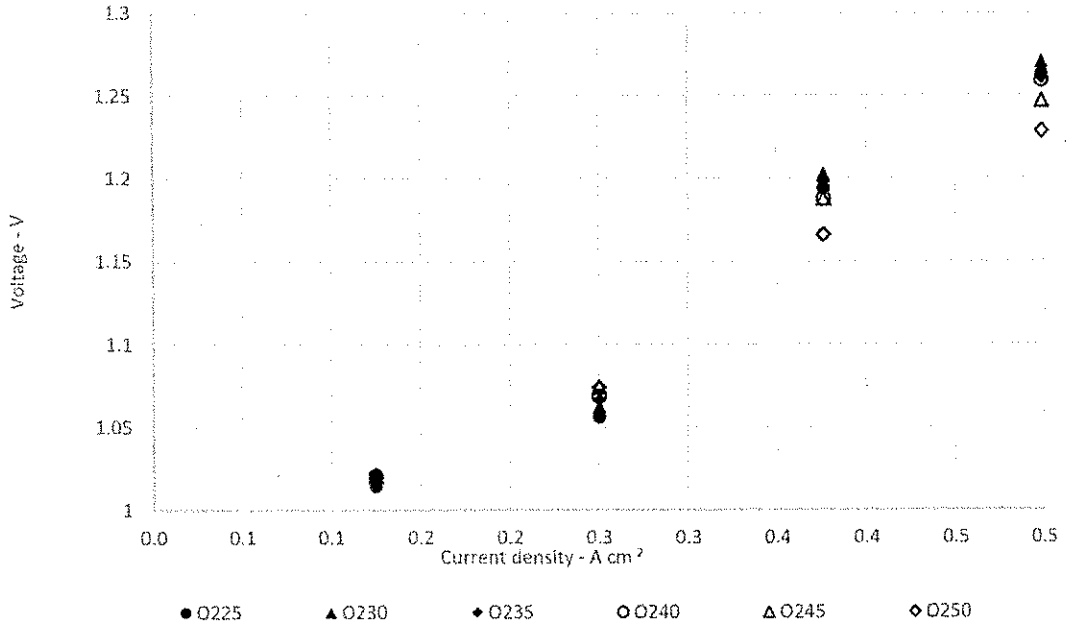

Fig. 6 – Variation of cell voltage as function of current density in RU tests.

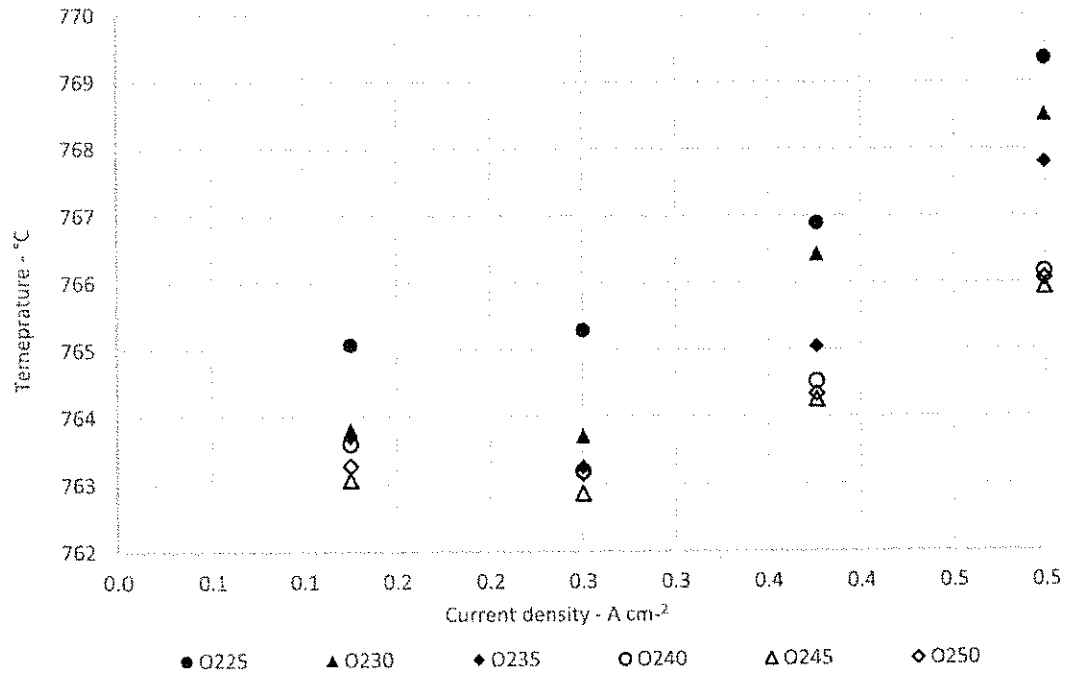

Fig. 7 – Oxygen electrode outlet temperature as function of current density.

cell voltage as function of current density for different values of the air flow rate (higher flow rates correspond to lower oxygen concentrations here investigated from 25% to 50%). Here again it emerges that the effect on the voltage of the different test conditions is negligible and all values have a random variation in the range of 2%. The figure shows a wider distribution of values for high current densities due to voltage instability occurring under these operating conditions.

Oxygen electrode temperature outputs are reported in Fig. 7. Temperature data did not suffer from the electrical instability and, therefore, show a coherent relation with

Please cite this article in press as: Barelli L, et al., Air variation in SOE: Stack experimental study, International Journal of Hydrogen Energy (2018), https://doi.org/10.1016/j.ijhydene.2018.01.070

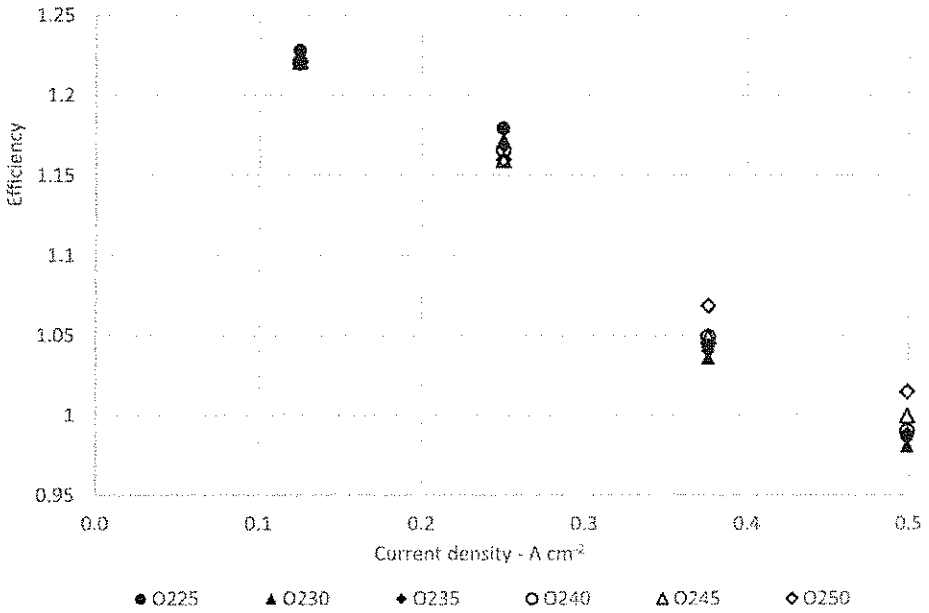

Fig. 8 – Stack efficiency during RU tests.

respect to what highlighted for the polarization tests. Specifically, reducing the air flow rate, the oxygen electrode outlet temperature slightly decreases. Concerning the variation with current density, all temperature trends exhibit an initial stable behavior and then an increase. Such trend is related to the heat equilibrium of the stack inside the furnace due to the chemical reaction that adsorbs part of the heat and compensate losses due to irreversibility: when current increases losses are higher and temperature raises.

Finally, in Fig. 8 stack efficiency of RU tests is reported. Efficiency values are calculated as the ration between the produced chemical energy, in terms of low heat value of produced hydrogen (n_{H2out}), and electrical power input. As expected the efficiency values start from values about the unit and reaches the thermoneutral condition, 100% efficiency, at 500 mA cm^{-2} of current density. Values greater than 1 are possible due to the definition of efficiency used in the graph that does not consider the heat absorbed by the stack and supplied in the test ring by the furnace. Efficiencies values suffer of voltage instability at high current, therefore, like for voltages, the difference between the curves reported in the figure can not be used to make any compartment evaluations.

Conclusions

The performed experimental study permitted to evaluate the effect of air flow reduction when operating a SOE stack for hydrogen production. Both polarization and RU tests indicated that effect of air reduction down to 9.2% of initial value is negligible. All measured variations are in the range of 2% maximum. Thermoneutral condition was achieved at current density of 0.5 A cm^{-2}. The study demonstrated that air reduction can be performed with no electrochemical losses compared to full air conditions. A reduction in air flow will introduce system advantages in terms of blower consumption and heat exchanger dimension. Moreover, a concentration of 50% of oxygen can open the route for a low-cost production of pure oxygen from SOE operation as additional product. Future development will focus on the material stability due to high oxygen concentration.

Acknowledgments

The research activity has been carried out within the project FUEL CELL LAB, funded by the Italian MIUR (PON03PE_00109_1).

REFERENCES

[1] Bičáková O, Straka P. Production of hydrogen from renewable resources and its effectiveness. Int J Hydrogen Energy 2012;37:11563–78. https://doi.org/10.1016/j.ijhydene.2012.05.047.
[2] Holladay JD, Hu J, King DL, Wang Y. An overview of hydrogen production technologies. Catal Today 2009;139:244–60. https://doi.org/10.1016/j.cattod.2008.08.039.
[3] O'Brien JE, Stoots CM, Herring JS, Hartvigsen JJ, Lessing PA, Hartvigsen JJ, et al. Performance measurements of solid-oxide electrolysis cells for hydrogen production. J Fuel Cell Sci Technol 2005;2:156. https://doi.org/10.1115/1.1895946.
[4] AlZahrani AA, Dincer I. Thermodynamic and electrochemical analyses of a solid oxide electrolyzer for hydrogen production. Int J Hydrogen Energy 2017:1–10. https://doi.org/10.1016/j.ijhydene.2017.03.186.
[5] Chen B, Xu H, Zhang H, Tan P, Cai W, Ni M. A novel design of solid oxide electrolyser integrated with magnesium hydride bed for hydrogen generation and storage – a dynamic simulation study. Appl Energy 2017;200:260–72. https://doi.org/10.1016/j.apenergy.2017.05.089.

[6] Gomez SY, Hotza D. Current developments in reversible solid oxide fuel cells. Renew Sustain Energy Rev 2016;61:155–74. https://doi.org/10.1016/j.rser.2016.03.005.

[7] Zahadat P, Milewski J. Modeling electrical behavior of solid oxide electrolyzer cells by using artificial neural network. Int J Hydrogen Energy 2015;40:7246–51. https://doi.org/10.1016/j.ijhydene.2015.04.042.

[8] Zhang L, Zhu X, Cao Z, Wang Z, Li W, Zhu L, et al. Pr and Ti co-doped strontium ferrite as a novel hydrogen electrode for solid oxide electrolysis cell. Electrochim Acta 2017;232:542–9. https://doi.org/10.1016/j.electacta.2017.02.168.

[9] Liu L, Zhou X, Wang Y, Li S, Yin R, Guo P, et al. Composite ceramic cathode La 0.9 Ca 0.1 Fe 0.9 Nb 0.1 O 3-δ/Sc 0.2 Zr 0.8 O 2−δ towards efficient carbon dioxide electrolysis in zirconia-based high temperature electrolyser. Int J Hydrogen Energy 2017:1–11. https://doi.org/10.1016/j.ijhydene.2017.04.291.

[10] Schefold J, Brisse A, Poepke H. 23,000 H steam electrolysis with an electrolyte supported solid oxide cell. Int J Hydrogen Energy 2016;2:3–14. https://doi.org/10.1016/j.ijhydene.2017.01.072.

[11] Mizusawa T, Araki T, Mori M. Temperature and reactive current distributions in microtubular solid oxide electrolysis cells. Int J Hydrogen Energy 2016;41:13888–900. https://doi.org/10.1016/j.ijhydene.2016.05.161.

[12] Ferrero D, Lanzini A, Santarelli M, Leone P. A comparative assessment on hydrogen production from low- and high-temperature electrolysis. Int J Hydrogen Energy 2013;38:3523–36. https://doi.org/10.1016/j.ijhydene.2013.01.065.

[13] Nguyen VN, Fang Q, Packbier U, Blum L. Long-term tests of a Jülich planar short stack with reversible solid oxide cells in both fuel cell and electrolysis modes. Int J Hydrogen Energy 2013;38:4281–90. https://doi.org/10.1016/j.ijhydene.2013.01.192.

[14] Xu Z, Zhang X, Li G, Xiao G, Wang JQ. Comparative performance investigation of different gas flow configurations for a planar solid oxide electrolyzer cell. Int J Hydrogen Energy 2017;2. https://doi.org/10.1016/j.ijhydene.2017.02.097.

[15] Wang X, Yu B, Zhang W, Chen J, Luo X, Stephan K. Microstructural modification of the anode/electrolyte interface of SOEC for hydrogen production. Int J Hydrogen Energy 2012;37:12833–8. https://doi.org/10.1016/j.ijhydene.2012.05.093.

[16] Wind-hydrogen used for first time at vehicle fuelling station in Germany. Fuel Cells Bull 2012;2012:14. https://doi.org/10.1016/S1464-2859(12)70148-7.

[17] Khan MS, Xu X, Zhao J, Knibbe R, Zhu Z. A porous yttria-stabilized zirconia layer to eliminate the delamination of air electrode in solid oxide electrolysis cells. J Power Sources 2017;359:104–10. https://doi.org/10.1016/j.jpowsour.2017.05.049.

[18] Nechache A, Mansuy A, Petitjean M, Mougin J, Mauvy F, Boukamp BA, et al. Diagnosis of a cathode-supported solid oxide electrolysis cell by electrochemical impedance spectroscopy. Electrochim Acta 2016;210:596–605. https://doi.org/10.1016/j.electacta.2016.05.014.

[19] Moçoteguy P, Brisse A. A review and comprehensive analysis of degradation mechanisms of solid oxide electrolysis cells. Int J Hydrogen Energy 2013:1–16. https://doi.org/10.1016/j.ijhydene.2013.09.045.

[20] Zheng Y, Li Q, Chen T, Wu W, Xu C, Wang WG. Comparison of performance and degradation of large-scale solid oxide electrolysis cells in stack with different composite air electrodes. Int J Hydrogen Energy 2015;40:2460–72. https://doi.org/10.1016/j.ijhydene.2014.12.101.

[21] Herring JS, O'Brien JE, Stoots CM, Hawkes G, Hartvigsen JJ, Shahnam M. Progress in high-temperature electrolysis for hydrogen production using planar SOFC technology. Int J Hydrogen Energy 2007;32:440–50. https://doi.org/10.1016/j.ijhydene.2006.06.061.

[22] Kim S-D, Yu J-H, Seo D-W, Han I-S, Woo S-K. Hydrogen production performance of 3-cell flat-tubular solid oxide electrolysis stack. Int J Hydrogen Energy 2012;37:78–83. https://doi.org/10.1016/j.ijhydene.2011.09.079.

[23] Li Q, Zheng Y, Guan W, Jin L, Xu C, Wang WG. Achieving high-efficiency hydrogen production using planar solid-oxide electrolysis stacks. Int J Hydrogen Energy 2014;39:10833–42. https://doi.org/10.1016/j.ijhydene.2014.05.070.

[24] Zheng Y, Li Q, Guan W, Xu C, Wu W, Wang WG. Investigation of 30-cell solid oxide electrolyzer stack modules for hydrogen production. Ceram Int 2014;40:5801–9. https://doi.org/10.1016/j.ceramint.2013.11.020.

[25] Ebbesen SD, Høgh J, Nielsen KA, Nielsen JU, Mogensen M. Durable SOC stacks for production of hydrogen and synthesis gas by high temperature electrolysis. Int J Hydrogen Energy 2011;36:7363–73. https://doi.org/10.1016/j.ijhydene.2011.03.130.

[26] Liu T Le, Wang C, Hao SJ, Fu ZQ, Peppley BA, Mao ZM, et al. Evaluation of polarization and hydrogen production efficiency of solid oxide electrolysis stack with La0.6Sr0.4Co0.2Fe0.8O3?????- Ce0.9Gd0.1O1.95 oxygen electrode. Int J Hydrogen Energy 2016;41:15970–8. https://doi.org/10.1016/j.ijhydene.2016.04.243.

[27] Reytier M, Di Iorio S, Chatroux A, Petitjean M, Cren J, De Saint Jean M, et al. Stack performances in high temperature steam electrolysis and co-electrolysis. Int J Hydrogen Energy 2015;40:11370–7. https://doi.org/10.1016/j.ijhydene.2015.04.085.

[28] Barelli L, Bidini G, Cinti G, Ottaviano PA. Study of SOFC-SOE transition on a RSOFC stack. Int J Hydrogen Energy 2017;42:26037–47. https://doi.org/10.1016/j.ijhydene.2017.08.159.

[29] Penchini D, Cinti G, Discepoli G, Desideri U. Theoretical study and performance evaluation of hydrogen production by 200 W solid oxide electrolyzer stack. Int J Hydrogen Energy 2014;39:9457–66. https://doi.org/10.1016/j.ijhydene.2014.04.052.

Please cite this article in press as: Barelli L, et al., Air variation in SOE: Stack experimental study, International Journal of Hydrogen Energy (2018), https://doi.org/10.1016/j.ijhydene.2018.01.070

Journal of Energy Storage 20 (2018) 190–195

Contents lists available at ScienceDirect

Journal of Energy Storage

journal homepage: www.elsevier.com/locate/est

Steam as sweep gas in SOE oxygen electrode

L. Barelli, G. Bidini, G. Cinti*

Università degli Studi di Perugia, Department of Engineering, via Duranti 93, Perugia, Italy

ARTICLE INFO

Keywords:
SOE
Oxygen electrode
Steam
Oxygen production

ABSTRACT

The interest in producing hydrogen as energy storage medium for renewable electricity brought to the development to high efficient electrolyzers such as Solid Oxide Electrolyzer (SOE). Recent studies on SOEs focus mainly on the effect of the Hydrogen Electrode composition into performances varying the concentration of steam and hydrogen. This study investigates the Oxygen Electrode side where normally air is used as a sweep gas to flow pure oxygen, produced by SOE operation, out of the system. Water, in the form of steam, is proposed as an innovative sweep gas in oxygen electrode. The use of a different gas, such as steam, has the effect both of reducing oxygen concentration and changing thermodynamic local conditions of the SOE. Both phenomena influence electrochemical reaction and, consequently, cell voltage. At system level, this operation strategy allows to easily produce an oxygen flow as SOE by-product because no nitrogen in present in the oxygen electrode off gas and steam can be easily separated by condensation. Experimental study performed on a SOE single cell demonstrated that steam can be used in the oxygen electrode with the production of 100% oxygen on dry base. Negligible reduction of performance was measured and can be hardly distinguish from normal aging due to the test campaign. Open circuit voltage of 0.804 V and Area Specific Resistance of 0.582 $\Omega\,cm^{-2}$ were obtained at 800 °C. The new concept was for the first time assessed on experimental base and opens new paths for system design and integration of SOE electrolyzer units.

1. Introduction

The new energy requirements related to the development of renewable energy sources brought researchers to increase the study on the use of hydrogen as energy storage medium. Economic viability of electrolysis for hydrogen production as energy storage is strongly limited by the cost of the technology [1–3]. Main efforts are focused on achieving higher efficiency and lower cost and other advantages (e.g. no caustic, power density) moving from standard alkaline technology to PEM and, as a third generation, SOE. High temperature electrolyzers, such as SOE, allow high efficiency and, in future, low cost [4–6].

Research on SOE moved from the recent development on the same technology applied for power production: Solid Oxide Fuel Cell (SOFC). While knowledge derived from SOFC was recovered for what concerns stack design, interconnect materials and production process, research activities is extremely active on development of innovative materials for the electrodes.

In particular main issues are related to the oxygen electrode (OE) that has higher contribution to ohmic losses during operation [7] and degradation due to delamination of the electrode/electrolyte interface [8–11]. Literature studies dedicated to hydrogen electrode (HE) are mainly focused on the performance evaluation varying temperature and steam to hydrogen ratio [12–14]. A relatively new field of research evaluates hydrogen electrode strategies introducing carbon dioxide as reactant for the production of CO and/or syngas [15–17].

The present paper proposes an additional pathway to reduce hydrogen production cost. Specifically, technology productivity is increased by the valorization of by-products, such as oxygen, through an innovative management of the oxygen electrode. An interesting potential development of the technology involves the study of the oxygen electrode gas. In general air is used as a sweep gas to flow oxygen out of the system and reduce O_2 concentration in the electrode surface. High oxygen concentrations drive against electrolysis reaction and increase polarization losses. Authors already investigated on the reduction of air flow to improve system efficiency and increase O_2 concentration in the OE off gasses [18]. Results indicate that an increase in efficiency can be achieved and oxygen concentration can reach up to 50% at the oxygen electrode output. The latter aspect is extremely interesting considering the SOE not only as a hydrogen production device but, at the same time, as an oxygen generator. Even if oxygen is not a fuel and no energy can be recovered from the molecule, pure O_2 has an important market value that accelerates the economic feasibility of the concept. An additional

* Corresponding author.
E-mail address: giovanni.cinti@unipg.it (G. Cinti).

https://doi.org/10.1016/j.est.2018.09.009
Received 27 April 2018; Received in revised form 14 September 2018; Accepted 15 September 2018
Available online 29 September 2018

study, based on experimental study, demonstrated that air reduction down to 9.2% of nominal value has negligible effect on performances [19].

Literature reports also the so called fuel enhanced electrolysis. Hydrogen or, in general, a fuel, is added to the oxygen electrode. Oxygen is reduced chemically or electrochemically in the electrode reducing partial pressure of produced hydrogen. The electrolyzer acts as a concentration cell, with the overall result of moving hydrogen from the oxygen electrode to the hydrogen electrode [20–22].

The use of steam in the OE, as air substitute, can bring to further improvements in hydrogen production efficiency and, at the same time, produces a mixture of oxygen and steam that can be easily separated providing an additional chemical product of a SOE system. In this study we propose the use of steam as a carrier gas for produced oxygen. Compared with other gases such solution has two main advantages: (i) steam is already available in the system for the production of hydrogen in the HE and (ii) separation of oxygen from steam can be easily realized just condensing water. As a drawback additional heat is necessary for the production of steam but energy recovery can be implemented in the system and optimized. In this study a single SOE cell was tested using air and steam as a sweep gas to compare differences in performances. Literature reports only one study that deals with the use of steam as sweep gas [23]. In details the study, focused only on assessments at system level, provides the theoretical analysis of a tri-generation system. Three different strategies for hydrogen electrode sweep gas are evaluated (air, syngas and steam) and steam was selected as the most profitable one.

An open issue on the use of steam is related to electrode stability and material corrosion. To this regards, literature reports a large experience in using humidified air as reaction gas in SOFC operation [24]. Even if preliminary results show electrode degradation for both most diffused electrode materials LSM and LSCF [25], literature does not give a clear indication due to experience where LSCF did not show any degradation [26]. In general, such aspects are poorly studied and very little is clarified in terms of degradation mechanism and no experience is presented in electrolysis operation. Regarding corrosion issue, both the presence of steam and oxygen can cause material degradation [24] due to the production of volatile chromium both in form of CrO3(g) and CrO2(OH)2(g) that can contaminate cell material [27]. Strategies to prevent chromium production are the doping of cathode composition or the use of special stainless steel that can prevent the formation of contaminants [28].

For what is in the knowledge of the authors this is the first study that reports an experimental activity of a SOE operating with steam as sweep gas in the oxygen electrode demonstrating the feasibility of the concept and the production of pure oxygen.

2. Materials and methods

Experimental test was performed on a single square commercial planar cell, active area 16 cm^2, anode supported with Ni/8YSZ as HE, 8YSZ electrolyte and GDC + LSCF as OE. Thicknesses of each layer are reported in Table 1.

Nickel mesh was used as HE current collector and gold mesh for OE. Steel manifolds were used to distribute gasses to the electrodes. Water was evaporated inside the furnace in a pre-reactor for the HE gas flow and in the pipes for the OE flow. Two voltage and two temperature sensors were placed in the meshes and in the manifolds respectively. Gas and water flows were regulated through flow meters controllers. A scheme of the set-up in the furnace is depicted in Fig. 1. The set-up, developed for this study, allows to obtain stable voltage values even with high steam content in the gas mixture feeding the OE.

Table 1
Details of cell layers.

Layer	Composition	Thickness
Anode	Ni/8YSZ	240 ± 20 μm
Electrolyte	8YSZ	8 ± 2 μm
Bilayer Cathode	GDC + LSCF	50 ± 10 μm

Performance analysis was realized; polarization curves were measured at constant furnace temperature of 800 °C. OE gas was pre heated up to 200 °C. For each polarization curve, steps of 1 A were kept for one minute up to maximum current of 1000 mA cm^{-2}. Results are reported in the following paragraph 2 in terms of average profiles; each number is calculated as the average of the values acquired in the time interval, one minute, at 1 Hz. Data standard deviations is always below 0.5%, even if not indicated in the graphs to guarantee their readability in consideration of the multiple depicted trends. HE gas flow was kept constant during all tests. Gas quality and quantity were defined via two indirect parameters: hydrogen inlet molar concentration (x_{H2}) and reactant utilization at 1000 mA cm^{-2} (RU@1000). The latter is defined as follows (1):

$$RU@1000 = \frac{1000 \cdot A}{2 \cdot F \cdot H_2O} \quad (1)$$

Where A is the cell surface in cm^2, F is Faraday constant and H_2O is molar flow of steam. Thus while x_{H2} indicates the amount of hydrogen in the HE necessary to keep a reducing atmosphere, RU@1000 indicated the maximum conversion rate that can be achieved in the cell and, once defined, can be used to calculate steam flow. Based on literature 10% of H_2 was used in all tests. Hydrogen flow is not necessary for the reaction and, vice versa, due to the fact that it is a reaction product, its presence inhibits the electrochemical reaction and increases operative voltage. Thus, minimum amount was used to keep higher performance results. RU@1000 was fixed at 0.5 so to achieve nearly operative conditions and, at the same time, to reduce the contribution of HE to polarization losses and focus on OE contribution. Three groups of five polarizations each were performed changing OE composition: standard air flow (AIR), mixture of steam and air 50:50 (H2O) and, finally, steam and air mixture with composition variation (MIX) up to the case of 100% H_2O fed to the OE. To design OE flows, the parameter m_{O2}@1000 was used. This parameter was introduced as an indirect criteria to define inlet gas flows of air and steam; it is defined as the molar flow of oxygen produced at 1000 mA cm^{-2} with respect to the inlet flow (2):

$$m_{O2}@1000 = \frac{O_2@1000 + 0.21 \cdot Air_{in}}{n_{OEin}} \quad (2)$$

Where O_2@1000 is the molar flow of oxygen produced at 1000 mA cm^{-2}, Air_{in} is the molar flow of air entering (when fed to the electrode) the OE electrode and n_{OEin} is the total molar flow of inlet gas. O_2@1000 is calculated as follows (3):

$$O_2@1000 = \frac{1000 \cdot A}{4 \cdot F} \quad (3)$$

In AIR and H2O tests, m_{O2}@1000 was varied from 30 to 70% at steps of 10. In MIX tests, m_{O2}@1000 was kept constant at 50% and steam concentration was varied to values of 0, 25, 50 and 100%. Test campaign is reported in Table 2. In the table also x_{H2O} and x_{air} are reported, calculated as molar concentrations of steam and air respectively at the oxygen electrode inlet.

Based on design condition reported in Table 2 gas flows were calculated as reported in Table 3. The table reports also parameters such as O_2@1000, already defined, and the equivalent H_2@1000, calculated as the hydrogen production of the system when operating at 1000 mA cm^{-2}. Finally the table reports the HE/OE parameter, calculated as the ratio between the hydrogen electrode and oxygen electrode total flows. Table 3 reports also oxygen concentration on wet (xO2) and dry (xO2d) basis of OE off gasses at 1000 mA cm^{-2}.

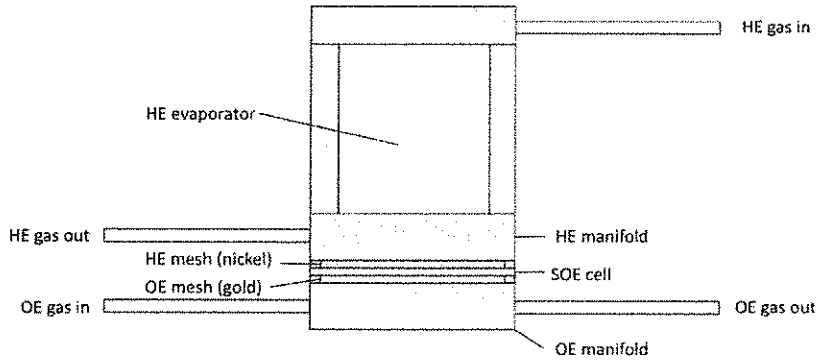

Fig. 1. Scheme of the cell set-up in the furnace.

Table 2
Test campaign design.

	Hydrogen electrode		Oxygen electrode		
	x_{H2} %	RU@1000 %	m_{O2}@1000 %	x_{H2O} %	x_{Air} %
AIR1	10%	50%	30%	0%	100%
AIR2	10%	50%	40%	0%	100%
AIR3	10%	50%	50%	0%	100%
AIR4	10%	50%	60%	0%	100%
AIR5	10%	50%	70%	0%	100%
H2O1	10%	50%	30%	50%	50%
H2O2	10%	50%	40%	50%	50%
H2O3	10%	50%	50%	50%	50%
H2O4	10%	50%	60%	50%	50%
H2O5	10%	50%	70%	50%	50%
MIX1	10%	50%	50%	0%	100%
MIX2	10%	50%	50%	25%	75%
MIX3	10%	50%	50%	50%	50%
MIX4	10%	50%	50%	75%	25%
MIX5	10%	50%	50%	100%	0%

3. Results

Polarization results, in terms of voltage as function of current density, are reported in Figs. 2, 4 and 6 for AIR, H2O and MIX tests respectively. In general, all results show negligible differences in performance, with voltage variation always below 3%. Very low differences, in terms of voltage, is a common trend for all the tests indicating that, in the short period, the introduction of steam does not cause major issues to the cell operation. A deeper discussion of each graph is here below reported trying to correlate voltage variation to physical parameters. However, due to low difference in values, each comment to voltage suffers of high uncertainty. Even if the same cell was operated in all cases, variability may come from environmental variations, hysteresis of materials or aging effect on the cell due to the intensive test campaign.

In details, Fig. 2a reports the polarization curves as voltage Vs current density, while Fig. 2b is a zoom of the differences, reported as voltage variation, in percentage, as function of current density. As expected, polarization curves show an almost linear increase in voltage as function of current density. Even if variation is always below 3%, see Fig. 2b, it is possible to identify a trend in the curves. The decrease of air flow, from AIR1 to AIR5, causes a performances decrease in terms of higher voltage. The increase in air flow has a positive effect on diffusion losses that increase when the flow is reduced. Same results were already obtained in a previous study by authors [19]. For the smallest values, AIR4 and AIR5, the differences between curves are even smaller and differences can be hardly appreciated. It is interesting to note that voltage difference starts from smallest values, close to zero, and reaches again values close to zero at maximum current density. Such behavior might be related to temperature trend in the cell.

Fig. 3 reports temperature variations of AIR tests. Temperature was calculated as average of the two sensors in oxygen and hydrogen electrode manifold. Temperature trends are typical of SOE curves, with an initial decrease, due to heat absorbance caused by endothermic

Table 3
Gas flows and additional parameter used during the experimental tests.

	HE			OE			Products				
	H2 Nl/h	H2O g/h	TOT Nl/h	H2O g/h	Air Nl/h	TOT Nl/h	HE/OE	O2@1000 Nl/h	H2@1000 Nl/h	xO2	xO2d
AIR1	1.49	10.75	14.87	0.00	37.17	37.17	0.40	3.35	6.69	0.25	0.43
AIR2	1.49	10.75	14.87	0.00	17.61	17.61	0.84	3.35	6.69	0.31	0.50
AIR3	1.49	10.75	14.87	0.00	11.54	11.54	1.29	3.35	6.69	0.36	0.56
AIR4	1.49	10.75	14.87	0.00	8.58	8.58	1.73	3.35	6.69	0.40	0.60
AIR5	1.49	10.75	14.87	0.00	6.83	6.83	2.18	3.35	6.69	0.44	0.64
H2O1	1.49	10.75	14.87	6.89	8.58	17.15	0.87	3.35	6.69	0.28	0.28
H2O2	1.49	10.75	14.87	4.55	5.67	11.34	1.31	3.35	6.69	0.34	0.34
H2O3	1.49	10.75	14.87	3.40	4.23	8.47	1.76	3.35	6.69	0.39	0.39
H2O4	1.49	10.75	14.87	2.71	3.38	6.76	2.20	3.35	6.69	0.43	0.43
H2O5	1.49	10.75	14.87	2.26	2.81	5.62	2.64	3.35	6.69	0.47	0.47
MIX1	1.49	10.75	14.87	0.00	11.54	11.54	1.29	3.35	6.69	0.39	0.39
MIX2	1.49	10.75	14.87	1.96	7.33	9.77	1.52	3.35	6.69	0.37	0.46
MIX3	1.49	10.75	14.87	3.40	4.23	8.47	1.76	3.35	6.69	0.36	0.56
MIX4	1.49	10.75	14.87	4.50	1.87	7.48	1.99	3.35	6.69	0.35	0.72
MIX5	1.49	10.75	14.87	5.37	0.00	6.69	2.22	3.35	6.69	0.33	1.00

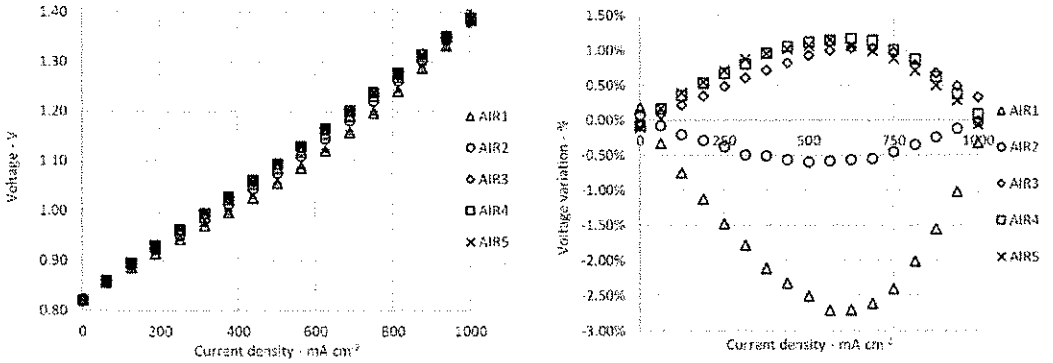

Fig. 2. Results of Air test.

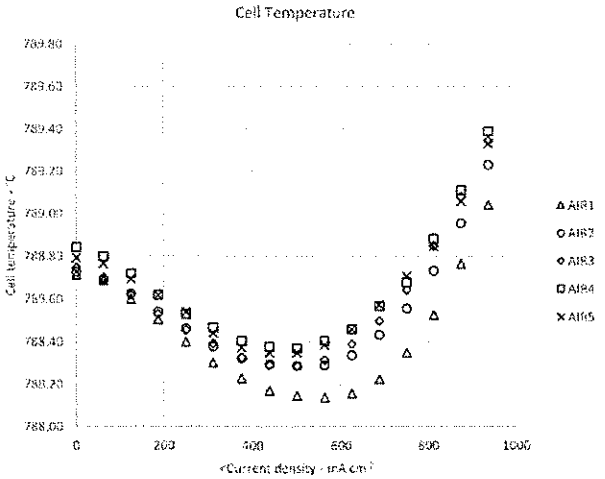

Fig. 3. Temperature variation of AIR tests.

reactions, followed to an increase up to initial conditions and above due to heat production of polarization losses. Comparing the values, it is possible to correlate the performances to temperature trends, with lower temperatures at higher air flows, due to coolant effect of fresh gas. Going back to the performances, it is possible to correlate temperature and voltages. The trend on voltage could be explained by the temperature initial decrease and its following increase. Compositions that cause bigger temperature difference, such as AIR1, have also higher voltage variation with conditions that get closer at the beginning and at the end when temperature goes back to initial value as previously explained. It is possible to argue that temperature differences, as reported in Fig. 3, are negligible but it is important to notice that thermocouples are placed in the metal manifold and temperature variation inside the electrode chamber may be amplified.

As for Air tests, also H2O tests results are reported in Fig. 4 a, polarization curves, and Fig. 4b, voltage difference in percentage. Voltage variations, with the exceptions of polarization curve H2O4, are below 1% and with a trend that goes from H2O1, lower voltage, up to H2O5. Also these tests, like the AIR ones, indicate a relation between performances and total gas flow. Here again total gas flow in the OE has a negative effect (even if negligible), increasing polarization losses and, consequently, cell voltage.

Temperature trends of H2O tests are reported in Fig. 5. Also in this graph, trends are similar to the ones gathered in AIR tests; it is possible to identify a distribution of curves, with the only exception of H2O4, that correlate higher temperatures to higher total OE flows. This results is different from AIR tests. In this case the temperature increase seems correlated to an increase of total flow. This might be related to the content of steam in the flow. Specific heat of steam is higher of the air one, contributing to cell temperature equilibrium. Note that steam may play a role in temperature stabilization reducing the effect on voltage differences that, as reported in Fig. 4b, have a linear behavior compared to AIR tests. In any case differences in terms of temperature are negligible, less than 1 °C.

MIX test results are reported in graphs of Fig. 6a and b. Unfortunately, there were problems in performing MIX4 test and data are not available. Also for MIX tests differences, in term of performances, are minimum. Results, as detailed in Fig. 6b, do not show any trend between different compositions. The curve with MIX5 was performed with only steam, demonstrating that it is possible to operate SOE using only H2O at the oxygen electrode without negative effects on performances.

Temperature results of MIX tests are reported in Fig. 7. Temperatures show same trends of previous tests but, like for polarization curves, it is impossible to provide a data correlation among different compositions. The trend of voltage differences seems similar to the case of H2O tests. Such evidence can be considered as a confirmation of the role of steam in stabilizing cell temperature reducing the parabolic effect seen in AIR tests.

Polarization main parameters are reported in Table 4. In particular the table reports the open circuit voltage (OCV) and the linear regression coefficient of the curves called Area Specific Resistance (ASR). In Air tests there is a decrease of OCV moving from AIR1 to AIR5, mainly due to the effect of temperature. Due to Nernst potential higher temperature, caused by smaller air flows, brings to smaller OCV. Same behavior can't be derived for H2O and MIX compositions, where OCV values are random distributed. For all tests OCV has very small variation, with a maximum of 1.2%. Regarding Area Specific Resistance, deviation of values is always below 5% and with a random distribution with no clear correlation with the test conditions.

4. Oxygen separation

The new technology solution presented in this study aims to develop a system for contextual production of hydrogen and oxygen. Hydrogen production realized via steam electrolysis falls in the power to gas technology, currently under investigation at both scientific and technical level, with the aim of enhancing the diffusion of renewable energy sources reducing the stress in the electric grid. If oxygen is considered as a byproduct of the system, it is possible to evaluate an additional economic benefit. Usually oxygen is produced starting from air, separating nitrogen through air separation units (ASU). Most developed ASU technologies are cryogenic separation and membrane technology. In detail, cryogenic separation, mainly used for large oxygen production plants, is realized with a cryogenic process performed in several condensing reactor that separate liquid nitrogen from gaseous oxygen. Membrane technology is based on polymeric or ceramic membranes

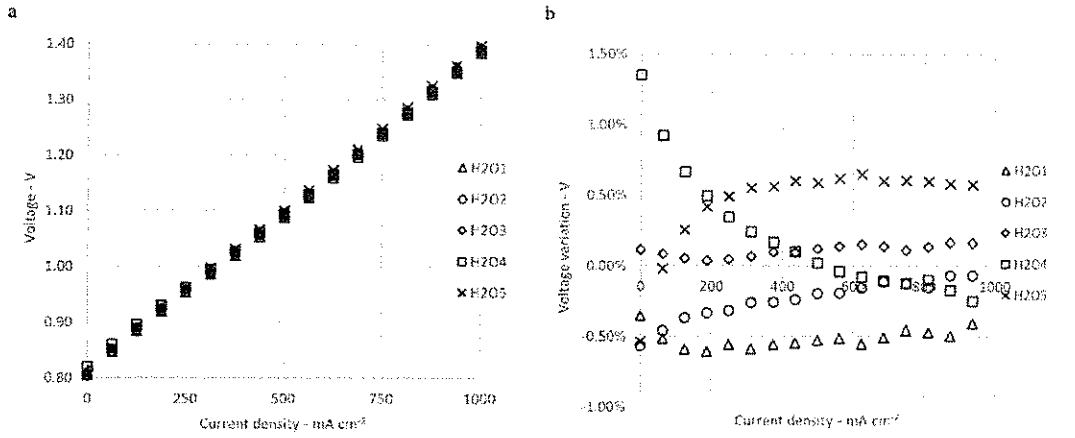

Fig. 4. Results of H2O test.

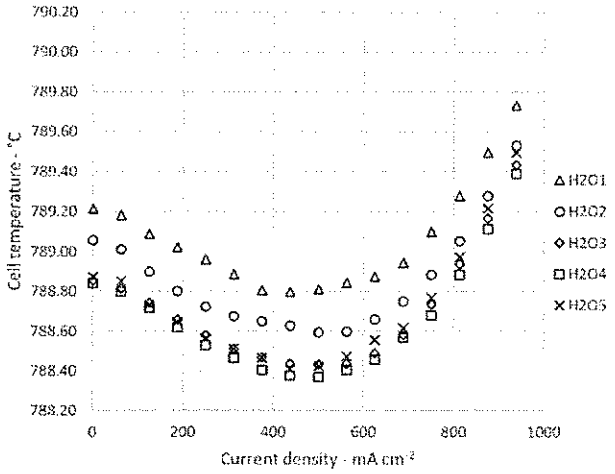

Fig. 5. Temperature values of H2O test as function of current density.

that separate oxygen from nitrogen with lower energy consumption. Based on reference [29], it is possible to evaluate production cost of oxygen as 14.3 \$ kg_{O2}^{-1} and 22.2 \$ kg $_{O2}^{-1}$ considering membrane technology and cryogenic air separation unit respectively. Those are indicative numbers that show potential benefit, in term of saved cost, of the concept presented in this study.

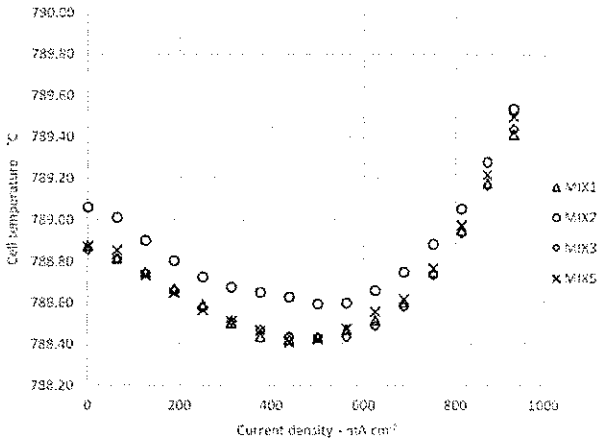

Fig. 7. Temperature curves of MIX tests.

5. Conclusions

The use of steam as a sweep gas for SOE oxygen electrode was demonstrated. This technical solution allows to produce pure oxygen with no performance decrease in terms of diffusion losses or material oxidation. It is therefore possible to substitute air with steam on the OE side without any decrease in performance and achieving the mentioned advantages in terms of oxygen production without any separation cost.

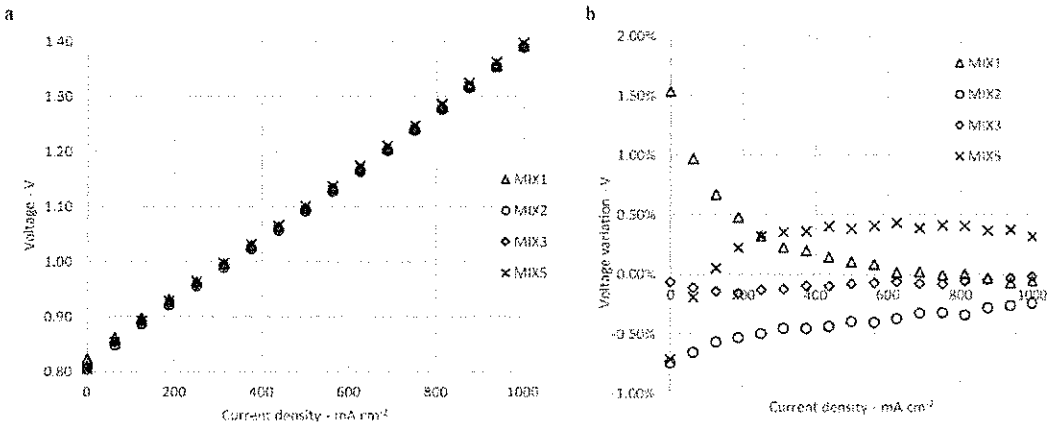

Fig. 6. Results of MIX test.

Table 4
OCV and ASR values of polarization curves.

	OCV V	ASR Ω cm²
AIR1	0.822	0.540
AIR2	0.821	0.554
AIR3	0.820	0.564
AIR4	0.820	0.562
AIR5	0.819	0.559
H2O1	0.806	0.572
H2O2	0.804	0.576
H2O3	0.810	0.575
H2O4	0.820	0.562
H2O5	0.804	0.582
MIX1	0.823	0.564
MIX2	0.804	0.576
MIX3	0.810	0.575
MIX4		
MIX5	0.804	0.582

Oxygen production can be evaluated, considering the SOE unit operation at 1.28 V and 800 mA cm^{-2}, in 2.39 kg h^{-1} m^{-2} storing, at the same time, a power of 10.24 kW m^{-2}.

The study investigated also the use of steam and air mixtures. In general, the decrease in air flow has minimum effect on performances, with an increase in voltage when total flow is reduced. Long term tests and complete system study have to be performed to evaluate the technical feasibility of the concept and any degradation issues.

In perspective, a new technology can be developed obtaining the coupled production of hydrogen and oxygen from steam and renewable electrical energy. The combined renewable energy storage and chemical production is potentially performed at high efficiency introducing a new solution that can be easily integrated in a smart community, increasing the sustainability of the grid and of oxygen production.

Acknowledgment

This study was supported by Fondazione Cassa di Risparmio di Perugia – project H2 in ICE - 2016.0030.021.

References

[1] H. Chen, T.N. Cong, W. Yang, C. Tan, Y. Li, Y. Ding, Progress in electrical energy storage system: a critical review, Prog. Nat. Sci. 19 (2009) 291–312, https://doi.org/10.1016/j.pnsc.2008.07.014.
[2] J. Kim, Y. Suharto, T.U. Daim, Evaluation of Electrical Energy Storage (EES) technologies for renewable energy: a case from the US Pacific Northwest, J. Energy Storage 11 (2017) 25–54, https://doi.org/10.1016/J.EST.2017.01.003.
[3] A.K. Rohit, K.P. Devi, S. Rangnekar, An overview of energy storage and its importance in Indian renewable energy sector: part I—technologies and comparison, J. Energy Storage 13 (2017) 10–23, https://doi.org/10.1016/J.EST.2017.06.005.
[4] E. Giglio, A. Lanzini, M. Santarelli, P. Leone, Synthetic natural gas via integrated high-temperature electrolysis and methanation: part I—energy performance, J. Energy Storage 1 (2015) 22–37, https://doi.org/10.1016/j.est.2015.04.002.
[5] C.M. Berger, O. Tokariev, P. Orzessek, A. Hospach, Q. Fang, M. Bram, et al., Development of storage materials for high-temperature rechargeable oxide batteries, J. Energy Storage 1 (2015) 54–64, https://doi.org/10.1016/J.EST.2014.12.001.
[6] M.N. Manage, D. Hodgson, N. Milligan, S.J.R. Simons, D.J.L. Brett, A techno-economic appraisal of hydrogen generation and the case for solid oxide electrolyser cells, Int. J. Hydrogen Energy 36 (2011) 5782–5796, https://doi.org/10.1016/j.ijhydene.2011.01.075.
[7] S.J. Kim, K.J. Kim, G.M. Choi, A novel solid oxide electrolysis cell (SOEC) to separate anodic from cathodic polarization under high electrolysis current, Int. J. Hydrogen Energy 40 (2015) 9032–9038, https://doi.org/10.1016/j.ijhydene.2015.05.143.
[8] M.S. Khan, X. Xu, J. Zhao, R. Knibbe, Z. Zhu, A porous yttria-stabilized zirconia layer to eliminate the delamination of air electrode in solid oxide electrolysis cells, J. Power Sources 359 (2017) 104–110, https://doi.org/10.1016/j.jpowsour.2017.05.049.
[9] P. Moçoteguy, A. Brisse, A review and comprehensive analysis of degradation mechanisms of solid oxide electrolysis cells, Int. J. Hydrogen Energy (2013) 1–16, https://doi.org/10.1016/j.ijhydene.2013.09.045.
[10] K. Chen, S.P. Jiang, Failure mechanism of (La,Sr)MnO3 oxygen electrodes of solid oxide electrolysis cells, Int. J. Hydrogen Energy 36 (2011) 10541–10549, https://doi.org/10.1016/J.IJHYDENE.2011.05.103.
[11] M.A. Laguna-Bercero, Recent advances in high temperature electrolysis using solid oxide fuel cells: a review, J. Power Sources 203 (2012) 4–16, https://doi.org/10.1016/j.jpowsour.2011.12.019.
[12] Q. Cai, C.S. Adjiman, N.P. Brandon, Optimal control strategies for hydrogen production when coupling solid oxide electrolysers with intermittent renewable energies, J. Power Sources 268 (2014) 212–224, https://doi.org/10.1016/j.jpowsour.2014.06.028.
[13] J.E. O'Brien, C.M. Stoots, J.S. Herring, J.J. Hartvigsen, P.A. Lessing, J.J. Hartvigsen, et al., Performance measurements of solid-oxide electrolysis cells for hydrogen production, J. Fuel Cell Sci. Technol. 2 (2005) 156, https://doi.org/10.1115/1.1895946.
[14] D. Penchini, G. Cinti, G. Discepoli, U. Desideri, Theoretical study and performance evaluation of hydrogen production by 200 W solid oxide electrolyzer stack, Int. J. Hydrogen Energy 39 (2014) 9457–9466, https://doi.org/10.1016/j.ijhydene.2014.04.052.
[15] C. Graves, S.D. Ebbesen, M. Mogensen, Co-electrolysis of CO2 and H2O in solid oxide cells: performance and durability, Solid State Ionics 192 (2011) 398–403, https://doi.org/10.1016/j.ssi.2010.06.014.
[16] J.E. O'Brien, M.G. McKellar, C.M. Stoots, J.S. Herring, G.L. Hawkes, Parametric study of large-scale production of syngas via high-temperature co-electrolysis, Int. J. Hydrogen Energy 34 (2009) 4216–4226, https://doi.org/10.1016/j.ijhydene.2008.12.021.
[17] L. Barelli, G. Bidini, A. Ottaviano, Hydromethane generation through SOE (solid oxide electrolyser): advantages of H2O-CO2 co-electrolysis, Energy 90 (2015) 1180–1191, https://doi.org/10.1016/j.energy.2015.06.052.
[18] L. Barelli, G. Bidini, G. Cinti, Airflow management in solid oxide electrolyzer (SOE) operation: performance analysis, Chem. Eng. 1 (2017) 13, https://doi.org/10.3390/chemengineering1020013.
[19] L. Barelli, G. Bidini, G. Cinti, Air variation in SOE: stack experimental study, Int. J. Hydrogen Energy (2018) 1–8, https://doi.org/10.1016/j.ijhydene.2018.01.070.
[20] W. Wang, R.J. Gorte, J.M. Vohs, Analysis of the performance of the electrodes in a natural gas assisted steam electrolysis cell, Chem. Eng. Sci. 63 (2008) 765–769, https://doi.org/10.1016/j.ces.2007.10.026.
[21] J. Martinez-Frias, A.-Q. Pham, S.M. Aceves, A natural gas-assisted steam electrolyzer for high-efficiency production of hydrogen, Int. J. Hydrogen Energy 28 (2003) 483–490.
[22] G. Cinti, G. Bidini, K. Hemmes, An experimental investigation of fuel assisted electrolysis as a function of fuel and reactant utilization, Int. J. Hydrogen Energy 41 (2016), https://doi.org/10.1016/j.ijhydene.2016.05.205.
[23] N. Perdikaris, K.D. Panopoulos, P. Hofmann, S. Spyrakis, E. Kakaras, Design and exergetic analysis of a novel carbon free tri-generation system for hydrogen, power and heat production from natural gas, based on combined solid oxide fuel and electrolyser cells, Int. J. Hydrogen Energy 35 (2010) 2446–2456, https://doi.org/10.1016/J.IJHYDENE.2009.07.084.
[24] Z. Yang, M. Guo, N. Wang, C. Ma, J. Wang, M. Han, A short review of cathode poisoning and corrosion in solid oxide fuel cell, Int. J. Hydrogen Energy 42 (2017) 24948–24959, https://doi.org/10.1016/J.IJHYDENE.2017.08.057.
[25] M. Niania, In-Situ Analysis of La0.6Sr0.4Co0.2Fe0.8O3-δ Surfaces in Ambient Atmospheres, (2016).
[26] J. Nielsen, A. Hagen, Y.L. Liu, Effect of cathode gas humidification on performance and durability of solid oxide fuel cells, Solid State Ionics 181 (2010) 517–524, https://doi.org/10.1016/j.ssi.2010.02.018.
[27] K. Hilpert, D. Das, M. Miller, D.H. Peck, R. Weiß, Chromium vapor species over solid oxide fuel cell interconnect materials and their potential for degradation processes, J. Electrochem. Soc. 143 (1996) 3642, https://doi.org/10.1149/1.1837264.
[28] M. Palcut, L. Mikkelsen, K. Neufeld, M. Chen, R. Knibbe, P.V. Hendriksen, Corrosion stability of ferritic stainless steels for solid oxide electrolyser cell interconnects, Corros. Sci. 52 (2010) 3309–3320, https://doi.org/10.1016/j.corsci.2010.06.006.
[29] Prakash Rao, Michael Muller, Industrial oxygen: its generation and use, 2007 ACEEE Summer Study Energy Efficiency in Industry, (2007), pp. 124–135.

chemengineering

MDPI

Article

Airflow Management in Solid Oxide Electrolyzer (SOE) Operation: Performance Analysis

Linda Barelli, Gianni Bidini and Giovanni Cinti *

Department of Engineering, University of Perugia, 06123 Perugia, Italy; linda.barelli@unipg.it (L.B.); gianni.bidini@unipg.it (G.B.)

* Correspondence: giovanni.cinti@unipg.it; Tel.: +39-075-585-3991

Received: 5 September 2017; Accepted: 26 October 2017; Published: 6 November 2017

Abstract: Hydrogen is being studied as a means of energy storage and can be synthetized to store renewable energy and successively used as a fuel for power production or transport purposes. High temperature solid oxide electrolyzers (SOE) are proposed as a technology to produce hydrogen with high energy efficiency and high power density. Within the studies on SOE operation, little attention has been given to the oxygen electrode side, where air is normally used as a sweep gas. In this study, we consider the option of reducing the air flow rate when operating an SOE stack. The advantages in terms of efficiency are calculated, showing that efficiency increases up to 2.8% when reducing the air flow rate down to 7% of nominal value.

Keywords: solid oxide electrolyzer; hydrogen production; energy storage; air flow

1. Introduction

Solid oxide electrolyzer (SOE) is considered a new potential technology for the production of hydrogen. Such a device achieves very high efficiencies in keeping power density higher than low-temperature electrolyzers. A promising application for SOE is in the energy storage field, where a high-efficient hydrogen production offers a viable path for the use of hydrogen as a storage medium. A well-known problem for the exploitation of renewable energy sources is the unpredictability of electrical production with a consequent unbalancing of the electrical grid. To restore equilibrium between generation and consumption requires the significant integration of an energy storage system (ESS) into the energy system. Today, installed energy storage capacity is very limited in the European scenario, mainly due to technological and economic issues. Innovative solutions with enhanced features with respect to conventional technologies have to be developed. High temperature electrolyzers, such as SOE, offer a very interesting path for high-efficiency and low-cost hydrogen production. The cost of the technology is an open issue. Important results where recently achieved at the industrial level, taking advantage of the improvements of solid oxide fuel cell technology that share many aspects of design, materials, and system integration with SOE. SOE technology, due to recent development, lacks system study regarding energy balance and the impact of operative parameter on performances. Open challenges are the management of the hydrogen cooling and compression and the optimization of air flow in the system. This study performs a preliminary study on the latter aspect, specifically focusing on the role played by air flow with impacts at the system level.

The electrolysis reaction is the following (1):

$$H_2O \rightarrow H_2 + \frac{1}{2}O_2 \quad (1)$$

In electrolysis, efficiency is calculated as follow Equation (2):

$$\eta = \frac{P_{out}}{P_{in}} = \frac{n_{H_2} \cdot LHV_{H_2}}{V \cdot I} \quad (2)$$

where P_{out} and P_{in} are system power output and input, respectively, n_{H_2} is molar flow rate of hydrogen, LHV_{H_2} is low heating value of hydrogen, and V and I are voltage and current of electrolyzer, respectively. Hydrogen and current are related by Equation (3):

$$n_{H_2} = \frac{I}{2 \cdot F} \quad (3)$$

where F is Faraday constant. Thus, efficiency can be expressed by Equation (4):

$$\eta = \frac{LHV_{H_2}}{2 \cdot F \cdot V} \quad (4)$$

An additional efficiency, η_s, can be defined at system level (5), considering the heat absorbed by H_2O, from room temperature to SOE operation temperature, as further energy input.

$$\eta_s = \frac{n_{H_2} \cdot LHV_{H_2}}{V \cdot I + Q_w} \quad (5)$$

where Q_w is the heat necessary for heating and water vaporization to guarantee steam at 650 °C at the hotbox inlet.

Efficiency therefore is only dependent on voltage. Considering that LHV is the enthalpy variation, ΔH, of electrolysis reaction in Equation (1), it is possible to define thermoneutral voltage E_{th} as the voltage equivalent to 100% efficiency as follows (6):

$$E_{th} = \frac{\Delta H}{2 \cdot F} \quad (6)$$

Once the system operates at a thermoneutral voltage, efficiency is 100%, and the electrolyzer is in equilibrium. Depending on the relation between voltage and current density, which is called the polarization curve, it is possible to find the thermoneutral current density, J_{th}. Figure 1 reports polarization curves and thermoneutral values of different electrolyzer technologies. Compared to a low-temperature electrolyzer, SOE allows higher thermoneutral current densities and relative power densities to be achieved. Real systems usually operate above thermoneutral due to thermal losses, and operative current densities are higher than thermoneutral one.

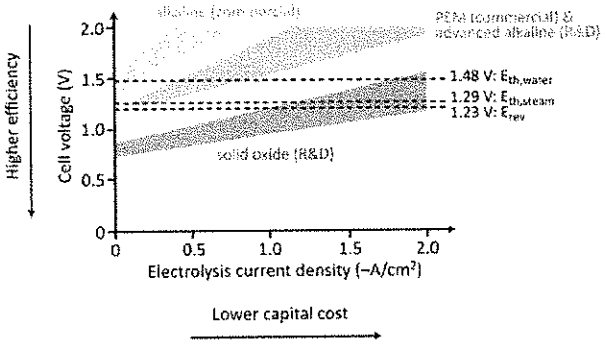

Figure 1. Comparison between alkaline, polymer electrolyzer membrane (PEM), and solid oxide electrolyzers in terms of voltage vs. current density [1].

Considering a general polarization curve, like $V(j)$ reported in Figure 2, real operating conditions, V and J in the figure, are higher than thermoneutral due to system losses.

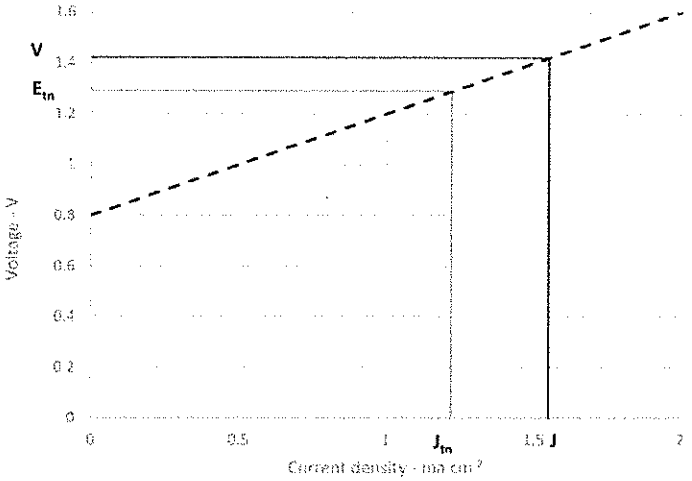

Figure 2. Example of operating condition of a solid oxide electrolyzer (SOE).

Operative voltage, V, can be related to the energy balance of the stack by following relation:

$$V = \frac{\Delta H_S}{2 \cdot F} = \frac{\Delta H + Q}{2 \cdot F} > V_{tn} \tag{7}$$

where ΔH_S is the total enthalpy requirement of the stack that is the sum of reaction enthalpy ΔH and thermal losses Q.

The scheme of an SOE stack is reported in Figure 3. In the hydrogen electrode, steam is supplied mixed with hydrogen. Hydrogen is added due to material restrictions that require a reductive atmosphere to protect the reaction catalyst from oxidation. During operation, the steam reacts and produces hydrogen and oxide ions. Hydrogen electrode output is a mixture of hydrogen and unreacted steam. The reactant utilization parameter (RU) is introduced to calculate the amount of steam that reacts in the cell and has a direct impact on the steam hydrogen mixture. Reactant utilization is defined as follows:

$$\mathrm{RU} = \frac{m_{\mathrm{H_2O_r}}}{m_{\mathrm{H_2O_{in}}}} = \frac{I}{2 \cdot F \cdot m_{\mathrm{H_2O_{in}}}} \tag{8}$$

where $m_{\mathrm{H_2O_r}}$ is the mole of steam reacting and $m_{\mathrm{H_2O_{in}}}$ is the total steam molar inlet flow.

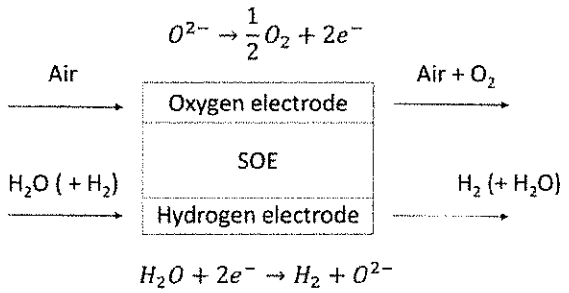

Figure 3. Scheme of a solid oxide electrolyzer.

Regarding the oxygen electrode side, pure oxygen is produced by the electrochemical reaction, and air is usually fed as a sweep gas for obvious reasons of low cost and availability. This study focuses on the air feeding and on the effect of air flow rate on stack equilibrium and performance.

Studies on SOE are mainly focused on the material development [2,3] and on the operation potentialities in specific applications such as CO-electrolysis [4] and reversible RE-SOFC [5]. SOE integration in complete systems is also addressed in the literature [6]. Air flow is an important parameter at the system level because it has to be managed in the unit. In detail, air needs to be heated up to stack temperature and has to be cooled down when mixed with produced oxygen. Such an operation can be realized with a heat exchanger (regenerator) using a similar solution to the SOFC system. The main difference with SOFC is that in SOE air flow is not necessary for the operation of the stack and must be optimized only for the sweeping of oxygen. Compared to SOFC, the stack does not have to be cooled; on the contrary, as previously explained, any thermal loss causes a decrease in performances. It is impossible to obtain an operative air-air heat exchanger to supply all the required heat to heat air flow rate up to the stack operating temperature. The consequence is that part of the heat must be obtained directly from the stack and becomes an energy request that has to be subtracted from the heat available for the chemical reactions. No studies in the literature address air flow management and optimization.

Within this study, a zero-dimensional model of a stack and heat exchanger was developed, and the effect of air flow rate reduction on the performances was investigated. The model is supported by an experimental test giving the main parameters of SOE operation in the designed condition.

2. Materials and Methods

A zero-dimensional thermodynamic model, including an SOE stack and an air-air heat exchanger, was developed. Thermodynamic properties were obtained by the FluidProp library supplied by Asimptote and based on JANAF tables [7]. A scheme of the developed model is reported in Figure 4. The SOE stack was operated at 750 °C with an RU of 0.7. Operative temperature is derived from SOFC state of technology, while the RU is a trade-off between reduction of steam production and higher availability of steam in the electrode to feed the reaction. Based on literature data, H_2O:H_2 composition was kept as 90:10 [8]. In this case, the aim is to keep hydrogen concentration as low as possible. Air flow enters the system at ambient conditions and is heated in the heat exchanger (AIR HEX) up to 650 °C. This temperature was derived from typical SOFC stack operation where, with the aim of reducing thermal shocks to the stack materials, 100 K are considered as maximum temperature difference [9]. A hydrogen electrode mixture, H_2 and H_2O, is fed to the stack at 650 °C.

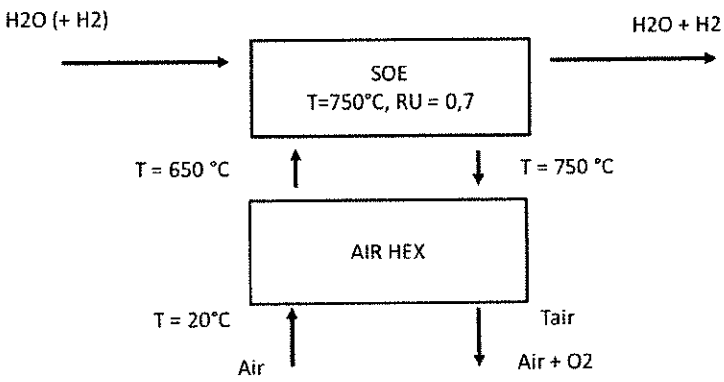

Figure 4. Scheme of the hotbox studied in the model.

The mixture of air and oxygen exits the stack at the operating temperature and enters the heat exchanger. Note that this design guarantees a temperature difference of 100 K for the high temperature

side of the heat exchanger. Moreover, the mass flow of the cooling flow (right side in the figure) is higher of the heating one because oxygen produced by the reaction is added to the same mass flow. This means that there is no risk of insufficient heat to bring the air flow rate up to 650 °C.

The model was calculated to have thermal equilibrium in the stack. Once stack the physical parameters—the number of cell and cell active area—are defined, the model calculates the operative voltage based on air flow, RU, and polarizations parameters, specifically ASR and OCV. ASR is the area specific resistance, and OCV is the open circuit voltage. ASR and OCV are derived from the experimental part of the study. A commercial SOFC short stack was operated in SOE conditions at 750 °C. The short stack is based on six SOFC planar cells with a Ni/8YSZ anode, an LSCF cathode, a GDC barrier layer, and an 8YSZ electrolyzer. The test was performed in a test rig designed to perform stack start-up and experimental testing. The test rig was adapted in the furnace connected to the hydrogen and air piping. Hydrogen piping was fed with a mixture of hydrogen and steam. Water was evaporated in a controlled evaporator mixer, and the H_2-H_2O mixture was kept at an acceptable temperature with a cable heating system to avoid recondensation of water. Both air flow and steam were preheated in specific piping inside the furnace that increases gas temperature up to stack temperature. Mica sealing was used to connect the piping to the stack to avoid gas leakage inside the furnace. Off gasses were kept at high temperature using isolated piping to avoid water condensation in the test rig, which could introduce pressure variation and pipe plugging. Further details of the test rig are reported in [10].

No heat losses are considered in the model, and further heat requirements (Q) are needed to bring the hydrogen electrode and oxygen electrode gasses from 650 °C to the operative temperature of 750 °C. The stack is considered to operate under adiabatic conditions; thus, heat losses due to overpotentials are calculated in the stack equilibrium and participate to supply heat to the reactions.

All input parameters of the model and relative values are reported in Table 1.

Table 1. List of constant parameters used in the model.

Component	Parameter	Value	Unit
Heat Exchanger	Low temperature air—T_{airin}	20	°C
	High temperature air—T_{airout}	650	°C
	High temperature off gasses (Air + O_2)—T_{offin}	750	°C
STACK	Reactant utilization—RU	0.7	
	Hydrogen electrode composition—H_2O:H_2	90:10	mol:mol
	Area Specific Resistance—ASR	0.67	Ω cm^2
	Open circuit voltage—OCV	0.85	V
	Number of cells—N	12	
	Cell active area—A	80	cm^2

The model is developed so that main design parameter is the number of cells. This value was fixed to 12 in order to have a reference power up to 1 kW. Air flow in the system was initially fixed to be twice the molar flow of the hydrogen electrode side. The study was designed to analyze the effect of air variation and air flow rate is the parameter changed during the study. The flow values were calculated introducing, as a parameter, the ration between the oxygen electrode and the hydrogen electrode molar flow rate (Oe/He). In detail, starting from the initial value of 2, the Oe/He was lowered to 0.5 at steps of 0.25. Input Oe/He values and relative air flow rates are reported in Table 2. To improve the readability of the values, air flow is reported in Nl h^{-1}.

Table 2. Air flow values used for the study.

Oe/He	Air Flow—Nl h^{-1}
0.5	228.07
0.75	346.95
1	469.05
1.25	594.38
1.5	722.93
1.75	854.72
2	989.64

3. Results

To supply input parameters (ASR and OCV) to the electrochemical part of the model, a polarization test was performed at 750 °C operating temperature. The hydrogen electrode was fed with a mixture H_2O:H_2 90:10 with an input flow rate chosen to reach a reactant utilization of 0.7 at final current of 500 mA cm^2. Oe/He condition was set to 1, in the middle of the range used in the model. Test inputs are reported in Table 3. The experimental result is reported in Figure 5. The graph also reports the regression curve and relative linear equation.

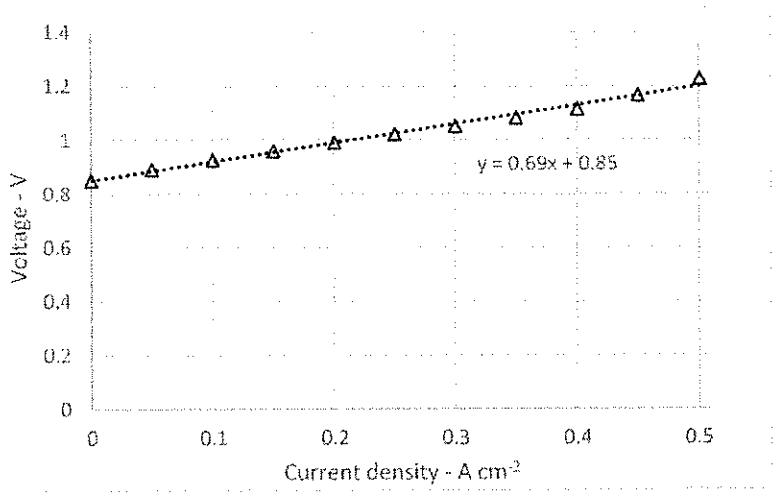

Figure 5. Polarization curve obtained from the experimental test at 750 °C.

Table 3. Test condition of the polarization curve.

Stack temperature	750 °C
H_2O:H_2	90:10
Oe/He	1
RU @ 500 A cm^{-2}	0.7
Current step	0.05 mA cm^{-2}
Holding time	60 s

Based on the experimental results, ASR was fixed to 0.69 Ω cm^2 and OCV to 0.85 V. Both values are used to linearize cell voltage as a function of current density as follows Equation (9):

$$V = \text{OCV} + \text{ASR} \cdot J \tag{9}$$

The main electrochemical results of the model are reported in Figure 6. In detail, the two graphs report cell voltage and current density as a function of Oe/He and as a function of each other. When air

flow decreases—i.e., Oe/He decreases—both voltage and current density drop. The equilibrium of the stack moves to lower values of voltage and current. If we consider the second graph in the figure—graph b—we can find the behavior predicted when describing Figure 2. Higher values of air flow increase the heat demand to the stack, moving the operative point to the right.

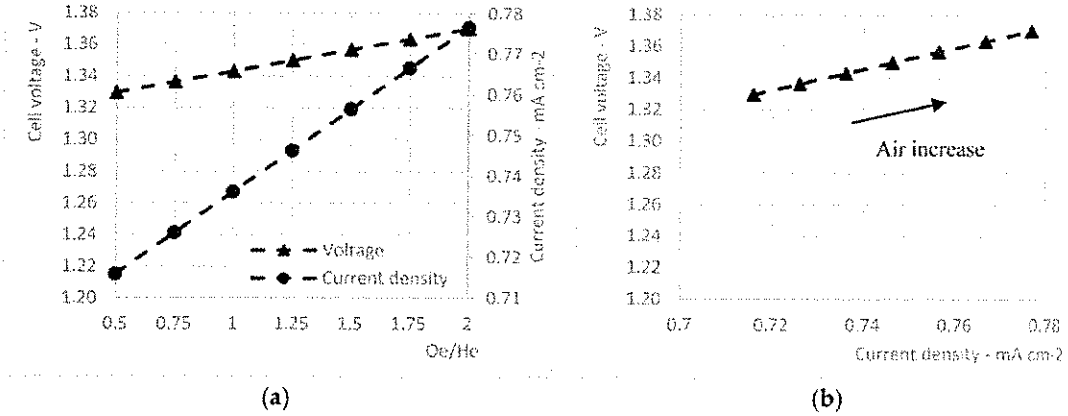

Figure 6. Cell voltage and current density plotted as function of Oe/He (**a**) and as function of each other (**b**).

In Figure 7, electrical power and efficiency are reported as a function of air flow rate. For a higher value of air flow the electrical power absorbed by the system increases due to the increase of both voltage and current density. Concerning efficiency, the heat adsorbed by the airflow, subtracted to the reaction, causes a decrease in chemical energy produced, which has a negative effect on efficiency. Therefore, it is possible to reduce air flow rate with benefits in terms of efficiency. Specifically, reducing the air flow rate from 989.64 (Oe/He = 2) to 228.07 Nl h^{-1} (Oe/He = 0.5), the power increases by 10.8% with respect to nominal conditions (Oe/He = 2), while efficiency increases by 2.8 percentage points.

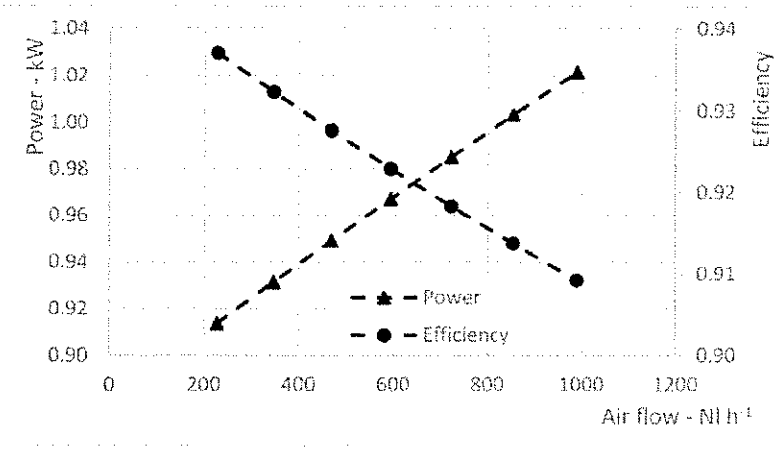

Figure 7. Power and efficiency as function of air flow rate.

Figure 8 reports the efficiency vs. hydrogen production trend that can be considered as the characteristic curve of the electrolyzer. The graph clearly shows that varying air flow can increase or reduce hydrogen production. The system suffers of the well-known tradeoff between hydrogen production and efficiency, already commented in Figure 1, with high efficiency for lower hydrogen

production and, consequently, higher system costs to produce the same amount of hydrogen. Note that system efficiency has smaller variation due to the contribution of water evaporation combined with the variation of water flow. Such efficiency is not a complete description of the system because the optimization of the hydrogen electrode flows, e.g., heat exchanger, is not implemented in the model and is not in the aim of this study.

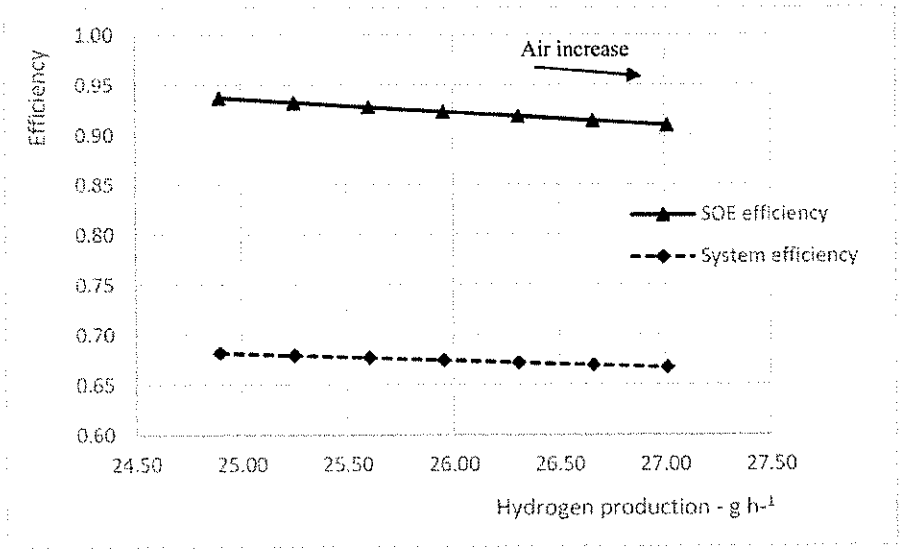

Figure 8. Efficiency vs. hydrogen production.

Figure 8 perfectly describes how the air variation can be used to rate hydrogen production of the system keeping constant operating temperature.

Looking to the heat exchanger, in Figure 9. It is reported the variation of the thermal power exchanged in the device as function of air flow. As expected, such value increases with the increase of air flow. This parameter is necessary to design the heat exchanger once best operative condition is selected.

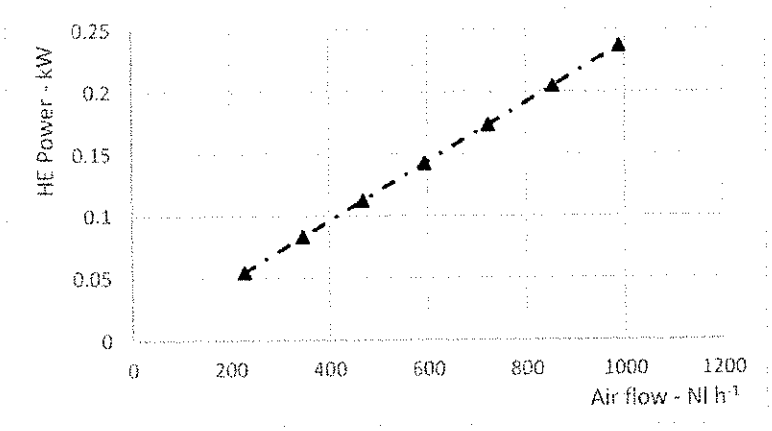

Figure 9. HE sizing as function of the air flow rate.

Finally, Figure 10 reports the outlet temperature of the system and the heat available in case a cogeneration is possible, decreasing the off gasses temperature down to 50 °C. Even if the temperature

is still acceptable for any cogeneration purpose, the total amount of heat available is very small—the values reported are in W.

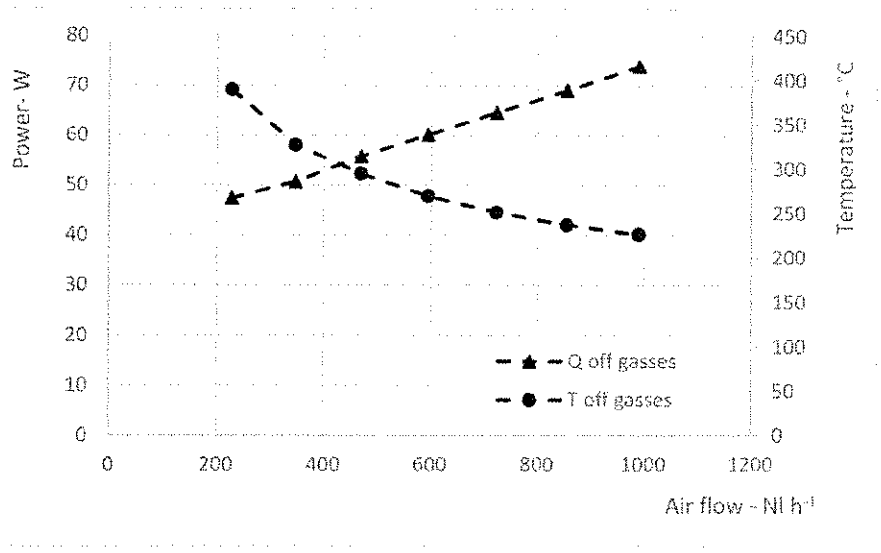

Figure 10. Temperature and heat available in off gasses as function of air flow.

4. Conclusions

The study shows how the reduction of air flow allows the increase of SOE performances. As a consequence, hydrogen production and electrical adsorbed power are reduced. At the operative temperature of 750 °C, a reduction of air down to 23% allows for an increase of efficiency of 2.8 percentage points. In this sense, air regulation represents a regulation strategy for hydrogen production when keeping a constant device temperature. Open issues are related to the effect of air variation on operative voltage. The model does not consider the effect that the variation of oxygen concentration in the relative electrode can introduce into the voltage. Such aspect as to be deeply investigated with the mean of experimental activity. Even if these advantages, in terms of efficiency, may not appear significant, it is important to highlight the additional benefits coming from the reduction of air flow. First of all, the heat exchanger that has to be realized involves smaller gas flows, and minor heat is transferred from high to low temperature gas flows. This, in general, corresponds to a smaller size of the heat exchanger and lower cost due to the smaller amount of material used. With a different approach, the air regulation can be used to rate the power of the SOE keeping a constant operative temperature. Any load variation causes an increase or reduction in operative temperature. Load variation allows us to rate the production both of hydrogen and electrical energy stored. Finally, an additional benefit of air reduction is represented by the increase of oxygen concentration in the off gasses. A higher concentration means a lower cost and a simpler separation of oxygen. The production of oxygen as a byproduct improves the cost-effective benefits of the system and can help this technology reach economic feasibility.

Acknowledgments: This research was carried out within the FUEL CELL LAB project funded by the Italian MIUR (PON03PE_00109_1).

Author Contributions: G.C. and L.B. conceived and designed the model; G.C. performed the model test; G.C. and G.B. analyzed the data; G.C. wrote the paper.

Conflicts of Interest: The authors declare no conflict of interest.

References

1. Graves, C.; Ebbesen, S.D.; Mogensen, M.; Lackner, K.S. Sustainable hydrocarbon fuels by recycling CO_2 and H_2O with renewable or nuclear energy. *Renew. Sustain. Energy Rev.* **2011**, *15*, 1–23. [CrossRef]
2. Gomez, S.Y.; Hotza, D. Current developments in reversible solid oxide fuel cells. *Renew. Sustain. Energy Rev.* **2016**, *61*, 155–174. [CrossRef]
3. Laguna-Bercero, M.A. Recent advances in high temperature electrolysis using solid oxide fuel cells: A review. *J. Power Sources* **2012**, *203*, 4–16. [CrossRef]
4. Ebbesen, S.D.; Mogensen, M. Electrolysis of carbon dioxide in Solid Oxide Electrolysis Cells. *J. Power Sources* **2009**, *193*, 349–358. [CrossRef]
5. O'Brien, J.E.; Stoots, C.M.; Herring, J.S.; Lessing, P.A.; Hartvigsen, J.J.; Elangovan, S. Performance Measurements of Solid-Oxide Electrolysis Cells for Hydrogen Production. *J. Fuel Cell Sci. Technol.* **2005**, *2*, 156–163. [CrossRef]
6. Ferrero, D.; Lanzini, A.; Santarelli, M.; Leone, P. A comparative assessment on hydrogen production from low- and high-temperature electrolysis. *Int. J. Hydrog. Energy* **2013**, *38*, 3523–3536. [CrossRef]
7. Gordon, S. , *McBride, B.J. Computer Program for Calculation of complex Chemical Equilibrium Compositions*; NASA Lewis Research Center: Cleveland, OH, USA, 1976; NASA SP-273.
8. Penchini, D.; Cinti, G.; Discepoli, G.; Desideri, U. Theoretical study and performance evaluation of hydrogen production by 200 W solid oxide electrolyzer stack. *Int. J. Hydrog. Energy* **2014**, *39*, 9457–9466. [CrossRef]
9. Liso, V.; Olesen, A.C.; Nielsen, M.P.; Kær, S.K. Performance comparison between partial oxidation and methane steam reforming processes for solid oxide fuel cell (SOFC) micro combined heat and power (CHP) system. *Energy* **2011**, *36*, 4216–4226. [CrossRef]
10. Penchini, D.; Cinti, G.; Discepoli, G.; Sisani, E.; Desideri, U. Characterization of a 100 W SOFC stack fed by carbon monoxide rich fuels. *Int. J. Hydrog. Energy* **2013**, *38*, 525–531. [CrossRef]

catalysts

MDPI

Article

Steam vs. Dry Reformer: Experimental Study on a Solid Oxide Fuel Cell Short Stack

Linda Barelli, Gianni Bidini and Giovanni Cinti *

Department of Engineering, University of Perugia, via G. Dranti 1/4A, 06125 Perugia, Italy; linda.barelli@unipg.it (L.B.); gianni.bidini@unipg.it (G.B.)

* Correspondence: giovanni.cinti@unipg.it; Tel.: +39-075-585-3991

Received: 30 September 2018; Accepted: 15 November 2018; Published: 2 December 2018

check for updates

Abstract: Solid Oxide Fuel Cell (SOFC) systems operating with methane usually are equipped with an external reformer to produce syngas. The conventional applied technology is steam methane reforming. Recent studies, instead, are presenting dry reforming as potential alternative. Advantages come from the substitution of steam with CO_2 to be handled in the system, representing a potential strategy of CO_2 reuse. This study compares, the performance of a SOFC short stack operating with dry reforming and with steam reforming mixtures respectively. Results show that higher performances can be obtained under same operating conditions, due to the high concentration of syngas (that has low content of inert species) produced via dry reforming. The analysis of different dry reforming concentrations shows that the amount of methane seems to be more relevant, in terms of voltage performances, than high hydrogen concentration. Among tested dry reforming compositions, the most performing exhibits an improvement of at least 5% in produced voltage in the range 150–375 mA cm^{-2} with respect to mixture produced by steam reforming (S/C ratio of 2.5). It was also proved that this performance enhancement does not imply greater thermal stresses, since stack temperature slightly reduces and lower temperature variations arise at anode and cathode when operating current varies.

Keywords: dry reforming; steam reforming; microCHP; SOFC stack

1. Introduction

One of the potential path to increase the efficiency of the energy system is the deployment of distributed production of energy with particular attention to high efficient cogeneration systems. In the range of micro systems (<100 kW) the most promising technology is the Solid Oxide Fuel Cell (SOFC) due to the high conversion efficiency and flexibility towards fuel composition [1]. SOFC systems integrate a high temperature fuel processing unit. To optimize temperature equilibrium and control, the SOFC stack and the fuel processor are integrated in a so called hot box where fuel is introduced and off gases are exiting the unit. Heat recovery is optimized inside the hotbox. Natural gas is transformed in the system into a mixture of hydrogen and carbon monoxide (i.e., syngas) before entering the SOFC stack. According to the conventional steam methane reforming (SMR) technology, steam is mixed with methane so that hydrogen is recovered from both species according to the following reaction (1):

$$CH_4 + H_2O \leftrightarrow 3H_2 + CO \qquad \Delta h_0 = 205 \text{ kJ mol}^{-1} \tag{1}$$

The product of the reaction is a mixture of hydrogen and carbon monoxide with higher concentration of the first compound. Thermodynamic conditions and system peculiarities are main cause for composition variation, with a predominant effect produced by steam content in the reactants. The increase in the steam to carbon ratio (S/C) moves the reaction to the products but, at the same

time, increases the dilution of active species, H_2 and CO, of the produced syngas into unreacted steam. An advancement of SMR process is represented by Sorption-Enhanced Steam Methane Reforming (SE-SMR), already investigated by the authors at both material development and process optimization levels [2–4]. This technique, in the frame of pre-combustion CCS technologies, consists in the in-situ adsorption of the CO_2 produced during a steam reforming reaction by means of regenerable adsorbents. Consequently, reaction thermodynamic limits are shifted and methane conversion increases at same operating temperature; conversely thermal energy, also at high temperature (up to 850–900 °C) according to the sorbent material typology, is needed for the sorbent regeneration phase. An alternative interesting reaction is dry reforming of methane (DRM). According to Equation (2) methane reacts with carbon dioxide, under a 1:1 molar ratio, to produce an equimolar hydrogen and carbon monoxide mixture as syngas.

$$CH_4 + CO_2 \leftrightarrow 2H_2 + 2CO \qquad \Delta h_0 = 247\ \text{kJ mol}^{-1} \tag{2}$$

Dry reforming is an extremely interesting reaction from the environmental point of view, since it allows the conversion of captured CO_2 (e.g., from fossil CO_2 sources), thus constituting a carbon capture and utilization technology (CCU), in a hydrogen-rich gas under high conversion rates (according to catalyst performance) [5–7]. With regards to the CO_2 bio-source, DRM can be considered as implementation process of biogas, that is already a mixture of methane and carbon dioxide, notwithstanding any upgrading process [8,9]. With respect to other reforming processes, as steam reforming coupled to CO-shift or partial oxidation, DRM provides a higher concentration of active species in the produced syngas and avoids the use of distilled water or oxygen/air, necessary for steam reforming and partial oxidation respectively. Thus, in a Circular Economy view, it contributes to resources preservation as well as the valorization of CO_2. Conversely, DRM is highly endothermic, but such a penalty can be overcome in case waste heat is made available by upstream processes, as possible in the integration in energy systems (as the application here investigated) and in particular processes of carbon-intensive industry (e.g., steel) where hydrogen is needed. Despite described potentialities, the development and commercialization of dry reforming technology is slowed mainly due to critical issues on catalysts, such as sintering and deactivation, caused by carbon deposition. In steam reforming process, such risk is reduced through the introduction of steam. Numerous metals such as Ni, Co and noble metals have been used as activator of DRM reaction and literature reports achieved results and open challenges [2,5,10,11]. Thermodynamic studies [12–14] indicate as best operating condition for the reaction high temperature (up to 900–1000 °C) and low pressure (1 bar). In particular, high pressure enhances both carbon and steam production. Increase of CO_2 has a positive effect on methane conversion with drawback on carbon dioxide one. Peculiarities of DRM are extremely interesting if combined with SOFC technology. Compared to low temperature fuel cells, SOFC can operate directly with syngas and no upgrade of the fuel is required. In addition, during operation SOFC produces high temperature heat that can be used to supply thermal energy to the DRM reactor. Those aspects can be found also in the state of art of SOFC system that integrates external steam methane reforming, but DRM technology has the additional advantage of higher system efficiencies and no use of steam with a significate simplification of the process and, consequently, of the system. For the case of DRM coupling to SOFC, here investigated, the system analysis previously performed by the authors [15] certifies the advantage of using dry reforming compared to steam reforming technology in SOFC systems. The new presented design, based on a two stacks integration strategy with partial recirculation of off anode exhausts from one stack into the DRM reactor, achieves 65% efficiency, 6.4 percentage points higher than equivalent system based on steam reforming reactor. Also the thermal integration of DRM reactor and SOFC stack is provided. Specifically, aiming to allow the recovery of waste heat, a temperature of the dry reforming process in the 700–750 °C range, so lower than conventional operating values, is imposed. It implies the development of customized catalysts to face coking issues, addressed also by the authors in a separate study under review. In DRM coupling to SOFC, the produced syngas directly

feeds the stack due to the high operating temperatures and the presence of catalyst (Ni) at the SOFC anode side. It allows CO to be converted in hydrogen through shift reaction (3).

$$CO + H_2O \leftrightarrow H_2 + CO_2 \qquad \Delta h_0 = -41 \text{ kJ mol}^{-1} \tag{3}$$

Peculiarities of the reactions have a relevant effect on system design. Specifically, the recirculation of off gasses requires a separation process that involves water in steam reforming configuration and carbon dioxide in dry reforming one. It is important to highlight that stack off gasses are constituted by carbon dioxide, steam and, in minor part, unreacted hydrogen. An important advantage of dry reforming, compared to steam reforming, is that once steam is separated from system off gasses, usually thanks to condensation, both hydrogen and carbon dioxide can be recirculated obtaining an additional advantage at system level. In particular, carbon dioxide is a reactant for the dry reformer and recirculation plays an important role in reactor equilibrium. The integration of DRM in SOFC system is reported in literature also considering integrated SOFC-gas turbine power system [5,6]. In particular, Wu et al. [5] implemented recirculation of anodic off-gasses into a dry reforming reactor, achieving a total power efficiency of 52.51% and an increase of CO_2 concentration in plant off gasses. Kushi [7] analyzed, by means of numerical study, an integrated hotbox containing dry reforming reactor, SOFC stack and combustor. The calculations focus on thermal equilibrium and show how same operating temperature of steam reforming could be maintained also in dry reforming design. Literature reports also few experimental studies on the operation of SOFC with dry reforming mixtures. In general, main issue of this technology is degradation caused by carbon deposition [8–12] on SOFC anode. Therefore, the optimization of DRM operating conditions has to be investigated also in consideration of the effect of reformate composition on SOFC degradation. The catalytic activity of SOFC anode for dry reforming reaction was assessed in [13], where experimental results identify an optimal temperature window above 620 °C for methane conversion. In [14], both steam and dry reforming compositions were studied in a single cell planar SOFC operating at 750 °C. Despite higher voltage obtained for steam reforming composition, dry reforming mixture achieved higher fuel utilization. In the same study, a short durability study demonstrates how internal dry reforming, already addressed by Cordigliano and Fragiacomo [16,17] and Zhu et al. [18] in case of biogas and methane feeding, is disadvantageous compared to external process. Durability studies of SOFC cell operating in dry reforming configuration are reported also in Papadam et al. [19] were stable conditions are reported for both low (650 °C) and high (850 °C) operating temperature over more than 200 h. Finally, in our previous study [20] a performance assessment of dry reforming composition was tested in a SOFC short stack to support strategies for the integration of an external dry reforming reactor in a SOFC cogeneration system. The present study, focusing the attention on the stack, presents, for the first time, an experimental comparison between SOFC operation when fed with steam reforming and dry reforming mixtures. The use of reformate gas produced via dry reforming was demonstrated to be a more efficient and cleaner option. Different compositions were tested on a short stack simulating syngas produced by steam and dry reforming. Experimental results show how dry reforming compositions are more efficient than steam reforming ones. Comparing equivalent gas mixtures in terms of chemical inputs (same number of equivalent hydrogen moles as defined in the following according to Equation (5)), the dry reforming ones allowed an increase in SOFC operating voltages up to 4.9%, if compared to steam reforming compositions. With the aim of supporting dry reforming SOFC design, the study focuses on the thermal equilibrium of the system highlighting additional advantages in terms of thermal stability and integration potentialities. Specifically, dry reforming compositions produce lower temperature variations mitigating thermal shocks to stack materials.

2. Results and Discussion

Details on experimental test campaign and SOFC stack design are reported in following paragraph. Results in terms of cell voltage as function of current density are reported in Figure 1. Cell voltage is calculated as average among the six cells of the stack. Voltage value is averaged also over time.

In details, each reported value is the average calculated in a period of five minutes sampled at 1 Hz. Such time interval is taken at the end of the one hour test. Such approach offers reliable values calculated over a wide range of samples. The calculated distribution of sampled values, in fact, is below 0.2% for voltages and below 0.01% for temperatures. Error bar could not be reported in all the graphs. As expected, all curves show a decrease in voltage when current increases due to polarization losses. Steam reforming compositions have lower values if compared with dry reforming ones, with higher value of the curve at S/C = 2 with respect to the one at S/C = 2.5. The role of steam concentration seems dominant reducing voltage values even if hydrogen concentration reaches the highest value for these compositions. Lower performances of SMR are related to the dilution of the active species, H_2 and CO, into diluents such as CO_2 and H_2O. Moreover compared to compositions A1 and A3 with similar amount of diluent (see Table 1) the DRM compositions have higher concentration of CH_4 in the active species. Methane gives a higher contribution to the reaction with a potential contribution equivalent to 4 hydrogen (see H_{2eq} definition in following paragraph). Methane contribution in the DRM compensate the dilution concentration with a final result of higher performances of all DRM mixture compared to SMR ones.

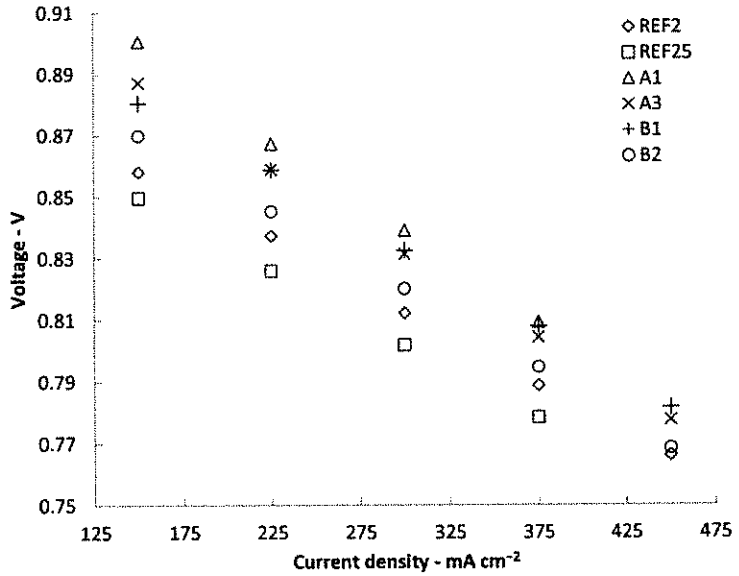

Figure 1. Stack performances in terms of Voltage vs. Current density for the compositions under study.

Table 1. Gas composition used for the experimental planning.

		H_2	CO	CO_2	CH_4	H_2O	DF	H_2/CO
1	REF2@700	62.79%	13.32%	5.71%	1.59%	16.58%	22.29%	4.71
2	REF25@700	59.52%	11.02%	6.61%	0.85%	22.00%	28.61%	5.40
3	A1	25.00%	37.00%	21.00%	11.00%	6.00%	27.00%	0.68
4	A3	31.00%	43.00%	14.00%	6.00%	6.00%	20.00%	0.72
5	B1	41.31%	44.46%	4.38%	5.46%	4.38%	8.77%	0.93
6	B2	44.35%	46.24%	3.55%	2.31%	3.55%	7.10%	0.96

Regarding dry reforming compositions, A1 is the best performing composition, A3 and B1 have very similar values, while B2 is the less performing. Compared to the other compositions, A1 has higher amount of methane while the level of concentration of active species is like to A3. If we compare A3 with B1 they have very different DF values but, again, comparable amounts of methane concentration, lower than A1 but higher than B2. Methane concentration, therefore, seems a relevant parameter to evaluate composition performances. We can also extend such consideration to

steam reforming compositions where methane concentrations are again coherent with the previous assumption. In addition, it is interesting to analyze also the voltage variation as function of current density. By applying linear regression to these values, the slope of each voltage curve was calculated. It can be defined, as absolute value, as the Area Specific Resistance (ASR) of the cells in the stack and permits to evaluate the effect of composition on the polarization losses. Results are reported in Figure 2. It is interesting to note that we have a different indication compared to voltage values. Dry reforming compositions, in fact, have higher ASR values, i.e., higher losses, if compared to steam reforming ones, even if the differences are minimal. A possible explanation, already discussed elsewhere [21], may come from a positive effect on ASR of total gas flow entering the anode, as reported in Figure 3. The increase in gas flows has a general positive effect mainly related to the reduction of diffusion losses under polarization conditions. For what above, we can conclude that dry reforming compositions provide enhanced performance in terms of produced power density, due to an increase in Open Circuit Voltage (OCV) proportional to the methane concentration in the feeding mixtures.

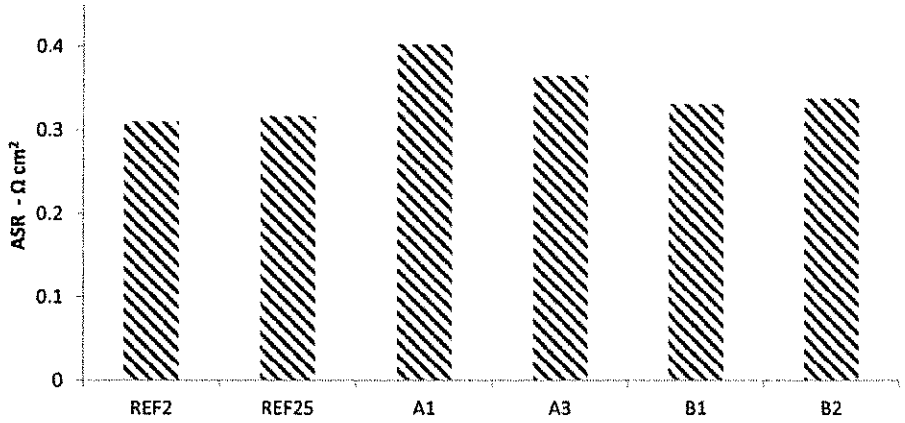

Figure 2. Area Specific Resistance (ASR) of the analyzed compositions.

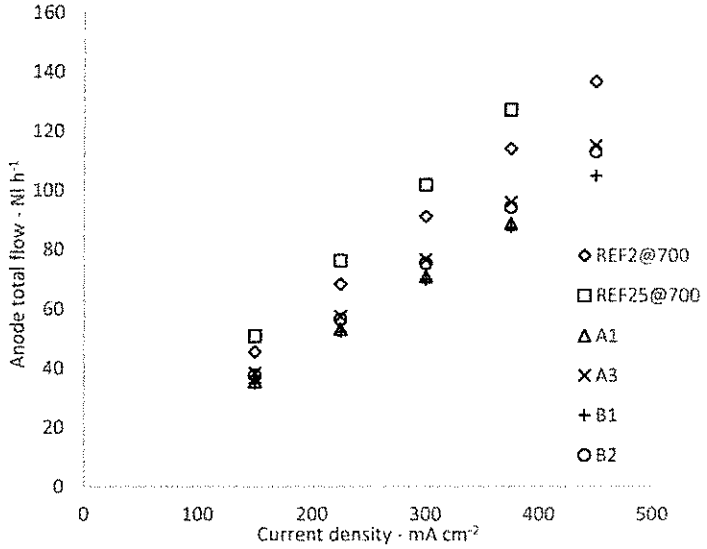

Figure 3. Total flow variation as function of Current density for the studied compositions.

Figure 4 reports stack efficiency for each investigated composition. Efficiency is calculated as follows (4):

$$\eta = \frac{V_s \cdot I}{m_{H2} \cdot LHV_{H2} + m_{CO} \cdot LHV_{CO} + m_{CH4} \cdot LHV_{CH4}} \quad (4)$$

where V_s is stack voltage, I is total current, m and LHV are mass flow and low heating value of each fuel gas. Note that the curves have not linear behaviors, like voltages, because the tests are designed with the same H_{2eq} and not same inlet energy in terms of LHV. Considering the efficiency equation, all curves have same current but different voltage values and different inlet energy amounts. Composition A1 provides also the highest efficiency.

With regards to the short-stack thermal behavior, temperature trends measured at cathode and anode outlet are depicted respectively in Figures 5 and 6. Cathodic temperature is related mainly to air flow and, therefore, current density: air flow is the same for all compositions. This means that the variation is mainly related to the power losses during operation. With the increase of current density there is an increase in temperature and, even if utilization of oxidant is very low, air variation does not completely compensate the internal thermal losses. From minimum to maximum current density there is an increase of 10 °C in temperature. The effect of composition is very low and only A1 and B2 mixtures exhibit a difference coherently with the voltage trends.

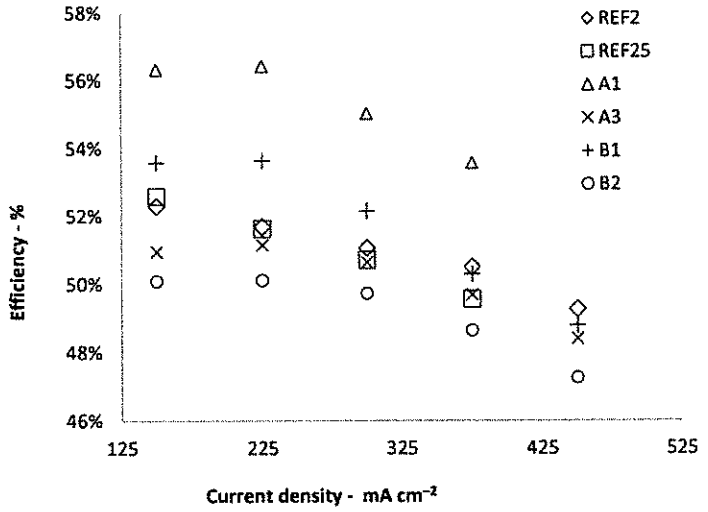

Figure 4. Stack efficiency for different gas compositions as function of current density.

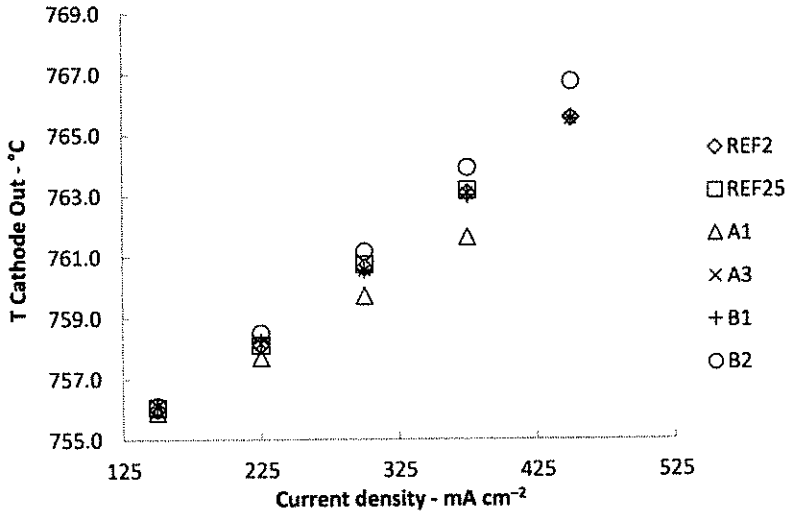

Figure 5. Cathodic outlet temperatures as function of current density.

For what concerns anodic outlet, the variation of temperature among compositions is mainly related to anodic inlet flow rate, its composition and, consequently, the occurred internal reactions.

The concentration of methane is the main factor. Due to the presence of nickel, methane reacts in the anode following both steam and dry reforming reactions, which are highly endothermic and reduce gas temperature. For all compositions, the global result consists in a temperature increase with current; it is due to the dominant role played by heat produced by polarization losses compared to the chemical reactions contribution. Due to chemical contribution to the equilibrium, curves reported in Figure 6 are not linear due to the dominant chemical contribution at low current density.

After SOFC operation with each specific mixture, a polarization curve with reference composition was performed as indicated in section "Materials and Methods". These additional tests aim to evaluate the effect of the dry reforming compositions on the materials before and after each test. Figure 7 reports the result of such analysis. Values are reported, for each current density, as percentage decay of voltage average with respect to the reference polarization performed after the start-up. Negative values indicate voltage degradation, while positive ones indicate an increase in performances.

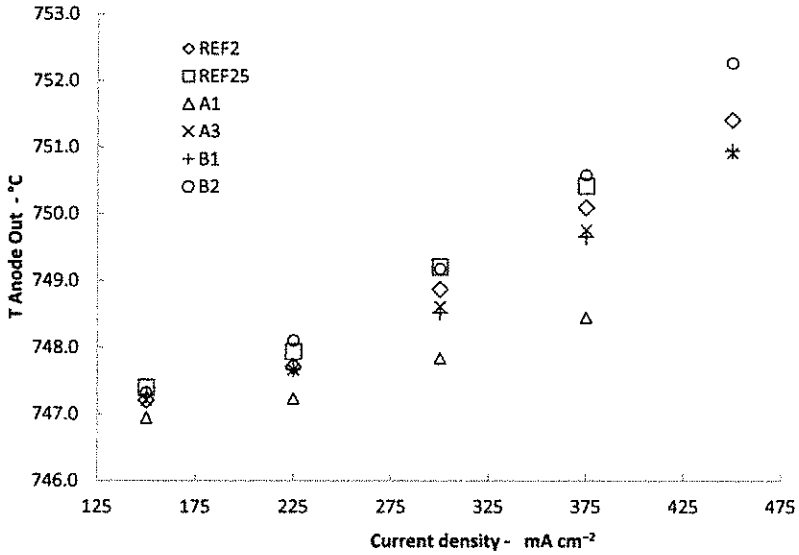

Figure 6. Anode outlet temperatures as function of current density.

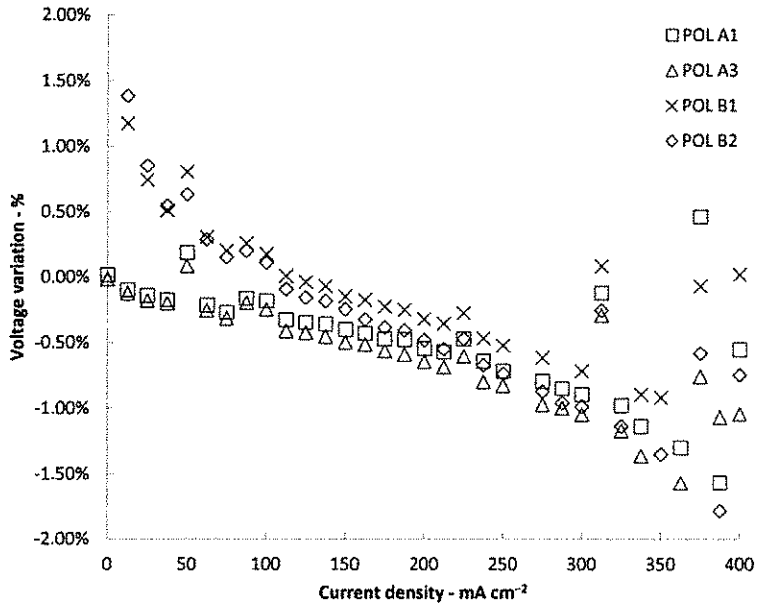

Figure 7. Voltage degradation during polarization curves.

For all reported polarization the variation in term of voltage is very low, smaller than 2%. It isn't possible to identify a linear behavior, indicating an increase in internal resistance, but it is important to notice that absolute values are higher for the last tested concentration. This means that for sure there was no fast degradation related to the tested compositions and that all the considerations on previous results are consistent and not caused by previous used mixtures.

3. Materials and Methods

The experimental runs were performed in a Solid Oxide Fuel Cell short stack supplied by SOLIDPower. The stack is composed of six planar single cells of 80 cm^2 of active area each. Standard nickel and Yttrium Stabilized Zirconia (Ni-YSZ) anode-supported cells are used, on which a barrier layer and a Lanthanum Strontium Cobalt Ferrite (LSCF) composite cathode are deposited and sintered. The stack is based on metallic cassettes, coated, low-cost ferritic alloy shaped by standard sheet metal forming processes [22]. To follow start-up specific procedure and operate a complete test planning, the stack is integrated in a test rig where temperature, gas flows and current are controlled and measured. Detailed description of the test rig can be found in literature [23,24]. No thermocouple could be placed inside the stack, but two thermocouples are located in the furnace close to the stack. Moreover, four additional thermocouples are placed inside the pipes, specifically two in the inlets, anodic and cathodic, and two in the outlet, anodic and cathodic. Figure 8 reports the simplified scheme of the test rig, included thermocouples position.

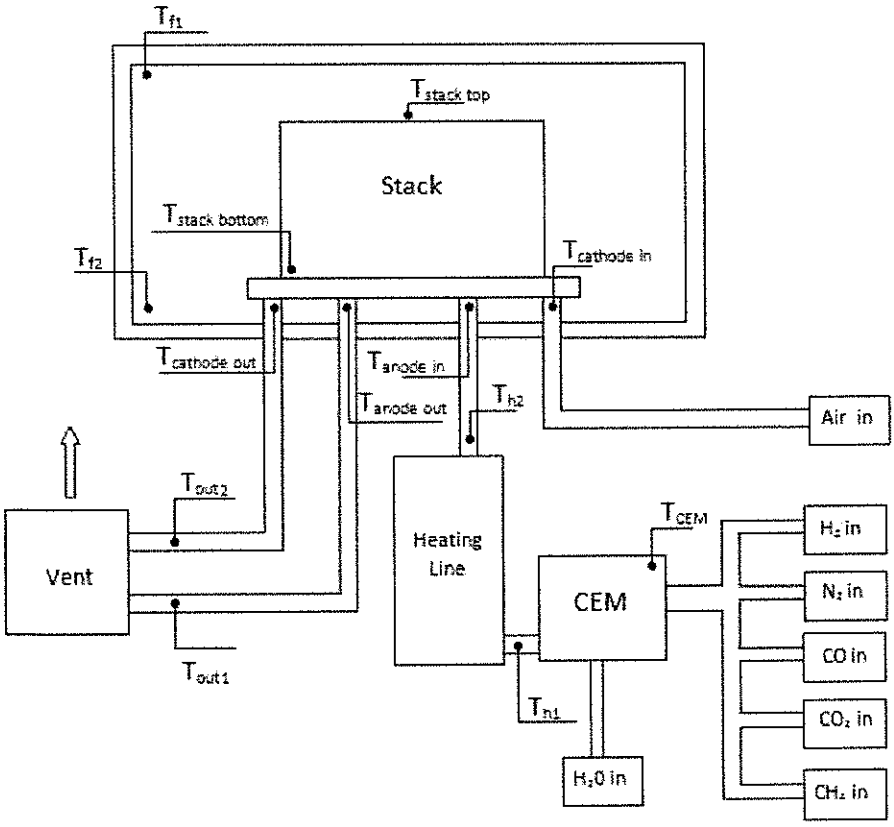

Figure 8. Scheme of the test rig.

The test rig allows to feed the anode with a composition of pure gasses such as H_2, CO, CO_2, H_2O and CH_4. Thus, mixing such gasses, it is possible to reproduce outlet compositions from a dry or a steam reformer. With the purpose of comparing steam and dry process, six gas mixtures where selected, four simulating dry reforming compositions and two simulating steam reforming ones.

Gas compositions are reported in Table 1 where molar concentrations of pure gasses are reported with the addition of: (i) dilution factor (DF) calculated as the sum of inert gasses, CO_2 and H_2O, on the total flow; (ii) molar ration between H_2 and CO concentration (H_2/CO). The two steam reforming compositions were obtained, with a thermodynamic model based on Gibbs equilibrium, simulating reformer operation at 700 °C; they differ for the steam to carbon ration (S/C). In detail, compositions 1 and 2 relate to S/C of 2 and 2.5 respectively. As expected, an increase in steam composition and a reduced amount of methane arise for S/C 2.5. A greater steam content entering the reformer permits a higher conversion of methane but, at the same time, a higher concentration of water in the off gasses.

Regarding the dry reforming compositions, mixtures 3 and 4 relate to a system model design deeply described in a previous study [15]. Specifically, A1 refers to a DRM reactor temperature of 809 °C and A3 to a higher temperature of 960 °C, while a constant CH_4/CO_2 ratio of 0.6 was set according to [15,20] at the reactor inlet. Compositions 5 and 6 where obtained from a previous experimental activity performed by the authors on dry reforming reactor deeply described elsewhere in [20], with reactor temperatures of 700 °C and 750 °C respectively, chosen compatibly with the SOFC/DRM reactor thermal integration, and under an equimolar CH_4-CO_2 mixture ($CH_4/CO_2 = 1$) at the reactor inlet. As expected, all dry reforming compositions have a reduced amount of steam. Mixtures 3 and 4, obtained by simulation under different operating conditions, e.g., $CH_4/CO_2 < 1$, have CO_2 concentrations significantly higher (with consequent high DF values). Moreover, specifically for composition 3, also higher concentration of methane and lower concentration of hydrogen are detected with respect to the other mixtures. Experimental compositions, instead, are characterized by an equilibrium between hydrogen and carbon monoxide concentrations. In all tests air was used as oxidant at the cathode. Finally, a reference anodic composition was used to evaluate any performance decrease on stack performance. Such a composition is derived from start-up procedure and is a dry mixture of hydrogen (103 Nl h^{-1}) and nitrogen (69 Nl h^{-1}) for the anode, while the cathode is fed with 1434 Nl h^{-1} of air.

The experimental planning is designed varying both current density and gas flows, to perform tests at constant utilization coefficients, i.e., the utilization of fuel, U_f, and the utilization of oxidant, U_{ox}. Utilization of fuel is defined as follows (5):

$$U_f = \frac{A \cdot N}{2 \cdot F \cdot H_{2eq}} \tag{5}$$

where A is the total current, N the number of cells (six in this case), F is the Faraday constant and H_{2eq} is defined according to Equation (6) as follows:

$$H_{2eq} = H_2 + CO + 4 \cdot CH_4 \tag{6}$$

where H_2, CO and CH_4 are hydrogen, carbon monoxide and methane molar flow rates respectively. Utilization of fuel is a well-known parameter used in fuel cells technology and, in this case, the definition includes also additional fuel species (CO, CH_4) beyond that hydrogen. Such modification is carried out considering the contribution, in terms of electrons in the electrochemical reaction, that the additional fuels species can provide through direct and indirect reactions. H_{2eq} is an established parameter in literature [20,25]. Utilization of oxidant is defined as expressed by Equation (7):

$$U_{ox} = \frac{A \cdot N}{2 \cdot F \cdot 0.21 \cdot Air} \tag{7}$$

where Air is the molar flow of air in the cathode. Once U_f and U_{ox} are defined it is possible to easily calculate gas compositions for a specific value of current. For each composition reported in Table 1 five constant utilization tests were designed and gas flows were calculated after selection of the constant parameters ($U_f = 0.8$, $U_{ox} = 0.15$) and five current values: 12, 18, 24, 30 and 36 A. Such current values correspond to current density distribution between 150 and 450 mA cm^{-2} that is the typical operation

area of a SOFC stack. Also the U_f and Uox chosen values are close to the ones used in real systems to obtain high efficiency and temperature control of the stack. A total of 30 constant utilization tests were calculated and the complete test planning is reported in Table 2. Due to constrains of the test rig two tests, strikethrough in the table, could not be performed. It hasn't effect on the relevance of the results.

Table 2. Test planning.

	H_2eq	H_2eq	U_f	Uox	H_2	CO	CO_2	CH_4	H_2O	Air	I	J
	Nl h^{-1}	mL min^{-1} cm^{-2}			Nl h^{-1}	Nl h^{-1}	Nl h^{-1}	Nl h^{-1}	g h^{-1}	Nl h^{-1}	A	mA cm^{-2}
REF2@700	38	1.31	0.80	0.15	28.65	6.08	2.61	0.73	6.08	477.89	12	150
REF2@700	56	1.96	0.80	0.15	42.98	9.12	3.91	1.09	9.11	716.83	18	225
REF2@700	75	2.61	0.80	0.15	57.31	12.16	5.21	1.45	12.15	955.77	24	300
REF2@700	94	3.27	0.80	0.15	71.63	15.20	6.51	1.81	15.19	1194.71	30	375
REF2@700	113	3.92	0.80	0.15	85.96	18.23	7.82	2.18	18.23	1433.66	36	450
REF25@700	38	1.31	0.8	0.15	30.29	5.61	3.36	0.43	8.99	477.89	12	150
REF25@700	56	1.96	0.8	0.15	45.44	8.41	5.05	0.65	13.49	716.83	18	225
REF25@700	75	2.61	0.8	0.15	60.59	11.22	6.73	0.87	17.98	955.77	24	300
REF25@700	94	3.27	0.8	0.15	75.74	14.02	8.41	1.08	22.48	1194.71	30	375
~~REF25@700~~	~~113~~	~~3.92~~	~~0.8~~	~~0.15~~	~~90.88~~	~~16.83~~	~~10.09~~	~~1.30~~	~~26.98~~	~~1433.66~~	~~36~~	~~450~~
A1	38	1.31	0.80	0.15	8.88	13.14	7.46	3.91	1.71	477.89	12	150
A1	56	1.96	0.80	0.15	13.31	19.70	11.18	5.86	2.57	716.83	18	225
A1	75	2.61	0.80	0.15	17.75	26.27	14.91	7.81	3.42	955.77	24	300
A1	94	3.27	0.80	0.15	22.19	32.84	18.64	9.76	4.28	1194.71	30	375
~~A1~~	~~113~~	~~3.92~~	~~0.80~~	~~0.15~~	~~26.63~~	~~39.41~~	~~22.37~~	~~11.72~~	~~5.13~~	~~1433.66~~	~~36~~	~~450~~
A3	38	1.31	0.8	0.15	11.90	16.51	5.38	2.30	1.85	477.89	12	150
A3	56	1.96	0.8	0.15	17.86	24.77	8.06	3.46	2.78	716.83	18	225
A3	75	2.61	0.8	0.15	23.81	33.03	10.75	4.61	3.70	955.77	24	300
A3	94	3.27	0.8	0.15	29.76	41.28	13.44	5.76	4.63	1194.71	30	375
A3	113	3.92	0.8	0.15	35.71	49.54	16.13	6.91	5.55	1433.66	36	450
B1	38	1.31	0.80	0.15	14.45	15.55	1.53	1.91	1.23	477.89	12	150
B1	56	1.96	0.80	0.15	21.67	23.32	2.30	2.86	1.85	716.83	18	225
B1	75	2.61	0.80	0.15	28.90	31.10	3.07	3.82	2.46	955.77	24	300
B1	94	3.27	0.80	0.15	36.12	38.87	3.83	4.77	3.08	1194.71	30	375
B1	113	3.92	0.80	0.15	43.34	46.65	4.60	5.73	3.69	1433.66	36	450
B2	38	1.31	0.8	0.15	16.72	17.43	1.34	0.87	1.07	477.89	12	150
B2	56	1.96	0.8	0.15	25.07	26.14	2.01	1.31	1.61	716.83	18	225
B2	75	2.61	0.8	0.15	33.43	34.86	2.68	1.74	2.15	955.77	24	300
B2	94	3.27	0.8	0.15	41.79	43.57	3.35	2.18	2.69	1194.71	30	375
B2	113	3.92	0.8	0.15	50.15	52.28	4.01	2.62	3.22	1433.66	36	450

To get stable results both for voltage and temperature measurements, each test condition at same current and gas flow was kept for one hour. At each composition change a polarization curve was performed under reference composition. The aim of such polarization curves is to evaluate if any degradation occurs during the test planning. Those tests allow to evaluate if the investigated composition caused any rapid degradation effect on the stack materials, improving the quality of the study. In this way, it is possible to distinguish any performance deterioration phenomena on the performances from the gas mixture effect, which is the aim of the study. Polarization curves were performed after one hour of operation at open circuit voltage conditions (OCV) under reference composition, varying current from OCV up to 34 A, with 1 A width step kept for one minute. Once maximum current was achieved, same procedure was performed in reverse mode down to OCV. All the tests, constant utilization and polarization curves, were performed maintaining the stack operating temperature at 750 °C.

4. Conclusions

The experimental study revealed that dry compositions can be used with higher performances in a SOFC short stack. Evidence shows that while high concentration of steam, like in steam reforming operation, strongly reduces performances, the substitution of H_2O with CO_2 causes less decay as diluent into the gasmix. In this case, lower dilution of the active species, H_2 and CO, into diluents (such as CO_2 and H_2O) and, for similar dilution (see mixtures A1 and A3 in Table 1), the higher concentration of CH_4 (which according to Equation (v) significantly impacts on H_{2eq} parameter) result

in higher performances. This positive effect overcomes the negative impact on the ASR due to the lower total gas flows of dry reforming mixtures compared to SMR ones. It results in an improvement in produced voltage of 4.9% (with reference to REF25) in the range 150–375 mA cm^{-2} when the SOFC short-stack is fed with A1 composition. Moreover, higher amount of methane in the dry reforming mix permits: (i) higher efficiency over 56% at low currents with a mean increment, in the range 150–375 mA cm^{-2}, of 4 percentage points (corresponding to about 8%) with respect to REF25 mixture; (ii) lower temperature variation at both anode and cathode outlet from minimum to maximum operating current values, proving that the performance enhancement doesn't imply greater thermal stresses. No fast degradation effect was revealed after the tests. In the future, an endurance test will be performed to provide a complete analysis of the long-term effect on material stability, especially for what concerns carbon deposition.

Author Contributions: G.C. and L.B. conceived and designed the study; G.C. performed the experimental test; G.C. and G.B. analyzed the data; G.C. wrote the paper.

Funding: This research was funded by EUROPEAN UNION'S HORIZON 2020 research and innovation program under project Net-Tools, Grant Agreement-736648.

Conflicts of Interest: The authors declare no conflict of interest.

References

1. Lo Faro, M.; Antonucci, V.; Antonucci, P.L.; Aricó, A.S. Fuel flexibility: A key challenge for SOFC technology. *Fuel* **2012**, *102*, 554–559. [CrossRef]
2. Barelli, L.; Bidini, G.; Corradetti, A.; Desideri, U. Production of hydrogen through the carbonation–calcination reaction applied to CH_4/CO_2 mixtures. *Energy* **2007**, *32*, 834–843. [CrossRef]
3. Barelli, L.; Bidini, G.; Gallorini, F. SE-SR with sorbents based on calcium aluminates: Process optimization. *Appl. Energy* **2015**, *143*, 110–118. [CrossRef]
4. Barelli, L.; Bidini, G.; Di Michele, A.; Gallorini, F.; Petrillo, C.; Sacchetti, F. Synthesis and test of sorbents based on calcium aluminates for SE-SR. *Appl. Energy* **2014**, *127*, 81–92. [CrossRef]
5. Wu, W.; Chen, S.A.; Hwang, J.J.; Hsu, F.T. Optimization and control of a stand-alone hybrid solid oxide fuel cells/gas turbine system coupled with dry reforming of methane. *J. Process Control* **2017**, *54*, 90–100. [CrossRef]
6. Wu, W.; Chen, S.-A.; Chiu, Y.-C. Design and Control of an SOFC/GT Hybrid Power Generation System with Low Carbon Emissions. *Ind. Eng. Chem. Res.* **2016**, *55*, 1281–1291. [CrossRef]
7. Kushi, T. Heat balance of dry reforming in solid oxide fuel cell systems. *Int. J. Hydrogen Energy* **2017**, *42*, 11779–11787. [CrossRef]
8. Girona, K.; Laurencin, J.; Fouletier, J.; Lefebvre-Joud, F. Carbon deposition in CH_4/CO_2 operated SOFC: Simulation and experimentation studies. *J. Power Sources* **2012**, *210*, 381–391. [CrossRef]
9. Baldinelli, A.; Barelli, L.; Bidini, G. Performance characterization and modelling of syngas-fed SOFCs (solid oxide fuel cells) varying fuel composition. *Energy* **2015**, *90*, 2070–2084. [CrossRef]
10. Pillai, M.; Lin, Y.; Zhu, H.; Kee, R.J.; Barnett, S.A. Stability and coking of direct-methane solid oxide fuel cells: Effect of CO_2 and air additions. *J. Power Sources* **2010**, *195*, 271–279. [CrossRef]
11. Shiratori, Y.; Ijichi, T.; Oshima, T.; Sasaki, K. Internal reforming SOFC running on biogas. *Int. J. Hydrogen Energy* **2010**, *35*, 7905–7912. [CrossRef]
12. Lanzini, A.; Guerra, C.; Leone, P.; Santarelli, M.; Smeacetto, F.; Fiorilli, S.; Gondolini, A.; Mercadelli, E.; Sanson, A.; Brandon, N.P. Influence of the microstructure on the catalytic properties of SOFC anodes under dry reforming of methane. *Mater. Lett.* **2016**, *164*, 312–315. [CrossRef]
13. Guerra, C.; Lanzini, A.; Leone, P.; Santarelli, M.; Brandon, N.P. Optimization of dry reforming of methane over Ni/YSZ anodes for solid oxide fuel cells. *J. Power Sources* **2014**, *245*, 154–163. [CrossRef]
14. Kushi, T. Performance and durability evaluation of dry reforming in solid oxide fuel cells. *Int. J. Hydrogen Energy* **2016**, *41*, 17567–17576. [CrossRef]
15. Barelli, L.; Ottaviano, P.A. Solid oxide fuel cell technology coupled with methane dry reforming: A viable option for high efficiency plant with reduced CO_2 emissions. *Energy* **2014**, *71*, 118–129. [CrossRef]

16. Corigliano, O.; Fragiacomo, P. Numerical modeling of an indirect internal CO_2 reforming solid oxide fuel cell energy system fed by biogas. *Fuel* **2017**, *196*, 352–361. [CrossRef]
17. Corigliano, O.; Fragiacomo, P. Numerical simulations for testing performances of an Indirect Internal CO_2 Reforming Solid Oxide Fuel Cell System fed by biogas. *Fuel* **2017**, *196*, 378–390. [CrossRef]
18. Zhu, T.; Yang, Z.; Han, M. Performance evaluation of solid oxide fuel cell with in-situ methane reforming. *Fuel* **2015**, *161*, 168–173. [CrossRef]
19. Papadam, T.; Goula, G.; Yentekakis, I.V. Long-term operation stability tests of intermediate and high temperature Ni-based anodes' SOFCs directly fueled with simulated biogas mixtures. *Int. J. Hydrogen Energy* **2012**, *37*, 16680–16685. [CrossRef]
20. Barelli, L.; Bidini, G.; Cinti, G.; Gallorini, F.; Pöniz, M. SOFC stack coupled with dry reforming. *Appl. Energy* **2017**, *192*, 498–507. [CrossRef]
21. Barelli, L.; Bidini, G.; Cinti, G.; Ottaviano, A. Study of SOFC-SOE transition on a RSOFC stack. *Int. J. Hydrogen Energy* **2017**, *42*, 26037–26047. [CrossRef]
22. Wuillemin, Z.; Ceschini, S.; Antonetti, Y.; Beetschen, C.; Modena, S.; Montinaro, D.; Cornu, T.; Bucheli, O.; Bertoldi, M. High-performance SOFC stacks tested under different reformate compositions A0901 High-performance SOFC stacks tested under different reformate compositions. In Proceedings of the 11th European SOFC and SOE Forum, Lucerne, Switzerland, 1–4 July 2014.
23. Penchini, D.; Cinti, G.; Discepoli, G.; Sisani, E.; Desideri, U. Characterization of a 100 W SOFC stack fed by carbon monoxide rich fuels. *Int. J. Hydrogen Energy* **2013**, *38*, 525–531. [CrossRef]
24. Penchini, D.; Cinti, G.; Discepoli, G.; Desideri, U. Theoretical study and performance evaluation of hydrogen production by 200 W solid oxide electrolyzer stack. *Int. J. Hydrogen Energy* **2014**, *39*, 9457–9466. [CrossRef]
25. Papurello, D.; Lanzini, A.; Fiorilli, S.; Smeacetto, F.; Singh, R.; Santarelli, M. Sulfur poisoning in Ni-anode solid oxide fuel cells (SOFCs): Deactivation in single cells and a stack. *Chem. Eng. J.* **2016**, *283*, 1224–1233. [CrossRef]

energies

MDPI

Article

Modelling and Experimental Analysis of a Polymer Electrolyte Membrane Water Electrolysis Cell at Different Operating Temperatures

Vincenzo Liso [1,*], Giorgio Savoia [1], Samuel Simon Araya [1], Giovanni Cinti [2] and Søren Knudsen Kær [1]

[1] Department of Energy Technology, Aalborg University, 9220 Aalborg, Denmark; giorgio.savoia@mip.polimi.it (G.S.); ssa@et.aau.dk (S.S.A.); skk@et.aau.dk (S.K.K.)
[2] Department of Engineering, Universitá degli Studi di Perugia, 06125 Perugia PG, Italy; giovanni.cinti@unipg.it
* Correspondence: vli@et.aau.dk; Tel.: +45-2137-0207

Received: 23 October 2018; Accepted: 20 November 2018; Published: 23 November 2018

Abstract: In this paper, a simplified model of a Polymer Electrolyte Membrane (PEM) water electrolysis cell is presented and compared with experimental data at 60 °C and 80 °C. The model utilizes the same modelling approach used in previous work where the electrolyzer cell is divided in four subsections: cathode, anode, membrane and voltage. The model of the electrodes includes key electrochemical reactions and gas transport mechanism (i.e., H_2, O_2 and H_2O) whereas the model of the membrane includes physical mechanisms such as water diffusion, electro osmotic drag and hydraulic pressure. Voltage was modelled including main overpotentials (i.e., activation, ohmic, concentration). First and second law efficiencies were defined. Key empirical parameters depending on temperature were identified in the activation and ohmic overpotentials. The electrodes reference exchange current densities and change transfer coefficients were related to activation overpotentials whereas hydrogen ion diffusion to Ohmic overvoltages. These model parameters were empirically fitted so that polarization curve obtained by the model predicted well the voltage at different current found by the experimental results. Finally, from the efficiency calculation, it was shown that at low current densities the electrolyzer cell absorbs heat from the surroundings. The model is not able to describe the transients involved during the cell electrochemical reactions, however these processes are assumed relatively fast. For this reason, the model can be implemented in system dynamic modelling for hydrogen production and storage where components dynamic is generally slower compared to the cell electrochemical reactions dynamics.

Keywords: PEM electrolysis; modelling of experimental validation; hydrogen production

1. Introduction

With the increasing production of electricity from intermittent renewable energy sources (e.g., wind and solar), the need for an effective energy storage is becoming imperative. It is therefore necessary to accumulate energy at the time it is not requested, and use it later when renewable energy is lacking, and energy is still demanded.

The European Union (EU-28) has seen an increased renewable energy production over the years and it is aiming to reach 20% of the gross final energy consumption by 2020. It is estimated that between 2006 and 2016 there was an increase in renewable energy production by two-thirds [1].

Among the different options for energy storage, PEM electrolysis has recently attracted attention because it utilizes the same technology as PEM fuel cells, which has been developed for a long time and

proven successful. The electrolyzer is able to produce hydrogen from electricity by an electrochemical reaction for later use in a fuel cell, moreover hydrogen can be used to produce other carbon-neutral fuels such as syngas and alcohols (e.g., methanol) which despite containing carbon, can be produced by renewable sources [2,3].

Early electrolyzer models and simulations in Matlab/Simulink® were developed among others by [4,5]. Such a dynamic modelling software platform is well suited for energy case scenarios where input and output are continuously changing over the time. In particular in [4], the authors describe a model with all the components from renewable energy generation including the wind turbines, electrolyzer, fuel cell and power conditioning. System transient responses to different case scenarios are also presented.

One of the first Simulink mathematical models of the gas porous diffusion electrode and ion exchange membranes of a PEM electrolyzer can be attributed to Görgün et al. [6]. This model is in fact a steady state model, as it does not consider thermal and electrical capacitance dynamic effects. Awasthi et al. [7] followed a similar approach.

Marangio et al. [8] presented a validated PEM electrolyzer semi-empirical model including overvoltages and resistances along the electrodes, flow plates and electrolyte. Abdin et al. [9] included Knudsen diffusion and molecular diffusion to characterize cathode and anode porous media. Choi et al. [10] developed an electrolyzer model with the Butler-Volmer kinetics including the effect of cell temperature on the exchange current density. More recently, Yigit et al. [11] developed a dynamic model of a high pressure PEM electrolyzer system, the model is only partially validated. This study gives detailed information of the energy losses in the system at different current density of the electrolyzer showing that above 1 A/cm^2 efficiency become significantly low.

In the aforementioned models, authors implemented the differential equations describing the physical phenomena directly in the software platform. Other authors have found other ways to approach this complex dynamic system modelling effort. For instance, Olivier et al. [12] developed a model based on the "bond graph" method. The model includes stack and BoP and simulates the behavior under intermittent condition. This graphical approach is helpful to simplify the representation of complex dynamic system behavior and convert the system in a state-space mode. The model was then implemented in Matlab/Simulink®, showing good agreement between experimental and model data.

Zhou et al. [13] developed a control oriented electrolyzer model and tested it in real time with a hardware-in-the-loop emulator of the electrolyzer and wind energy system. The emulator is able to test different electrolyzer specifications given by the manufacturers. In [14], Ruuskanen et al. followed a similar approach where only the power conditioning was experimentally tested and the rest of the system was implemented in a power-hardware-in-loop.

This paper provide a validated PEM electrolyzer model that includes the physical principles introduced in previous papers [4,5,8,9]. In addition, in this study we estimate cell efficiency and heat dissipation. Besides differently from [8,9], water gas pressure was calculated using the water saturation pressure. The model is able to predict cell performance at a large range of different temperatures. Exchange current densities parameters and membrane conductivity was chosen as closely depending on temperature.

This study is divided in two main parts. In the first part, the experimental test is described where an electrolyzer cell is characterized and performance are measured. In the second part, the model is detailed described and the experimental results are used to validate the model.

2. Experimental

The experimental setup is shown in Figure 1. The core of test is the electrolyzer cell assembly that is supplied by electrical power and the required reactants. The polarization curve was registered at two fixed operating temperatures, i.e., 60 °C and 80 °C. A start-up phase initiated each test in which the cell gradually reached the set temperature.

The cell has an active area of 2.89 cm^2. The cathode has a catalyst loading of 0.5 mg/cm^2 Pt/C, carbon cloth (C-cloth PTL) with parallel flow field. The anode has a catalyst loading of 0.3 mg/cm^2 IrO2, 2.7 mg/cm^2 Ir, porous Ti PTL, with an interdigitated flow field. The Nafion polymer membrane is type N117.

Since the first part of the cell polarization curve has a greater slope, measurement were more frequent at lower current densities than at high current density. At each step, the voltage was measured as average of 3 min measurements. Up to 0.289 A, steps were every 0.01 A cm^2; between 0.289 A and 0.578 A, steps were every 0.1 A cm^2. Finally, steps were every 0.2 A cm^2, from 0.578 A up to the maximum voltage which was fixed at 2.2 A.

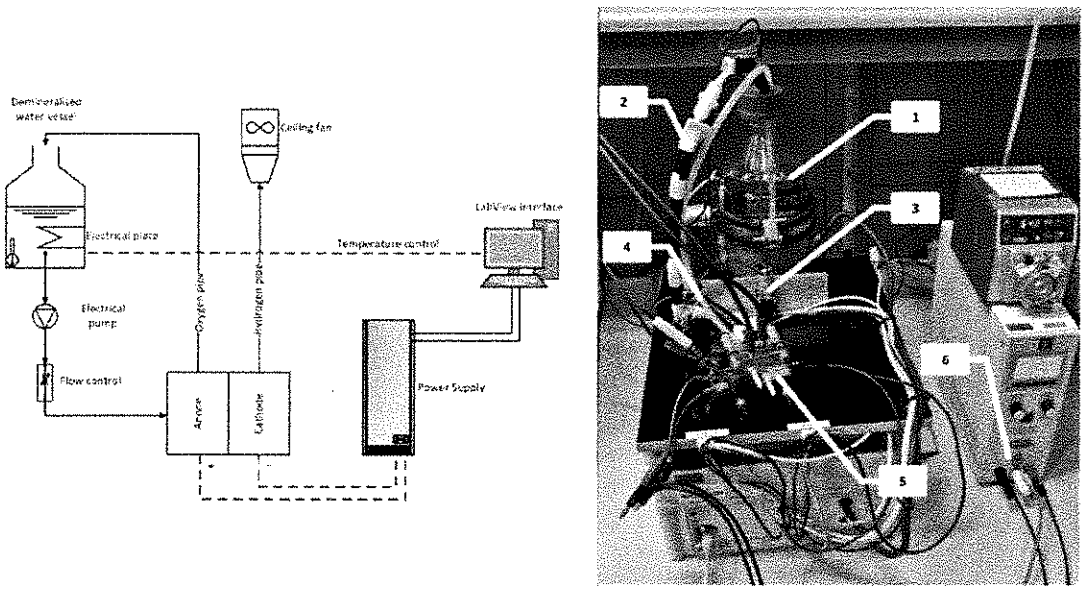

Figure 1. **(Left)** P&ID of the test setup; **(Right)** Experimental setup for single cell operation. (1) Deionized water bottle; (2) Anode water supply pipe; (3) Water supply pump; (4) Anode recirculation loop; (5) hydrogen outlet; (6) Electrical power supply.

3. Modelling

A simplified mathematical model was developed in Matlab/Simulink®. The approach follows the same modelling structure initiated by Abdin et al. [9] and Marangio et al. [8]. The model is divided into four sub-sections: Anode and Cathode chambers, Membrane and Voltage.

The model was fitted to experimental electrolyzer polarization curve operating at 60 °C and 80 °C. The electrodes reference exchange current densities at the anode and cathode, electrodes charge transfer coefficients and the membrane hydrogen ion diffusivity were estimated from the cell curve performance as they closely relate to the cell performance at different temperature.

As Figure 2 depicts at the anode side, water is introduced and then split into hydrogen ions and oxygen gas. Hydrogen positive ions cross the membrane and recombine at the cathode side forming hydrogen gas. At the same time electrons travel through the external circuit, which is connected to the power supply that provide the electromotive force for the electrochemical reaction to happen. The basic reactions taking place to the electrolyte/electrode interface are given below:

$$\text{Anode}: \ H_2O \rightarrow 2H^+ + \frac{1}{2}O_2 + 2e^{2-} \tag{1}$$

$$\text{Cathode}: \ 2H^+ + 2e^- \rightarrow H_2 \tag{2}$$

$$\text{Net reaction}: \ H_2O \rightarrow H_2 + \frac{1}{2}O_2 \tag{3}$$

The model follows similar approach to the one used by Görgün in [6] and later by [6,9]. The model is divided in four Simulink blocks in which mass flow rate of different species are computed (i.e., Anode chamber, Cathode chamber, Membrane, Voltage). Main assumption of this model is to consider steady-state electrochemical mechanism for the electrolyzer model and therefore there is an instantaneous response to input changes with no time delays. This approach is justified by the fact that transient response is very fast in PEM electrolyzer as shown in experimental work by [6,9].

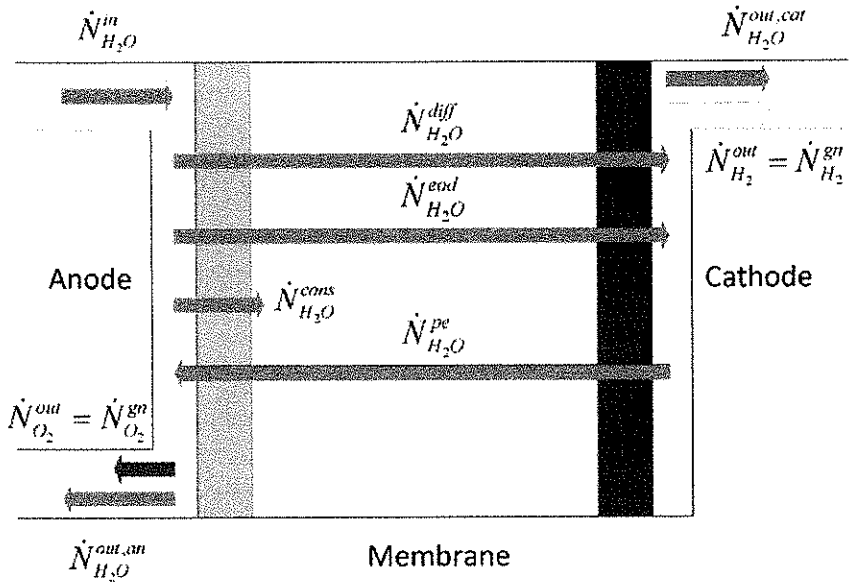

Figure 2. Molar balance in the PEM electrolyzer assembly (adapted from [8]).

3.1. Anode Chamber

In the anode chamber, four moles of oxygen are generated for each electron. According to the "Faraday's law" we can define the molar flow rate of generated oxygen as:

$$\dot{N}^{gen}_{an,O_2} = \frac{I}{4F} \text{ [mol/s]} \tag{4}$$

Similarly, two moles of water are consumed for each electron.

$$\dot{N}^{cons}_{an,H_2O} = \frac{I}{2F} \text{ [mol/s]} \tag{5}$$

I is the current which is function of the current density, i, and the cell area, A, i.e., $I = iA$.

The accumulation of oxygen gas in the anode chamber is calculated as the difference between the oxygen gas at the chamber inlet and outlet plus the oxygen generated by the electrochemical reaction [9]:

$$\frac{dN_{an,O_2}}{dt} = \dot{N}^{in}_{an,O_2} - \dot{N}^{out}_{an,O_2} + \dot{N}^{gen}_{an,O_2} \text{ [mol/s]} \tag{6}$$

Similarly the accumulation of water takes into account the water consumed by the electrochemical reaction and the net water flow through the membrane which is the combination of multiple processes as described in section "Membrane" [9].

$$\frac{dN_{an,H_2O}}{dt} = \dot{N}^{in}_{an,H_2O} - \dot{N}^{out}_{an,H_2O,l} - \dot{N}^{cons}_{an,H_2O} - \dot{N}^{mem}_{H_2O} \text{ [mol/s]} \tag{7}$$

The partial pressure of the species in the channel can be calculated using the "Dalton law" in which oxygen, water and hydrogen are considered in the gas phase. Such an approach was used,

among others, in [8,9]. As in the anode chamber water is in liquid phase, we calculate the oxygen gas partial as a difference between the anode total pressure and the water saturation pressure. In this way, the water gas phase is accounted equal to its saturation pressure.

In the present study, the anode pressure was considered atmospheric, i.e., $p_{an} = 101,325$ Pa

$$p_{O_2} = p_{an} - p_{H_2O,sat} \text{ [Pa]} \tag{8}$$

The water saturation pressure can be calculated using the "Antoine equation" which is function of temperature and other parameters shown in Table 1:

$$p_{H_2O,sat} = 10^{A - \frac{B}{C+T}} \text{ [Pa]} \tag{9}$$

Table 1. Parameter for the Antoine equation with T [°C] and p_{sat} [mm Hg] [15].

A	B	C	T_{min}	T_{max}
807.131	1730.63	233.426	1	100

Similar approach for the gas species partial pressures calculation was used for the cathode.

3.2. Cathode Chamber

At the cathode side, hydrogen is generated by the electrochemical reaction. The molar balance and the gas partial pressure can be calculated similarly to the anode side.

The hydrogen gas accumulation is calculated as a difference between the hydrogen molar flow rate at the inlet and outlet plus the product hydrogen:

$$\frac{dN_{H_2}}{dt} = \dot{N}_{H_2}^{in} - \dot{N}_{H_2}^{out} + \dot{N}_{H_2}^{gen} \text{ [mol/s]} \tag{10}$$

$$\frac{dN_{H_2O}}{dt} = \dot{N}_{H_2O}^{in} - \dot{N}_{H_2O}^{out} + \dot{N}_{H_2O}^{mem} \text{ [mol/s]} \tag{11}$$

Product hydrogen is calculated using "Faraday's law" considering that for two moles of electrons one mole of hydrogen is generated:

$$\dot{N}_{H_2}^{gen} = \frac{I}{2F} \text{ [mol/s]} \tag{12}$$

The hydrogen partial pressure is calculated as a difference between the cathode pressure, $p_{cat} = 101,325$ Pa, and the water saturation pressure:

$$p_{H_2} = p_{cat} - p_{H_2O,sat} \text{ [Pa]} \tag{13}$$

3.3. Membrane

Abdin et al. [9] identify three main relevant phenomena for water transport, namely diffusion, electro osmotic drag and hydraulic pressure, which combined provide the membrane net water flow:

$$\dot{N}_{H_2O}^{mem} = \dot{N}_{H_2O}^{diff} + \dot{N}_{H_2O}^{eod} - \dot{N}_{H_2O}^{pe} \text{ [mol/s]} \tag{14}$$

Diffusion mechanism refers to the transport phenomena due to concentration gradients across the membrane, whereas electro-osmotic drag refers to water which is dragged by hydrogen protons in the membrane, and hydraulic pressure refers to pressure asymmetries between the anode and cathode that cause water transport. We describe these three water transport processes in the next three sections.

3.4. Water Diffusion

Diffusion of water refers to the transport of water from high to low concentration regions prevalently from anode to cathode as water is formed at anode side. Fick's law is used to calculate the water transport by integrating water concentration across the membrane between the two electrodes [16]:

$$\dot{N}_{H_2O}^{diff} = AD_w \frac{dc_w}{dy} = \frac{A}{\delta_{mem}} \int_{c_w^{anode}}^{c_w^{cathode}} D_w dy \text{ [mol/s]} \quad (15)$$

Water diffusion is function of active area of the membrane A, the water diffusion coefficient, D_w, and the water concentration in the membrane, c_w. In Figure 3, the concentration of the species at the membrane interface and inside the membrane is illustrated. We can assume that the water concentration at the electrode/membrane interface is approximated with the water concentration in the electrode channel.

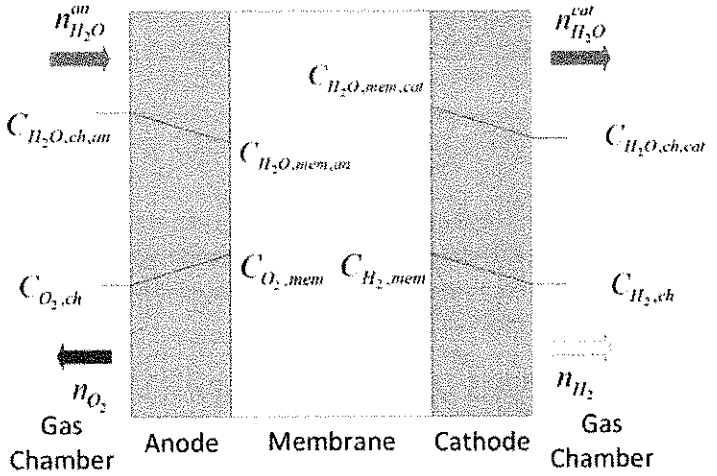

Figure 3. Species concentration inside the membrane and in the reactant channels (adapted from [8]).

Assuming a linear water concentration gradient, we can simply calculate the concentration gradients across the membrane as a difference instead of using integral function [8,9,11,17]. With this assumption in mind, we calculate the water molar flow rate due to diffusion as:

$$\dot{N}_{H_2O}^{diff} = \frac{AD_w}{\delta_{mem}} (C_{H_2O,mem,cat} - C_{H_2O,mem,an}) \text{ [mol/s]} \quad (16)$$

where D_w is the membrane water diffusion coefficient, δ_{mem} is the thickness of the membrane and $C_{H_2O,mem,cat}$, $C_{H_2O,mem,an}$ are the water concentration at the electrolyte/electrode interfaces.

The diffusion process of a multi-component gas mixture across the electrode porous media is accounted using the Stefan-Maxwell approach, which considers an effective binary diffusion coefficient. Such a coefficient is used to estimate the diffusivity as a function of temperature, pressure and other geometric parameters [18]. Similarly to the approach described in [3,8], we can calculate the water concentration using the Fick's law of diffusion in the electrolyte as shown in the equations below:

$$C_{H_2O,mem,cat} = C_{H_2O,ch,cat} + \frac{\delta_{el}^{cat} n_{H_2O}^{cat}}{D_{eff,cat}^{H_2-H_2O}} \text{ [mol/L]} \quad (17)$$

$$C_{H_2O,mem,an} = C_{H_2O,ch,an} - \frac{\delta_{el}^{an} n_{H_2O}^{an}}{D_{eff,an}^{O_2-H_2O}} \text{ [mol/L]} \quad (18)$$

where $D_{eff,an}^{O_2-H_2O}$ is the anode effective binary diffusion coefficient for $O_2 - H_2O$, $D_{eff,cat}^{H_2-H_2O}$ is the cathode effective binary diffusion coefficient for the gas pair $H_2 - H_2O$, δ_{el}^{an} and δ_{el}^{cat} are the thicknesses of the electrodes and $C_{H_2O,ch,an}$ and $C_{H_2O,ch,cat}$ are the water gas molar concentration.

The anode and cathode electrodes effective binary diffusion coefficient of transport, D_{eff}, is calibrated by applying the porosity correction [7,8]:

$$D_{eff,A-B} = D_{A-B}\varepsilon\left(\frac{\varepsilon - \varepsilon_p}{1-\varepsilon}\right)^{\alpha} \left[\mathrm{cm}^2/\mathrm{s}\right] \tag{19}$$

ε is the porosity correction, ε_p is the percolation threshold and α is an experimental factor. The binary diffusion coefficient is a proportionality factor that depends on temperature and pressure of generic two gas species A and B:

$$D_{A-B} = \left(a\left(\frac{T}{\sqrt{T_{c,a}T_{c,b}}}\right)^{b}(p_{c,a}p_{c,b})^{\frac{1}{3}}(T_{c,a}T_{c,b})^{\frac{5}{12}}\left(\frac{1}{M_{m,A}}+\frac{1}{M_{m,B}}\right)^{\frac{1}{2}}\right)\frac{1}{p}\left[\mathrm{cm}^2/\mathrm{s}\right] \tag{20}$$

In the equation, p is the electrode pressure, a and b are coefficients that depends on the gas type, M_m is the molar mass of species A and B. The water concentration in liquid form at anode and cathode can be expressed as:

$$C_{H_2O,ch,cat} = \frac{\rho_{H2O}(T_{cat})}{M_{m,H2O}};\ C_{H_2O,ch,an} = \frac{\rho_{H2O}(T_{an})}{M_{m,H2O}}\ [\mathrm{mol/L}] \tag{21}$$

The water density in this equation is calculated as [19]:

$$\rho = A/B^{1+(1-\frac{T}{C})^{D}}\left[\mathrm{Kg/m}^3\right] \tag{22}$$

The empirical parameters, A, B, C and D are provided in Table 2.

Table 2. Parameter for the water density equation with T [K] [19].

A	B	C	D	$T_{\min}$ [K]	$T_{\max}$ [K]
0.14395	0.0112	649.727	0.05107	273	685

3.5. Electro Osmotic Drag

The water transport due to electro osmotic drag $\dot{N}_{H_2O}^{eod}$ represents the number of moles of water molecules which are dragged by each mole of hydrogen ions through the membrane and it is proportional to the osmotic drag coefficient and the hydrogen ions i.e., I/F.

$$\dot{N}_{H_2O}^{eod} = \frac{n_d I}{F}\ [\mathrm{mol/L}] \tag{23}$$

The osmotic drag coefficient, n_d, represents the number of water molecules carried by each hydrogen ions and it has been measured experimentally by different authors and resulted values have shown large variance. Awasthi et al. considered a value $n_d = 5$ which is in line with the relationship below that is function of temperature and pressure [17]:

$$n_d = 0.0252P_c - 1.9073i + 0.0189T_m - 2.7892\ [\mathrm{mol_{H2O}/mol_{H+}}] \tag{24}$$

In this work we consider the experimental relationship by Onda et al. [20] which applies to a fully hydrated membrane:

$$n_d = 0.0134T + 0.03\ [\mathrm{mol_{H2O}/mol_{H+}}] \tag{25}$$

3.6. Hydraulic Pressure

Water transport due to pressure asymmetry, Δp, between anode and cathode depends on permeability of the membrane and can be calculated using the Darcy's Law. Similar approach was followed by [7–9,17]. The relationship is function of the membrane permeability to water, K_{darcy}, the viscosity, μ_{H_2O}, and the molar mass of water, M_{m,H_2O}:

$$\dot{N}_{H_2O}^{pe} = K_{darcy} \frac{A \rho_{H_2O}}{\delta_{mem} \mu_{H_2O} M_{m,H_2O}} \Delta p \text{ [mol/s]} \tag{26}$$

4. Voltage

The electrolyzer voltage is the sum of the cell potential at open circuit, V_{oc}, and three overpotentials V_{act}, V_{ohm} and V_{con}:

$$V = V_{oc} + V_{act} + V_{ohm} + V_{con} \text{ [V]} \tag{27}$$

Below we provide the description of the four voltage components included in this model. The three overpotentials are called non faradaic losses as they are mainly caused by mass transport and resistance to the flow of protons in the electrolyte membrane and electric current in the cell components as described in Chapter 2 of [21].

4.1. Open-Circuit Voltage (OCV), V_{oc}

Equilibrium electrical potential is usually described by the Nernst equation [9]:

$$V_{oc} = V_{rev}^0 - \frac{RT}{zF} \ln\left(\frac{a_{H_2O}}{a_{H_2} \cdot a_{O_2}^{1/2}}\right) \text{ [V]} \tag{28}$$

The reversible cell voltage, V_{rev}^0, and the species activities, a, can be rewritten using the partial pressure instead:

$$V_{oc} = E^0 + \frac{RT}{zF} \ln\left(\frac{p_{H_2}}{p_{cat}} \sqrt{\frac{p_{O_2}}{p_{an}}}\right) \text{ [V]} \tag{29}$$

The reversible cell voltage is E^0 is expressed as:

$$E^0 = \frac{\Delta G_R^0}{zF} \text{ [V]} \tag{30}$$

4.2. Activation over Potential, V_{act}

The activation overvoltage can be deduced by the Butler-Volmer equation, which accounts for the electrochemical kinetics of the reaction. V_{act} can be made explicit as follows:

$$V_{act} = \frac{RT}{\alpha F} \text{arcsin}h\left(\frac{i}{2i_0}\right) \text{ [V]} \tag{31}$$

where, α, is the charge coefficient. The activation overpotential represents the potential difference above the equilibrium potential (i.e., OCV) required to overcome the activation barriers to transfer electrons from the electrolyte to the electrode. The same relationship can be applied to anode and cathode electrodes of the electrolyzer cell so that the final value will be the sum of anode and cathode overpotentials:

$$V_{act} = V_{act}^{an} + V_{act}^{cat} \text{ [V]} \tag{32}$$

i_0 represents the exchange current density value which is function of the physical characteristics of the membrane material and catalyst and temperature of operation [8,9,22]. i_0 is computed both for

anode and cathode and can be represented using the same expression used by [8,18] in which i_0 is function of the roughness factor γ_M and the exchange current density, i_0^* depending on temperature:

$$i_0 = \gamma_M i_0^* \left[\mathrm{A/cm^2}\right] \tag{33}$$

The roughness factor γ_M [23] is the ratio between the electrochemically active area and the geometric area of the membrane electrolyte assembly [23]:

$$\gamma_M = \varphi_I m_M \frac{6}{\rho_M d_M} \left[\mathrm{cm^2/cm^2}\right] \tag{34}$$

In the equation, ρ_M is the catalyst density, m_M is the catalyst leading, d_M is the supported or unsupported catalyst crystallite diameter, φ_I is the fraction of metal catalyst surface in contact with the ionomer.

The exchange current density temperature dependence is modelled though an Arrhenius type relationship according to similar models [23–25]:

$$i_0^* = i_{0,ref} e^{\left[-\frac{E_a}{R}\left(\frac{1}{T}-\frac{1}{T_{ref}}\right)\right]} \left[\mathrm{A/cm^2}\right] \tag{35}$$

where $i_{0,ref}$ is the exchange current density at reference temperate, T_{ref}. $i_{0,ref}$ for both anode and cathode was empirically fitted to the experimental data at reference temperature, T_{ref}.

4.3. Ohmic Overpotential, V_{ohm}

The ohmic overpotential is dominated by ionic loss predominantly in the membrane [8,9,11,23,25]:

$$V_{ohm}^{mem} = \frac{\delta_{mem}}{\sigma_{mem}} i \ [\mathrm{V}] \tag{36}$$

The ohmic voltage is dependent on the membrane thickness, δ_{mem}, and the membrane conductivity, σ_{mem}. In many studies (e.g., the membrane conductivity, σ_{mem}, is expressed as a function of the membrane water content, λ, defined as the moles of water molecules for each mole of Sulfonic acid group, SO^{3-}, in the Nafion membrane. λ is generally constant in the electrolyzer case as the membrane is fully hydrated. In this study, σ_{mem}, was estimated using the relationship suggested by Bernardi and Verbrugge [18]:

$$\sigma_{mem} = \frac{F^2 C_{H^+} D_{H^+}}{RT} \ [\mathrm{S/cm}] \tag{37}$$

The relationship depends on C_{H^+} and D_{H^+}, which are the membrane concentration and diffusivity of hydrogen ions, H^+, the only two mobile ions, and they strongly influence performance. For our case, we considered a fixed value of $C_{H^+} = 1000\ \mathrm{mol/m^3}$ as suggested in [6]. The temperature dependent D_{H^+} value was empirically estimated to match experimental polarization curve.

4.4. Concentration over Potential, V_{con}

Marangio et al. [6] refer to this class of overpotential as "diffusion" overpotential as it considers the potential difference due to concentration difference of charge-carriers between the electrolyte and electrode surface. This mass flow in the membrane is unually described using the Nerst potential and calculating the voltage loss from a reference concentration [26].

The derivation and expression below is from [6]:

$$V_{con} = V_1 - V_0 = \frac{RT}{zF} \ln \frac{C_1}{C_0} \ [\mathrm{V}] \tag{38}$$

where C_1 is the gas concentration at operating condition and C_0 is the concentration in standard condition. The V_{con} relationship can be applied both at anode and cathode and the total concentration overpotential can be calculated as:

$$V_{con} = \frac{RT}{4F} \ln \frac{C_{an/mem,O_2}}{C_{an/mem,O_2,0}} + \frac{RT}{2F} \ln \frac{C_{cat/mem,H_2}}{C_{cat/mem,H_2,0}} \text{ [V]} \quad (39)$$

where the anode and cathode component of the overpotential can be calculated as [6] $C_{O_2,mem}$ and $C_{H_2,mem}$ represent the oxygen and hydrogen concentration at the electrode/electrolyte interface. The values can be obtained as described in the "Membrane" section.

5. Efficiency

A simplified system input-output thermodynamic analysis to determine the electrolyzer efficiency is provided in [23]. For a PEM electrolyzer we consider as input the electric work, the cooling and water for the electrochemical reaction. The system output will be the hydrogen and oxygen gas formed by the electrochemical reaction. This steady-state approach disregards, among other things, losses due mechanical work provided by ancillary equipment and the mass accumulation due to the dynamic performance.

The electrolyzer first law efficiency considers as input the electric work W provided by the power supply and as output the enthalpy change in standard condition of the electrochemical reaction to obtain hydrogen gas ΔH_R^0.

$$\varepsilon_{\Delta H} = \frac{\Delta H_R^0}{W} \text{ [-]} \quad (40)$$

We assume that the remaining part of the electrical work, which is not converted in hydrogen gas, is the rejected heat, Q. We notice that Q has a negative sign for a mere convention as in fact we provide cooling to the electrolyzer stack. We can write the cooling as a function of the electrical work and first law efficiency as:

$$-Q = W(1 - \varepsilon_{\Delta H}) \text{ [J/mol]} \quad (41)$$

The electrolyzer second law efficiency considers as input the electric work W provided by the power supply and as output the Gibbs free energy change in standard condition of the electrochemical reaction to obtain hydrogen gas, ΔG_R^0:

$$\varepsilon_{\Delta G} = \frac{\Delta G_R^0}{W} \text{ [-]} \quad (42)$$

The Gibbs free energy at standard condition, ΔG_R^0, is calculated by subtracting from ΔH_R^0, the reversible heat:

$$Q_{rev} = T\Delta S_R^0 \text{ [J/mol]} \quad (43)$$

The electrical work is function of the cell voltage, V and the faradaic efficiency:

$$W = 2F\frac{V}{\varepsilon_i} \text{ [J/mol]} \quad (44)$$

In [20] the faradaic efficiency, ε_i, is function of hydrogen and oxygen membrane crossover and is close to unity, however at low current densities it can be significant. Gas crossover occurs generally due to solution-diffusion mechanism. The relationship is function of the equivalent current of hydrogen and oxygen crossover:

$$\varepsilon_i = 1 - \left(\frac{i_{H_2,X} + i_{O_2,X}}{i} \right) \text{ [-]} \quad (45)$$

The equivalent current of hydrogen crossover, $i_{H_{2,X}}$, is defined as [20]:

$$i_{H_{2,X}} = \frac{2Fk_{H2}}{L_B} p_{H2,C} \left[\mathrm{A/cm^2}\right] \quad (46)$$

The hydrogen permeability in Nafion is defined as [20]:

$$k_{H_2} = 6.6 \times 10^{-13} \exp\left(-\frac{21030}{RT}\right) \left[\mathrm{mol\ bar^{-1}\ cm^{-1}\ s^{-1}}\right] \quad (47)$$

The equivalent current of oxygen crossover, $i_{O_{2,X}}$, is calculated similarly to that of hydrogen:

$$i_{O_{2,X}} = \frac{2Fk_{O_2}}{L_B} p_{O_2,C} \left[\mathrm{A/cm^2}\right] \quad (48)$$

The membrane permeability of oxygen is approximated as one-half of the hydrogen permeability as mentioned in [15,27]:

$$k_{O_2} = k_{H_2}/2 \left[\mathrm{mol\ bar^{-1}\ cm^{-1}\ s^{-1}}\right] \quad (49)$$

6. Results and Discussion

In order to fit the model to the experimental data, five empirical parameters were calibrated i.e., $i_{0,an,ref}$, $i_{0,ca,ref}$, α_{an}, α_{ca} and D_{H^+}. Other fixed parameters were from experimental measurements and various sources as shown in Table 3.

Table 3. Fixed model parameters from experimental measurements or various references.

Parameters	Value	Unit	Reference
A	2.89	$\mathrm{cm^2}$	
δ_{mem}	175×10^{-4}	cm	
$\delta_{el,cat}$	8×10^{-3}	cm	
$\delta_{el,an}$	8×10^{-3}	cm	
D_w	1.28×10^{-10}	$\mathrm{m^2\ s^{-1}}$	[8]
ε	0.3	-	[8]
ep	0.11	-	[8]
$alfa$	0.785	-	[8]
$T_{c,H2}$	33.3	K	[8]
$T_{c,O2}$	154.4	K	[8]
$P_{c,H2}$	12.8	atm	[8]
$P_{c,O2}$	49.7	atm	[8]
$M_{m,H2}$	2	$\mathrm{g\ mol^{-1}}$	
$M_{m,O2}$	16	$\mathrm{g\ mol^{-1}}$	
a	3.640×10^{-4}	-	[8]
b	2.334	-	[8]
μH_2O	1.1×10^{-2}	$\mathrm{gm\ cm^{-1}\ s^{-1}}$	
K_{Darcy}	1.58×10^{-14}	$\mathrm{cm^2}$	[8,9]
ΔG_R	237.2	$\mathrm{kJ\ mol^{-1}}$	[23]
ΔS_R	8.46×10^{-4}	$\mathrm{kJ\ mol^{-1}\ K^{-1}}$	[23]
z	2	-	
F	96.485	$\mathrm{C\ mol^{-1}}$	
P_{ano}	101,325	Pa	
P_{cat}	101,325	Pa	
R	8.314	$\mathrm{J\ mol^{-1}\ K^{-1}}$	
$E_{a,ano}$	76	$\mathrm{kJ\ mol^{-1}}$	[23]
$E_{a,cat}$	4.3	$\mathrm{kJ\ mol^{-1}}$	[23]
T_{ref}	298	K	
φ_f	0.75	-	[23]
$m_{M,an}$	1.0×10^{-3}	$\mathrm{g\ cm^{-2}}$	[23]
$m_{M,cat}$	0.3×10^{-3}	$\mathrm{g\ cm^{-2}}$	[23]
$\rho_{M,IrO2}$		$\mathrm{g\ cm^{-3}}$	[23]
$\rho_{M,Pt}$	21.45	$\mathrm{g\ cm^{-3}}$	[23]
$d_{M,an}$	2.9	nm	[23]
$d_{M,cat}$	2.7	nm	[23]
C_{H^+}	1000	$\mathrm{mol\ m^{-3}}$	[8]

The fitting results are given in the Table 4. Exchange current densities have high impact on the activation overpotential [9]. Among others, Espinoza et al. [28] and Biaku et al. [29] found similar values of α_{an} and α_{ca}. Choi et al. [10] suggested values of $i_{0,an,ref}$ and $i_{0,ca,ref}$ in the same range as the ones found in this model validation. Regarding the diffusivity of hydrogen protons in water, D_{H^+}, the value obtained in this study is consistent with the ones found, among others, in [8,30]. It is worth mentioning that as suggested in [30], this coefficient is strongly correlated to the cell temperature and in particular, hydrogen diffusivity increases with temperature. In [30], in the temperature range similar to the one in this study it was found a limear increase in 20% of the D_{H^+}. For this reason, we assumed two different values for D_{H^+} at the temperature of 60 °C and 80 °C as shown in the Table 4.

Table 4. Fitted model parameters.

Parameter	Value	Units
$i_{0,an,ref}$	5×10^{-12}	A/cm^2
$i_{0,ca,ref}$	1×10^{-3}	A/cm^2
α_{an}	1.2	-
α_{ca}	0.5	-
D_{H^+} ($T_{cell} = 60\,^{\circ}$C)	2.4×10^{-9}	m^2/s
D_{H^+} ($T_{cell} = 80\,^{\circ}$C)	3×10^{-9}	m^2/s

Figures 4 and 5 provide a comparison of the results obtained by both model and experimental tests using the empirically fitted parameters in Table 4. A small discrepancy in the polarization curve is seen due to the model assumption of negligible Ohmic overpotentials in the electrodes and plates, which indeed contribute in limited proportion [9]. Besides as mention before, the temperature dependence of D_{H^+} gives a good prediction for the cell performance.

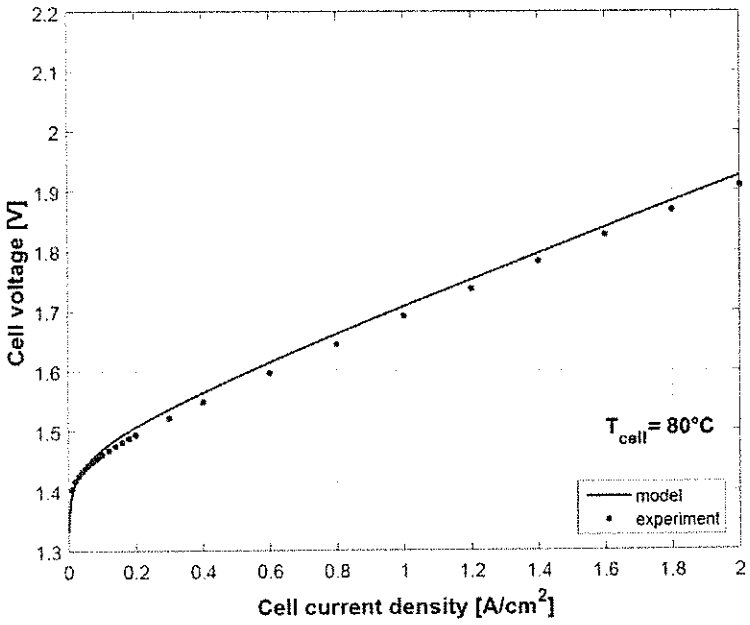

Figure 4. Model prediction and experimental data of the cell polarization at 80 °C.

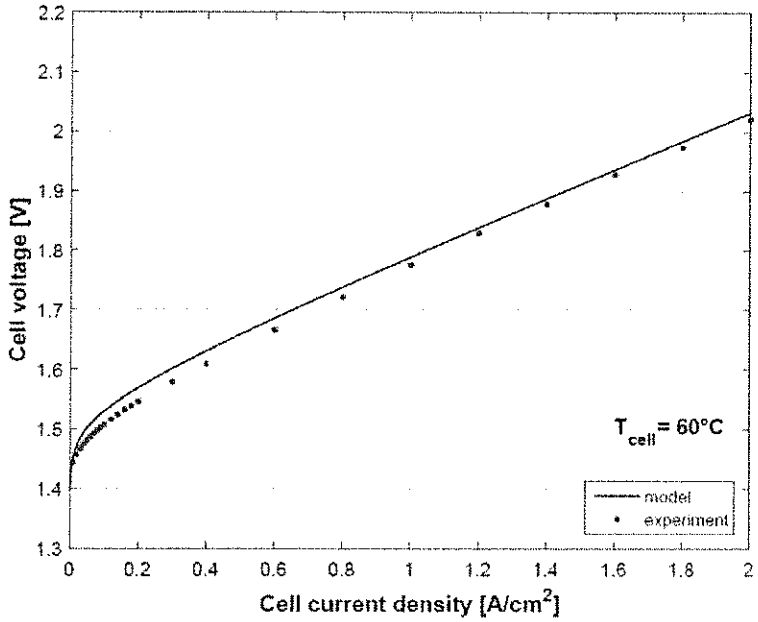

Figure 5. Model prediction and experimental data of the cell polarization at 60 °C.

In Figure 6, the effect of temperature on cell performance is depicted. Increasing temperature of operation will reduce the Gibbs free energy of the electrochemical reaction thereby increasing the cell performance and energy conversion. This is in agreement with results provided in [9].

The Ohmic overpotential depends on temperature through the conductivity relationship. This is reflected on a slight increase in the slope of the curves at mid-high current densities.

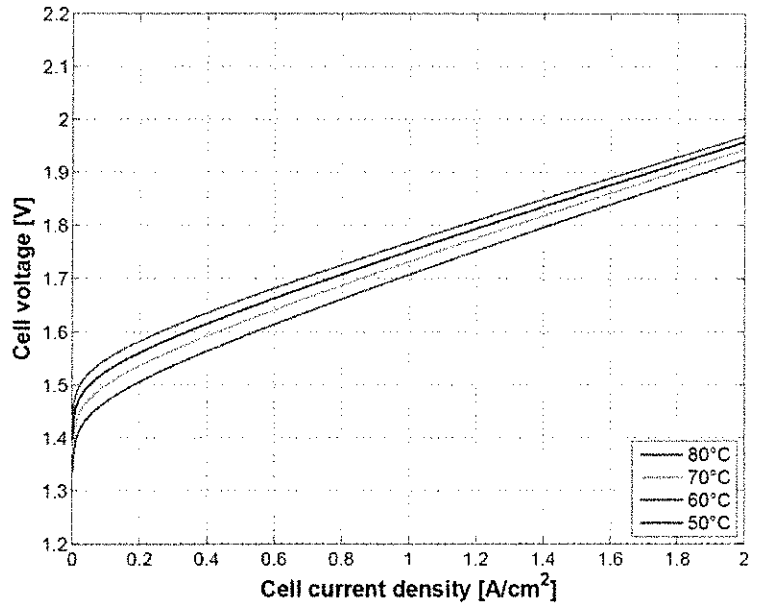

Figure 6. Modelling results of the polarization curve at different temperature of operation.

Figure 7 shows the relatively higher contribution of the anode activation overpotential to the overall activation over potential. The kinetics of the oxygen evolution reaction at the anode side is slower than the hydrogen evolution reaction at cathode side resulting in higher overpotentials at the anode. Nevertheless, the reaction kinetics also depends on physical properties of the electrode material

e.g., roughness factor. The charge transfer coefficients at anode and cathode, α_{an} and α_{ca}, gave values similar to those in [9].

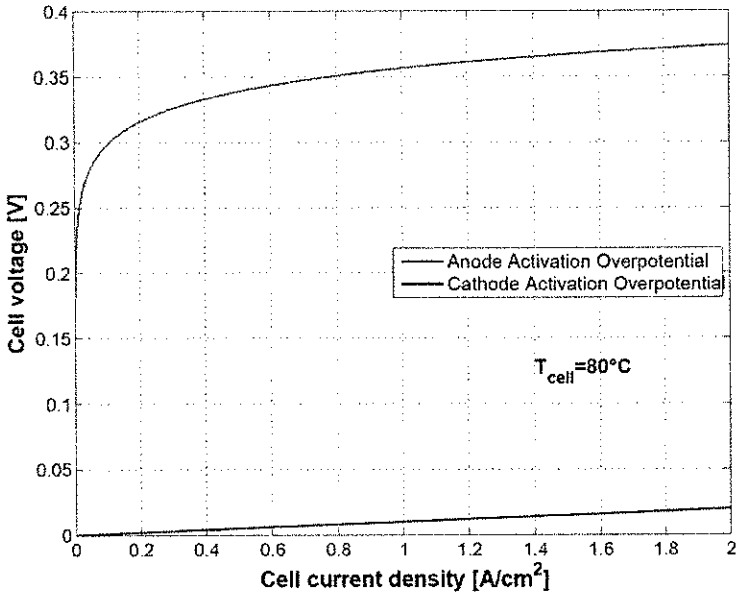

Figure 7. Anode and cathode activation overpotentials.

Figures 8 and 9 show the effect of using different exchange current densities at anode and cathode. This parameter mainly affects activation overvoltage as a consequence of different kinetics of charge transfer reactions.

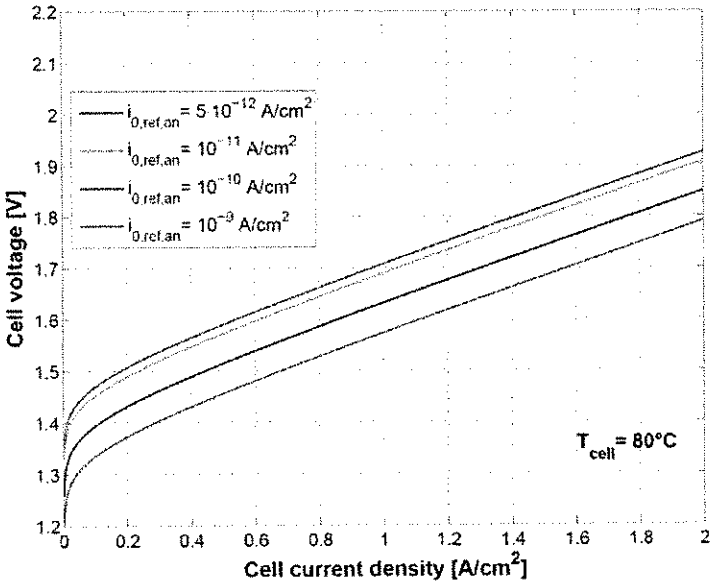

Figure 8. Impact of anode exchange current density on cell polarization curve.

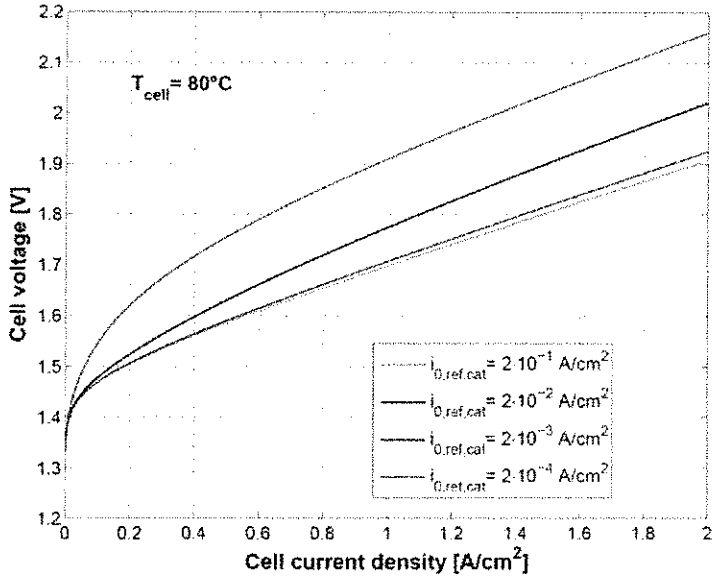

Figure 9. Impact of anode exchange current density on cell polarization curve.

The sensitivity on the cell model to the diffusivity of H^+ ions is shown in Figure 10. The link of diffusivity of H^+ ions to membrane conductivity and therefore to ohmic losses is evident as previously shown in Equation (34) and [8].

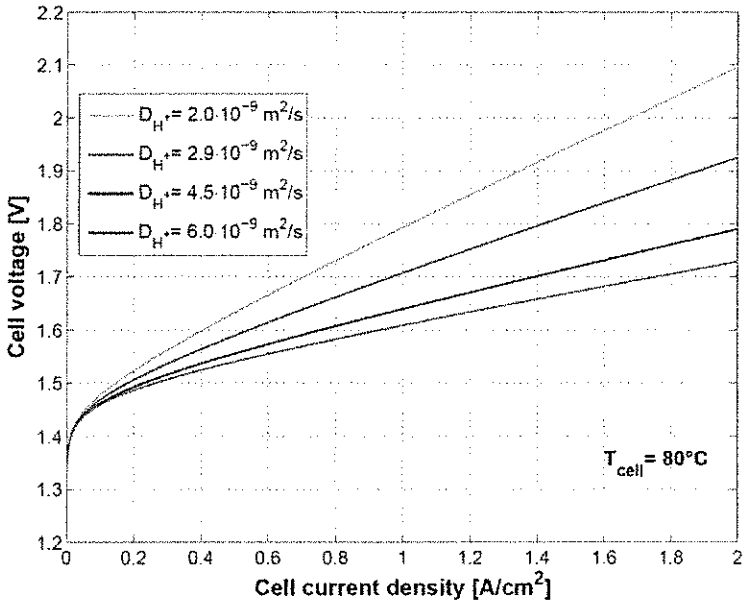

Figure 10. Influence of the cell polarization on H^+ ions diffusivity in Nafion membrane.

In Figure 11, the impact of the temperature on the first and second law efficiencies defined in Equations (37) and (39) is shown. First law efficiency can reach values higher than 100% at low current density due to cell heat absorption and strongly reduces with the increase of current density by around 30% over the current density range of operation.

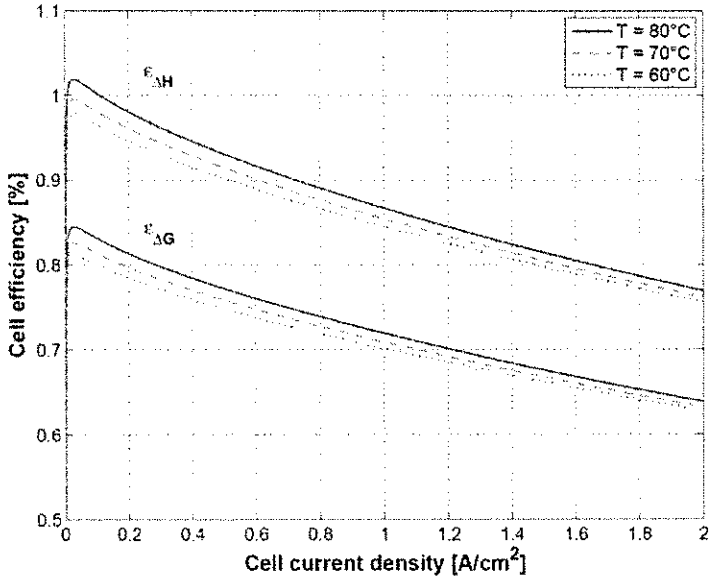

Figure 11. Cell efficiency curve along different current densities.

In Figure 12, cell heat loss is shown. At low current density, heat dissipation is negative, meaning that the cell absorbs heat from the surroundings. When hydrogen production is low, the enthalpy change of the electrochemical reaction is higher than the electrical work [23]. At high current density, a high increase in heat dissipation is to be expected.

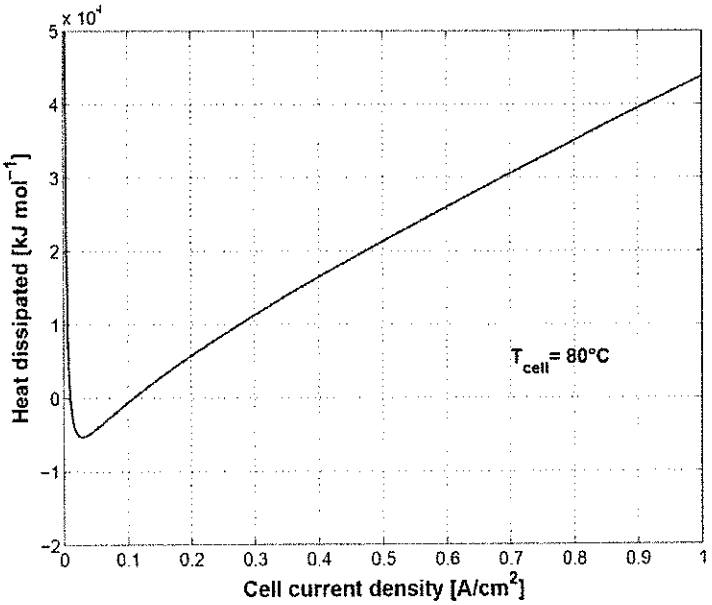

Figure 12. Predicted cell heat loss at temperature of 80 °C.

7. Conclusions

A model of a PEM electrolyzer cell was developed including electrochemical mechanism at the anode, cathode and in the membrane. Cell performance were analyses by defining an efficiency relationship. The model was able to reasonably fit the experimental data at two different temperature values i.e., 60 °C and 80 °C.

In previous studies it has been shown that activation and ohmic over voltages are closely related to temperature. For this reason, key parameters in the overvoltages relationship were chosen for the performance fitting. The electrodes reference exchange current density and electrodes change transfer coefficients showed a sensitivity to temperature; these parameters are related to the activation overvoltage. The hydrogen ion diffusivity is closely related to temperature in the ohmic overvoltage relationship.

Finally, the connection between cell polarization curve, efficiency and heat dissipation was shown. Specifically, because of the heat absorption at low current densities, first principle efficiency can reach values higher than 100%. At high current density efficiency decreases as a result of the reduced performance and related heat dissipation. Oxygen and hydrogen crossover played a less relevant role in this case as the test was conducted at ambient pressure.

Author Contributions: Conceptualization, V.L., G.S. and S.S.A.; Methodology, V.L. and G.S.; Software, G.S.; Validation, V.L. and G.S.; Formal Analysis, V.L., G.S., S.S.A. and G.C.; Writing-Original Draft Preparation, V.L.; Writing-Review & Editing, V.L.; G.S.; S.S.A. and G.C.; Supervision, S.K.K.; Project Administration, S.K.K.; Funding Acquisition, S.K.K.

Funding: This research received no external funding.

Conflicts of Interest: The authors declare no conflict of interest.

References

1. Eurostat Renewable Energy Statistics. Available online: http://ec.europa.eu/eurostat/statistics-explained/index.php/Renewable_energy_statistics (accessed on 22 November 2018).
2. Liso, V.; Cinti, G.; Nielsen, M.P.; Desideri, U. Solid oxide fuel cell performance comparison fueled by methane, MeOH, EtOH and gasoline surrogate C8H18. *Appl. Therm. Eng.* **2016**, *99*, 1101–1109. [CrossRef]
3. Dominković, D.F.; Bačeković, I.; Pedersen, A.S.; Krajačić, G. The future of transportation in sustainable energy systems: Opportunities and barriers in a clean energy transition. *Renew. Sustain. Energy Rev.* **2018**, *82*, 1823–1838. [CrossRef]
4. Khan, M.J.; Iqbal, M.T. Dynamic modeling and simulation of a small wind–fuel cell hybrid energy system. *Renew. Energy* **2005**, *30*, 421–439. [CrossRef]
5. Busquet, S.; Hubert, C.E.; Labbé, J.; Mayer, D.; Metkemeijer, R. A new approach to empirical electrical modelling of a fuel cell, an electrolyser or a regenerative fuel cell. *J. Power Sources* **2004**, *134*, 41–48. [CrossRef]
6. Görgün, H. Dynamic modelling of a proton exchange membrane (PEM) electrolyzer. *Int. J. Hydrogen Energy* **2006**, *31*, 29–38. [CrossRef]
7. Awasthi, A.; Scott, K.; Basu, S. Dynamic modeling and simulation of a proton exchange membrane electrolyzer for hydrogen production. *Int. J. Hydrogen Energy* **2011**, *36*, 14779–14786. [CrossRef]
8. Marangio, F.; Santarelli, M.; Calì, M. Theoretical model and experimental analysis of a high pressure PEM water electrolyser for hydrogen production. *Int. J. Hydrogen Energy* **2009**, *34*, 1143–1158. [CrossRef]
9. Abdin, Z.; Webb, C.J.; Gray, E.M. Modelling and simulation of a proton exchange membrane (PEM) electrolyser cell. *Int. J. Hydrogen Energy* **2015**, *40*, 13243–13257. [CrossRef]
10. Choi, P.; Bessarabov, D.G.; Datta, R. A simple model for solid polymer electrolyte (SPE) water electrolysis. In *Solid State Ionics*; Elsevier: Amsterdam, The Netherlands, 2004; Volume 175, pp. 535–539.
11. Yigit, T.; Selamet, O.F. Mathematical modeling and dynamic Simulink simulation of high-pressure PEM electrolyzer system. *Int. J. Hydrogen Energy* **2016**, *41*, 13901–13914. [CrossRef]
12. Olivier, P.; Bourasseau, C.; Bouamama, B. Dynamic and multiphysic PEM electrolysis system modelling: A bond graph approach. *Int. J. Hydrogen Energy* **2017**, *42*, 14872–14904. [CrossRef]
13. Zhou, T.; Francois, B. Modeling and control design of hydrogen production process for an active hydrogen/wind hybrid power system. *Int. J. Hydrogen Energy* **2009**, *34*, 21–30. [CrossRef]
14. Ruuskanen, V.; Koponen, J.; Huoman, K.; Kosonen, A.; Niemelä, M.; Ahola, J. PEM water electrolyzer model for a power-hardware-in-loop simulator. *Int. J. Hydrogen Energy* **2017**, *42*, 10775–10784. [CrossRef]
15. Abtew, W.; Melesse, A. *Evaporation and Evapotranspiration: Measurements and Estimations*; Springer: Dordrecht, The Netherlands, 2013.

16. Liso, V.; Simon Araya, S.; Olesen, A.C.; Nielsen, M.P.; Kær, S.K. Modeling and experimental validation of water mass balance in a PEM fuel cell stack. *Int. J. Hydrogen Energy* **2015**, *41*, 3079–3092. [CrossRef]
17. Kim, H.; Park, M.; Lee, K.S. One-dimensional dynamic modeling of a high-pressure water electrolysis system for hydrogen production. *Int. J. Hydrogen Energy* **2013**, *38*, 2596–2609. [CrossRef]
18. Bernardi, D.M.; Verbrugge, M.W. Mathematical model of a gas diffusion electrode bonded to a polymer electrolyte. *AIChE J.* **2004**, *37*, 1151–1163. [CrossRef]
19. DDBST GmbH Liquid Density Calculation by DIPPR105 Equation (Water). 2018. Available online: http://ddbonline.ddbst.de/DIPPR105DensityCalculation/DIPPR105CalculationCGI.exe?component=Water (accessed on 29 November 2018).
20. Onda, K.; Murakami, T.; Hikosaka, T.; Kobayashi, M.; Notu, R.; Ito, K. Performance Analysis of Polymer-Electrolyte Water Electrolysis Cell at a Small-Unit Test Cell and Performance Prediction of Large Stacked Cell. *J. Electrochem. Soc.* **2002**, *149*, A1069–A1078. [CrossRef]
21. Bessarabov, D.; Wang, H.; Li, H.; Zhao, N. *PEM Electrolysis for Hydrogen Production*; CRC Press: Boca Raton, FL, USA, 2015.
22. Smolinka, T.; Ojong, E.; Lickert, T. Fundamentals of PEM Water Electrolysis. In *PEM Electrolysis for Hydrogen Production*; CRC Press: Boca Raton, FL, USA, 2015; pp. 11–33.
23. Datta, R.; Martino, D.J.; Dong, Y.; Choi, P. Modeling of PEM Water Electrolyzer. In *PEM Electrolysis for Hydrogen Production—Principles and Applications*; CRC Press: Boca Raton, FL, USA, 2016; pp. 243–265, ISBN 9781482252323.
24. Carmo, M.; Fritz, D.L.; Mergel, J.; Stolten, D. A comprehensive review on PEM water electrolysis. *Int. J. Hydrogen Energy* **2013**, *38*, 4901–4934. [CrossRef]
25. García-Valverde, R.; Espinosa, N.; Urbina, A. Simple PEM water electrolyser model and experimental validation. *Int. J. Hydrogen Energy* **2012**, *37*, 1927–1938. [CrossRef]
26. O'Hayre, R.; Cha, S.-W.; Colella, W.G.; Prinz, F.B. *Fuel Cell Fundamentals*; Wiley: New York, NY, USA, 2016.
27. Kocha, S.S.; Deliang Yang, J.; Yi, J.S. Characterization of gas crossover and its implications in PEM fuel cells. *AIChE J.* **2006**, *52*, 1916–1925. [CrossRef]
28. Espinosa-López, M.; Darras, C.; Poggi, P.; Glises, R.; Baucour, P.; Rakotondrainibe, A.; Besse, S.; Serre-Combe, P. Modelling and experimental validation of a 46 kW PEM high pressure water electrolyzer. *Renew. Energy* **2018**, *119*, 160–173. [CrossRef]
29. Biaku, C.Y.; Dale, N.V.; Mann, M.D.; Salehfar, H.; Peters, A.J.; Han, T. A semiempirical study of the temperature dependence of the anode charge transfer coefficient of a 6kW PEM electrolyzer. *Int. J. Hydrogen Energy* **2008**, *33*, 4247–4254. [CrossRef]
30. Lee, S.H.; Rasaiah, J.C. Proton transfer and the mobilities of the H+ and OH− ions from studies of a dissociating model for water. *J. Chem. Phys.* **2011**, *135*, 124505. [CrossRef] [PubMed]

Applied Energy 238 (2019) 69–77

Contents lists available at ScienceDirect

Applied Energy

journal homepage: www.elsevier.com/locate/apenergy

Comparison of the solid oxide fuel cell system for micro CHP using natural gas with a system using a mixture of natural gas and hydrogen

G. Cinti[a,*], G. Bidini[a], K. Hemmes[b]

[a] Università degli Studi di Perugia, Dipartimento di Ingegneria, via Duranti 93, Perugia, Italy
[b] TU Delft, Faculty of Technology, Policy and Management, Jaffalaan 5, 2628 BX Delft, the Netherlands

HIGHLIGHTS

- A mixture of methane and hydrogen was considered as fuel for a SOFC mCHP system.
- System model was implemented with both internal and external reforming solution.
- The model has been implemented with a gradual mix change from 0% to 99% of H2.
- The introduction of hydrogen allows to achieve higher overall efficiency.

ARTICLE INFO

Keywords:
SOFC
μCHP
Hythane
Distributed generation

ABSTRACT

Solid oxide fuel cell systems for combined heat and power production (SOFC μCHP) fueled by natural gas are attractive because of their high electrical and total efficiency even at small scale. The development of a hydrogen economy will increase the availability of distributed hydrogen as a pure gas. Alternatively, hydrogen may be blended with natural gas in the grid. This study investigates the performance of SOFC μCHP systems, while using a fuel varying from pure hydrogen to pure methane via mixtures of hydrogen and methane called Hythane. Flowsheet models of external as well as internal reforming fuel cell systems were developed in Cycle-Tempo simulation software. Results show that both the external as well as the internal reforming system can operated on all fuel gas compositions varying from pure hydrogen to pure methane, thus allowing for a transition towards a hydrogen economy via the mixing of hydrogen into the natural gas grid. Although the natural gas based systems have a higher electrical efficiency, the introduction of hydrogen into the gas leads to a higher total efficiency of the combined heat and power system. The addition of hydrogen into the fuel minimizes the problems of thermal stress and thermal shock associated with the use of methane in internal reforming fuel cell systems. The internal reforming system showed a higher performance compared to the external reforming system for all Hythane gas mixtures in terms of not only electrical efficiency but also in terms of thermal and total efficiency.

1. Introduction

One of the ways to lower CO_2 emissions is a transition towards a hydrogen economy. One of the main obstacles for the development of hydrogen as an energy carrier is the cost of the development of a hydrogen distribution infrastructure. To avoid this obstacle several studies proposed to take advantage of the existing wide spread natural gas grid. Hydrogen can be mixed with methane in the present pipelines. The mixture of hydrogen and methane is sometimes called Hythane. In order to accelerate the transition towards a hydrogen economy the introduction of hydrogen into the natural gas grid is studied in several projects and reported in literature [1–6]. Van de Beld et al. showed that it is not just about the mixing of hydrogen into the natural gas grid, but that also specific production methods can be developed for producing the mixture directly. This has several advantages compared to the production of pure components first and later mixing them [1]. In a large EU project called NATURALHY the blending of hydrogen into natural gas has been extensively studied from many different perspectives [2]. The allowable percentages of hydrogen that can be mixed into a natural gas system has been studied specifically by Altfeld and Pinchbeck [3]. Lewinsky et al. focussed on the impact of natural gas/hydrogen mixtures on the performance of end-use equipment and domestic appliances [4], while Guandalini et al. [5] focussed on the consequences for the high pressure transport pipelines and Abeysekera

* Corresponding author.
E-mail address: giovanni.cinti@unipg.it (G. Cinti).

https://doi.org/10.1016/j.apenergy.2019.01.039
Received 15 April 2018; Received in revised form 2 December 2018; Accepted 4 January 2019
Available online 16 January 2019

Nomenclature

(μ)CHP	(micro) combined heat and power
RES	renewable energy sources
SOFC	solid oxide fuel cell
OCV	open circuit voltage
ER	external reforming
IR	internal reforming
AB	after burner
HE	heat exchanger
ASR	area specific resistance
Uf	fuel utilization in the SOFC
Uox	oxygen utilization in the SOFC
S2C	steam to carbon ratio
LHV	lower heating value
HHV	higher heating value

et al. [6] studied the network as a whole under distributed injection of hydrogen containing gas mixtures.

A system operating with Hythane instead of natural gas can reduce overall CO_2 emissions due to the use of hydrogen produced from renewable energy sources (RES). Moreover, we propose, in this study, the use of fuel cell technology, that is well known for its quasi zero emission in terms of pollutants.

Hythane can be used in all applications of methane in the residential field (heating, cooking), in the stationary power generation field, such as cogeneration and power production, and in the transport sector where natural gas fueled vehicles can also be operated on Hythane with significant advantages in terms of emission reductions [7–10]. In other words, Hythane can substitute methane in many of the applications where combustion occurs with the advantage of reduced CO_2 emissions due to the contribution of hydrogen. Compared to a pure hydrogen system, power units operating on Hythane are limited in terms of sustainability because the fuel still contains carbon that is most likely but not necessarily fossil based. The share of renewable energy can be increased somewhat further if the methane used in the grid comes from biomass treatment (e.g. upgraded biogas from anaerobic digestion) [11–14], from renewable electricity (power to gas) [15–17] or a combination of both [18].

In our vision three potential paths for the introduction of Hythane into our energy system can be envisioned:

- A blend of hydrogen and natural gas available in the present natural gas grid. Such a scenario is strongly dependent on the evolution of a hydrogen economy. A huge amount of hydrogen is required to increase the hydrogen concentration in the grid even if only up to a few percent. Such a scenario may develop if power to gas technology with hydrogen, as a storage option for renewable electricity, will strongly increase. Or if carbon capture and storage will be applied on a large scale in the production of hydrogen for the natural gas grid from fossil fuel resources such as from natural gas itself. Due to the extra cost it is obvious that strong incentives, such as a high carbon tax should be in place. In addition several studies reported in literature [4,19,20] and a FP6 EU project called Naturalhy [2] investigated the tolerance limits of the natural gas grid for hydrogen addition. Levinsky et al. assessed that the safety limit for the maximum amount of hydrogen to be mixed into natural gas depends on the composition of the natural gas [4]. A, maximum value of 10 vol % of hydrogen is generally considered, due to safe combustion limits in end user appliances [5]. Still even this maximum of 10 vol% of hydrogen is only 3% in terms of energy content. If we consider a future scenario where the use of combustion based technologies will be strongly reduced and the burners in remaining appliances adapted, such a limit can move up to 50 vol% and above.
- An interesting second option comes from processes that avoid the production of pure hydrogen and instead directly yield Hythane as output. Such technologies can be based on natural gas or biomass methane and encompasses conversion technologies such as steam methane reforming with low CH_4 conversion, incomplete plasma or thermal decomposition of methane and possibly internal reforming fuel cells as well. Incomplete thermal decomposition of natural gas has, for example, been studied in conjunction with concentrated solar energy by the authors of this paper [21]. We have proposed large-scale thermal decomposition of natural gas in the North of Africa while transporting the directly produced Hythane through existing natural gas pipelines to Europe. In this option, we would not be talking about mixing hydrogen into the natural gas but rather look at it as taking the carbon out. When taking biomass as the fuel both bio-reactors using bacteria and super critical gasifiers can produce a blend of methane and hydrogen with inherent advantages in the process itself compared to pure hydrogen production. Advantages and opportunities of such paths are reported in literature [1].
- As a third option the gas blend can be obtained at a local level by mixing natural gas from the grid with hydrogen locally produced from renewable energy sources. Natural gas might be used to support hydrogen energy supply when the energy from Renewable energy sources (RES) stored in the form of hydrogen is not sufficient to feed the system and fulfill the demand. Strategies can be elaborated to take maximum advantage of the use of hydrogen from RES and natural gas from the grid.

In parallel with new concepts such as Hythane, a development towards distributed generation can be observed for electricity as well as for the gas sector [22]. In particular, the distributed production of electricity in combination with the development of smart grids supported the development of small power cogeneration plants connected to the natural gas grid as well as the electricity grid while waste heat is used locally. In this cogeneration or combined heat and power application, fuel cells and, especially, high temperature fuel cells such as Solid Oxide Fuel Cells (SOFC), can achieve the highest energy efficiencies in terms of power production compared to competitive technologies [23]. The market opportunity for micro cogeneration of heat and power (μCHP) application on the scale of a household or group of houses, brought several SOFC producers and system developers to start demonstrating this technology mainly in Europe [24–26] and in Japan [27,28]. Recent research focuses on the optimization of system design [29–35] and the study of μCHP integration strategies [36–40]. System design studies have been performed applying external reforming [29,31,33], innovative designs with low temperature SOFC's [32], with and without gas recirculation [30] and substitution of steam reforming by dry reforming [34,35]. The integration strategy studies focus mainly on the economical valorization of heat and power depending on the specific geographical application conditions [36], on the type of building [37,38] and on the network integration strategy [39]. Recently also the integration of SOFC systems fed with biogas at an industrial scale was studied [40].

Simultaneous technology developments can reinforce each other or can have a negative influence on the diffusion of one or both of the technologies. Up to our knowledge the interaction between the developments sketched above and the possible consequences for SOFC operation and development have not been studied. Therefor the aim of this study in particular is to evaluate the performance of a μCHP system based on SOFC technology when fed with Hythane compared to standard operation using methane (natural gas). This study starts from the idea of placing an existing (semi-)commercial μCHP unit based on the SOFC in a future scenario where Hythane will feed the system. No

modification nor optimization of this SOFC system design is considered. The research questions we would like to answer are:

1. What would be the efficiency of the system operating on a mixture of hydrogen and natural gas compared to the same system running on pure natural gas? Would it increase or would it decrease due to the addition of hydrogen?
2. Irrespective of the efficiency would there be other advantages or disadvantages running the system on a mixture of natural gas and hydrogen?
3. Would it make a difference if the SOFC system was based on an internal reforming SOFC or if external reforming was applied in the cogeneration system?

2. System design

By mixing hydrogen into the natural gas, we expect the Nernst potential to increase due to the higher hydrogen partial pressure in the mixture. A higher Nernst potential or open circuit voltage (OCV) in general means a higher efficiency. On the other hand, the reforming of natural gas is an endothermic reaction taking away a lot of the waste heat produced in the fuel cell thereby upgrading the waste heat into chemical energy again, which makes, in particular, internal reforming fuel cells so very attractive from a thermodynamic point of view. Moreover, a higher Nernst potential often also induces a higher Nernst loss in the fuel cell because, on average, the Nernst potential is still comparable with the situation in which less hydrogen would be introduced in the fuel yielding more or less the same averaged Nernst potential over the whole cell, making the average deviation (by definition, the Nernst loss) with the higher OCV larger. Therefore, in our simulations we must be careful to include Nernst loss in a proper way and not simply model the fuel cell with an internal resistance or just with a fixed polarization. The flow sheet program we are using is called Cycle-Tempo and has this calculation of the Nernst loss in the fuel cell module in the correct way. The flow sheet program Cycle-Tempo is described elsewhere and is used in many studies of energy systems [41] and also in many fuel cell energy systems studies [21,42,43].

A cogeneration system based on SOFCs is usually composed of the SOFC stack, the fuel processing unit with external reformer, the air flow management, off gasses treatment and the thermal control network. Fuel processing in the reformer allows to obtain a hydrogen rich mixture from the supplied fuel and to reach the SOFC inlet temperature. As is well known, steam reforming of methane is endothermic so next to methane and steam also heat has to be supplied. This is accomplished by connecting the reformer to the outlet of the after-burner. Air flow management ensures the supply of the required amount of preheated air to the cathode. Usually excess air is supplied to cool the SOFC. Anode off-gas treatment is generally realized by using an after- burner that completes the oxidation of unreacted fuel. Finally, in order to provide proper heat recovery and effective heat integration the system design is complemented by heat exchangers, mixers and gas stream dividers.

The scheme of the SOFC system under study is shown in Fig. 1 and was modeled using Cycle Tempo. The design is derived from an online standard model that can be downloaded from Cycle Tempo website [44]. The system integrates a SOFC stack, an external reforming unit (ER) and an after burner (AB). It represents a typical design of an intermediate temperature SOFC system (750 °C). In detail, the complete oxidation of anode off-gas is achieved in the after burner (AB) where the fuel gas flow is mixed with the cathode outlet. The off gasses of the cathode have more oxygen than required for the after burner since there always is an excess cathode air flow to cool down the stack. Thus, a gas flow divider (S1) is added to supply only a limited amount of oxidant flow to the burner to obtain the right design temperature of the AB exhausts. After burner off gasses flow through the reformer (ER) and a heat exchanger (HE1) that pre-heats the inlet fuel up to mixer M1, where steam and fuel are premixed before entering the reformer. In the mixer M2, the AB off gasses are mixed with the other part of the

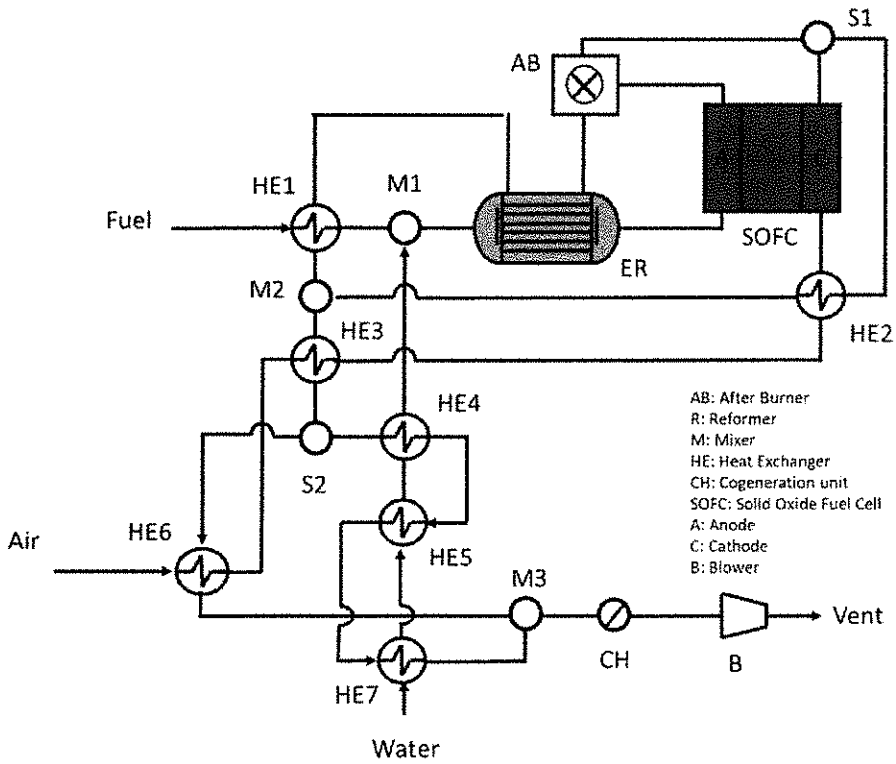

Fig. 1. Scheme of the SOFC CHP system design.

cathodic off-gas that is separated in S1. Before reaching M2, this cathodic stream preheats the cathode inlet gas in the high temperature heat exchanger HE2 up to stack inlet temperature. M2 gas outlets reach heat exchanger HE3 that provides intermediate preheating of the air inlet flow. The residual heat in the gas flow is then split in S2. Part of the S2 outlet reaches HE6 where low temperature heating is performed from room temperature while the rest of the gas from S2 is required to heat up the water stream in three different stages: economizer (HE7), evaporator (HE5) and superheater (HE4). The two streams separated in S2 are mixed back in mixer M3 before reaching the cogeneration unit (CH) and vented finally into atmosphere via the blower B. Heat extracted in CH is the thermal output of the system. Table 1 reports the design temperatures used in this study. Thermal equilibrium of the stack is defined by the gas inlet (700 °C) and outlet (800 °C) temperature. Thermal equilibrium of the SOFC is obtained by the model by controlling the air inlet gas flow. Thermal equilibrium of the reformer is obtained by recovering more or less heat from the afterburner (AB) exhaust gas stream. In the modelling of the reformer unit, chemical equilibrium of all reformer reactions is assumed at the outlet temperature. Both fuel and steam inlet flows are designed to be at 400 °C and the syngas outlet is set at the same temperature as the SOFC inlet: 700 °C. Pressure drops of 20 mbar were considered for all heat exchangers, the reformer and in the after burner. Regarding the SOFC stack, pressure losses of 20 mbar are implemented at the anode and 50 mbar at the cathode.

In the internal reforming based system, the reformer is substituted by a heat exchanger and the cell was operated in internal reforming mode. System design temperature and pressure losses are reported in Table 1.

The SOFC input design parameters, in addition to the temperatures defined in Table 1 are: total active area, area specific resistance (ASR) and fuel utilization (U_f). The model calculates utilization of oxygen (Uox) from the air flow and current density. ASR is the slope of the voltage versus current density curve. For this study the ASR value was obtained from commercial SOLiDPower ASC700 cells that, at 750 °C have a value of $2.8 \cdot 10^{-5}\,\Omega\,m^2$ [45]. The gas utilization Uf and Uox parameters are defined as follows:

$$U_f = \frac{N \cdot I}{2 \cdot F \cdot n_{H2}} \quad \text{(i)}$$

$$U_{ox} = \frac{N \cdot I}{4 \cdot F \cdot n_{O2}} \quad \text{(iii)}$$

In the equations N is the number of cells, I is cell current, F is Faraday's constant an n_{H2} and n_{O2} are hydrogen and oxygen molar flow respectively.

Air flow is obtained from stack thermal equilibrium as to maintain the design output temperatures. The reformer is designed to operate at a constant reaction equilibrium temperature of 700 °C and a steam to carbon ratio of 2.2. The same steam to carbon ratio was maintained for both internal as well as external reforming system operation.

Note that the model is designed to evaluate the system performances once changing the gas mixture inlet composition. In this sense, the model simulates the performances of a system designed for natural gas application that operates with the new blends. Thus, the analysis was performed by keeping the stack design parameters such as active area and internal resistance constant. Also fuel utilization and stack power were kept constant during the simulation. In detail, a DC stack power output of 1.25 kW was imposed in the model! Thereby a net system power in the range of 1 kW is obtained. We assume that components such as reformer, heat exchangers and burner can operate with the new gas flow composition under otherwise the same conditions. SOFC stack design parameters are reported in Table 2.

The aim of this study is to evaluate the systems operating on pure methane with the same systems operating on Hythane, therefore the model was run with 6 different gas compositions from pure methane to 1% of CH_4 into hydrogen (the software does not allow 0% CH_4 nor 100% H2). Table 3 reports the six gas compositions used in the simulations.

The introduction of hydrogen in the fuel mixture allows additional system considerations. Looking to methane as a fuel, one of the main operation limits is related to the risk of carbon deposition in pipes and in the reformer catalyst. Decreasing the concentration of carbon fuel in the input gas mixture eventually permits to bypass the pre-reactor and therefore permits the use of a direct internal reforming fuel cell configuration.

Gas mixtures can be plotted in a ternary diagram to predict the effect in terms of carbon deposition or re-oxidation of the catalyst (Fig. 2). All gas compositions used in this study are shown in Table 3. By adjusting the amount of added steam to the chosen CH_4/H_2 blends we have imposed a S2C ratio of 2.2 to all the gas compositions and therefore they all lie in the safe area in between carbon deposition and nickel oxidation.

The fuel gas compositions used are reported in Fig. 2, and are acceptable for the catalyst in the reformer and in the cell. For internal reforming configurations the addition of hydrogen to the fuel may improve the reaction equilibrium and the electrochemical reaction kinetics and reduce the potential of thermal shocks that is the main drawback of internal reforming designs.

In conclusion two SOFC cogeneration system configurations were simulated; one with external reforming (ER) and one with an internal reforming (IR) SOFC using six fuel gas compositions.

3. Results

3.1. External reforming

For each simulation the gas composition was changed. Due to the imposed constant steam to carbon ratio of 2.2, a change of gas composition brings about an increase of water consumption for higher values of the CH_4 concentration. Reformer operation is strongly affected by the fuel gas composition in terms of thermal equilibrium and chemical products. Fig. 3(a) depicts the gas flows and relative chemical power supplied through the fuel inlet and anode inlet. Fuel inlet is the fuel mixture entering the system while anode inlet is the same as external reformer outlet i.e. the syngas mixture entering the fuel cell stack. The graph shows an increase of fuel inlet flow (mass based) when moving from Hythane to pure methane but at the same time a decrease in terms of energy flow. This opposite trend is caused by the different mass energy ratio of the different Hythane compositions. The decrease in terms of inlet power is caused by the varying system efficiency as will be discussed in the following. The anode inlet flow is higher than the fuel flow due to the introduction of steam, the concentration of which increases with an increase in methane concentration. For pure hydrogen fuel, no steam is added in the reformer and the anode inlet flow is the same as the fuel inlet flow. Anode inlet power is nearly constant for all fuel gas mixtures. Even if the mass flow is higher, the heating

Table 1
Design specifics of the system.

SOFC stack temperature (°C)	750
SOFC stack inlet temperature (°C)	700
SOFC stack outlet temperature (°C)	800
Reformer reaction temperature (°C)	700
Burner outlet temperature (°C)	1200
Reformer gas inlet temperature (°C)	400
Reformer gas outlet temperature (°C)	700
HE6 air outlet temperature (°C)	350
HE7 water outlet temperature (°C)	99
HE5 steam outlet temperature (°C)	101
HE4 steam outlet temperature (°C)	400
Pressure losses in Heat exchangers (bar)	0.02

Table 2
SOFC stack input data.

Total active area – m^2	300
Area specific resistance (ASR) – Ωm^2	$2.8 \cdot 10^{-5}$
Utilization of fuel	0.8
Power output (DC) – W	1225
Anodic pressure losses – bar	0.02
Cathodic pressure losses – bar	0.05

Table 3
Gas composition and S/C ratio of inlet fuel used in the simulations.

#	CH_4:H_2	S2C
1	100:0	2.2
2	80:20	2.2
3	60:40	2.2
4	40:60	2.2
5	20:80	2.2
6	1:99	2.2

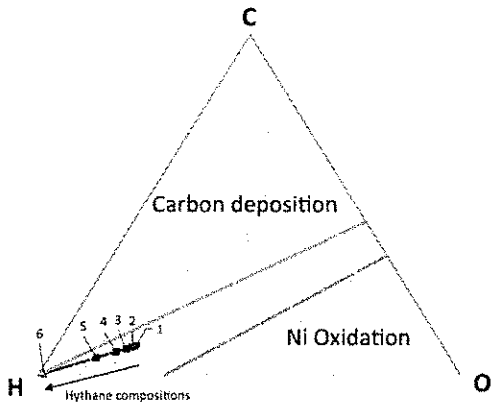

Fig. 2. Ternary HCO diagram of the selected compositions.

value of the mixture is lower due to the diluting effect of adding steam. As a net result the chemical power entering the stack is nearly constant. Anodic inlet gas composition as a function of methane concentration in the fuel gas is shown in Fig. 3(b). As anticipated, the increase of methane content in the flow has a diluting effect due to the corresponding imposed increase of steam and the formation of more CO_2 in the reformer due to this addition of steam.

Stack equilibrium is calculated at constant fuel utilization and constant electric output power. This results in a cell voltage and current density as a function of methane concentration in the fuel gas as shown in Fig. 4(a). The efficiency of the fuel cell stack is shown in Fig. 4(b). The cell voltage is higher when the system is operated with Hythane with a higher hydrogen content. As discussed in the introduction a higher hydrogen concentration results in a higher OCV and in general also in a higher cell voltage during operation. Vice versa, the current density has to decrease when cell voltage increases in order to fulfill the boundary condition of constant electric output power that we imposed on the system. A lower cell voltage of the SOFC obviously leads to a lower stack efficiency as shown in Fig. 4(b).

Moving to system level, the introduction of hydrogen in the inlet gas brings two interesting results. Fig. 5(a) reports net-, thermal- and total efficiency at system level. When the system operates with pure methane, the electrical efficiency is found to be 48.44% and total efficiency is 75.07%, both based on LHV. Such values are in line with the state of the art of the technology as reported in [46]. Efficiencies are calculated as heat-, power- and total energy output divided by the lower heating value (LHV) of the chemical energy in the input fuel flow in terms of energy per unit time (kW). Curves show a higher electrical efficiency of the system operating on pure methane compared to the same system operating on Hythane. On the other hand, when using Hythane higher thermal efficiencies and – in general - higher total efficiencies are obtained in the simulations. The lower electrical efficiency when using Hythane instead of methane is caused by a reduced contribution of the reformer to the system. The reformer reactor converts internally dissipated heat into chemical energy via the endothermic reforming reaction(s) in the reactor. This leads to higher hydrogen flows and increased chemical energy input into the stack and, therefore, via the imposed boundary condition of constant power output to a reduction of primary energy (fuel) input. When adding hydrogen into the gas mixture, the reduced heat absorption in the reactor results in a higher heat content in the off gasses and a higher heat production of the total system. This increase in thermal efficiency is also related, yet for a smaller amount, to the larger higher heating value (HHV) of Hythane compared to methane. As stated, our efficiency calculations are based on the lower heating value but heat recovery in our cogeneration system is performed down to 40 °C and therefore, condensation heat is included in the heat output but not accounted for in the input following the most frequently used convention for

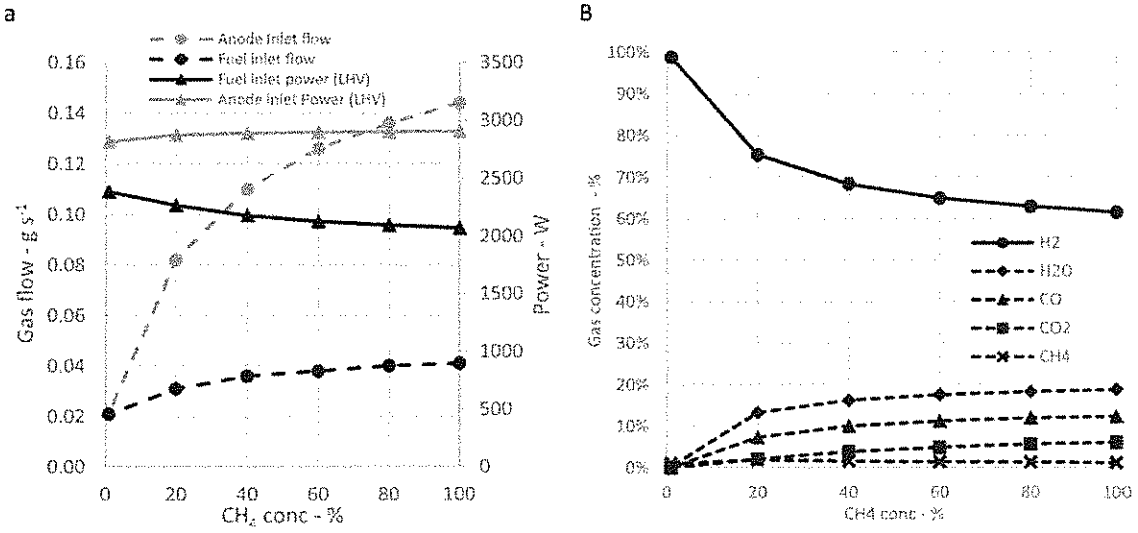

Fig. 3. (a) System fuel and anode inlet flue and (b) Anode inlet composition as function of CH_4 concentration in the Hythane.

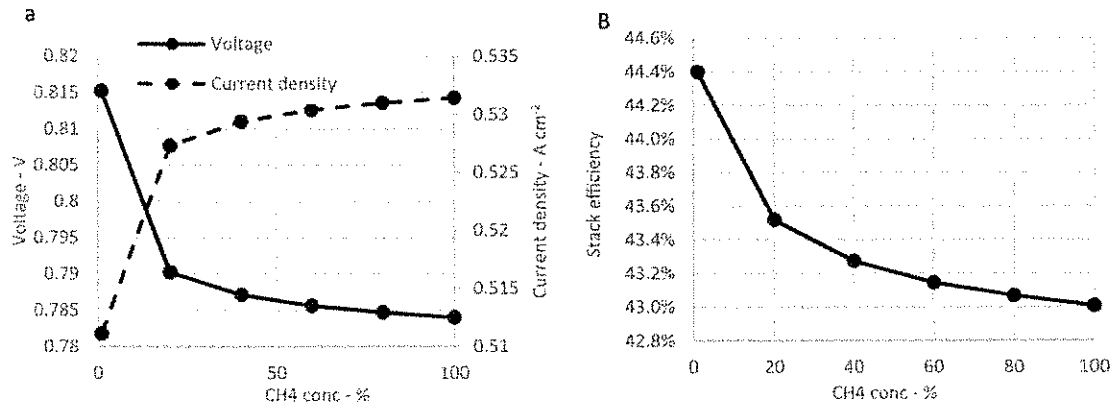

Fig. 4. SOFC performances in external reforming case. Voltage and current density Vs CH4 concentration (a) and efficiency Vs CH4 concentration (b).

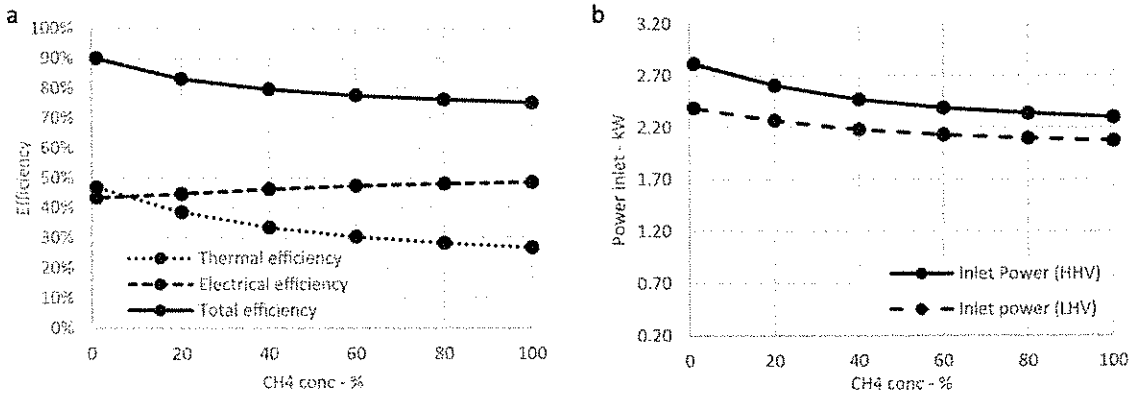

Fig. 5. (a) System electric, thermal and total efficiency and (b) Inlet Power HHV and LHV as a function of Hythane composition.

condensing boilers. In general, as shown in Fig. 5(b), more chemical energy input is necessary as more hydrogen is introduced into the fuel under the boundary condition of constant electric power output as used in our simulations.

This trend is partially balanced by the auxiliary power consumption. Figure shows this contribution using two parameters: (a) utilization of oxygen – U_{ox} (Figure a), and (b) the auxiliary power rate itself calculated as the ratio between auxiliary energy consumption and net electrical power output (Figure b). As previously commented, the introduction of hydrogen into the system leads to an increase of stack performance, less thermal losses in the stack and consequently a lower air flow being the main gas flow cooling the fuel cell. A lower air flow obviously results in a higher U_{ox} and a lower amount of auxiliary power needed for the air blower as shown in Fig. 6a and b. (Note that a higher hydrogen concentration is to be found at the left hand side of the X-axis).

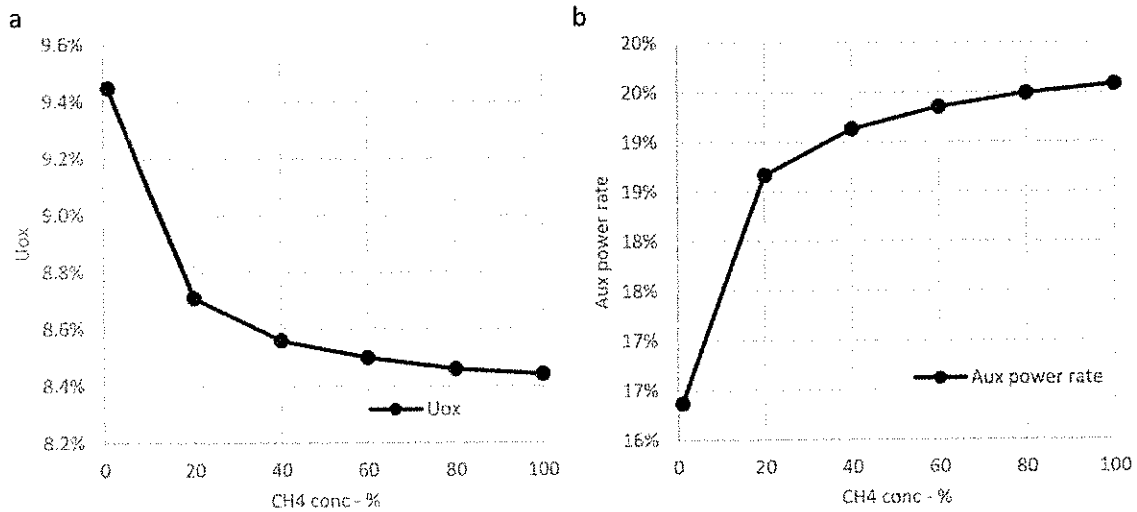

Fig. 6. (a) Uox and (b) auxiliary power rate as a function of Hythane composition.

3.2. Internal reforming

In this section we will present and discuss the main results of our simulations on the internal reformer SOFC cogeneration system. In Figs. 7 and 8 cell voltage, current density and stack- and system efficiencies are depicted and compared with the results presented above for the external reforming system. Fig. 7a reports voltage and current values as function of Hythane concentration. The internal reforming configuration always shows a better performance compared to external reforming. Fig. 7b shows that maximum stack efficiency is obtained for pure methane with a difference in stack efficiency of more than 10 percent points between external and internal reforming. This result is mainly related to the higher cell voltage of the direct internal reforming stack as shown in Fig. 7a.

System efficiencies are reported in Fig. 8. The internal reforming configuration brings several advantages in terms of electrical efficiency due to improved stack performance and reduced auxiliary power consumed in the blower. The air flow needed to cool down the stack can be lower thanks to the endothermic internal reforming reactions. Nevertheless, thermal efficiency is higher due to the higher temperature of the off gasses. Fig. 9 reports oxidant utilization U_{ox} and auxiliary power rate as a function of CH_4 concentration for the internal reforming configuration. Both graphs have opposite trends compared to the ER configuration. Oxidant utilization U_{ox} increases almost linearly with increasing methane concentration. Again, the increase is due to the endothermic reforming reaction that reduces the need for coolant and consequently power consumption by the air blower, the main constituent of the auxiliary power rate, also decreases with increased methane concentration in the fuel blend.

As already stated, system efficiencies depend on the percentage of hydrogen in the natural gas grid used to fuel the system. Then it is better possible to decide how to operate the system, depending mainly on (time dependent) demand for power and heat and their time dependent market prices in order to achieve the economic optimum operating conditions. A useful parameter, typical of cogeneration analysis, is the Electric Index (EI), defined as the ratio between the amount of electrical power and thermal power produced. As an example, Fig. 10 reports the Electric Index of the system with external reforming. In the figure and arrow indicates the direction in which CH_4 concentration increases; a higher CH_4 concentration gives a lower total efficiency. The plot shows that when total efficiency increases (for decreasing CH_4 concentration) a decrease of the Electric index is found. This is accompanied by a higher production of heat from the CHP system.

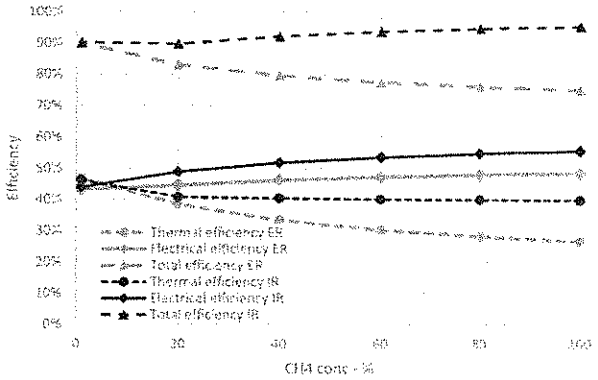

Fig. 8. System efficiencies of internal (IR) and external (ER) reforming configurations compared. as a function of Hythane composition.

4. Discussion.

We emphasize that a transition of natural gas (methane) to a mixture of methane and hydrogen has consequences for applications based on combustion where possibly gas burners need to be replaced. (Such a huge substitution of burners in gas stoves and furnaces in individual homes has already once taken place namely in the Netherlands in the early 60-ies of last century, when the largest natural gas field of Europe was found in the province of Groningen. However, also for (future) systems based on (high temperature) fuel cells such as SOFC's in CHP applications. A change of fuel from methane or hydrogen to a mixture of both can have consequences for the operation and performance of such combined heat and power systems.

In future scenario's where CHP will be deployed at a local (household) level systems fed by the natural gas grid, as well as units operating on stored hydrogen may be envisaged. As we have shown in this study that SOFC based μCHP units can operate on both fuels; hydrogen and methane and all mixture thereof. This allows for efficient and convenient hydrogen integration strategies in an energy transition to lower carbon fuels in order to reduce CO_2 emissions while using in principle, the same SOFC CHP unit. However, our study also shows that a possible future switch from natural gas to Hythane will have consequences for the operation and performance of such μCHP systems. Surprisingly, electrical efficiency decreases with an increase in hydrogen content while, on the other hand, thermal efficiency and total efficiency increases. Moreover, the use of Hythane allows for the use of an internal reforming SOFC with additional advantages in terms of increased thermal and electrical efficiency with respect to external

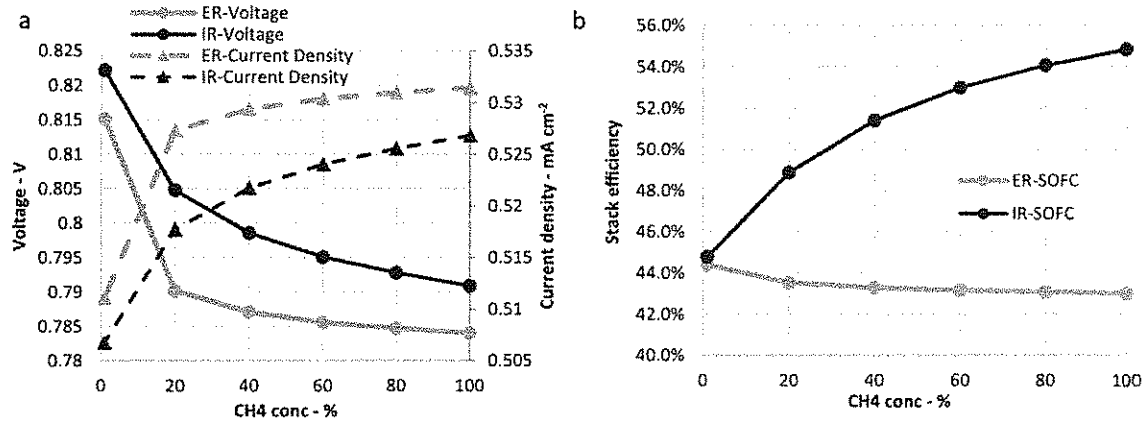

Fig. 7. A comparison of Stack performances of internal and external reforming configurations in terms of (a) voltage and current and (b) in terms of efficiency as a function of Hythane composition.

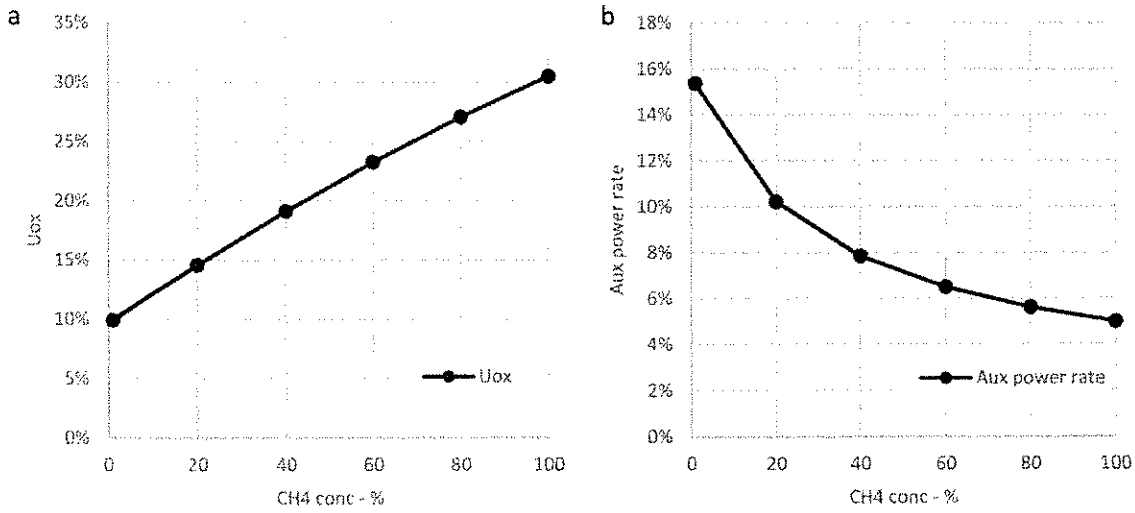

Fig. 9. (a) U_{ox} and (b) auxiliary power rate of IR SOFC system as a function of Hythane composition.

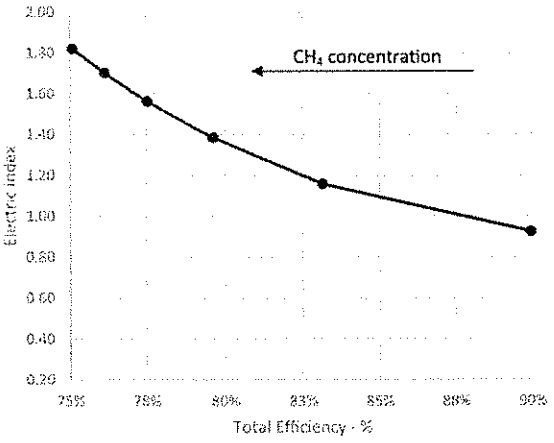

Fig. 10. Electric Index as function of total efficiency.

reforming and relaxed design and operating conditions with respect to the prevention of temperature gradients and shocks in de SOFC stack as would normally occur with the use of pure methane due to its fast reforming reaction and the endothermic nature of this reaction. The presence of hydrogen in the fuel mixture at the inlet prevents the presence of a strong heat sink at the inlet side of the stack.

The practical consequences for the operation of such systems in the future can be found in the detailed design modification next to the modified operation of these systems that might be necessary in particular if the composition of the fuel may vary in time during operation of the CHP unit. Moreover, a recalculation of the economic return on investment would be necessary since a shift from electricity to heat production occurs for increasing hydrogen content in the Hythane fuel blend.

5. Conclusions

This study evaluates the performance of a SOFC based μCHP system in a future scenario where the system is fed with Hythane: a mixture of methane and hydrogen. We have shown that the use of Hythane compared to pure methane increases total efficiency in terms of power plus heat of a SOFC combined heat and power system, yet at the expense of a decrease in electric efficiency with a few point percent. When one accounts for these changes in efficiency the SOFC based cogeneration systems are suitable for operation in an energy system in transition from natural gas to Hythane and pure hydrogen. Internal reforming systems show higher thermal, electric and overall efficiencies and are very suitable for operation with Hythane since those gas compositions reduce internal temperature gradients in the IR-SOFC stack compared to operation on methane and pre-reformers may no longer be needed in those system designs.

References

[1] van de Beld L, Bouwmans I, Claassen PAM, Hemmes K, de Wit H, Woudstra N, et al. Exploring new production methods of hydrogen/natural gas blends for mixing into the natural gas network of the Netherlands. ECOS 2003; 16th Int. Conf. Effic. Costs, Optim. Simul. Environ. Impact Energy Syst. Copenhagen, Denmark (30-06 to 02-07-2003), Copenhagen. 2003.

[2] Florisson O. NATURALHY: assessing the potential of the existing natural gas network for hydrogen delivery. GERG Acad Netw Event, 4 June 2010, Brussles, Belgium. 2010.

[3] Altfeld K, Pinchbeck D. Admissible hydrogen concentrations in natural gas systems. Gas Energy 2013:1–16. doi:ISSN 2192-158X.

[4] de Vries H, Mokhov AV, Levinsky HB. The impact of natural gas/hydrogen mixtures on the performance of end-use equipment: Interchangeability analysis for domestic appliances. Appl Energy 2017;208:1007–19. https://doi.org/10.1016/J.APENERGY.2017.09.049.

[5] Guandalini G, Colbertaldo P, Campanari S. Dynamic modeling of natural gas quality within transport pipelines in presence of hydrogen injections. Appl Energy 2017;185:1712–23. https://doi.org/10.1016/J.APENERGY.2016.03.006.

[6] Abeysekera M, Wu J, Jenkins N, Rees M. Steady state analysis of gas networks with distributed injection of alternative gas. Appl Energy 2016;164:991–1002. https://doi.org/10.1016/J.APENERGY.2015.05.099.

[7] Talibi M, Balachandran R, Ladommatos N. Influence of combusting methane-hydrogen mixtures on compression–ignition engine exhaust emissions and in-cylinder gas composition. Int J Hydrogen Energy 2016:1–16. https://doi.org/10.1016/j.ijhydene.2016.10.049. Article.

[8] Battistoni M, Poggiani C, Grimaldi CN. Experimental investigation of a port fuel injected spark ignition engine fuelled with variable mixtures of hydrogen and methane; 2013. http://doi.org/10.4271/2013-01-0226.

[9] Navarro E, Leo TJ, Corral R. CO_2 emissions from a spark ignition engine operating on natural gas–hydrogen blends (HCNG). Appl Energy 2013;101:112–20. https://doi.org/10.1016/J.APENERGY.2012.02.046.

[10] Sen AK, Wang J, Huang Z. Investigating the effect of hydrogen addition on cyclic variability in a natural gas spark ignition engine: wavelet multiresolution analysis. Appl Energy 2011;88:4860–6. https://doi.org/10.1016/J.APENERGY.2011.06.030.

[11] O'Shea R, Wall D, Kilgallon I, Murphy JD. Assessment of the impact of incentives and of scale on the build order and location of biomethane facilities and the feedstock they utilise. Appl Energy 2016;182:394–408. https://doi.org/10.1016/J.APENERGY.2016.08.063.

[12] O'Shea R, Wall DM, Kilgallon I, Browne JD, Murphy JD. Assessing the total theoretical, and financially viable, resource of biomethane for injection to a natural gas network in a region. Appl Energy 2017;188:237–56. https://doi.org/10.1016/J.APENERGY.2016.11.121.

[13] Horschig T, Adams PWR, Gawel E, Thrän D. How to decarbonize the natural gas sector: a dynamic simulation approach for the market development estimation of renewable gas in Germany. Appl Energy 2018;213:555–72. https://doi.org/10.

1016/J.APENERGY.2017.11.016.
[14] Cucchiella F, D'Adamo I, Gastaldi M, Miliacca M. A profitability analysis of small-scale plants for biomethane injection into the gas grid. J Clean Prod 2018;184:179–87. https://doi.org/10.1016/J.JCLEPRO.2018.02.243.
[15] Li G, Zhang R, Jiang T, Chen H, Bai L, Li X. Security-constrained bi-level economic dispatch model for integrated natural gas and electricity systems considering wind power and power-to-gas process. Appl Energy 2017;194:696–704. https://doi.org/10.1016/J.APENERGY.2016.07.077.
[16] Bailera M, Espatolero S, Lisbona P, Romeo LM. Power to gas-electrochemical industry hybrid systems: a case study. Appl Energy 2017;202:435–46. https://doi.org/10.1016/J.APENERGY.2017.05.177.
[17] Frank E, Gorre J, Ruoss F, Friedl MJ. Calculation and analysis of efficiencies and annual performances of Power-to-Gas systems. Appl Energy 2018;218:217–31. https://doi.org/10.1016/J.APENERGY.2018.02.105.
[18] Huang Z, Lu L, Jiang D, Xing D, Ren ZJ. Electrochemical Hythane production for renewable energy storage and biogas upgrading. Appl Energy 2017;187:595–600. https://doi.org/10.1016/J.APENERGY.2016.11.099.
[19] Judd R, Pinchbeck D. Hydrogen admixture to the natural gas grid. Compend. Hydrog. Energy Elsevier; 2016. p. 165–92. https://doi.org/10.1016/B978-1-78242-364-5.00008-7.
[20] Schiebahn S, Grube T, Robinius M, Tietze V, Kumar B, Stolten D. Power to gas: Technological overview, systems analysis and economic assessment for a case study in Germany. Int J Hydrogen Energy 2015;40:4285–94. https://doi.org/10.1016/J.IJHYDENE.2015.01.123.
[21] Cinti G, Hemmes K. Integration of direct carbon fuel cells with concentrated solar power. Int J Hydrogen Energy 2011;36:10198–208. https://doi.org/10.1016/j.ijhydene.2010.11.019.
[22] Guerrero J, Blaabjerg F, Zhelev T, Hemmes K, Monmasson E, Jemei S, et al. Distributed Generation: Toward a New Energy Paradigm. IEEE Ind Electron Mag 2010;4:52–64. https://doi.org/10.1109/MIE.2010.935862.
[23] Verda V, Caliquaglia M. Solid oxide fuel cell systems for distributed power generation and cogeneration. Int J Hydrogen Energy 2008;33:2087–96. https://doi.org/10.1016/j.ijhydene.2008.01.046.
[24] Elcogen. Convion supply SOFC CHP systems to business district smart grid project in Finland. Fuel Cells Bull 2018;2018:1. https://doi.org/10.1016/S1464-2859(18)30034-8.
[25] Callux residential demonstrations reach 1m hours of operation. Fuel Cells Bull 2012;2012:5–6. http://doi.org/10.1016/S1464-2859(12)70162-1.
[26] European ene.field project highlights fuel cell micro-cogeneration. Fuel Cells Bull 2017;2017:6–7. http://doi.org/10.1016/S1464-2859(17)30392-6.
[27] Kadowaki M. Current status of national SOFC projects in Japan. ECS Trans 2015;68:15–22. https://doi.org/10.1149/06801.0015ecst.
[28] Ito H. Economic and environmental assessment of residential micro combined heat and power system application in Japan. Int J Hydrogen Energy 2016;41:15111–23. https://doi.org/10.1016/j.ijhydene.2016.06.099.
[29] Andersson M, Nakajima H, Kitahara T, Shimizu A, Koshiyama T, Paradis H, et al. Comparison of humidified hydrogen and partly pre-reformed natural gas as fuel for solid oxide fuel cells applying computational fluid dynamics. Int J Heat Mass Transf 2014;77:1008–22. https://doi.org/10.1016/j.ijheatmasstransfer.2014.06.033.
[30] Liso V, Nielsen MP, Kær SK. Influence of anodic gas recirculation on solid oxide fuel cells in a micro combined heat and power system. Sustain Energy Technol Assessments 2014;8:99–108. https://doi.org/10.1016/j.seta.2014.08.002.
[31] Liso V, Olesen AC, Nielsen MP, Kær SK. Performance comparison between partial oxidation and methane steam reforming processes for solid oxide fuel cell (SOFC) micro combined heat and power (CHP) system. Energy 2011;36:4216–26. https://doi.org/10.1016/j.energy.2011.04.022.
[32] Pfeifer T, Nousch L, Lieftink D, Modena S. System design and process layout for a SOFC micro-CHP unit with reduced operating temperatures. Int J Hydrogen Energy 2013;38:431–9. https://doi.org/10.1016/J.IJHYDENE.2012.09.118.
[33] Ni C, Yuan Z, Wang S, Li D, Zhang C, Li J, et al. Study on an integrated natural gas fuel processor for 2-kW solid oxide fuel cell. Int J Hydrogen Energy 2015;40:15491–502. https://doi.org/10.1016/j.ijhydene.2015.09.067.
[34] Kushi T. Heat balance of dry reforming in solid oxide fuel cell systems. Int J Hydrogen Energy 2017;42:11779–87. https://doi.org/10.1016/j.ijhydene.2017.02.112.
[35] Barelli L, Bidini G, Cinti G, Gallorini F, Pöniz M. SOFC stack coupled with dry reforming. Appl Energy 2017;192:498–507. https://doi.org/10.1016/j.apenergy.2016.08.167.
[36] Liso V, Zhao Y, Brandon NP, Nielsen MP, Kær SK. Analysis of the impact of heat-to-power ratio for a SOFC-based mCHP system for residential application under different climate regions in Europe. Int J Hydrogen Energy 2011;36:13715–26. https://doi.org/10.1016/j.ijhydene.2011.07.086.
[37] Naimaster EJ, Sleiti AK. Potential of SOFC CHP systems for energy-efficient commercial buildings. Energy Build 2013;61:153–60. https://doi.org/10.1016/j.enbuild.2012.09.045.
[38] Adam A, Fraga ES, Brett DJL. Options for residential building services design using fuel cell based micro-CHP and the potential for heat integration. Appl Energy 2015;138:685–94. https://doi.org/10.1016/J.APENERGY.2014.11.005.
[39] Fubara TC, Cecelja F, Yang A. Modelling and selection of micro-CHP systems for domestic energy supply: the dimension of network-wide primary energy consumption. Appl Energy 2014;114:327–34. https://doi.org/10.1016/J.APENERGY.2013.09.069.
[40] Giarola S, Forte O, Lanzini A, Gandiglio M, Santarelli M, Hawkes A. Techno-economic assessment of biogas-fed solid oxide fuel cell combined heat and power system at industrial scale. Appl Energy 2018;211:689–704. https://doi.org/10.1016/j.apenergy.2017.11.029.
[41] Thallam Thattai A, Oldenbroek V, Schoenmakers L, Woudstra T, Aravind PV. Experimental model validation and thermodynamic assessment on high percentage (up to 70%) biomass co-gasification at the 253 MWe integrated gasification combined cycle power plant in Buggenum, The Netherlands. Appl Energy 2016;168:381–93. https://doi.org/10.1016/J.APENERGY.2016.01.131.
[42] Seo H-K, Park W, Lim HC. The efficiencies of internal reforming molten carbonate fuel cell fueled by natural gas and synthetic natural gas from coal. J Electrochem Energy Convers Storage 2016;13:011005https://doi.org/10.1115/1.4033255.
[43] Ghadamian H, Hamidi AA, Farzaneh H, Ozgoli HA. Thermo-economic analysis of absorption air cooling system for pressurized solid oxide fuel cell/gas turbine cycle. J Renew Sustain Energy 2012;4:43115. https://doi.org/10.1063/1.4742336.
[44] http://www.asimptote.nl/software/cycle-tempo/cycle-tempo-model-examples/ [access date 01-09-2019].
[45] SOLIDPower. ASC-700 Datasheet.
[46] FCH2 JU. Multi – Annual Work Plan 2014 – 2020; 2014.

UNIVERSITÀ DEGLI STUDI DI PERUGIA
Dipartimento di Ingegneria
Corso di Laurea in Ingegneria Industriale
Laboratorio Prove su Strutture e Materiali
(Ufficiale ai sensi della Legge 1086/71)

Prot. 500/19 del 23/05/19

PU12/19

Spett.le
Arch. Paolo Leonelli

Oggetto: preventivo per prove di carotaggio, pull-out in situ da effettuarsi a Terni.

Si rimette nostra migliore offerta per le prove in oggetto:

Descrizione della prova	Prezzo unitario (€)	Prove previste	Totale (€)
Compressione su carote in calcestruzzo (senza determinazione del modulo di elasticità)	20.00	1	20.00
Rimborso personale tecnico (per 1 h)	80.00	2	160.00
Prova di pull out con tassello preinglobato o post (UNI 9536) (per ogni tassello)	25.00	24	600.00
D.C. Diritto di Certificazione	10.00	13	130.00
	Totale		**910.00 + IVA**

N.B. validità della seguente offerta: 30 giorni, sono esclusi le aperture ed i ripristini delle zone di prova dei saggi da indagare e gli scavi della fondazione, l'estrazione delle barre di armatura e relativo ripristino.
L'estrazione delle carote di calcestruzzo è effettuata mediante carotaggio ad acqua la successiva rettifica delle stesse e prova sono comprese nel preventivo, sono esclusi i ripristini delle zone d prova.
Prove su barre in acciaio: l'estrazione dei provini ed il relativo ripristino delle zone di prova non sono compresi nel preventivo sopra riportato.
E' richiesta la fornitura di elettricità e di acqua corrente.

Terni, 20/05/2019

Il direttore del Laboratorio
(Prof. Ing. Antonio Borri)

Nome e Cognome..PAOLO LEONELLI STUDIO LS

Per accettazione del preventivo (firma).....

Dati per la fatturazione:
Partita Iva.....00117100552.....Codice fiscale.....00117100552.....

Indirizzo: ...VIA LANZI N.5..... C.U.: W7YVJK9 PEC: paolo.leonelli@archiworld.pec.it

(Nota: le prove verranno fatturate esclusivamente a chi accetta il preventivo firmando e compilando in ogni sua parte la presente)
Allegare fotocopia di un documento di identità del legale rappresentante del richiedente.

* W7YVJK9

Strada di Pentima, 4 – 05100 TERNI
☎ 0744/492908 – Tel/Fax 0744/492901

Gabriele Discepoli

Università degli Studi di Perugia - Dipartimento di Ingegneria

RELAZIONE II° ANNO RTD-A

PUBBLICAZIONI

Cruccolini, V., Discepoli, G., Zembi, J., Battistoni, M., Mariani, F., & Grimaldi, C. N. (2018). Experimental Assessment of a Pressure Wave Charger for Motorcycle Engines. *Energy Procedia*, *148*, 1254–1261. https://doi.org/10.1016/j.egypro.2018.08.002

Discepoli, G., Cruccolini, V., Dal Re, M. A., Zembi, J., Battistoni, M., Mariani, F., & Grimaldi, C. N. (2018). Experimental assessment of spark and corona igniters energy release. *Energy Procedia*, *148*(Ati), 1262–1269. https://doi.org/10.1016/j.egypro.2018.08.001

DESCRIZIONE GENERALE

L'attività condotta nel corso del secondo anno del contratto RTDa ha riguardato principalmente due linee di ricerca distinte: la sviluppo sperimentale di un sistema di sovralimentazione per il settore motociclistico e lo studio di sistemi di accensione, sia convenzionali che innovativi, per motori a combustione interna ad accensione comandata. Quest'ultima attività, in prosecuzione del lavoro svolto nell'anno precedente, è stata la preponderante e ha compreso anche lo sviluppo contestuale di un banco prova dedicato alla caratterizzazione energetica dei sistemi di accensione presi in esame tramite la misura, in ambiente controllato, dell'energia assorbita e rilasciata in differenti condizioni operative.

Attività secondarie hanno riguardato:

- la caratterizzazione sperimentale al banco prova delle prestazioni di motori elettrici;
- le prime fasi della progettazione e sviluppo di un motore ad accesso ottico ad accensione per compressione a benzina *LTC* (combustione a basse temperature).

IMPULSE DRUM CHARGER

Lo sviluppo di un sistema di alimentazione di tipo motociclistico rappresenta una sfida a causa degli stringenti requisiti di leggerezza, semplicità e immediatezza di risposta. Nel corso di questa attività ci si è proposto lo studio di un sovralimentatore cosiddetto a onde di pressione, l'*Impulse Drum Charger*. Lo studio si è incentrato nel confronto delle prestazioni al banco prova di un motore motociclistico commerciale a 4 tempi (KTM 390) equipaggiato con e senza sistema di sovralimentazione. In particolare, lo studio è stato condotto sull'analisi indicata (interno motore) e sulla pressione all'aspirazione dimostrando che effettivamente il sistema di sovralimentazione è in grado di migliorare le performance del motore esaminato (fino a 1.4 kW a 9500 giri/minuto) anche senza una ricalibrazione della centralina dedicata. In particolare, sono stati mantenuti costanti parametri quali il rapporto di miscelazione e l'anticipo d'accensione per garantire la confrontabilità dei due casi. Il sistema di sovralimentazione si è dimostrato più prestazionale a bassi (4500 giri/minuto) e alti (9500 giri/minuto) regimi di rotazione al

contrario di quelli intermedi (7000 giri/minuto), che hanno visto invece preponderante la dipendenza dal silenziatore adottato. Di fatto, pur garantendo un aumento di pressione fino a 100/200 mbar, l'incidenza del sistema di sovralimentazione è legata alla sincronizzazione delle onde di pressione con un'opportuna fasatura delle valvole di aspirazione.

Il lavoro ha previsto anche l'ottimizzazione del sistema di scarico così da garantire la corretta propagazione delle onde di pressione e contemporaneamente contenere le temperature entro livelli accettabili per il testing di esemplari di sovralimentatori prodotti mediante prototipazione rapida, quindi non adatti alle condizioni di temperatura dettate dal sistema di scarico di serie.

Da questo lavoro è poi stata prodotta una pubblicazione, allegata alla presente relazione, alla quale si rimanda per i dettagli.

CARATTERIZZAZIONE SPERIMENTALE DI SISTEMI DI ACCENSIONE CONVENZIONALE E INNOVATIVI

Il sistema di accensione basato sull'effetto Corona è una tecnologia promettente capace di produrre più centri di accensione in camera di combustione attraverso la generazione di più "streamers", canali di plasma a (relativamente) bassa temperatura. Il sistema si avvale della capacità di operare su volumi maggiori di un sistema convenzionale, oltre che sulla produzione di cascami di particelle attive (radicali), in grado di stimolare positivamente la combustione e accelerarla notevolmente nelle sue prime fasi. Queste caratteristiche lo rendono capace di produrre una combustione stabile anche con concentrazioni di combustile molto basse, tipiche delle condizioni operative di "magro" o con alto EGR, tipiche del moderno automotive e necessarie alla riduzione delle emissioni nocive. Nel corso di questo studio, un sistema prototipale a effetto corona è stato confrontato con uno convenzionale (stesso produttore con in quale esiste una convenzione) operante sia in condizioni standard che "multispark", ossia con più eventi consecutivi. Il confronto è avvenuto sulle base sia dell'energia assorbita che, soprattutto, su quella rilasciata dagli stessi sistemi d'accensione nel mezzo contenuto in un calorimetro a pressione. I test sono stati condotti con vari livelli di pressione del mezzo e variando i parametri di funzionamento dell'accenditore a effetto corona (durata dello streamer e tensione di pilotaggio dello streamer stesso) all'interno della loro rispettiva finestra di funzionamento. I risultati hanno mostrato che l'energia assorbita dagli accenditori testati è circa indipendente dalla pressione del mezzo. Al contrario, l'energia rilasciata nel mezzo si è dimostrata funzione crescente linearmente per gli accenditori convenzionali e, conseguente, ha portato a un miglioramento della bassa efficienza di sistema. Questo comportamento è chiaramente dovuto all'aumento della densità del mezzo tra gli elettrodi con conseguente necessità di una tensione maggiore per lo scocco della scintilla e quindi dell'energia depositata. L'accenditore a effetto Corona ha mostrato un'energia rilasciata nel mezzo dipendente sia dalla tensione di pilotaggio (secondo una legge quadratica) che dal tempo di durata dello streamer (dipendenza lineare). La dipendenza dalla pressione è decrescente: all'aumentare della densità del mezzo serve un'energia maggiore per produrre streamers di pari intensità. Il comportamento discende dal fatto che la tensione dell'elettrodo è indipendente dalla pressione mentre il campo elettrico ridotto (campo elettrico su densità del mezzo), responsabile della produzione di streamers nel mezzo stesso, diminuisce per effetto dell'aumento della densità del mezzo

stesso. Questo comportamento viene compensato aumentando parallelamente la tensione di pilotaggio in modo da garantire sia un'alta quantità di energia depositata che un'alta efficienza di sistema. L'aumento della tensione di pilotaggio non è indefinito ma viene limitato dal prodursi di indesiderate condizioni di scarica che portano l'accenditore a comportarsi come uno convenzionale.

Da questo lavoro è poi stata prodotta una pubblicazione, allegata alla presente relazione, alla quale si rimanda per i dettagli.

Altre attività

Nel corso dell'anno sono state condotte attività di aggiornamento (partecipazione ai congressi SAE Detroit 2018 e ATI Pisa 2018), di disseminazione (pubblicazione di due articoli scientifici e presentazione orale all'ATI Pisa 2018) e di trasferimento della conoscenza (collaborazione e incontri con Federal Mogul Powertrain, AlterEgo-Hardware, IET e HPE COXA).

Available online at www.sciencedirect.com

ScienceDirect

Energy Procedia 148 (2018) 1254–1261

Energy Procedia

www.elsevier.com/locate/procedia

73rd Conference of the Italian Thermal Machines Engineering Association (ATI 2018), 12–14 September 2018, Pisa, Italy

Experimental Assessment of a Pressure Wave Charger for Motorcycle Engines

V. Cruccolini[a,*], G. Discepoli[a], J. Zembi[a], M. Battistoni[a], F. Mariani[a], C. N. Grimaldi[a]

[a] *Dipartimento di Ingegneria – Università di Perugia, via G.Duranti 93, 06125, Perugia (Italy)*

Abstract

Charging a motorcycle engine is challenging, since requirements of lightness, system simplicity and engine responsiveness are key factors. This paper reports on a preliminary study on a pressure wave compressor, the "Impulse Drum Charger". Performances of a 4-stroke motorcycle engine with and without Drum Charger were compared at the test bench and a pressure analysis in the intake manifold was carried out as well. Results show that this system is able to effectively improve engine power (up to 1.4 kW at 9500 rpm WOT) without an ECU recalibration.

Keywords: SI engine; Motorcycle; Pressure Wave Charger; Impulse Drum Charger.

1. Introduction

Charging intake air of an internal combustion engine is a well-known technique, that allows to increase the density of the working medium before it enters the cylinder. Air compression can be used to increase power density and, depending on design and application, to improve the combustion process, in order to reduce exhaust pollutant emissions, noise emission or fuel consumption [1]. The medium temperature should not raise too much, in order not to adversely affect the high-pressure working cycle: in many applications a charge air cooler is used to decrease

* Corresponding author. Tel.: +39 075 585 3749;
E-mail address: valentino.cruccolini@studenti.unipg.it

10.1016/j.egypro.2018.08.002

Nomenclature

CAD	Crank Angle Degree
BTDC	Before Top Dead Center
DOHC	Double OverHead Camshaft
ECU	Engine Control Unit
FLC	Full-Load Curve
IDC(s)	Impulse Drum Charger(s)
MON	Motor Octane Number
PFI	Port Fuel Injection
RON	Research Octane Number
SA	Spark Advance
SI	Spark Ignition
UEGO	Universal Exhaust Gas Oxygen
WOT	Wide Open Throttle

such temperature [2].

Depending on the charging principle, it is possible to distinguish many families of air chargers [1,3]. A first possibility, the supercharging, consists on a mechanical driving of the charger: roots blower, sliding vane, screw compressor, but also reciprocating and centrifugal compressor belong to this group. Another possibility is to use part of the exhaust gas enthalpy to drive the compressor: turbocharging is the most common solution, especially in automotive and heavy/light duty applications. Finally, it is possible to exploit the pressure waves propagating through intake or exhaust ducts after valve opening or closing to obtain an impulsive boost effect (e.g. the Comprex [4]).

Charging a motorbike engine is not easy, due to different kinds of difficulties as reported by Zinner *et al.* [5]. Many attempts were tried in the past, but nowadays only few models (e.g. Kawasaki H2) are equipped with superchargers. As a matter of fact, motorbikes tend to be constructively "simple" and low-weight, with few add-ons. The insertion of a charger should not complicate engine nesting inside the frame, and auxiliary elements like intercooler are disliked. Another key factor is power-to-weight ratio, which is high in motorbike applications: a turbocharger or supercharger insertion can adversely affect this feature. Usually, naturally aspirated engines are characterized by an overabundant max power for motorcycles: charging, in this case, can be attractive to improve low-end torque, something that can be particularly useful in city riding. In these conditions, rideability is of absolute importance: an air charger should guarantee a high responsiveness, and this factor often penalizes turbocharged solution [6], since turbo-lag can be a strong limit. Turbomatching (the coupling between engine and turbocharger [1]) is not easy: benefits could be limited only to a part of engine map. Finally, the cost of the charging system is not low: it could encumber too much on the total engine cost [3]. Just out of curiosity, when a motorbike engine is transferred to a 4-wheel vehicle, many of these limitations become less influent, and charging is possible and desirable, as found in Formula SAE application (Romani *et al.* [7], Wang *et al.* [8]).

Even if charging a motorcycle engine is not easy, as said, interesting solutions can be found. One of these, the Impulse Drum Charger (IDC), by *AlterEgo Hardware*, can be classified as a compressor that exploits exhaust pressure pulses. Externally, it is composed of two shells: inside the lower one there are two cavities, separated by an elastic membrane (Fig. 1). One cavity (the "hot side") is in communication with the exhaust manifold through a dedicated duct, receiving pressure waves when the exhaust valves open. This pulse is able to deflect the membrane, forcing fresh air in the other cavity (the "cold side") to exit the IDC with an overpressure (Fig. 2b) through a chamber in the upper shell towards the airbox. When the pulse is over, a bow-spring allows the membrane to return to its rest position: in this moment, thanks to this movement, external fresh air at atmospheric pressure is aspirated in the cold side (Fig. 2a) coming from another chamber, located in the upper shell too, connected to the external environment. Two sets of reed valves separate upper and lower shells, avoiding backflows (boosted air can only go towards the airbox). This behavior occurs once per engine cycle (i.e. 2 crankshaft revolutions). It must be remarked that exhaust gases and fresh air, separated by the elastic membrane, never mix together.

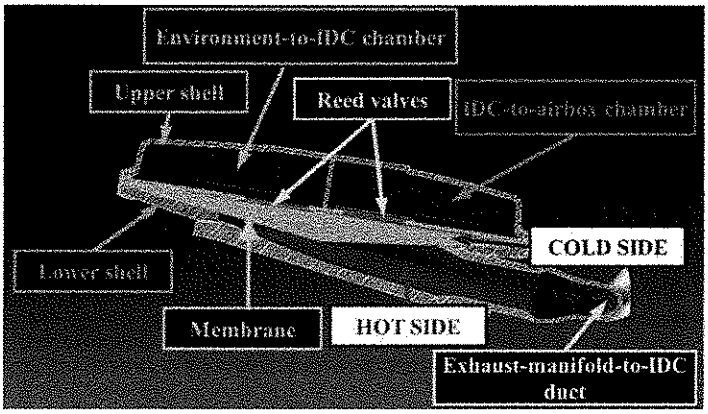

Fig. 1. Schematic of IDC (courtesy of *AlterEgo Hardware*).

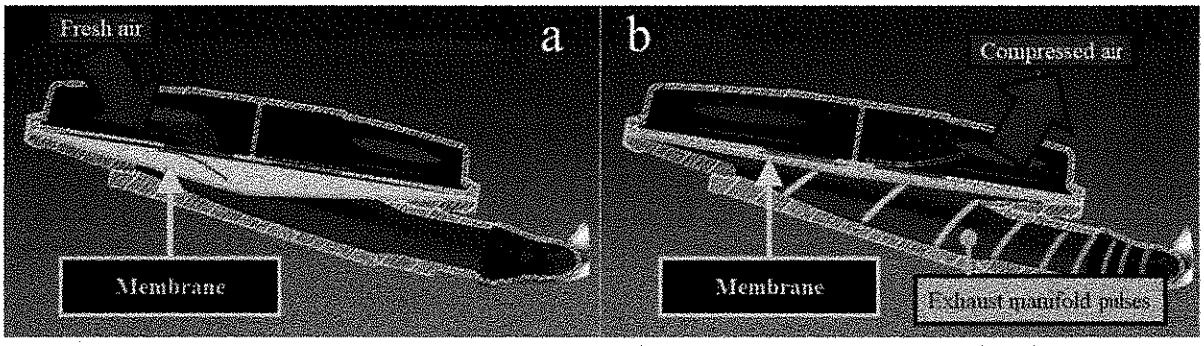

Fig. 2. IDC functioning principle (courtesy of *AlterEgo Hardware*): (a) fresh air suction in the cold side, caused by membrane returning to rest position, (b) air compressed and forced towards plenum, caused by membrane deflection when exhaust pulses arrive.

This work was focused on the first analysis of this new concept charger, in order to assess its behavior and performance. Besides the engine brake power evaluation, an analysis of intake pressure and a detection of possible knocking phenomena were carried out as well.

2. Experimental Setup

2.1. Original Engine

Test were carried out on a KTM RC390 4-stroke engine (year 2015). Table 1 lists the engine specifications.

Table 1. Engine specifications of the tested model (KTM RC390).

Parameters	Value/Description
Bore x Stroke (mm x mm)	89 x 60
Number of cylinders (-)	1
Displacement Volume (cm^3)	373
Compression Ratio (-)	12.6:1
Connecting-Rod Length (mm)	105
Valve System	DOHC 4 valves
Fuel system	PFI, Standard European market gasoline RON 95 MON 85

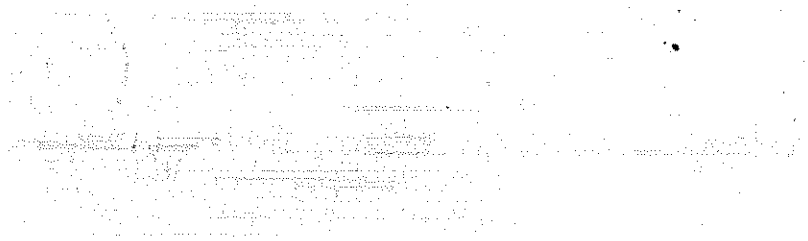

2.2. Drum Charger coupling and engine modifications

In the tested engine (displacement of 373 cm^3) two IDCs in parallel were necessary. In fact, the ratio between engine displacement and IDC volume is a key factor to obtain sufficient boost. It is necessary to modify both intake and exhaust engine ducts to properly couple IDCs with the engine (Fig. 3a). Concerning the intake, the airbox is modified in order to receive the airflow from the IDCs. Downstream, the remaining intake line parts (throttle valve, intake manifold, intake ports) are the same of original engine. The original exhaust line with one duct from the exhaust manifold to the muffler was also modified (Fig. 3b), adding in parallel two ducts which connect the manifold to the hot side of drum IDCs. Because of the modified layout, it was also necessary to replace the original muffler with a new one supplied by *Egb*.

It must be remarked that the presence of two IDCs makes the analysis much more critical. As a matter of fact, exhaust pipes to left and right IDCs cannot be identical, because of exhaust ducts nesting around the motorcycle frame. Inside the ducts, the measured gas temperatures resulted to be different because of 3-D effects related to exhaust geometry and external air cooling. Consequently, since, as well known, the pulse propagation is strongly affected by medium temperature, the operation of the two IDCs could be not perfectly phased. Many efforts were made in order to minimize this effect, but it was not possible to completely avoid it in this preliminary phase. This should be taken into account during an optimized design phase.

2.3. Test bench and instrumentation

The engine was installed on the test bench and coupled with a Borghi & Saveri FE600-SD eddy-current brake. In addition to the original KTM ECU, an Athena GK-ECUJ5-0010 was used in series to modify both spark advance and PFI energizing time to reach lambda target. Engine was instrumented with temperature sensors located in the engine intake and exhaust pipes, as well as in the cooling and lubrication circuits [9]. In-cylinder pressure was measured by a piezo-electric sensor (Kistler 6052C) flush-installed in the cylinder head, while pressure in the intake manifold (downstream of throttle valve), in the exhaust manifold and in IDC hot side were recorded using piezo-resistive transducers (Kistler 4075A5). Crankshaft angular position was measured by means of an optical encoder (AVL 365). These signals, together with ignition timing from a current clamp, were sampled at 0.1 CAD resolution and acquired by a Kistler KiBox combustion analysis system. For each tested point, 200 consecutive indicated cycles were recorded to have a statistically significant amount of data. Lastly, a UEGO lambda sensor (Horiba MEXA-720) was installed in the exhaust line upstream of muffler.

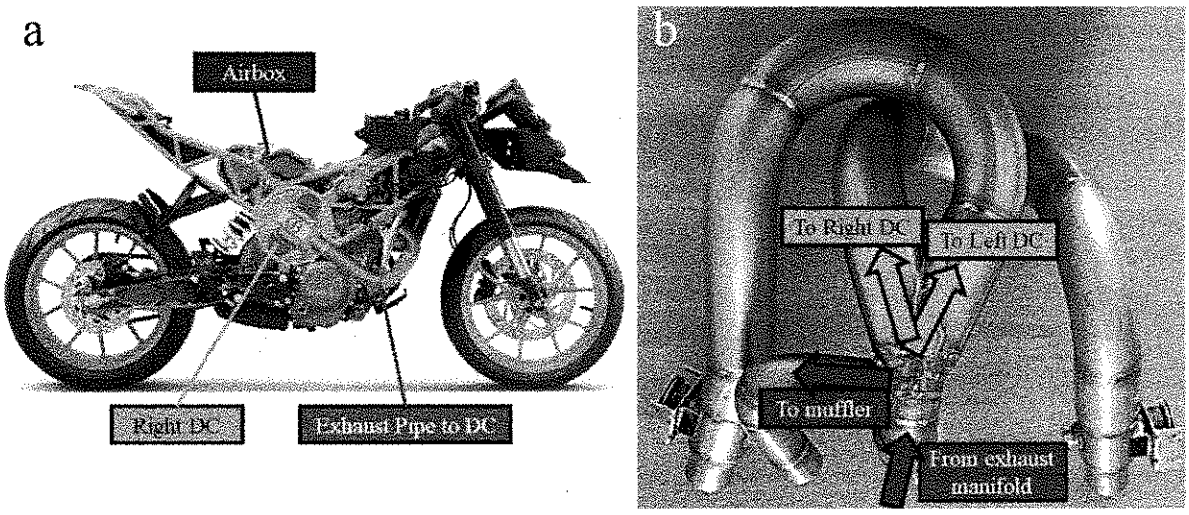

Fig. 3 (a) schematic of IDC installed on a KTM RC390 (courtesy of *AlterEgo Hardware*), (b) new exhaust duct to couple two IDCs with the engine. In the latter, red arrows represent exhaust mass flows while orange arrows represent pressure wave pulses.

3. Test Table

In a first phase of the work, an observation of the pressure trends at the IDCs inlet (exhaust gas pulses, i.e. the driving force) and at the outlet (boost, i.e. the desired effect) was performed in order to understand the main phenomena and the waves phasing.

The main campaign consisted of a comparison among three different layouts: the engine in its original configuration ("Original"), with the muffler to be used with IDCs ("Baseline") and with the complete Drum Charger setup ("IDC"). Besides the FLC in the original configuration, the modified ones were thoroughly analyzed in three significant engine points: 4500 rpm WOT (representative of low-speed), 7000 rpm WOT (representative of medium-speed and close to original engine max torque point) and 9500 rpm WOT (representative of high speed, max power point). In Table 2 further details about main test campaign can be found.

Since original KTM ECU is not open and its correction algorithms are unknown, in order to avoid that the results were affected by Spark Advance (SA) or relative air-fuel ratio (λ) variations, these two parameters were maintained equal to the Original configuration values by means of the additional Athena system (Table 3).

Table 2. Main test campaign

Layout	Tested points	Performance analysis	Intake Pressure analysis	Knocking analysis
Original	FLC	x	x	x
Baseline (Engine with new muffler)	4500 – 7000 – 9500 rpm WOT	x		
IDC (Engine with new muffler and Drum Chargers)	4500 – 7000 – 9500 rpm WOT	x	x	x

Table 3. ECU fixed parameters

Tested point	Spark advance [CAD BTDC]	Lambda [-]
4500 rpm WOT	31	1.03
7000 rpm WOT	27	0.93
9500 rpm WOT	31.5	0.97

4. Results and Discussion

The pressure trends analysis was carried out at 4500 rpm WOT and 6000 rpm WOT in order to evaluate the effects of the IDCs insertion. Tests were performed by comparing two configurations: the complete system (blue curve in Fig. 4 "IDC on"), and the system with the IDCs disconnected from the airbox (black curve, "IDC off"): in the latter layout, IDCs are connected to the engine exhaust, but not to the airbox, which is free to directly aspirate environmental air. In this manner, engine operates with an identical exhaust configuration, and it is possible to focus the analysis on the boost effect only.

Analyzing the results in Fig. 4 it is possible to observe that, as expected, the exhaust pulse (red curve, near 200 CAD) deflects the membrane producing a subsequent intake pulse delayed by about 60-70 CAD. Obviously, the angular interval between these two pulses is dependent on engine speed: since exhaust valve opening angle is fixed and the wave propagation physical time is almost constant, the crankshaft position in which boost waves reach the engine intake varies with regimes. Consequently, since the air charging effect depends on engine speed, the more precise the synchronization between boost pulse and intake valve opening phase, the higher the engine performance.

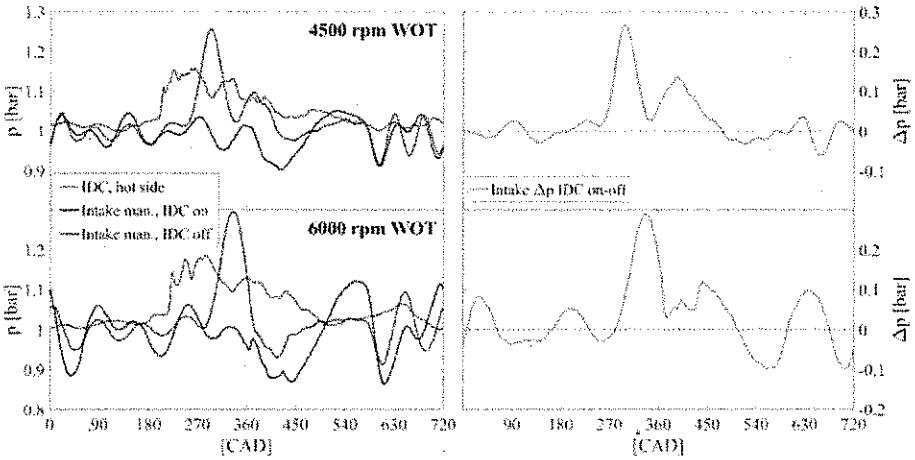

Fig. 4. Pressure characterization versus crank angle at different engine speeds (top: 4500 rpm, bottom: 6000 rpm). Left side: pressure in IDC hot side (red); intake manifold pressure with IDC inserted (blue) or removed (black). Right side: intake manifold pressure difference (green) between IDC inserted and removed. When green curve is negative, the naturally aspirated configuration (IDC off) guarantees in that moment an intake pressure higher than the one with IDCs.

The following performance characterization started with a knocking analysis, since, when charging a SI engine, especially in oversquare (short-stroke) engines such as the tested one, a wide safety margin against knock must be preserved. During the tests, indicating analysis over 200 consecutive cycles with Kistler KiBox allowed us to determine the so-called "k-ratio", an experimental knocking detection index based on a Siemens VDO algorithm [11]. If the threshold of 1.4 is exceeded, it can be stated that knocking begins to occur [12]. In Fig. 5, k-ratio values for Original and IDC configurations are reported. It can be seen that Original configuration is near the threshold (i.e. engine is close to an incipient knock); it is interesting to note that IDC does not change this behavior significantly. In particular, 4500 rpm WOT is the only point where a small increase of k-ratio was found, slightly worsening knock. At 7000 rpm, instead, a small decrease occurs, while no effect was found at 9500 rpm. It must be remarked that all these points were recorded with no changes in SA nor lambda (Table 3).

It is worth saying that engine intake temperature does not rise passing from Original to IDC configuration, owing to the limited overpressure and to the negligible heat transfer between the IDC hot and cold sides.

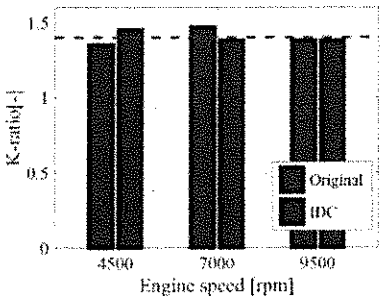

Fig. 5. Calculated k-ratio. Dashed red line represents the 1.4 threshold.

Table 4. Performance comparison for the three tested layouts.

	Corrected Power [kW]		
Tested point	Original	Baseline	IDC
4500 rpm WOT	12.0	11.4	13.8
7000 rpm WOT	23.6	25.2	24.7
9500 rpm WOT	29.7	30.0	31.1

Performances (Fig. 6 and Table 4) were acquired and corrected by taking into account barometric pressure, humidity and room temperature according to SAE J1349 [10]. The most evident effect of IDC is at 4500 rpm: there is a significant power increase if compared to both Original Engine and Baseline (Original: +15.0%, Baseline: +21.1%). The same behavior, with a lower gain, can be found at 9500 rpm (+4.7% and +3.6% respectively). At 7000 rpm, instead, IDC is able to increase power if compared to Original layout (+4.6%) but performs less than Baseline (-2.0%). This can be probably due to effects superimposition: the new muffler has a positive effect at 7000 rpm (in fact, both Baseline and IDC show higher performances than Original), while the pulses from the two IDCs, are probably positioned in a not favorable timing with respect to intake valves opening phase and in-cylinder pressure level. As a matter of fact, by analyzing intake pressure oscillations during an engine cycle and focusing on the angular interval when intake valves are open (Fig. 7), one can see that at 7000 rpm IDC configuration is able to generate a pressure level almost always higher than the Original one. At 9500 rpm, even if in the first phase of intake valve opening (up to 400 CAD) IDC pressure is lower, performance continues to remain better. This can suggest that an air pulse is more effective during the second half of intake stroke, when piston starts to slow down (so, reducing suction effectiveness [2]).

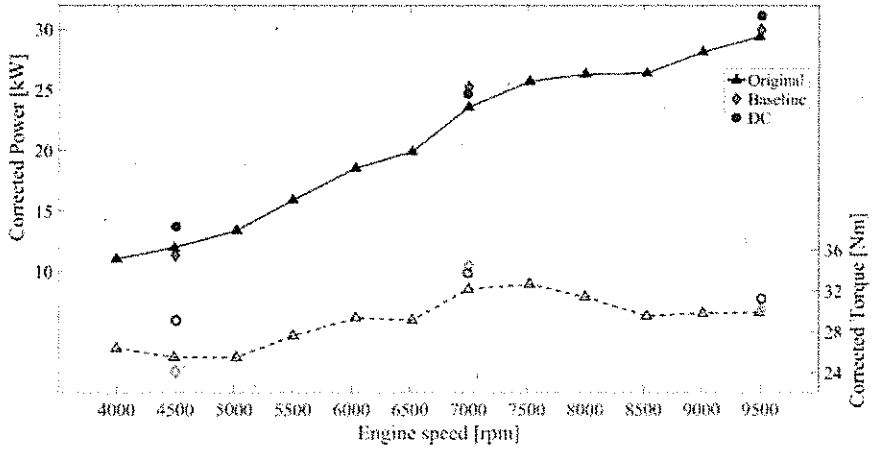

Fig. 6. Corrected performances of the three layouts: power (left) and torque (right) vs engine speed.

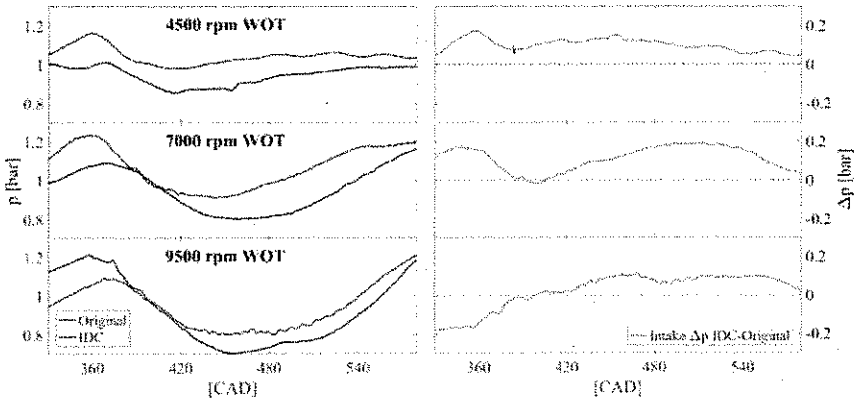

Fig. 7. Intake pressure (absolute bar) during intake valve opening period at different engine speeds (top: 4500 rpm, middle: 7000 rpm, bottom: 9500 rpm). Left side: Original (black) and IDC (blue) values. Right side: difference (green) between IDC and Original. When green curve is negative, Original engine guarantees in that moment an intake pressure higher than the one with IDCs.

4. Conclusions and Future Work

Drum Charger is a compressor designed to exploit the pulses generated by exhaust valve opening. In this work, a first study of the coupling of this system with a 4-stroke motorbike engine (KTM RC 390) was carried out. Knock characterization showed that IDC insertion does not worsen k-ratio significantly. After the performance characterization of the original engine, the differences in terms of brake power were studied with fixed ECU parameters (spark advance and lambda). At low-speed full-load (4500 rpm WOT) and high-speed full-load (9500 rpm WOT) the performances of the engine equipped with IDCs were found to be better than Original engine, with a max power gain of about 1.4 kW. At medium-speed full-load (7000 rpm WOT) the power improvement seems to be mainly due to the muffler, different from the Original one, and not to the boost itself. Pressure analysis confirmed that the IDC insertion allows the intake pressure to rise in any case, but its effect also depends on the proper timing with respect to intake valves opening phase and in-cylinder pressure level.

Future work will be based on a deeper analysis concerning pressure waves. Measurements will be carried out in several points, even inside the Drum Charger. This should allow to better understand the boost generation mechanism and should produce useful data for setup and tuning of CFD models.

Acknowledgements

The authors would like to thank Alexander Hohenegger of *AlterEgo Hardware* for the financial support to this research activity and Riccardo Capotosto of *Egb* for the supply of the prototypal exhaust system.

References

[1] Hiereth, H. and Prenninger, P., "Charging the Internal Combustion Engine", Springer Wien (2007), ISBN 978-3-211-33033-3

[2] Heywood, J.B., "Internal Combustion Engine Fundamentals", McGraw-Hill (1988), ISBN 007028637X

[3] Starodetko, K.E., Simand, S., Drobychevskj, T.B., Belyaev, V.J., Yurchuk, K.N., Vitsiaz, A.A., and Kuzmenkov, D. V., "High Performance Characteristics of a Motorcycle Powered by a Four-Stroke Small 50cc-125cc Engine at the Expense of a Positive Displacement Air Compressor as a Supercharger", *SAE Technical Paper*, 2013-32-9015 (2013), SAE International

[4] Doerfler, P.K., "Comprex Supercharging of Vehicle Diesel Engines", *1975 Automotive Engineering Congress and Exposition*, (1975), SAE International

[5] Zinner, C., Abart, M., Schargl, O., Schmidt, S., Leiber, S., and Schabetsberger, T., "Charging and Powersport for Motorcycles: A Contradiction?", *SAE/JSAE Technical Paper*, 2011-32-0585 (2011), SAE International

[6] Zinner, C., Stelzl, R., Schmidt, S., Leiber, S., and Schabetsberger, T., "Experimental Verification and Drivability Investigations of a Turbo Charged 2-Cylinder Motorcycle Engine", *SAE Technical Paper*, 2014-32-0112 (2014), SAE International

[7] Romani, L., Vichi, G., Bianchini, A., Ferrari, L., and Ferrara, G., "Optimization of the Performance of a Formula SAE Engine by Means of a Wastegate Valve Electronically Actuated", *Energy Procedia* 101(9) (2016): 654–661

[8] Wang, D., Qian, D., and Wang, B., "The Development of a Small Restricted Turbocharged Racecar Engine", *SAE/JSAE 2016 Small Engine Technology Conference & Exhibition*, (2016), SAE International

[9] Battistoni, M., Poggiani, C., and Grimaldi, C.N., "Experimental Investigation of a Port Fuel Injected Spark Ignition Engine Fuelled with Variable Mixtures of Hydrogen and Methane," *SAE Technical Paper*, 2013-01-0226 (2013), SAE International

[10] "Engine Power Test Code - Spark Ignition and Compression Ignition - Net Power Rating", SAE J1349 (2008), SAE International

[11] Kistler, "KiBox To Go instruction manual", (2009), Winterthur: Kistler Group

[12] Battistoni, M., Grimaldi, C.N., Cruccolini, V., Discepoli, G., and Cesare, M. De, "Assessment of Port Water Injection Strategies to Control Knock in a GDI Engine through Multi-Cycle CFD Simulations," *SAE Technical Paper*, 2017-24-0034 (2017), SAE International

Available online at www.sciencedirect.com

ScienceDirect

Energy Procedia 148 (2018) 1262–1269

Energy Procedia

www.elsevier.com/locate/procedia

73rd Conference of the Italian Thermal Machines Engineering Association (ATI 2018), 12-14 September 2018, Pisa, Italy

Experimental assessment of spark and corona igniters energy release

G. Discepoli[a,*], V. Cruccolini[a], M. Dal Re[b], J. Zembi[a], M. Battistoni[a], F. Mariani[a], C. N. Grimaldi[a]

[a]*Department of Engineering, Università degli Studi di Perugia, Via G. Duranti 95, Perugia 06125, Italy*
[b]*Federal-Mogul Powertrain Group*

Abstract

The Radio-Frequency (RF) Corona Ignition System is an innovative and promising technology able to produce multiple streamers to ignite the fuel throughout the combustion chamber. This system, compared to a conventional spark ignition system, involves wider initial combustion volumes and allows the engine to operate in stable conditions at leaner mixtures, higher EGR dilutions, with faster burning rates and enabling advanced combustion strategies. Due to the intrinsic operating features of the RF corona ignition system, the production of a plasma generated by a high frequency electrical field, the energy released to the surrounding medium is a fundamental parameter to understand its behaviour and impact on a given air-fuel mixture.

The aim of this paper is the energetic characterization of a prototype of corona igniter, called Advanced Corona Ignition System (ACIS), by measuring the pressure increase caused by the streamers in a controlled environment, a pressure based calorimeter. The ACIS results are also compared with a multiple spark discharges (MSD) ignition system based on standard Federal Mogul spark plug technology characterized by an integrated electronics capable of managing up to 17 consecutive discharges. The energy evaluation was carried out at room temperature with air at different pressure levels, up to 10 bar.

Keywords: Energy; Corona effect; Igniter; Lean combustion; Experimental

1. Introduction

Modern engine technology targets are to improve the energy conversion efficiency and reduce exhaust emissions of the combustion system for given operating conditions. To succeed in exploiting ultra lean air-fuel mixture combustion, opportunities are offered by applying innovative systems based on low temperature plasma-assisted ignition [1, 2].

These innovative ignition systems, by means of different ion and excited species production mechanisms, add new paths to start a reaction chain that leads to combustion [3]. Furthermore, transient plasma showed to accelerate the

*Corresponding author. Tel.: +39-075-585-3749.
E-mail address: gabriele.discepoli@unipg.it

10.1016/j.egypro.2018.08.001

early combustion phase and, more in general, improve engine performance thanks to the multiple spread ignition locations in the areas of greatest active species production [4, 5]. The oxygen, in atomic, ionic or excited state, seems to be the key chemical species for the plasma ignition [6, 7]. Engine combustion results stabilized and the lean limit is extended with respect to the conventional spark igniter [8, 9]. Also, it has been proved that the low temperature plasma can extend the EGR dilution tolerance [10, 11].

At present, there are only few attempts to model the plasma ignition process because of challenging issues due to the plasma formation timescale, which is orders of magnitude smaller than the ignition process timescale [12].

From a general point of view, the thermal energy delivered to the air-fuel mixture is a key parameter as it heavily affects the flame kernel formation and then the production of a correct ignition [13]. The aim of the present work is to assess the thermal energy released to the medium by the streamers produced by an RF Corona Ignition System and, then, to compare it with the energy released by a conventional system. This investigation concerning low temperature plasma ignition systems has not been reported in the literature yet, to the best of authors' knowledge. Indeed, even if the production of the ion and excited states that starts and promotes the combustion is supposed to be the main feature of the low temperature plasma produced by the ACIS, these chemical activities cannot be separated from the thermal phase that, actually, is spatially distributed, enhancing the chemical kinetics of the exothermic fuel oxidation, resulting in the combustion initiation [4]. Therefore, it is essential to measure and assess the deposited thermal energy.

To this end, the thermal energy delivered by the ignition systems is measured in a simplified and controllable environment, i.e. a constant volume cylindrical vessel, operated at different pressures. Furthermore, the primary electrical energy supplied to the ignition systems is also measured (for the conventional igniter) or calculated (for the ACIS) to address how much of the electrical energy supplied to the igniter is transmitted to the chamber medium.

Nomenclature

ACIS	Advanced Corona Ignition System
MSD	Multiple Spark Discharges
V_{off}	Supply Voltage Offset
E_{PS}	Energy Supplied to the Primary circuit
E_{TR}	Thermal Energy Released to the medium
σ^E_{PS}	Standard deviation of the E_{PS} data distribution
σ^E_{TR}	Standard deviation of the E_{TR} data distribution
η_E	Electric efficiency
$P_{chamber}$	Pressure in the bomb chamber

2. Experimental set-up and methodology

2.1. Test-bench description

The experimental campaign is carried out using a constant volume vessel to allow free management of the operating conditions as pressure, temperature, gas type, volume and geometry. The inner bomb volume ($22.5 \cdot 10^3\ mm^3$) is made out of Plexiglas for its low thermal conductivity ($0.187\ W \cdot m^{-1}K^{-1}$) and to allow optical access.

The bomb works as a calorimeter, equipped with a piezoelectric low-pressure sensor (Kistler Type 7261, sensitivity of 2200 $pC \cdot bar^{-1}$, max pressure resolution of $\approx\ 10^{-5}\ bar$) to measure the energy released in the chamber to the medium by the streamers. The pressure sensor and the igniter tip (fig. 1.a) are mounted opposed to each other (fig. 1.b). The charge signal produced by the pressure sensor is amplified and converted to a proportional voltage signal by a charge amplifier (*Kistler Type 5011*) and then acquired by a fast oscilloscope (*Teledyne LeCroy Wavesurfer 3000*). The oscilloscope also collects the signals produced by a thermocouple which monitors the chamber temperature, by a current probe (*Teledyne LeCroy CP030*, sensitivity of 10 $mA \cdot div^{-1}$) and by a *Teledyne LeCroy PP020* passive probe. In the case of the single or multi-spark tests, the electrical energy supplied to the primary circuit is estimated

by measuring voltage and current simultaneously. These measurements allow to accurately assess how much of the supplied energy is converted and deposited in the medium as thermal energy.

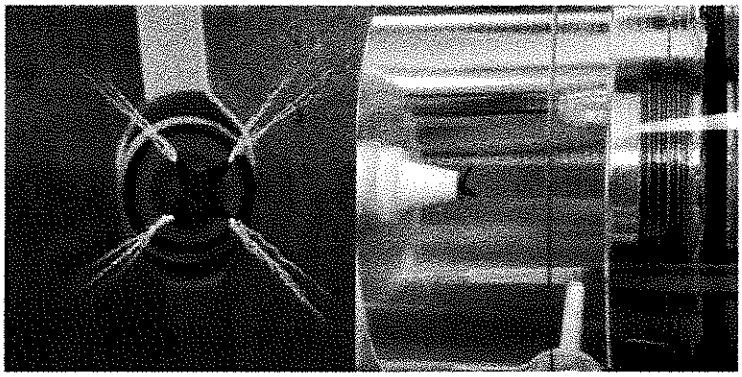

Fig. 1. Detail of the ACIS 4-tips electrode (a). Detail of the bomb chamber (b).

The conventional spark igniters are driven by an Arbitrary Wave Generator (*HP 33120A*) that triggers the spark and controls the frequency and the number of the multiple spark events [14]. The gas which fills the bomb is supplied by cylinders for its purity, since it can widely affect the behavior of the streamers (i.e., the induced plasma), in particular for the inclusion of electronegative species like oxygen [15, 16]. The medium is replaced before any test sequence.

2.2. *Methodology and procedures*

The oscilloscope sampling frequency is 10 MHz, 10 times bigger than the frequency of the ACIS current (about 1 MHz). The natural frequency of the pressure sensor is $\approx$ 13 kHz and therefore it can not be used to resolve pressure components above this frequency. When the current starts, it suddenly induces electronic noise that heavily affects the pressure (fig. 2.a) and only after some tens of μs a response is visible. This delay is compatible with the traveling time of a pressure wave across the bomb at the speed of sound, from the igniter tip to the sensor. The pressure rise is quite complex, probably due to the interference of the reflecting waves and the streamers persistence.

In fig. 2.a whole ACIS, single spark and MSD events are showed. The noise heavily affects the pressure signal with many components in the frequency domain (fig. 2.b). Therefore a low-pass filter at 2 kHz is needed to smooth out the signal adequately. Finally, the difference between the average pressure after and before the streaming/spark event generates a pressure step ΔP.

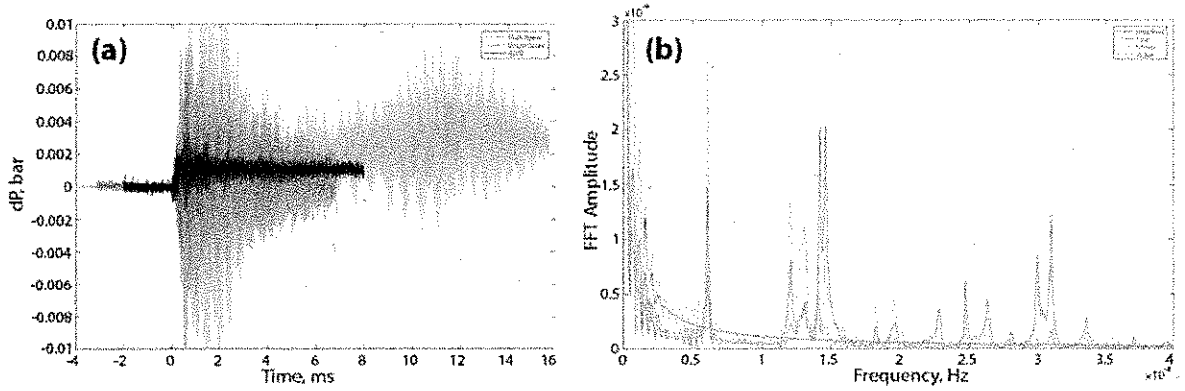

Fig. 2. Raw data acquired by the pressure sensor from three different events produced by the ACIS (black), Single Spark (red) and Multiple Spark (yellow) at $P_{chamber}$ = 10 *bar* (a). ACIS frequency spectrum of the smoothed signal at 5.5*bar* (black) and of the raw signals at 1 *bar* (red), 5.5 *bar* (yellow) and 10 *bar* (purple) (b).

From the evaluated ΔP, the energy E delivered to the chamber medium is then calculated, by assuming the chamber as an adiabatic system [13], because the increase of the gas temperature during the streaming is negligible, and the chamber wall is an excellent insulator. Under these conditions, applying the first law of thermodynamics the following equation is obtained

$$E = \frac{1}{\gamma - 1} V_c \cdot \Delta P \tag{1}$$

where γ is the specific heat ratio, and V_c is the chamber volume. For each operating condition, about one hundred ΔP are collected and averaged to obtain the value of E.

3. Results and discussion

The measurements were carried out at room temperature and at increasing chamber pressure levels to take into account the pressure influence on the released energy: 1 *bar*, 5.5 *bar* (5 *bar* in the MSD test) and 10 *bar*. In the *ACIS* case, we included a sensitivity analysis on the main control parameter, i.e. the *Supply Voltage Offset* (V_{off}), that sets the input to the high frequency amplifier to properly match the energy requirement of the working conditions [9, 8].

3.1. Single Spark

The energy supplied to the primary circuit (*primary energy supplied*, E_{PS}) is almost constant during the whole recorded data-set and approximately independent of the bomb condition, near 105 *mJ* for any pressure level. Indeed, the standard deviation (σ^E_{PS}) is around 1.5 *mJ* for any pressure, larger than the difference between each E_{PS} at the various $P_{chamber}$. Data are summarized in table 1.

For each $P_{chamber}$, the thermal energy released by the spark to the medium (E_{TR}) resulted to be constant for the whole tests. The distribution of E_{TR} data series is quite variable (see σ^E_{TR} column of tab. 1, the relative σ^E_{TR} is about 17%, 9% and 17% for 1 *bar*, 5.5 *bar* and 10 *bar*, respectively) but it does not show any particular trend as the pressure increases, even if measurement conditions are limited to clearly identify a trend.

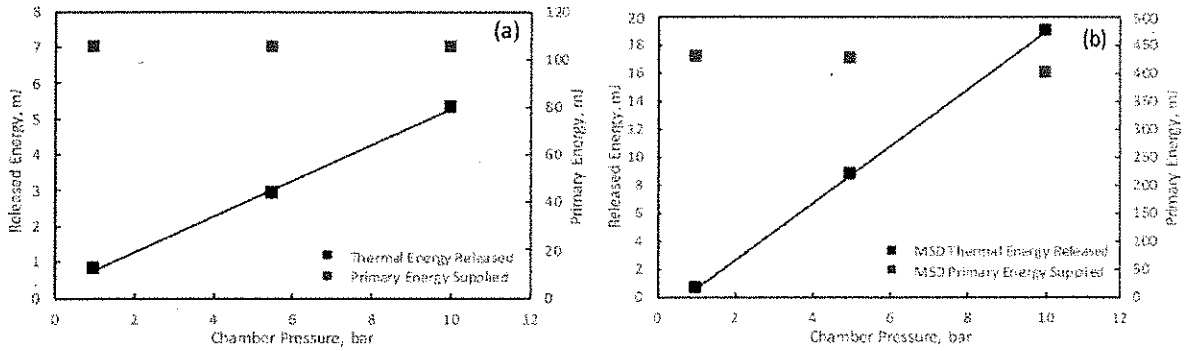

Fig. 3. Single Spark (a) and MSD (b) Ignition System: energetic assessment of the measured values for the three different bomb inner pressure $P_{chamber}$: E_{TR} (black squares) and E_{PS} (red squares).

As expected, E_{TR} depends on the chamber pressure: the higher the pressure, the larger the dielectric between the electrodes and the higher the power needed. In other words, stronger electric field is required to reach the breakdown and arc condition. The average value of the released thermal energy E_{TR} ranges from 0.83 *mJ* at ambient pressure to 5.31 *mJ* at 10 *bar*, showing an almost linear trend (fig. 3.a).

The efficiency increases as the chamber pressure increases, consistently with the released thermal energy, as the primary supplied energy is basically constant, and it reaches 5.1% at 10 *bar*. Table 1 summaries the results for the single spark case.

Table 1. Single-Spark and Multi-Spark: energy supplied to the primary circuit E_{PS}, thermal energy released in the bomb medium E_{TR}, relative standard deviation of the data distribution (σ^E_{PS} and σ^E_{TR}, respectively) and overall efficiency η_E.

Ignition System	$P_{chamber}$ [bar]	E_{PS} [mJ]	σ^E_{PS} [mJ]	E_{TR} [mJ]	σ^E_{TR} [mJ]	η_E
Single Spark	1	105.1	1.6	0.83	0.14	0.8%
	5.5	105.1	1.5	2.95	0.3	2.8%
	10	104.7	1.5	5.3	0.9	5.1%
MSD	1	429.5	11.0	0.53	0.08	0.1%
	5	424.5	5.2	8.75	0.8	2.1%
	10	401.0	9.2	19.1	1.9	4.8%

3.2. Multiple Spark

The MSD Ignition System is similar to the previous igniter as for the general features, but it produces many sparks in a short amount of time, belonging to the same event, and the energy management is therefore quite different. Fig. 4.a shows how the primary circuit is fed vs. time (E_{PS} per sample, black solid line), essentially reflecting the supply current trend during an event. The first charge is by far the most intense and longest; the first breakdown is well recognizable by the first sudden drop of the supplied energy. The breakdown characterizes the thermal energy release start (E_{TR} red line of 4.a). The released energy growth continues until a new spark recharge process starts (in E_{TR} this identifies a local maximum), beginning a new loop of the spark plug charge-discharge process. The last breakdown triggers a longer discharge and, consequently, a greater energy release phase, i.e. the last glow phase. This behaviour is in good agreement with the results of previous works on analogous ignition systems ([14, 17]).

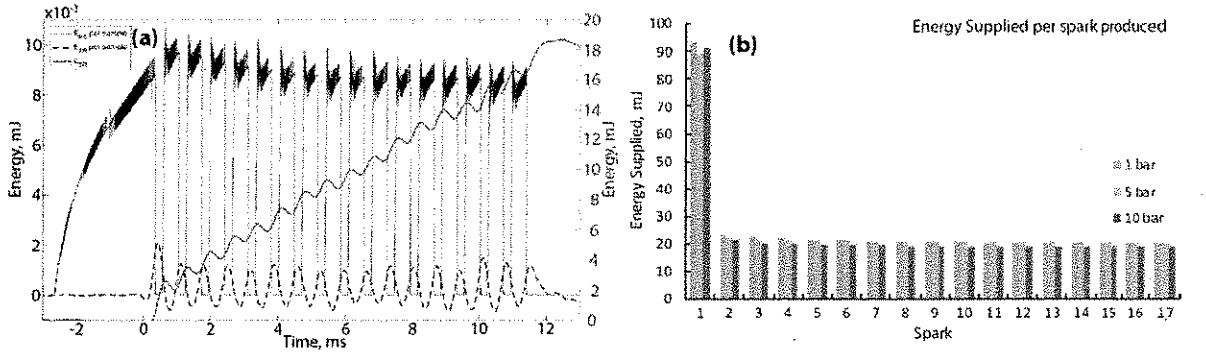

Fig. 4. Multi-spark test case. (a) example at $P_{chamber} = 10\ bar$: energy per sample supplied to the primary circuit (black solid line), thermal energy E_{TR} per sample released to the medium (black dotted line) and the overall thermal energy E_{TR} (the sum of each sample contribution, red line). (b): energy supplied to the spark plug primary circuit for each one of the 17 sparks produced by the MSD during a single event, equivalent to 17 breakdown for event.

After the breakdown, the arc and glow phases occur and require few *ms* to fully develop [13]; during these phases energy is released. In the MSD processes, a new charge-discharge loop breaks the previous arc-glow phase before it completes, except for the last breakdown.

The black dotted line of fig. 4.a represents the released thermal energy E_{TR} per sample. It is heavily affected by the data processing (in particular, by the low pass filter, see the yellow line in fig. 2.a) so that the local information is smoothed and spread out on a wider time interval. Nevertheless, it keeps track of the deposited energy amount of each spark. Each local maximum is centred on the intervals whose limits are defined by $E_{PS} = 0\ mJ$, i.e. charge and discharge are alternate; the last peak is asymmetrical, with a prolonged tail, that is due to the largest thermal energy released by the last discharge glow phase. E_{TR} per sample and E_{PS} per sample are plotted on the same axis on purpose, to allow their comparison, as their ratio is the energy efficiency.

The value of the sum of the E_{PS} per sample for each spark (fig. 4.b) is variable but the first discharge is by far the most energetic. The MSD system absorbs most of the required energy in the 3 *ms* preceding the first spark. This energy is then stored and partially refilled before each breakdown and finally dissipated with the last spark event.

The MSD showed a quite constant E_{PS} for the whole test, while it is slightly dependent on $P_{chamber}$, showing a decrease with pressure, which was negligible for the single spark. In this case, $P_{chamber}$ has an impact with such an high level of energy. The data dispersion is not so stable, but results independent of the $P_{chamber}$ (σ^E_{PS} column, tab. 1).

The E_{TR} follows the single spark trend, approximately linear (fig. 3,b): almost constant for the test duration and considerably affected by $P_{chamber}$, increasing quickly with $P_{chamber}$ (reaching about 19 mJ at 10 bar). The data dispersion does not affect the high pressure data distribution excessively (see σ^E_{TR} column in tab. 1). As expected from the E_{PS} and E_{TR} trends, the efficiency increases with the bomb pressure $P_{chamber}$. Data are summarized in tab. 1.

3.3. ACIS

The ACIS has different setting parameters that can be adjusted to modify the streamer behaviour. We took into account the main parameter V_{off} only, as exploring the full range of settings and control parameters would be beyond the scope of this work. On the other hand, the V_{off} exploration is fundamental, because it defines the power supplied to the igniter and its value is expected to be calibrated and set up for each engine operating condition [9]. Furthermore, we found there is not a common value of V_{off} that optimizes the three tested pressures of 1, 5.5 and 10 bar.

The V_{off} operating window is determined by finding the power conditions of minimum value, below which there is no streamers production, or of maximum value, above which the undesired arc condition appears and the ACIS works in spark mode [9]. The window is then divided in four intervals of about the same width. It should be noted that, while the lower limit depends on the medium density only, the upper limit is variable according the arc conditions due to $P_{chamber}$. At 1 bar the arc takes place between the igniter tip and its tip holder, while for higher pressure the arc conditions are achieved near the pressure sensor. The whole test campaign is summarized in table 2.

Table 2. ACIS results. σ_{TR} is the standard deviation of the released energy E_{TR} distribution assumed as width evaluation.

$P_{chamber}$ [bar]	V_{off} [V]	E_{PS} [mJ]	E_{TR} [mJ]	σ_{TR} [mJ]	σ_{TR} [%]	η_E
1	11	42.4	0.55	0.17	31.6%	1.3%
	18	99	2.53	0.21	8.3%	2.6%
	24	162.5	9.12	0.30	3.3%	5.6%
	30	238	20.0	0.6	2.9%	8.4%
	36	326	31.6	1.6	5%	9.7%
5.5	32	266	0.22	0.21	93.4%	0.1%
	40	391	4.06	0.46	11.3%	1.0%
	47	516	16.7	1.0	6.1%	3.2%
	54	655	43.2	5.0	11.7%	6.6%
	62	831	64.5	5.5	8.5%	7.8%
10	44	460.5	0.77	0.25	31.9%	0.2%
	47	516	1.4	0.25	17.2%	0.3%
	50	574	2.9	0.25	8.6%	0.5%
	53	634.5	5.4	0.7	13%	0.9%
	56	697.5	8.35	0.84	10.1%	1.2%

The electrical energy supplied to the ACIS igniter can be evaluated as a function of the setting parameters. $E_{PS} \propto V_{off}^{1.7208}$, independently of the applied pressure inside the bomb: the trend of this function is well visible in fig. 5.a, where all the three cases overlap.

The thermal energy released to the medium quickly increases with the voltage offset V_{off}, while the pressure increase, at constant V_{off}, reduces E_{TR}, essentially because the conditions to establish streamers become harder. The measured points lie on the fitting curve $E_{TR} \propto V_{off}^2$ (fig. 5.b). The growth of $P_{chamber}$ moves those curves to higher voltages; it is difficult to derive a unique law which describes the three curves. The interval width of V_{off} heavily affects the energy development. However, the trend of E_{TR} being proportional to V_{off}^2 is well established.

The ACIS efficiency shows three different intervals, varying E_{off} (fig. 5.c):

1. low V_{off} - this interval is characterized by a slow increase, like the slow E_{TR} starting increase;
2. intermediate value of the V_{off} - it is characterized by a fast growth; in this section the increase of E_{TR} with V_{off} is much faster than the supplied energy growth E_{PS} in the same V_{off} phase;

3. high value of V_{off} - it is characterized by a new reduction of the growth rate, due to the dependence of E_{TR} and E_{PS} on the respective powers of V_{off}, namely 2 and 1.7208, such that, finally, $\eta \propto V_{off}^{0.2792}$. Of course, nothing is inferable for higher values of V_{off}.

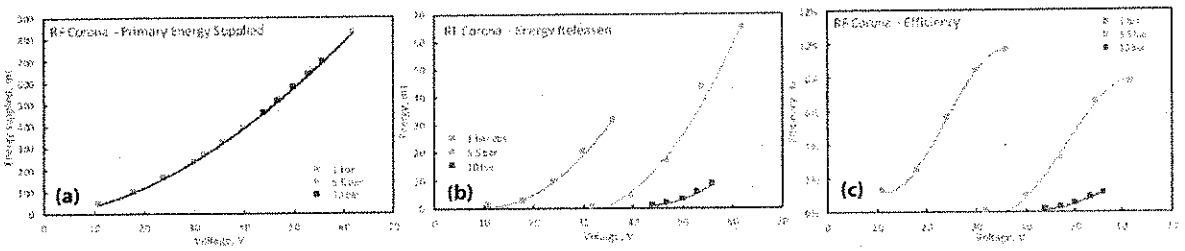

Fig. 5. ACIS; energy supplied to the primary circuit E_{PS} (a); thermal energy released to the chamber medium E_{TR} (b) a at 1 *bar* (orange), 5.5 *bar* (grey) and 10 *bar* (blue); energetic efficiency $\eta_e = E_{TR}/E_{PS}$ for the three different values of the bomb pressure $P_{chamber}$ (c).

Finally, the width of the released energy data distribution, produced by the sequence of the streamer events and estimated by the standard deviation σ_{TR} (5^{th} column of tab. 2), shows a very light increase with V_{off}, corresponding to a pronounced relative reduction. The σ_{TR} values corresponding to the lowest V_{off} suffer from the weak and noisy signal produced by the ACIS in those operating conditions.

4. Conclusions

The measurement of the energy deposited in pure air by three different ignition systems, one of which is a low temperature plasma-assisted igniter, has been carried out at three chamber pressures. The results showed that, varying the pressure, the energy supplied to the primary circuit for the single spark system is about constant while the trend of the multiple spark case is slightly decreasing. The energy fed to the ACIS system is fully independent from the bomb inner pressure.

The second result obtained is the measurement of the thermal energy provided to the chamber medium by the ignition systems: the single and multi-spark systems showed the same increasing trend with the pressure increase. Similarly, the efficiency of these two systems to release the absorbed electric energy increases with the pressure. The ACIS thermal energy released case is a bit more complex. The pressure increase produces a marked drop in the released energy, with the same V_{off} (same energy supplied). Actually, higher V_{off} operating values are available to the ACIS system, so that the system is capable of reaching very high E_{TR} values, if compared to the spark plug system. This energy can be increased until the system reaches the undesired arc conditions, established by the geometry of the chamber. The efficiency reaches the highest levels for low pressure and has a clear trend change for the highest V_{off}, but without an actual inversion towards low values.

Therefore, in a real engine application, in principle it is possible to manage the deposited thermal energy in the working medium, by properly setting the control ACIS parameters, in particular V_{off}, depending on the operating conditions (i.e. engine point, equivalence ratio and/or EGR rate).

Further analyses will be carried out to better understand the ACIS system, in particular as a function of the different working parameters and by exposing the streamers to various gas types and pressures.

Acknowledgements

The authors would like to thank Federal - Mogul Powertrain for supporting this research activity.

References

[1] Andrey Starikovskiy and Nickolay Aleksandrov. Plasma-assisted ignition and combustion. *Progress in Energy and Combustion Science*, 39(1): 61–110, feb 2013. ISSN 03601285. doi: 10.1016/j.pecs.2012.05.003. URL http://dx.doi.org/10.1016/j.pecs.2012.05.003http://linkinghub.elsevier.com/retrieve/pii/S0360128512000354.

[2] John Burrows and Kristapher Mixell. Analytical and Experimental Optimization of the Advanced Corona Ignition System. In Michael Günther and Marc Sens, editors, *Ignition Systems for Gasoline Engines*, volume 2, pages 267–292. Springer International Publishing, Cham, 2017. ISBN 978-3-319-45503-7. doi: 10.1007/978-3-319-45504-4_17. URL http://link.springer.com/10.1007/978-3-319-45504-4{_}17.

[3] S M Starikovskaia. Plasma assisted ignition and combustion. *Journal of Physics D: Applied Physics*, 39(16):R265–R299, aug 2006. ISSN 0022-3727. doi: 10.1088/0022-3727/39/16/R01. URL http://stacks.iop.org/0022-3727/39/R265http://stacks.iop.org/0022-3727/39/i=16/a=R01?key=crossref.978ad5eef7e6c1e79038889cadc11150.

[4] D. Singleton, S. J. Pendleton, and Martin A. Gundersen. The role of non-thermal transient plasma for enhanced flame ignition in C2H4-air. *Journal of Physics D: Applied Physics*, 44(2):022001, jan 2011. ISSN 00223727. doi: 10.1088/0022-3727/44/2/022001. URL http://stacks.iop.org/0022-3727/44/i=2/a=022001?key=crossref.7f71843701e9c11aedbdb4be72cb9047.

[5] Cherian A Idicheria and Paul M Najt. Potential of Advanced Corona Ignition System (ACIS) for Future Engine Applications. In *Ignition Systems for Gasoline Engines*, pages 315–331. Springer International Publishing, Cham, 2017. ISBN 978-3-319-45503-7. doi: 10.1007/978-3-319-45504-4_19. URL http://link.springer.com/10.1007/978-3-319-45504-4{_}19.

[6] Benjamin Matthew Wolk and Isaac Ekoto. Calorimetry and Imaging of Plasma Produced by a Pulsed Nanosecond Discharge Igniter in EGR Gases at Engine-Relevant Densities. *SAE International Journal of Engines*, 10(3):2017–01–0674, mar 2017. ISSN 1946-3944. doi: 10.4271/2017-01-0674. URL http://papers.sae.org/2017-01-0674/.

[7] Taisuke Shiraishi and Tomonori Urushihara. Fundamental Analysis of Combustion Initiation Characteristics of Low Temperature Plasma Ignition for Internal Combustion Gasoline Engine. apr 2011. doi: 10.4271/2011-01-0660. URL http://papers.sae.org/2011-01-0660/.

[8] Alessandro Cimarello, Carlo N. Grimaldi, Francesco Mariani, Michele Battistoni, and Massimo A. Dal Re. Analysis of RF Corona Ignition in Lean Operating Conditions Using an Optical Access Engine. In *SAE Technical Paper*, pages 1–22, mar 2017. doi: 10.4271/2017-01-0673. URL http://papers.sae.org/2017-01-0673/.

[9] Alessandro Cimarello, Valentino Cruccolini, Gabriele Discepoli, Michele Battistoni, Francesco Mariani, Carlo Grimaldi, and Massimo Dal Re. Combustion Behavior of an RF Corona Ignition System with Different Control Strategies. In *SAE Technical Paper*, pages 1–19, apr 2018. doi: 10.4271/2018-01-1132. URL http://www.sae.org/content/2018-01-1132/.

[10] James Sevik, Thomas Wallner, Michael Pamminger, Riccardo Scarcelli, Dan Singleton, and Jason Sanders. Extending Lean and Exhaust Gas Recirculation-Dilute Operating Limits of a Modern Gasoline Direct-Injection Engine Using a Low-Energy Transient Plasma Ignition System. *Journal of Engineering for Gas Turbines and Power*, 138(11):112807, may 2016. ISSN 0742-4795. doi: 10.1115/1.4033470. URL http://gasturbinespower.asmedigitalcollection.asme.org/article.aspx?doi=10.1115/1.4033470http://dx.doi.org/10.1115/1.4033470.

[11] Fabian Marko, Gerhard König, Tobias Schöffler, Steffen Bohne, and Friedrich Dinkelacker. Comparative Optical and Thermodynamic Investigations of High Frequency Corona- and Spark-Ignition on a CV Natural Gas Research Engine Operated with Charge Dilution by Exhaust Gas Recirculation. In *Ignition Systems for Gasoline Engines*, pages 293–314. Springer International Publishing, Cham, 2017. ISBN 978-3-319-45503-7. doi: 10.1007/978-3-319-45504-4_18. URL http://link.springer.com/10.1007/978-3-319-45504-4http://link.springer.com/10.1007/978-3-319-45504-4{_}18.

[12] Riccardo Scarcelli, Anqi Zhang, Thomas Wallner, Douglas Breden, Anand Karpatne, Laxminarayan Raja, Isaac Ekoto, and Benjamin Wolk. Multi-dimensional Modeling of Non-equilibrium Plasma for Automotive Applications. In *SAE Technical Papers*, volume 2018-April, pages 1–10, apr 2018. doi: 10.4271/2018-01-0198. URL http://www.sae.org/content/2018-01-0198/.

[13] Zainal Abidin and Christopher Chadwell. Parametric Study and Secondary Circuit Model Calibration Using Spark Calorimeter Testing. In *SAE Paper*, apr 2015. doi: 10.4271/2015-01-0778. URL http://papers.sae.org/2015-01-0778/.

[14] Claudio Poggiani, Michele Battistoni, Carlo N. Grimaldi, and Adriano Magherini. Experimental Characterization of a Multiple Spark Ignition System. *Energy Procedia*, 00:1–6, dec 2015. ISSN 18766102. doi: 10.1016/j.egypro.2015.11.887. URL http://linkinghub.elsevier.com/retrieve/pii/S1876610215026478.

[15] Sergey Leonov, Dmitry Opaits, Richard Miles, and Victor Soloviev. Time-resolved measurements of plasma-induced momentum in air and nitrogen under dielectric barrier discharge actuation. *Physics of Plasmas*, 17(11):113505, nov 2010. ISSN 1070-664X. doi: 10.1063/1.3494279. URL http://aip.scitation.org/doi/10.1063/1.3494279.

[16] C. L. Enloe, R. S. Mangina, and G. I. Font. Normalized Electronegative Species Effects in the Dielectric-Barrier-Discharge Plasma Actuator. *AIAA Journal*, 54(7):2061–2068, jul 2016. ISSN 0001-1452. doi: 10.2514/1.J054551. URL http://arc.aiaa.org/doi/10.2514/1.J054551.

[17] Claudio Poggiani, Alessandro Cimarello, Michele Battistoni, Carlo N. Grimaldi, Massimo A. Dal Re, and Matteo De Cesare. Optical Investigations on a Multiple Spark Ignition System for Lean Engine Operation. In *SAE Technical Papers*, number 2016-01-0711, apr 2016. ISBN 2016010711. doi: 10.4271/2016-01-0711. URL http://papers.sae.org/2016-01-0711/.

Relazione finale attività di ricerca

Dr. Giuseppe Venanzoni
Ricercatore a tempo determinato (L. 240/2010)

Introduzione

L'attività di ricerca svolta nei tre anni ha riguardato diversi aspetti della sintesi e della realizzazione di componenti a microonde. Una parte della ricerca si è concentrata sull'aspetto più tecnologico riguardante la costruzione di componenti a microonde mediante l'uso di tecniche di Additive Manufacturing. Un'altra parte ha riguardato, invece, lo sviluppo sia di nuove tecniche di progettazione che di nuovi componenti, concepiti in modo da trarre vantaggio dalla realizzazione mediante tecniche di stampa 3D.

Tecniche di additive manufacturing

Le tecniche di additive manufacturing prevedono l'uso di stampanti 3D per la realizzazione fisica di componenti meccanici in generale. Nello specifico è stata esplorata la possibilità di costruire componenti a microonde, tipicamente in guida d'onda, mediante stampa 3D. Tale possibilità è molto interessante sia per la realizzazione di prototipi sia per esplorare la possibilità di realizzazione di piccole serie di dispositivi. Le principali peculiarità della manifattura additiva, infatti, sono la possibilità di poter costruire in breve tempo e a costi ridotti prototipi di componenti che, invece, sarebbero costosi da produrre mediante tecniche classiche. Le stampanti 3D possono essere di vario tipo, con una differenziazione fondamentale per il tipo di materiale che utilizzano. In particolare esistono alcune stampanti che utilizzano plastica come materiale di stampa e altre che utilizzano delle leghe metalliche. Le prime sono più semplici e, quindi, meno costose. Entrambe costruiscono il componente accrescendo una serie di strati di materiale, in modo da dare la forma al componente. Questa è la differenza fondamentale dei processi additivi rispetto a quelli sottrattivi, che invece partono da un blocco di materiale grezzo per poi rimuovere ciò che non serve. Ovviamente, a seconda del tipo di materiale utilizzato per la stampa, cambiano anche i costi sia della stampante sia del prodotto finito. In particolare la stampa su plastica è la soluzione sicuramente più economica. La deposizione della plastica può avvenire in diversi modi. La tecnica più semplice è la FDM (Fused Deposition Modeling), dove un filo di materiale plastico (PLA o ABS) viene fuso attraverso un estrusore e depositato. Tale tecnica è molto economica ma poco precisa, quindi mal si adatta ala produzione di componenti a microonde. Un'altra tecnica è detta SLA o stereolitografica, dove una resina liquida viene polimerizzata attraverso un raggio laser. Questo metodo è molto più preciso, quindi maggiormente adatto alla costruzione di dispositivi a microonde. Infine c'è la cosiddetta tecnica PoliJet, dove un getto di materiale plastico liquido viene istantaneamente polimerizzato

attraverso l'uso di laser o raggi UV e depositato sul componente. Per quanto riguarda le stampanti a metallo, queste usano una polvere metallica che viene parzialmente fusa attraverso un laser ad alta potenza (o sinterizzata) in modo che una singola goccia possa aderire al corpo del componente. Se il metallo è riscaldato a bassa temperatura, una singola pallina di materiale si attacca al resto del componente già realizzato. Se, invece, la polvere è riscaldata ad alta temperatura questa si fonde completamente e si unisce al resto della parte meccanica in maniera più uniforme. La differenza tra i due casi consiste nella migliore resistenza meccanica dei componenti realizzati con il secondo processo. Ovviamente il processo stampa è più costoso rispetto alla stampa su plastica, sia per le polveri sia per i macchinari impiegati.
Per effettuare le sperimentazioni è stata impiegata la stampante in dotazione al Dipartimento di Ingegneria dell'Università di Perugia, ovvero una Formlabs Form2. Essa usa la tecnica stereolitografica, che come detto polimerizza una resina plastica. Il processo costruttivo avviene attraverso l'accrescimento di strati di materiale plastico, con una risoluzione, ovvero uno spessore dei singoli strati, che può essere di 25 um, 50 um oppure 100 um.

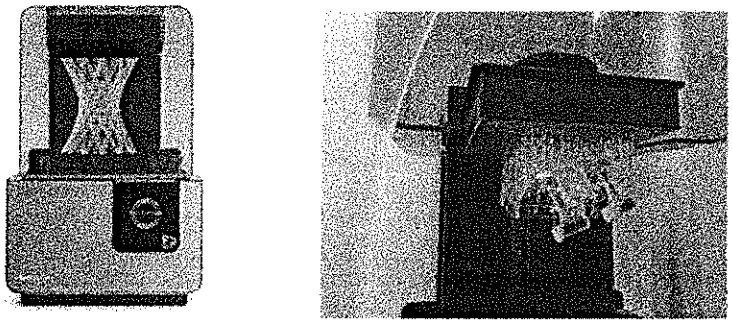

Figura 1 - Stampante FormLabs Form 2. A destra un esempio di componente realizzato dalla stampante.

In effetti l'accrescimento avviene dall'alto verso il basso, partendo da una base metallica piana che fornisce da sostegno. Per ragioni di produzione del pezzo, il software che controlla la stampante (FormLabs PreForm), aggiunge dei sostegni a traliccio come si vede sia in Figura 1 che in Figura 2.

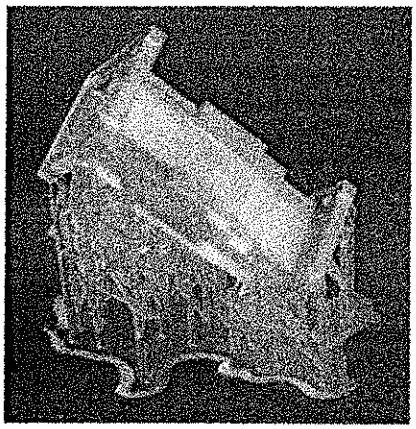

Figura 2 - Dettaglio di un OrthoMode Transducer (OMT) realizzato con le tecniche di Additive Manufacturing. Si notano i sostegni aggiunti dal software di stampa

I sostegni sono necessari perché, altrimenti, la resina potrebbe essere polimerizzata in punti dove non può attaccarsi al componente principale e si formerebbe un grumo di materiale plastico flottante nella resina.

Nella prima fase sono stati realizzati alcuni componenti noti, in modo da poter valutare l'accuratezza meccanica e la ripetibilità, oltre a poter confrontare le caratteristiche con i corrispettivi componenti costruiti mediante tecniche tradizionali. Questi comprendono semplici tratti di guida d'onda, risonatori in guida rettangolare, OMT e filtri a elica.

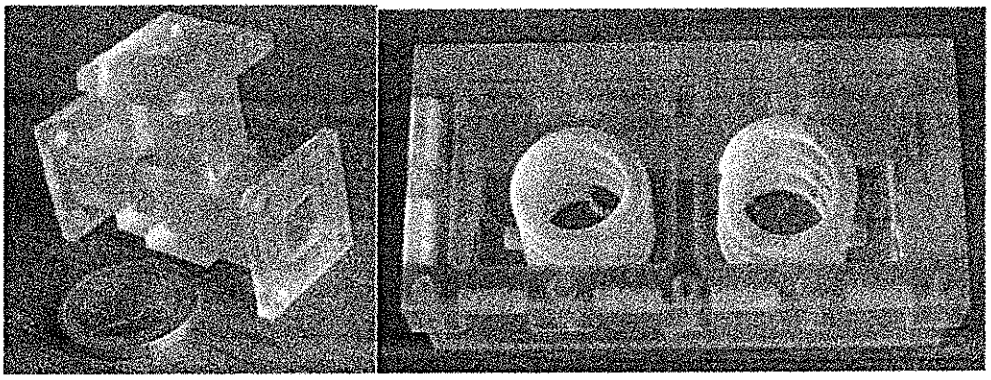

Figura 3 - Esempi di dispositivi. A sinistra un Ortho Mode Transducer, a destra un filtro con risonatori a elica

Dai test effettuati si nota una buona precisione nella realizzazione dei componenti. In particolare sono stati anche valutati gli effetti dell'orientazione del componente da realizzare sulla rugosità. Dato che il materiale viene depositato strato su strato, nelle pareti si formano inevitabilmente delle righe corrispondenti ai vari strati. Per ridurre questo effetto è conveniente ruotare leggermente il componente (con angoli da 30° a 45°), come mostrato in Figura 1 e Figura 2. In questo modo si minimizza il numero di pareti disposte orizzontalmente o verticalmente e la rugosità superficiale dovuta alla stampa 3D diminuisce.
Dopo le prove iniziali, la seconda fase dell'attività ha riguardato la messa a punto di una procedura affidabile per la metallizzazione dei componenti. Sono state prese in considerazione diverse tecniche, in particolare:

1. La deposizione di alluminio vaporizzato si è rivelata insufficiente, sia per lo spessore esiguo della metallizzazione che per la qualità della deposizione. I componenti realizzati con tale tecnica hanno manifestato perdite elevate a microonde. Questa tecnica necessita l'invio dei componenti ad aziende del settore, quindi con un incremento dei costi e dei tempi di attesa;
2. L'uso di vernice d'argento non consente di avere una copertura omogenea delle superfici. I difetti riscontrati sono la rugosità superficiale e la presenza di spazi vuoti senza metallo, lasciati sia in fase di deposito della vernice che in fase di asciugatura;
3. L'uso di vernici spray conduttive si è rivelato anch'esso non adeguato. Le vernici a base di grafite lasciano uno stato ben uniforme ma la resistenza misurata (in corrente continua) è dell'ordine della decina di KOhm, quindi troppo elevata. Le vernici a base di rame, invece, non lasciano uno strato uniforme di metallo, fatto confermato dall'impossibilità di misurare una resistenza in continua mediante tester, per via dell'estrema variabilità del valore indicato a seconda di dove si appoggiano i puntali del tester;
4. La tecnica che si è rivelata migliore è la combinazione della vernice conduttiva di argento con la deposizione elettrolitica di rame. Questa soluzione permette di avere una superficie ad elevata conducibilità e a bassa rugosità, in quanto l'elettrodeposizione del rame tende a livellare la superficie. Inoltre, vengono anche coperti eventuali piccoli buchi lasciati dalla verniciatura. La stessa tecnica è stata provata anche partendo da un substrato di grafite depositato tramite vernice spray, tuttavia la deposizione galvanica che ne deriva non è

uniforme come nel caso della vernice a base d'argento. La spiegazione è da ricercare nell'elevata resistività della grafite che non consente un'uniforme deposizione del rame su tutta la superficie del componente. Appare, inoltre, più difficile la deposizione galvanica del rame sopra l'alluminio vaporizzato del punto 1, poiché sarebbe necessario un ulteriore strato di nichel che fa da collante tra i materiali.

In definitiva la deposizione elettrolitica del rame appare come la soluzione migliore per la metallizzazione di componenti a microonde di plastica, sia per qualità della metallizzazione sia per il fatto di poter fare tutto il processo direttamente in casa. Rimane da valutare bene lo spessore ultimo della metallizzazione, che varia in funzione del tempo di esposizione. Inoltre, in base allo spessore del metallo sarà sicuramente necessario compensare le dimensioni interne dei componenti. Dato che la deposizione galvanica avviene su superfici in precedenza metallizzate con vernici, risulta necessario poter accedere liberamente alle superfici interne dei componenti. Per questo motivo appare sensata la realizzazione dei componenti in parti che saranno poi assemblate dopo la metallizzazione mediante viti di chiusura, come ad esempio per l'OMT in figura:

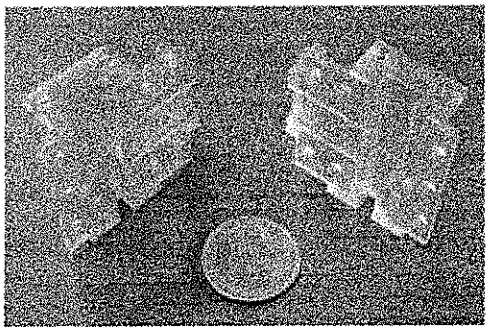

Figura 4 - Ortho Mode Transducer realizzato come due metà da unire tramite viti.

Come prima prova di componente metallizzato è stato considerato un semplice filtro del terzo ordine in guida d'onda rettangolare WR-90:

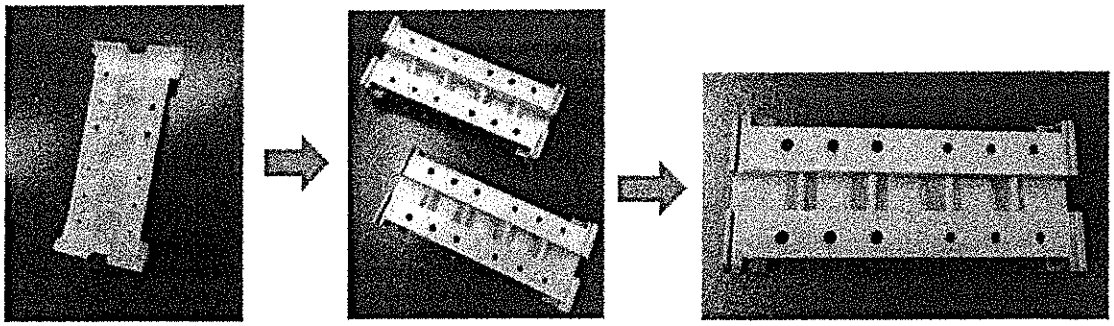

Figura 5 – Filtro del terzo ordine. In figura sono visibili anche le varie fasi di metallizzazione.

Come si vede in Figura 5, dal componente plastico con i supporti rimossi, si passa alla deposizione della vernice a base di argento e alla successiva deposizione elettrolitica di rame che porta al componente finale. Dalle misure effettuate tramite analizzatore vettoriale di reti, risulta una risposta in linea con la simulazione effettuata in precedenza. In particolare la banda è perfettamente centrata e le perdite sono in linea con le simulazioni. Siccome la banda del filtro è del 2% e che l'insertion loss in banda è di circa 0.1dB, il fattore di qualità risultante è pari a circa 6400, un valore più che buono ed in linea con quanto si ottiene mediante i classici processi sottrattivi.

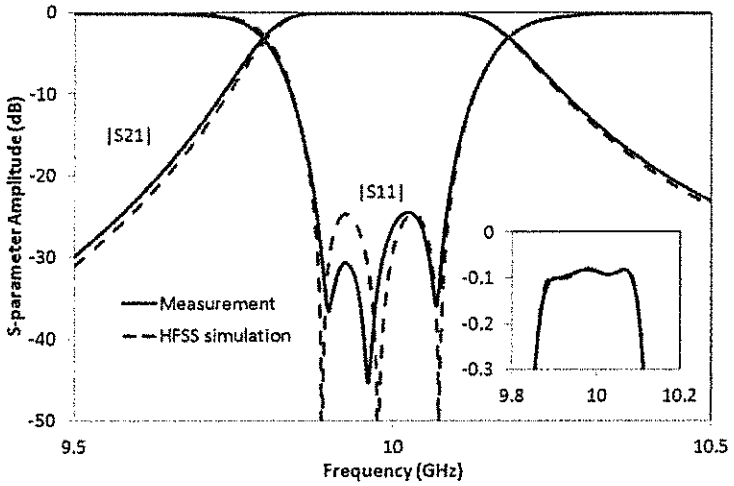

Figura 6 – Risposta in frequenza sperimentale del filtro mostrato in Figura 5.

Sviluppo di componenti innovativi

La seconda parte dell'attività di ricerca è stata concentrata sullo sviluppo di componenti a microonde innovativi che, in particolare, potessero avvantaggiarsi delle tecniche di manifattura additiva. Infatti, la stampa 3D consente di realizzare con relativa facilità delle geometrie che altrimenti sarebbero estremamente complicate, se non impossibili, con le tecnologie classiche o sottrattive.

Come primo esempio è stata sviluppata una famiglia di filtri in guida evanescente con diverse frequenze di funzionamento. I filtri sono particolarmente significativi per testare le prestazioni di una tecnologia costruttiva, poiché sono particolarmente sensibili alle tolleranze meccaniche e ai difetti della metallizzazione, come la rugosità superficiale, che hanno l'effetto di aumentare le perdite d'inserzione. In Figura 7 è raffigurata la struttura di base utilizzata per lo sviluppo di tali filtri.

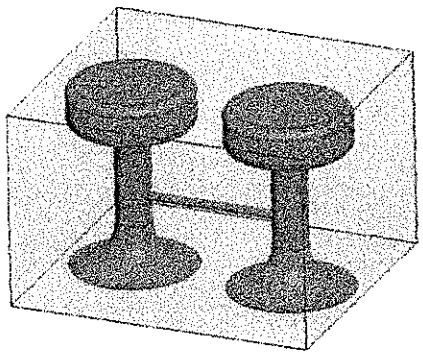

Figura 7 – Struttura di base a due risonatori in guida evanescente.

La struttura di base è composta da una coppia di risonatori inseriti all'interno di una guida sotto taglio (evanescente). La forma dei risonatori, che ricorda dei funghetti, è tale da permettere una notevole riduzione delle dimensioni, sia trasversale che lungo la direzione dei perni. Infatti, i dischi posti in cima ai post metallici permettono di ottenere una capacità relativamente elevata che carica i

post stessi, garantendo una frequenza di risonanza più bassa, a parità di volume complessivo occupato, rispetto al caso di post metallici uniformi. Questa geometria ha anche il vantaggio di allargare la banda soppressa fino alla terza armonica. L'accoppiamento tra i due risonatori è realizzato mediante un filo che connette i post metallici. L'altezza del filo può essere regolata per modificare l'accoppiamento tra i risonatori. Dal grafico di Figura 8 si nota come il modo dispari sia influenzato dalla posizione del filo di collegamento, mentre la frequenza di risonanza del modo pari rimanga praticamente invariata.

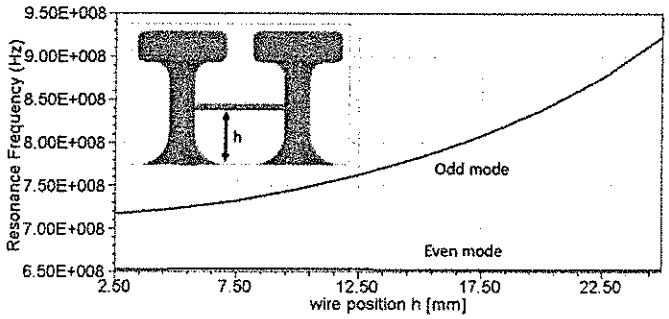

Figura 8 – Frequenze di risonanza pari e dispari.

Questo dimostra il fatto che l'accoppiamento tra i due risonatori, che può essere ricavato dalla formula:

$$k = \frac{f_{odd}^2 - f_{even}^2}{f_{odd}^2 + f_{even}^2}$$

aumenta all'aumentare dell'altezza h alla quale si connette il filo.
L'accoppiamento con l'esterno avviene mediante il collegamento di due cavi coassiali direttamente sul filo di interconnessione tra le cavità. Questa particolare soluzione consente di ottenere anche degli zeri di trasmissione, come si vede in Figura 9.

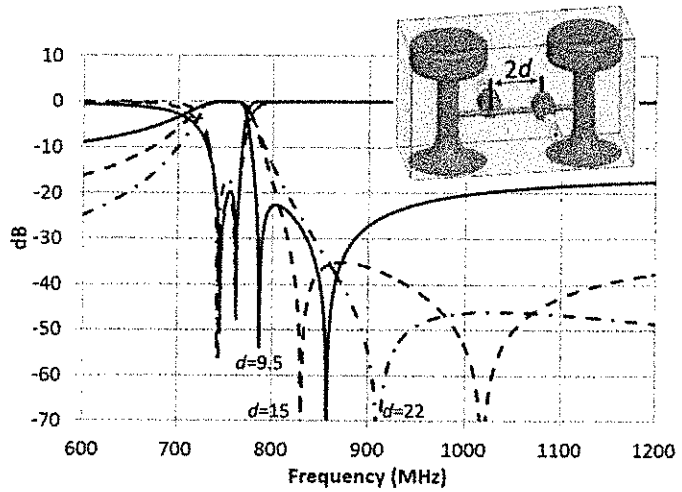

Figura 9 – Spostamento degli zeri di trasmissione al variare della distanza dei coassiali di ingresso/uscita

In particolare è mostrato come variando la distanza tra i punti di connessione dei coassiali, si ha uno spostamento dei due zeri di trasmissione posti a destra della banda passante.
Un semplice filtro a due cavità così progettato è stato costruito mediante la stampante 3D a disposizione del dipartimento.

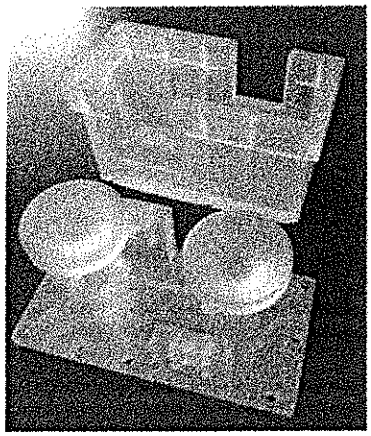

Figura 10 – Filtro a due cavità stampate in materiale plastico

Come si vede dalla Figura 10, il componente è stato realizzato in due parti, la base con i risonatori attaccati e il coperchio.
Per la metallizzazione delle superfici interne del componente è stato utilizzato il metodo illustrato in precedenza che consiste in una prima deposizione di una vernice conduttiva a base di argento seguita da una deposizione elettrolitica di rame.

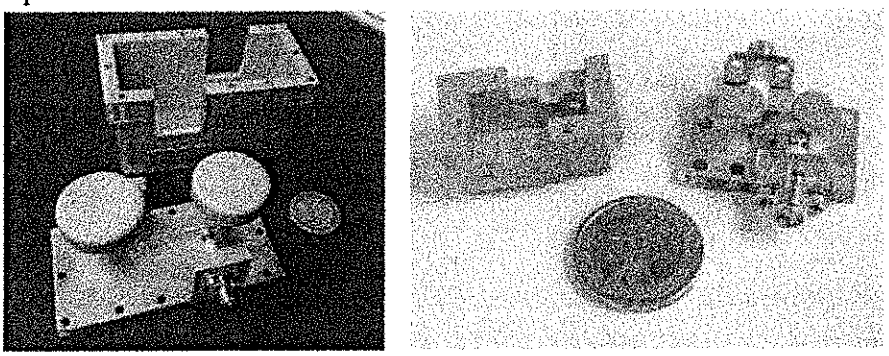

Figura 11 – Filtro a due cavità metallizzato funzionante a 750 MHz (sinistra) e a 2.8 GHz (Destra)

In Figura 11 si vede il componente finale con il rame depositato. Sono stati realizzati diversi prototipi dello stesso filtro, funzionanti a frequenze diverse, semplicemente scalando le varie dimensioni. Questo per verificare la ripetibilità della realizzazione anche quando si aumentano le frequenze di lavoro. I due filtri realizzati hanno una frequenza di centro banda di 750 MHz e 2.8 GHz ed una banda passante del 2.2% in entrambi i casi.

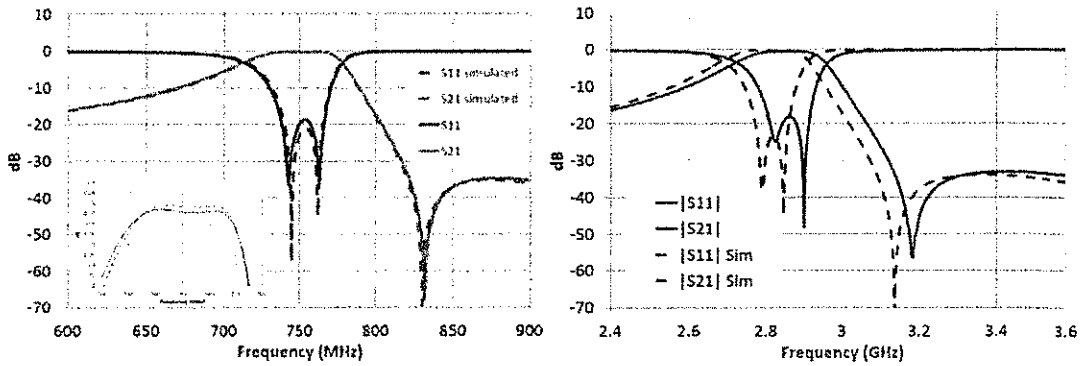

Figura 12 – Risposta in frequenza del filtro a 750 MHz (sinistra) e del filtro a 2.8 GHz (destra)

In Figura 12 sinistra è visibile la risposta in frequenza del filtro a 750 MHz. La banda è ben centrata con quanto simulato perché sono stati utilizzati due elementi di sintonia per regolare la frequenza di

risonanza delle cavità. Gli accoppiamenti, invece, non sono stati toccati. Si vede una sovrapposizione quasi perfetta tra le curve. Le perdite misurate in banda passante sono leggermente superiori a quanto simulato, per effetto, molto probabilmente, della rugosità dovuta sia alla stampa sia alla deposizione del metallo.
In Figura 12 destra è raffigurata la risposta in frequenza del filtro funzionante a 2.8 GHz. In questo caso non sono stati utilizzati elementi di sintonia per aggiustare la frequenza di risonanza delle cavità. Lo spostamento in frequenza osservato, comparabile con quanto ottenuto sul precedente filtro prima della sintonia, è davvero molto piccolo (minore del 2%). Lo spostamento è avvenuto verso le alte frequenze, segno di un accorciamento dei post interni alla cavità, dovuto probabilmente ad una riduzione di volume della resina durante la sua essiccazione. Anche in questo caso le perdite misurate sono leggermente superiori a quelle simulate, sempre per effetto della rugosità.
La struttura illustrata sopra è stata ulteriormente affinata utilizzando dei risonatori accoppiati mediante la tecnica del mixed coupling. Tale tecnica consente di aggiungere degli zeri di trasmissione senza la necessità di realizzare cross coupling tra i risonatori. La tecnica tradizionale del cross coupling crea più percorsi tra ingresso ed uscita. I segnali che viaggiano nei vari percorsi interferiscono tra loro creando degli zeri di trasmissione nella risposta in frequenza del filtro. La tecnica del mixed coupling o electric and magnetic coupling, invece, utilizza un accoppiamento sia induttivo che capacitivo tra due risonatori adiacenti in modo tale che, ad una specifica frequenza, l'accoppiamento complessivo risulti risonante, creando quindi lo zero desiderato.
La struttura di base presa in considerazione per tale scopo è mostrata in Figura 13.

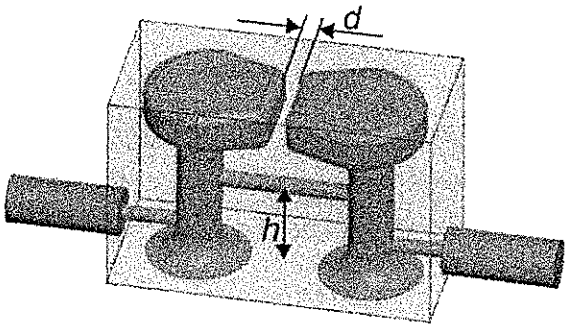

Figura 13 – Struttura di base a due risonatori accoppiati con l'esterno.

La struttura di base è formata da due risonatori inseriti all'interno di una guida sotto taglio (evanescente). I risonatori sono caricati con una capacità finale che ha l'effetto di ridurre la loro lunghezza a parità di frequenza di risonanza. L'accoppiamento tra i due risonatori avviene mediante due meccanismi. L'accoppiamento induttivo si ottiene mediante la presenza del filo che connette i perni. Esso può essere regolato variando l'altezza *h* del filo, in particolare, maggiore è l'altezza *h* più grande è l'accoppiamento induttivo tra i due risonatori. L'accoppiamento capacitivo è invece ottenuto mediante il gap di spessore *d* tra i cappelli dei risonatori. In questo caso, minore è la distanza *d* tra i cappelli maggiore è l'accoppiamento capacitivo. Da notare che i perni di base dei risonatori rimangono sempre alla stessa distanza.
Con questa tecnica è stato sintetizzato un filtro a quattro cavità (Figura 14).

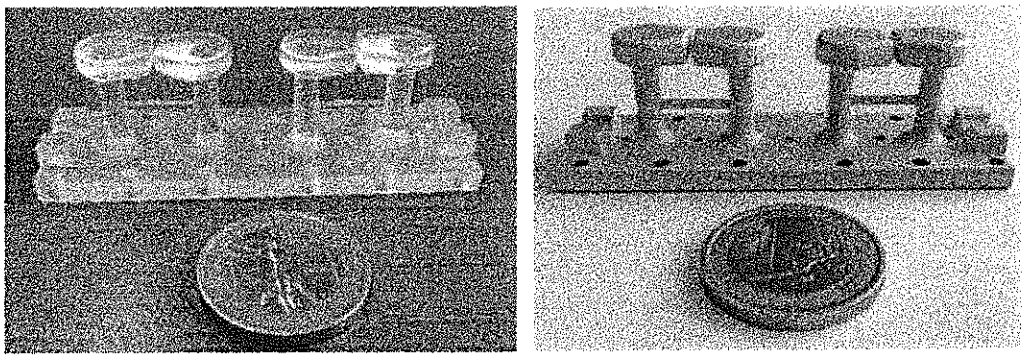

Figura 14 – Parte interna del filtro a 4 poli 2 zeri realizzato prima e dopo la metallizzazione.

Il filtro è stato misurato utilizzando l'analizzatore vettoriale di reti Keysight N5230A disponibile in dipartimento ed il risultato è mostrato in Figura 15.

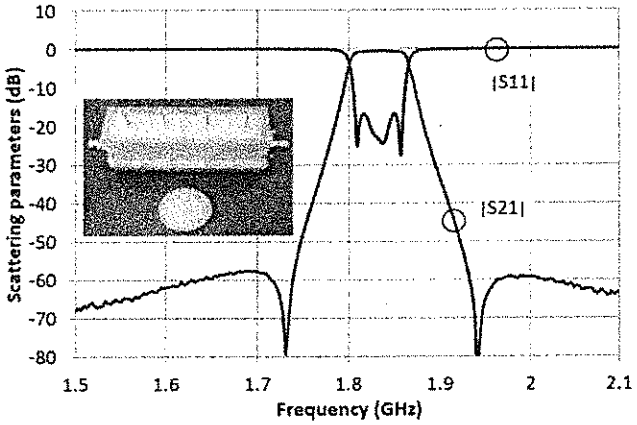

Figura 15 – Risposta sperimentale del filtro realizzato.

Da notare che, per compensare lo spostamento della risposta dovuta alle tolleranze meccaniche di produzione, sono state utilizzate anche delle viti M2 in corrispondenza dei risonatori e degli accoppiamenti.

Di particolare interesse anche la risposta del filtro a banda larga, dato che questa tipologia di filtri ha una soppressione delle spurie fino a frequenze superiori a 3*f0.

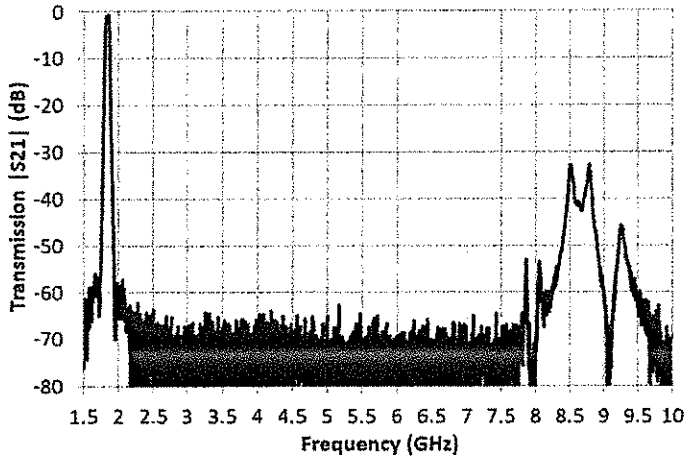

Figura 16 – Risposta sperimentale a banda larga del filtro realizzato.

Come si vede dalla Figura 16, il filtro garantisce la soppressione delle spurie fino a circa 8 GHz, quindi fino alla quarta armonica.
L'ultima tipologia di filtri studiata sono i filtri coassiali in linea come quelli raffigurati in Figura 7.

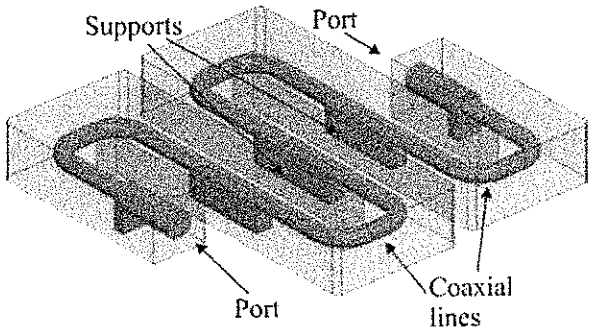

Figura 17 - Struttura dei filtri coassiali in linea.

La struttura è formata da una cascata di cavità coassiali, che possono essere anche ripiegate come in figura per occupare meno spazio. Le linee di trasmissione che formano tali risonatori sono ovviamente delle linee TEM. La linea coassiale deve essere sostenuta il qualche modo e questo avviene mediante l'uso di alcuni supporti metallici, indicati sempre in Figura 17. Tali supporti metallici funzionano come elementi di accoppiamento tra i risonatori, quindi sono utilizzati per fissare la banda ed il return loss dei filtri.
Per ridurre ulteriormente lo spazio occupato, sono stati inoltre sintetizzati dei filtri che utilizzano dei risonatori di tipo SIR (Stepped Impedance Resonator), ovvero risonatori con una linea coassiale con salti di impedenza caratteristica, e filtri con risonatori lunghi $\lambda/4$ (Figura 18).

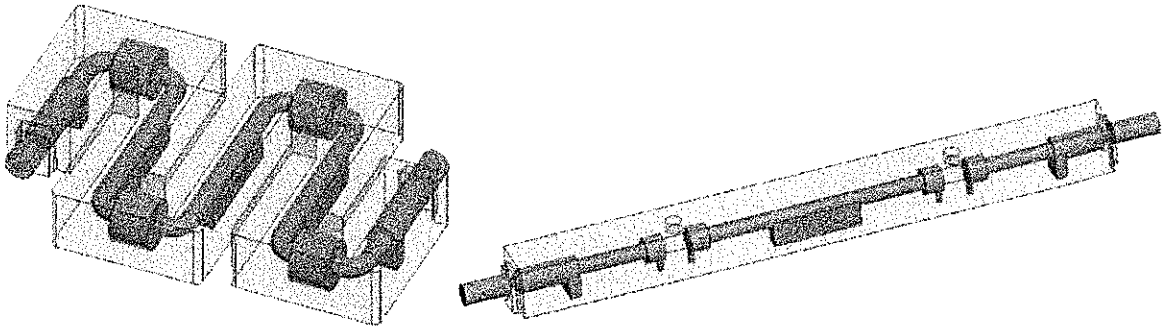
Figura 18 – Filtro con risonatori SIR (sinistra) e con risonatori λ/4 (destra).

Nel primo caso, la variazione di impedenza caratteristica della linea permette di ottenere un risonatore più corto di $\lambda/2$, pur mantenendo la stessa frequenza di risonanza. Nel secondo caso, la lunghezza dei risonatori è di fatto dimezzata rispetto al progetto iniziale, grazie al fatto che un capo del coassiale viene lasciato a circuito aperto. Un altro grosso vantaggio di queste soluzioni consiste nello spostare la risonanza del primo modo superiore a frequenze molto alto, tipicamente superiori alla 3*f0.
Tutti questi filtri sono stati costruiti utilizzando la tecnica additiva illustrata in precedenza.

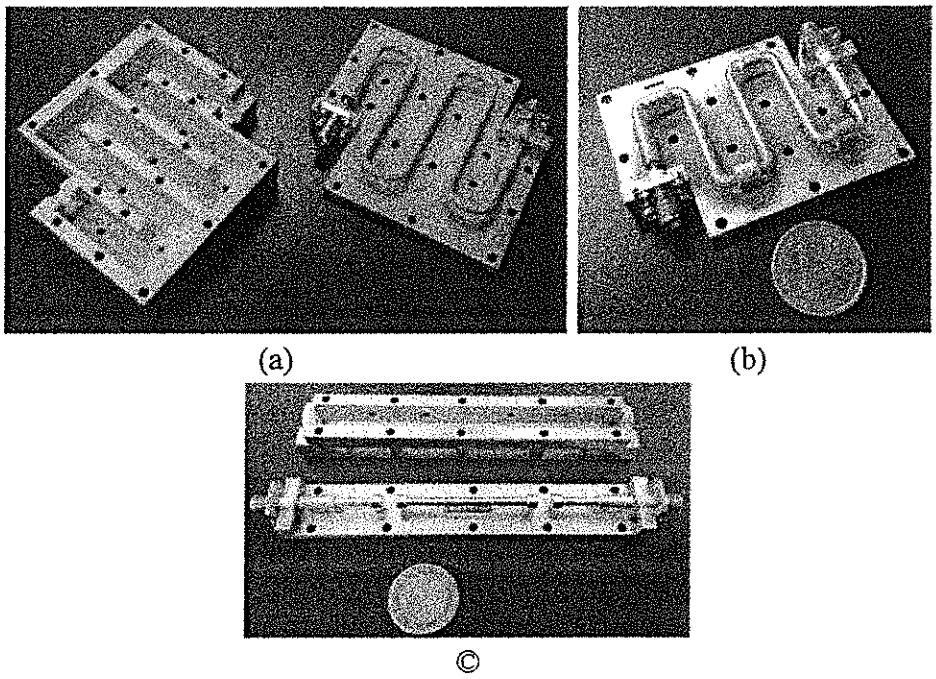

Figura 19 – Foto dei vari filtri a risonatori coassiali realizzati. (a) filtro con risonatori a λ/2, (b) filtro con «stepped impedance resonators», (c) filtro con risonatori a λ/4

In Figura 20 sono mostrati i confronti tra le simulazione e i risultati sperimentali per i vari filtri a risonatori coassiali.

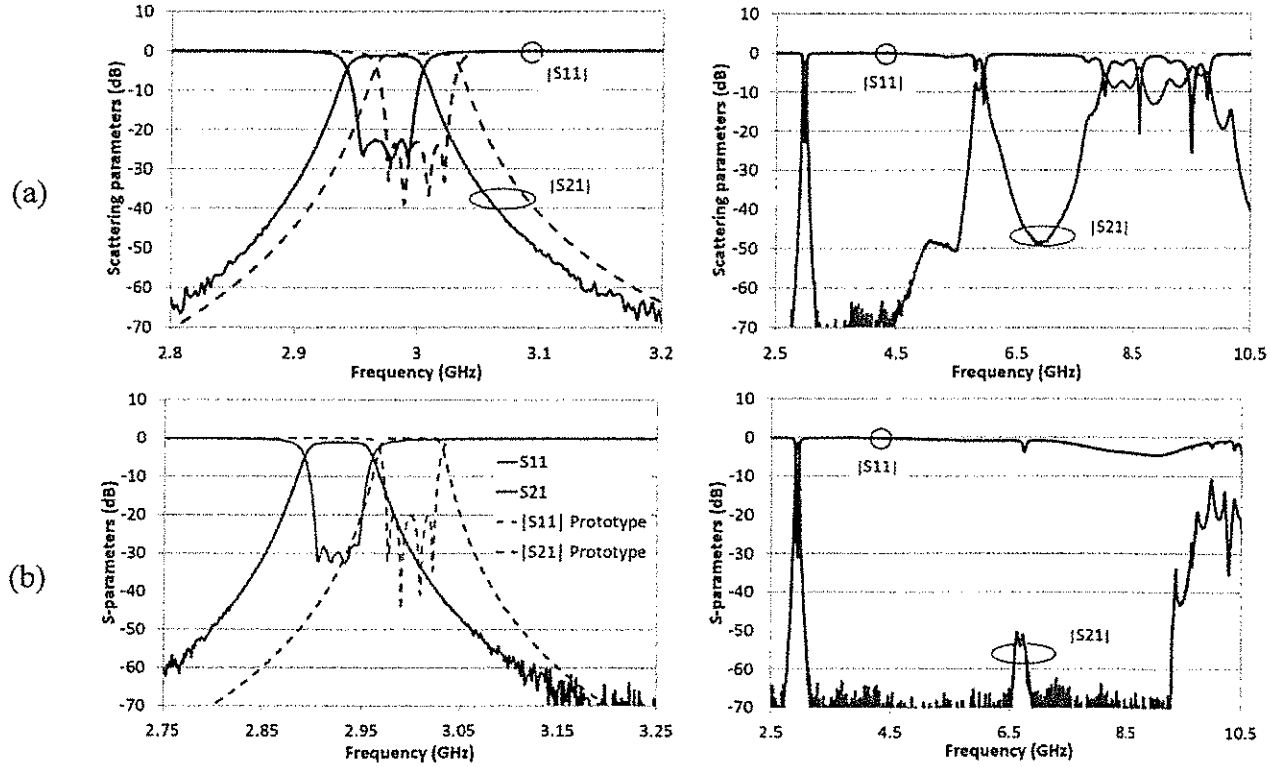

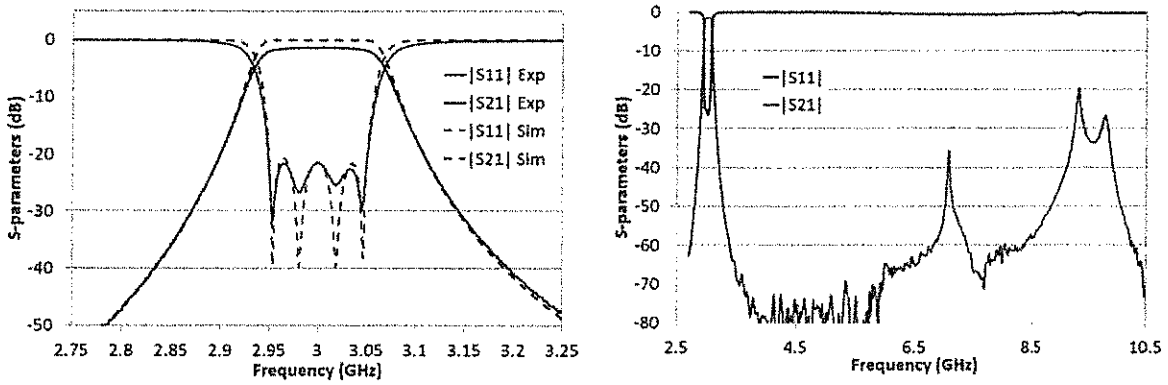

Figura 20 – Confronto tra risposta sperimentale e simulazione dei filtri coassiali realizzati. (a) filtro con risonatori a λ/2, (b) filtro con stepped impedance resonators, (c) filtro con risonatori a λ/4. (sinistra) Risposta in banda, (destra) Risposta fuori banda

Dai grafici si vede come il comportamento fuori banda sia molto migliore quando si usano risonatori SIR o λ/4, rispetto al progetto originale con risonatori λ/2.

Elenco pubblicazioni del periodo 20/6/2016 – 20/6/2019

Pubblicazioni su rivista:

1. G. G. Gentili, A. Morini, G. Pelosi, S. Selleri, G. Venanzoni, *"Modular Reciprocal Multiplexers"*, International Journal of RF and Microwave Computer-Aided Engineering, Vol. 26, No. 6, August 2016, pp. 538-546, DOI: 10.1002/mmce.21000
2. M. Farina, F. Piacenza, F. De Angelis, D. Mencarelli, A. Morini, G. Venanzoni, T. Pietrangelo, M. Malavolta, A. Basso, M. Provinciali, J. C. M. Hwang, X. Jin and A. Di Donato, *"Investigation of Fullerene Exposure of Breast Cancer Cells by Time-Gated Scanning Microwave Microscopy"*, IEEE Transactions on Microwave Theory and Techniques, Vol. 64, No. 12, pp. 4823-4831, Dec. 2016, DOI: 10.1109/TMTT.2016.2623312
3. A. Morini, M. Farina, M. Guglielmi, P. Angeletti, P. Iglesias, G. Venanzoni, *"Generalized Thru-Reflect-Line Calibration Technique for the Measurement of Multimodal Radiating Waveguides"*, IEEE Antennas and Wireless Propagation Letters, Vol. 16, No. 1, 2017, pp. 844-847, DOI: 10.1109/LAWP.2017.2683940
4. M. Dionigi, C. Tomassoni, G. Venanzoni, R. Sorrentino, *"Simple High-Performance Metal-Plating Procedure for Stereolithographically 3-D-Printed Waveguide Components"*, IEEE Microwave and Wireless Components Letters, Vol. 27, No. 11, Nov. 2017, pp. 953-955, DOI: 10.1109/LMWC.2017.2750090
5. G. Venanzoni, M. Dionigi, C. Tomassoni, R. Sorrentino, *"3-D-Printed Quasi-Elliptical Evanescent Mode Filter Using Mixed Electromagnetic Coupling"*, IEEE Microwave and Wireless Components Letters, Vol. 28, No. 6, Jun. 2018, pp. 497-499, DOI: 10.1109/LMWC.2018.2829627
6. A. Morini, G. Venanzoni, M. Farina, M. Villa, *"A Method for Fast and Reliable Analysis and Optimization of Side-Coupled Cavity Filters and Multiplexers"*, IEEE Transactions on Microwave Theory and Techniques, Vol. 66, No. 8, pp. 3847-3586, Aug. 2018, DOI: 10.1109/TMTT.2018.2841833
7. C. Tomassoni, G. Venanzoni, M. Dionigi, R. Sorrentino, *"Compact quasi-elliptic filters with mushroom-shaped resonators manufactured with 3-D printer"*, IEEE Transactions on Microwave

Theory and Techniques, Vol. 66, No. 8, pp. 3579-3588, Aug. 2018, DOI: 10.1109/TMTT.2018.2849067

8. A. Morini, G. Venanzoni, P.M. Iglesias, C. Ernst, N. Sidiropoulos, A. Di Donato, M. Farina, *"Systematic Evaluation of Spikes Due to Interference Between Cascaded Filters"*, IEEE Transactions on Microwave Theory and Techniques, Vol. 66, No. 11, pp. 4814-4819, Nov. 2018, DOI: 10.1109/TMTT.2018.2865568
9. G. Venanzoni, D. Mencarelli, A. Morini, M. Farina, F. Prudenzano, "Review of substrate integrated waveguide circuits for beam-forming networks working in X-band", Applied Sciences, Vol. 9, no. 5, 2019, Article number 1003, DOI: 10.3390/app9051003
10. O. Losito, V. Portosi, G. Venanzoni, F. Bigelli, D. Mencarelli, P. Scalmati, C. Renghini, P. Carta, F. Prudenzano, "Feasibility investigation of SIW cavity-backed patch antenna array for Ku band applications", Vol. 9, no. 7, 2019, Article number 1271, DOI: 10.3390/app9071271

Pubblicazioni in atti di convegno:

1. M. Longhi, J. Galdeano, A. Morini, M. Baldelli, P. Angeletti, G. Toso, G. Venanzoni, *"Dual-polarization beam forming networks based on high order directional couplers"*, 11th European Conference on Antennas and Propagation (EUCAP), Paris, France, 2017, pp. 2820-2823. DOI: 10.23919/EuCAP.2017.7928694
2. C. Tomassoni, M. Bozzi, M. Dionigi, G. Venanzoni, L. Perregrini and R. Sorrentino, *"Additive manufacturing of microwave components: Different approaches and methodologies"*, 2017 International Conference on Electromagnetics in Advanced Applications (ICEAA), Verona, 2017, pp. 848-851. DOI: 10.1109/ICEAA.2017.8065384
3. T. Rozzi, M. Mongiardo, F. Mastri, D. Mencarelli, G. Monti and G. Venanzoni, *"Electromagnetic field modeling through the use of Dirac matrices and geometric algebra"*, 2017 International Conference on Electromagnetics in Advanced Applications (ICEAA), Verona, 2017, pp. 757-760. DOI: 10.1109/ICEAA.2017.8065359
4. G. Venanzoni, M. Dionigi, C. Tomassoni, D. Eleonori and R. Sorrentino, *"3D printing of X band waveguide resonators and filters"*, 32nd General Assembly and Scientific Symposium of the International Union of Radio Science (URSI GASS), Montreal, QC, Canada, 2017, pp. 1-2. DOI: 10.23919/URSIGASS.2017.8105407
5. G. Venanzoni, C. Tomassoni, M. Dionigi, R. Sorrentino, *"Stereolitographic 3D Printing of Compact Quasi-Elliptical-Filters"*, IEEE MTT-S International Microwave Workshop Series on Advanced Materials and Processes (IMWS-AMP 2017), 20-22 September 2017, Pavia, Italy
6. C. Tomassoni, G. Venanzoni, M. Dionigi, R. Sorrentino, *"Compact Doublet Structure for Quasi-Elliptical Filters using Stereolitographic 3D Printing"*, in Proc. of 47th European Microwave Conference, 10-12 Oct. 2017, Nuremberg, Germany, pp. 993-996
7. G. Venanzoni, C. Tomassoni, M. Dionigi, R. Sorrentino, *"Stereolitographic 3D printing of compact quasi-elliptical filters"*, 2017 IEEE MTT-S Int. Microw. Workshop Series on Adv. Materials and Processes for RF and THz Appl. IMWS-AMP 2017, DOI: 10.1109/IMWS-AMP.2017.8247388
8. A.Morini M. Baldelli, P. Angeletti, D. Petrolati, G. Toso, G.Venanzoni, *"Directional coupler with 3 input / 3 output square waveguide dual-polarization ports"*, 12th European Conference on Antennas and Propagation (EuCAP 2018), London (UK), 9-13 Apr 2018
9. M. Dionigi, C. Tomassoni, G. Venanzoni, R. Sorrentino, *"Innovative Filter Structure in 3D printing Technology"*, 2nd URSI AT-RASC, Gran Canaria, 28 May – 1 June 2018

10. C. Tomassoni, G. Venanzoni, M. Dionigi, R. Sorrentino, *"A Very Compact 3D-Printed Doublet Structure based on Double Iris and a Pair of Slanting Rods"*, IEEE/MTT-S International Microwave Symposium, IMS 2018, Philadelphia, US, 10-15 Jun 2018, pp. 1103-1105, DOI: 10.1109/MWSYM.2018.8439368
11. C. Tomassoni, G. Venanzoni, M. Dionigi, R. Sorrentino, *"Additive Manufacturing of a Very Compact Doublet Structure with Asymmetric Filtering Function"*, IEEE/MTT-S International Microwave Workshop Series on Advanced Materials and Processes for RF and THz Applications (IMWS-AMP 2018), Ann Arbor, MI, USA, 16-18 Jun 2018, pp. 1-3, DOI: 10.1109/IMWS-AMP.2018.8457127
12. G. Venanzoni, M. Dionigi, C. Tomassoni, R. Sorrentino, *"Design of a Compact 3D Printed Coaxial Filter"*, Proc. Of the 48th European Microwave Conference (EuMC 2018), 25-27 Sept. 2018, Madrid (Spain), pp. 280-283

Perugia 20/6/2019

Il responsabile scientifico
Prof. Mauro Mongiardo

Giuseppe Venanzoni

Allegato N. 1 al punto
dell'ordine del giorno N. 15.B.1

Al Consiglio del Dipartimento di Ingegneria

Oggetto: Richiesta di un posto di Ricercatore tempo determinato ex art. 24, comma 3, lettera a) – SC 09/C1 SSD ING-IND/08

Il sottoscritto Linda Barelli, in qualità di Responsabile scientifico di Unità di Ricerca del progetto PRIN protocollo 2017F4S2L3_005 ammesso a finanziamento con Decreto Direttoriale MIUR **n. 1162 del 17/06/2019** e per il quale a seguito di rimodulazione del Coordinatore Scientifico è assegnato all'unità di ricerca il Contributo Miur pari a € 147.400 e Co-finanziamento di ateneo pari a € 29.000 (per un costo totale di €176.400), per le seguenti esigenze di ricerca di tale progetto pone all'attenzione del Consiglio del Dipartimento la necessità di chiedere al Consiglio di Amministrazione l'autorizzazione alla copertura di un posto di ricercatore tempo determinato **tempo definito** ex art. 24, comma 3, lettera a) – SC 09/C1 SSD ING-IND/08 per un periodo di tre anni, eventualmente prorogabile per ulteriori due**,** al fine di poter realizzare il progetto di ricerca HERMES - High Efficiency Reversible technologies in fully renewable Multi-Energy System.
Il costo complessivo del ricercatore a tempo determinato pari ad €112.085,13 verrà coperto con i fondi esterni derivanti dal finanziamento del PRIN HERMES - High Efficiency Reversible technologies in fully renewable Multi-Energy Systemalla voce COAN 07.70.01.01.01 "costi operativi progetti-quota di competenza per finanziamenti competitivi da miur – progetti di ricerca di rilevante interesse nazionale" - UA.PG.DING. PRIN_2017BARELLI.

Nel rispetto del Regolamento per l'assunzione di ricercatori a tempo determinato ai sensi della Legge 30.12.2010 n. 240 si forniscono di seguito le seguenti informazioni:

A) SETTORE CONCORSUALE**: 09/C1**

B) Profilo: SETTORE/I SCIENTIFICO DISCIPLINARE/I: ING-IND/08

C) ATTIVITA' DI RICERCA**:**

- Titolo del progetto in italiano: Analisi delle prestazioni di celle a ossidi solidi reversibili per la generazione elettrica e l'elettrolisi

- Titolo del progetto in inglese: Performance analysis of reversible solid oxide cells for power generation and electrolysis.

- Descrizione dell'attività di ricerca in italiano:
In accordo all'attività prevista per l'Unità di Ricerca dell'Università degli Studi di Perugia nell'ambito del progetto PRIN HERMES sopra citato, l'attività di ricerca sarà focalizzata sull'analisi sperimentale delle prestazioni di celle a ossidi solidi. Per quanto al funzionamento in modalità diretta (cella a combustibile) saranno analizzate differenti condizioni operative, incluse differenti modalità di alimentazione. Sarà inoltre investigato sperimentalmente il funzionamento reversibile in accordo a specifici ciclaggi con fase di generazione elettrica ed elettrolisi, quale efficiente tecnologia reversibile da implementare in sistemi energetici multi vettore ad elevata flessibilità.

The research activity is scheduled according to HERMES project tasks leaded by University of Perugia. Therefore, the attention is focused on the experimental characterization of solid oxide cells performance. Regarding the direct working mode (fuel cell) different operating conditions will be investigated, including several feeding conditions. Also the reversible working mode will be studied under specific fuel cell/electrolysis cycles, as an efficient reversible technology to be implemented in multy-energy systems with high flexibility.

Docente referente: Linda Barelli.

D) ATTIVITA' DIDATTICA, DIDATTICA INTEGRATIVA E SERVIZIO AGLI STUDENTI: 200 ore annue (regime a tempo definito) prevalentemente nell'ambito del SSD di cui alla lett. **B)**, di cui non più di 5 ore per attività di didattica ufficiale*;

E) Sede di servizio: Dipartimento di Ingegneria.

F) Lingua straniera: Inglese.

G) Numero massimo di pubblicazioni: 12.

H) REQUISITI DI AMMISSIONE ALLA VALUTAZIONE COMPARATIVA SONO:

- titolo di dottore di ricerca in Ingegneria Industriale e dell'Informazione o titolo equivalente.
- Esperienza maturata nel campo della ricerca comprovante il possesso di solide competenze di base nel SSD ING-IND/08

Prof. Linda Barelli

UNIVERSITA' DEGLI STUDI DI PERUGIA * DIPARTIMENTO DI INGEGNERIA

UNIVERSITA DEGLI STUDI DI PERUGIA
Dipartimento di Ingegneria

D.S.A. n. 24/2019

Il Segretario Amministrativo

Disposizioni per il finanziamento di 1 posto da Ricercatore TD SSD ING IND/08 Resp. prof. ssa Linda Barelli **Autorizzazione Ufficio Stipendi pagamento mensilità**

VISTA la Legge n. 240/2010;
VISTO l'art. 32 del vigente Regolamento per l'amministrazione, la finanza e la contabilità dell'Università degli Studi di Perugia;
VISTA la nota del Dirigente della Ripartizione Gestione Risorse Finanziarie prot. N. 3449 del 03.02.2015 recante "*Note operative U.GOV – modalità di attivazione/proroga/rinnovi assegni di ricerca ...*"
VISTA la direttoriale prot. n. 92123 del 15/12/2016 relativa alle nuove modalità *attivazione/proroga/rinnovi assegni di ricerca e ricercatori TD* dalla quale si evince chiaramente che per la richiesta inoltra dalla Prof.ssa Linda Barelli rientra nella nuova modalità;
VISTA la richiesta inoltrata dalla Prof.ssa Linda Barelli - per l'attivazione delle procedure necessarie all'emanazione di un bando per l'assunzione di un ricercatore universitario, con rapporto di lavoro subordinato a tempo determinato, con regime di impegno a tempo definito, ai sensi e per gli effetti dell'art.24, comma3, lettera a) della Legge 240/2010, SC 09/C1 SSD ING-IND/08, per un periodo di tre anni, eventualmente prorogabile per ulteriori due;
VISTA la delibera n. 15bis/1 del 8/07/2019, con cui il Consiglio di Dipartimento ha autorizzato le procedure necessarie all'emanazione di un bando per l'assunzione di un ricercatore TD proposto dalla prof.ssa Linda Barelli;
CONSIDERATO che la copertura finanziaria per il costo per il suddetto posto da ricercatore TD pari ad € 112.085,13 (centododicimilaottantacinque/13) per la durata di tre anni, non graverà sull'F.F.O. ma graverà interamente su fondi appostati sulla macrovoce "Finanziamento Ricercatori TD" nella voce di costo: COAN 07.70.01.01.01 - Costi operativi progetti – quota di competenza per finanziamenti competitivi da MIUR - progetti di ricerca di rilevante interesse nazionale - PJ.UA.PG.DING.PRIN_2017BARELLI di cui la richiedente è responsabile scientifico;
RITENUTO necessario procedere alle relative variazioni al Bilancio Unico di Ateneo di previsione annuale autorizzatorio dell'esercizio 2019;

DECRETA

1) di autorizzare l'Ufficio Stipendi al pagamento delle mensilità spettante al vincitore del bando di riferimento a gravare su fondi appostati sulla macrovoce "Finanziamento Ricercatori TD": PJ UA.PG.DING PRIN_2017BARELLI per un totale di € 112.085,13 di cui è la responsabile la Prof.ssa Linda Barelli.
2) di trasmettere scansione dell'originale del presente decreto al Collegio dei Revisori dei Conti, come previsto dall'art. 32 del vigente Regolamento per l'amministrazione, la finanza e la contabilità, richiamato in premessa.

Il presente decreto sarà portato a conoscenza del Consiglio di Dipartimento nella prima seduta utile.
Perugia, 9/07/2019

Il Segretario Amministrativo
(Giovanni Magara)

Ministero dell'Istruzione, dell'Università e della Ricerca

Dipartimento per la Formazione Superiore e per la Ricerca

Direzione Generale per il Coordinamento, la Promozione e la Valorizzazione della Ricerca

IL DIRETTORE GENERALE

VISTO il Decreto Legge n. 85 del 16 maggio 2008 convertito, con modificazioni, in Legge n.121 del 14 luglio 2008, istitutivo, tra l'altro, del Ministero dell'Istruzione, dell'Università e della Ricerca;

VISTO l'articolo 1, comma 870, della legge 27 dicembre 2006, n. 296 (legge finanziaria 2007), che istituisce nello stato di previsione della spesa del MIUR il Fondo per gli investimenti nella ricerca scientifica e tecnologica (FIRST);

VISTO il protocollo d'intesa MIUR-IIT-MEF del 27 dicembre 2017, firmato dal Ministro dell'Istruzione, dell'Università e della Ricerca, dal Ministro dell'Economia e delle Finanze e dal Presidente dell'Istituto Italiano di Tecnologia, con il quale sono stati destinati Euro 250.000.000,00 al finanziamento di progetti scientifici ricadenti nei macrosettori scientifici dell'European Research Council identificati con le sigle PE (Scienze fisiche, chimiche, ingegneristiche) e LS (Scienze della vita);

VISTO il D.D. n. 594 del 26 luglio 2016 con il quale sono state definite le procedure per gli interventi diretti al sostegno delle attività di ricerca fondamentale, a norma degli articoli 60, 61, 62 e 63 del decreto-legge 22 giugno 2012, n. 83, convertito, con modificazioni, dalla legge 7 agosto 2012, n. 134, nell'ambito degli atenei e degli enti pubblici di ricerca afferenti al MIUR;

VISTO il D.D. n. 3728 del 27 dicembre 2017 con il quale è stato emanato il bando destinato al finanziamento di Progetti di ricerca di Rilevante Interesse Nazionale (PRIN), diviso in tre linee d'intervento: a) "linea d'intervento Principale"; b) "linea d'intervento Giovani"; c) "linea d'intervento Sud";

VISTO il D.D. n. 1039 del 27 aprile 2018 con cui il MIUR, nel rispetto delle procedure di cui predetto art. 3 del D.D. n. 3728 del 27 dicembre 2017, ha determinato le disponibilità economiche per linea di intervento e settore ERC;

CONSIDERATO che, con il predetto D.D. n. 1039 del 27 aprile 2018, al settore PE8 sono state assegnate le seguenti disponibilità economiche, così suddivise per linea d'intervento:

a) Linea A: Euro 22.000.000,00;
b) Linea B: Euro 2.114.119,00;
c) Linea C: Euro 6.784.100;

VISTO il D.D. n. 453 del 13 marzo 2019, e relativi allegati (registrato alla Corte dei Conti il 26 aprile 2019 reg. n. 1-878), con il quale sono stati approvati, nell'ambito del settore PE8:

- n. 33 progetti della Linea A per un finanziamento totale di Euro 22.000.000,00;
- n. 5 progetti della Linea B per un finanziamento totale di Euro 2.114.119,00;
- n. 13 progetti della Linea C per un finanziamento totale di Euro 6.784.100,00;

stabilendo altresì il termine del 5 aprile 2019 per la presentazione, da parte dei coordinatori nazionali, delle rideterminazioni dei costi e dei contributi spettanti alle singole unità di ricerca, sulla base dei costi congrui definiti (per ogni progetto) dal Comitato di Selezione, e riportati nell'allegato B dello stesso decreto;

VISTO l'art. 4 del predetto D.D. n. 453 del 13 marzo 2019 con il quale si definiscono le fonti di finanziamento per ciascuna linea di intervento nell'ambito del settore PE8;

CONSIDERATE le rideterminazioni dei costi e dei contributi spettanti alle singole unità di ricerca, anche alla luce dei trasferimenti intervenuti ai sensi dell'art. 7, comma 4 della Legge n. 240/2010;

RITENUTO di procedere alla conseguente ammissione a contributo dei progetti approvati, con le ripartizioni dei costi e dei contributi per singola unità di ricerca stabilite dai coordinatori nazionali, al fine di consentire, nel rispetto di quanto stabilito dall'art. 6, comma 6 del Bando PRIN 2017, il successivo trasferimento ad ogni singolo ateneo/ente pubblico di ricerca della quota di contributo spettante, come somma dei singoli contributi relativi alle unità di ricerca ad essi afferenti;

VISTO il D.Lgs. n. 165/2001 e successive modifiche e integrazioni;

VISTO il D.Lgs. 14 marzo 2013, n. 33, recante "Riordino della disciplina riguardante gli obblighi di pubblicità, trasparenza e diffusione di informazioni da parte delle pubbliche amministrazioni";

D E C R E T A

ART. 1

1. La ripartizione dei costi e dei contributi per ogni progetto approvato nell'ambito del settore PE8 è indicata nella tabella di cui all'**Allegato A**, che costituisce parte

integrante ed essenziale del presente decreto. In detta tabella sono indicati il codice Cineca del progetto, il nome del coordinatore nazionale e, in particolare, per ciascuna unità di ricerca, il nome del responsabile di unità, l'ateneo/ente pubblico di ricerca di afferenza, il cofinanziamento, il contributo MIUR per la ricerca, la quota premiale e il contributo totale.

2. L'importo di Euro 22.000.000,00, relativo al finanziamento della linea di intervento A, grava sulle disponibilità di cui al protocollo d'intesa MIUR-IIT-MEF del 27 dicembre 2017, firmato dal Ministro dell'Istruzione, dell'Università e della Ricerca, dal Ministro dell'Economia e delle Finanze e dal Presidente della Fondazione dell'"Istituto Italiano di Tecnologia", con il quale sono stati destinati Euro 250.000.000,00 al finanziamento di progetti scientifici ricadenti nei macrosettori scientifici dell'European Research Council identificati con le sigle PE (Scienze fisiche, chimiche, ingegneristiche) e LS (Scienze della vita).

3. L'importo di Euro 2.114.119,00, relativo al finanziamento della linea di intervento B, grava sulle disponibilità di cui al protocollo d'intesa MIUR-IIT-MEF del 27 dicembre 2017, firmato dal Ministro dell'Istruzione, dell'Università e della Ricerca, dal Ministro dell'Economia e delle Finanze e dal Presidente della Fondazione dell'"Istituto Italiano di Tecnologia" con il quale sono stati destinati Euro 250.000.000,00 al finanziamento di progetti scientifici ricadenti nei macrosettori scientifici dell'European Research Council identificati con le sigle PE (Scienze fisiche, chimiche, ingegneristiche) e LS (Scienze della vita).

4. L'importo di Euro 6.784.100,00, relativo al finanziamento della linea di intervento C, grava sulle disponibilità di cui al protocollo d'intesa MIUR-IIT-MEF del 27 dicembre 2017, firmato dal Ministro dell'Istruzione, dell'Università e della Ricerca, dal Ministro dell'Economia e delle Finanze e dal Presidente della Fondazione dell'"Istituto Italiano di Tecnologia" con il quale sono stati destinati Euro 250.000.000,00 al finanziamento di progetti scientifici ricadenti nei macrosettori scientifici dell'European Research Council identificati con le sigle PE (Scienze fisiche, chimiche, ingegneristiche) e LS (Scienze della vita).

ART. 2

1. Il contributo per la realizzazione dei progetti, di cui ai commi 2, 3 e 4 dell'art. 1, è erogato direttamente agli atenei/enti sedi delle unità di ricerca dall'IIT per le Linee di intervento A, B e C, previa autorizzazione al pagamento da parte del MIUR.

2. L'erogazione avviene in tre tranche:
   - il 40% a titolo di anticipazione;
   - il 30% previa acquisizione, da parte del MIUR, di apposita dichiarazione, resa dal legale rappresentante dell'ateneo/ente entro il 15° giorno successivo alla conclusione della prima annualità (su formato predisposto dal MIUR, ed esclusivamente per il tramite del sito http://prin.miur.it/), che attesti il concreto sviluppo delle attività (con indicazione delle somme effettivamente spese al termine della prima annualità) e la regolarità delle procedure amministrative poste in essere;
   - il 30% residuo previa acquisizione, da parte del MIUR, di apposita dichiarazione, resa dal legale rappresentante dell'ateneo/ente entro il 15° giorno successivo alla conclusione della seconda annualità (su formato predisposto dal MIUR, ed esclusivamente per il tramite del sito http://prin.miur.it/), che attesti il concreto sviluppo delle attività (con indicazione delle somme effettivamente spese al termine della seconda annualità) e la regolarità delle procedure amministrative poste in essere.
3. Gli atenei/enti garantiscono, in ogni caso, la continuità delle attività dei progetti anche in pendenza delle erogazioni da parte del MIUR.

ART. 3

1. Ciascuna unità di ricerca dovrà garantire la completa realizzazione delle attività di propria competenza, assicurando la copertura sia del proprio cofinanziamento e, ove necessario, degli eventuali maggiori costi.

ART. 4

1. Fatta salva la necessità di coordinamento tra le unità di ricerca afferenti ad ogni singolo progetto (di responsabilità esclusiva del coordinatore di progetto), ogni unità di ricerca nello svolgimento delle attività di propria competenza e per l'effettuazione delle relative spese, opererà in piena autonomia e secondo le norme di legge e regolamentari vigenti, assumendone la completa responsabilità; pertanto, il MIUR resterà estraneo ad ogni rapporto comunque nascente con terzi in relazione allo svolgimento del progetto stesso, e sarà totalmente esente da responsabilità per eventuali danni riconducibili ad attività direttamente o indirettamente connesse col progetto.
2. I costi sostenuti nell'accertato mancato rispetto delle norme di legge e regolamentari non saranno riconosciuti come costi ammissibili.

ART. 5

1. La data di avvio ufficiale dei progetti è fissata al 90° giorno dalla data del presente decreto.
2. Le attività connesse con la realizzazione di ciascun progetto dovranno concludersi entro 36 mesi dalla data di avvio ufficiale di cui al comma 1.

ART. 6

1. La decorrenza per l'ammissibilità delle spese sostenute è fissata per i progetti del settore PE8 al 13 marzo 2019, data del decreto di approvazione dei progetti vincitori del bando PRIN 2017.

2. La data ultima per l'ammissibilità delle spese è fissata, per ogni singolo progetto, alla scadenza temporale indicata all'art. 5, comma 2. Sono fatti salvi i pagamenti sostenuti nei 60 giorni successivi a tale data, purché relativi a titoli di spesa emessi entro la data di scadenza del progetto.
3. Eventuali spese per la diffusione dei risultati (partecipazione a convegni, organizzazione di convegni, pubblicazione di libri), se non sostenute entro la data di scadenza del progetto, possono essere oggetto di una rendicontazione integrativa da sottoporre al MIUR entro il dodicesimo mese successivo alla scadenza del progetto.
4. I costi sostenuti al di fuori dei limiti temporali sopra indicati non saranno riconosciuti come costi ammissibili.

ART. 7

1. Le varianti alla sola articolazione economica del progetto non sono soggette ad approvazione preventiva da parte del MIUR; le varianti scientifiche relative alle modifiche degli obiettivi del progetto sono consentite soltanto previa approvazione del MIUR.
2. Tutte le varianti tecnico-scientifiche sostanziali dovranno essere preventivamente sottoposte alla valutazione del MIUR, mediante apposita esplicita richiesta che ne evidenzi le necessità e le motivazioni di carattere tecnico-scientifico, da inoltrare da parte del coordinatore di progetto. Con apposito successivo provvedimento il MIUR informerà il coordinatore di progetto dell'accoglimento della richiesta di variante o dell'eventuale motivato rigetto.
3. I costi sostenuti per varianti non autorizzate non saranno riconosciuti come costi ammissibili.
4. Nel caso di trasferimento del PI o di un responsabile di unità, in fase di esecuzione del progetto, da un ateneo/ente ad altro ateneo/ente, il regolare svolgimento delle attività deve essere garantito mediante accordo scritto tra i due atenei/enti (da

trasmettere al MIUR per la necessaria autorizzazione), con particolare riferimento all'uso delle attrezzature già acquistate e inventariate presso l'ateneo/ente originario ed alla prosecuzione dell'attività dell'eventuale personale a tempo determinato già contrattualizzato dall'ateneo/ente originario per lo svolgimento delle attività dell'unità di ricerca interessata. Il trasferimento del finanziamento (da intendersi comunque limitato alle somme non ancora spese o impegnate) dall'ateneo/ente originario all'ateneo/ente di destinazione del PI o del responsabile di unità non può essere soggetto ad ulteriori limitazioni, fatta salva la necessità (per quanto riguarda la linea d'intervento "Sud") di garantire che l'ubicazione dell'ateneo/ente di destinazione resti all'interno delle Regioni in ritardo di sviluppo o in transizione.

5. Per tutte le pubblicazioni e i prodotti scientifici realizzati nell'ambito del progetto di ricerca, il PI e gli eventuali altri responsabili di unità sono tenuti a indicare di aver usufruito di un finanziamento nell'ambito del Bando PRIN 2017.

ART. 8

1. Entro 15 giorni dalla scadenza delle annualità intermedie, deve essere acquisita da parte del MIUR apposita dichiarazione, resa dal legale rappresentante dell'ateneo/ente (su formato predisposto dal MIUR, ed esclusivamente per il tramite del sito http://prin.miur.it/), che attesti il concreto sviluppo delle attività (con indicazione delle somme effettivamente spese al termine della prima annualità) e la regolarità delle procedure amministrative poste in essere.
2. La rendicontazione contabile ordinaria finale è effettuata da ciascun responsabile di unità nel rispetto del "criterio di cassa" e mediante apposita procedura telematica, entro 60 giorni dalla conclusione del progetto. Eventuali spese per la diffusione dei risultati (partecipazione a convegni, organizzazione di convegni, pubblicazione di libri), se non sostenute entro la data di scadenza del progetto, possono essere oggetto di una rendicontazione integrativa da sottoporre al MIUR entro il dodicesimo mese successivo alla scadenza del progetto. In nessun caso l'insieme delle due distinte rendicontazioni può dar luogo a contributi MIUR superiori rispetto a quelli stabiliti nel presente decreto di ammissione a finanziamento.
3. Qualora le somme precedentemente erogate risultino superiori al contributo effettivamente spettante, il MIUR procederà in qualsiasi momento, nei confronti degli atenei/enti, al recupero delle somme erogate in eccedenza, anche attraverso compensazione su ogni altra erogazione o contributo da assegnare agli stessi in base ad altro titolo.
4. Entro 30 giorni dalla scadenza di ogni annualità, ogni PI trasmette al MIUR, per via telematica sul sito del bando e su apposita modulistica, una relazione scientifica

intermedia. La relazione è resa disponibile, nei successivi 10 giorni, dal MIUR al competente CdS, che, entro i successivi 30 giorni (sempre sulla base di apposita modulistica predisposta dal MIUR), relaziona sul concreto sviluppo dei progetti. In questa fase, il CdS può anche proporre al MIUR la revoca del contributo nel caso in cui si manifesti una grave inerzia nello sviluppo delle attività e/o un evidente disallineamento del progetto rispetto alle finalità e agli obiettivi originari.

5. Entro 90 giorni dalla conclusione del progetto, il PI redige una relazione scientifica conclusiva sullo svolgimento delle attività e sui risultati ottenuti, con allegato elenco delle pubblicazioni relative al progetto, specificando fra esse quali riportino come primo o ultimo nome, o come autore corrispondente, quello del PI o dei responsabili di unità. Questa relazione è trasmessa con modalità telematica al Ministero. Nel caso in cui sia prodotta la rendicontazione integrativa di cui al precedente comma 2, il PI redige, contestualmente a tale rendicontazione, anche una relazione scientifica integrativa, con allegato elenco delle ulteriori pubblicazioni relative al progetto, prodotte entro il dodicesimo mese successivo alla sua conclusione.
6. Per la necessaria attestazione di conformità alle norme di legge e regolamentari e alle disposizioni e procedure amministrative, la rendicontazione ordinaria (o l'insieme di quella ordinaria e di quella integrativa, ove esistente) è assoggettata ad appositi audit interni centrali da parte di idonee strutture degli atenei/enti sedi delle unità di ricerca. Il MIUR procede, a campione, agli accertamenti finali di spesa, mediante verifica documentale delle rendicontazioni e controlli in sito sugli audit interni centrali, secondo modalità e procedure stabilite nella nota MIUR prot. n. 8109 dell'8 aprile 2014, lettera B) "Nuove modalità di verifica amministrativo-contabile".

ART. 9

1. I controlli da parte del MIUR saranno effettuati nel pieno rispetto di quanto previsto dall'art. 1 del D.L. 9 febbraio 2012, n. 5, convertito con modificazioni dalla legge 4 aprile 2012, n. 35.
2. Ciascun responsabile di unità garantisce l'accesso gratuito e on-line (almeno in modalità green access) ai risultati ottenuti e ai contenuti delle ricerche oggetto di pubblicazioni scientifiche 'peer-reviewed' nell'ambito del progetto, secondo quanto previsto dall'art.4, commi 2 e 2 bis, del decreto legge 8 agosto 2013, n.91, convertito con modificazioni dalla legge 7 ottobre 2013, n.112.
3. Restano impregiudicati tutti gli eventuali obblighi di riservatezza o di tutela dei dati personali.

4. La mancata effettuazione degli audit, nonché l'accertamento da parte del MIUR di violazioni di norme di legge e/o regolamentari sulle singole rendicontazioni, o l'esistenza di casi di plagio e/o manipolazione e/o travisamento dei dati, ferme restando le responsabilità civili e penali, comporta la revoca del finanziamento e l'automatica esclusione del responsabile di unità dai successivi bandi MIUR per un periodo di cinque anni dalla data dell'accertamento.

Il presente decreto è inviato al competente organo di controllo.

IL DIRETTORE GENERALE
(Dott. Vincenzo Di Felice)
Documento firmato digitalmente ai sensi del c.d. Codice dell'Amministrazione Digitale e normativa connessa

Firmato digitalmente da DI FELICE VINCENZO
C=IT
O=MINISTERO ISTRUZIONE UNIVERSITA' E RICERCA

Allegato N. ...1... al punto dell'ordine del giorno N. ...15/1ter

UNIVERSITÀ DEGLI STUDI DI PERUGIA

Perugia, 3 luglio 2019

Al Direttore del Dipartimento di Ingegneria

e p.c.

Al Dott. Gabriele Discepoli

Oggetto: contratto di ricercatore a tempo determinato *ex* art. 24, comma 3, lettera a) – settore concorsuale 09/C1 – SSD ING-IND/08 - regime di impegno a tempo definito - Dott. Gabriele Discepoli. Richiesta di stipula *addendum* e di proroga biennale.

Il sottoscritto Carlo N. Grimaldi, in qualità di Professore Ordinario, per le seguenti esigenze di ricerca e didattica pone all'attenzione del Direttore del Dipartimento di Ingegneria, per l'approvazione nel prossimo Consiglio, la necessità di chiedere al Consiglio di Amministrazione l'autorizzazione alla proroga, per un periodo di due anni, del contratto di ricercatore a tempo determinato, stipulato in regime di impegno a tempo definito, ai sensi dell'art. 24, comma 3, lettera a) della Legge 240/2010 – SC-09/C1, SSD ING-IND/08 – di cui è titolare il Dott. Gabriele Discepoli.

L'attività di ricerca, oggetto del contratto RTD-A in parola, ha riguardato l'attuazione del progetto "Studio e definizione di sistemi innovativi per la riduzione delle emissioni inquinanti da sistemi propulsivi e di conversione dell'energia" nell'ambito del quale il Dott. Discepoli ha svolto attività di studio di sistemi applicati a motori a combustione interna, al fine di analizzarne le potenzialità in termini di riduzione sia delle emissioni gassose inquinanti, sia del consumo energetico e quindi delle emissioni di anidride carbonica. La ricerca ha riguardato diverse tipologie di dispositivo, fra cui un sovralimentatore innovativo, il controllo motore con sensori virtuali basati su reti neurali artificiali, tipologie innovative di sistemi di accensione della miscela aria-benzina

DIPARTIMENTO DI INGEGNERIA

Via G. Duranti, 93
06125 Perugia

Direttore
Segretario Amministrativo
Segreteria Amministrativa
Segreteria Didattica

Tel: +3975 585 3600
Tel: +3975 585 3653
Tel: +3975 585 3657-3652-3949-3686-3688 FAX 3654
Tel: +3975 585 3605-3603-3604

UNIVERSITÀ DEGLI STUDI
DI PERUGIA

per l'utilizzo di dosature magre. Numerosi sono stati i risultati della ricerca effettuata, pubblicati o in corso di pubblicazione, ma di altrettanto interessanti e promettenti se ne intravedono orientando lo studio a ulteriori sistemi finalizzati alla riduzione dell'impatto ambientale, quali i propulsori ibridi.

In tale ottica si pone il PRIN 2017 dal titolo "Study, development and prototyping of a novel compact hybrid powertrain for small/medium city cars, with multiple energy recovery systems", recentemente ammesso a finanziamento, nell'ambito del quale il sottoscritto è responsabile locale di unità di ricerca. In particolare, in piena *compliance* con i percorsi sperimentali già svolti, sarà studiata l'implementazione di un propulsore ibrido *motore a combustione interna-motore elettrico* di tipo avanzato, che possa utilizzare, anche nel caso di applicazione in veicoli di taglia medio-piccola, adeguati sistemi per il recupero energetico. L'attività sul sistema integrato allo studio, in piena continuità scientifica con gli esiti della ricerca fin qui svolta dal Dott. Discepoli, è espressamente finalizzata ad ottenere la riduzione dell'impatto ambientale da combustione di combustibili fossili, in termini sia di emissioni inquinanti sia di consumo energetico e quindi di anidride carbonica (gas serra), in particolare in ambito urbano.

Alla luce di quanto sin qui esposto è di tutta evidenza l'opportunità di prorogare il contratto RTD-A di cui è titolare il Dott. Discepoli consentendo, altresì, al ricercatore di prendere parte alle attività sperimentali del PRIN 2017 in parola sin dal suo avvio.

A tal fine il sottoscritto avanza anche la richiesta di stipula di un *addendum* al contratto RTD-A in essere che preveda, nel periodo di contestuale vigenza temporale dei due progetti in questione, la partecipazione del Dott. Discepoli ad entrambi, così da gestire in modo efficace le attività sperimentali che costituiscono il *trait-d'union* fra i due progetti.

Il sottoscritto stima che il Dott. Discepoli - nel periodo di sovrapposizione temporale dei due progetti in parola - possa dedicare al PRIN 2017, distogliendolo parimenti dal progetto di ricerca oggetto

DIPARTIMENTO DI INGEGNERIA

Via G. Duranti, 93
06125 Perugia

Direttore
Segretario Amministrativo
Segreteria Amministrativa
Segreteria Didattica

Tel: +3975 585 3600
Tel: +3975 585 3653
Tel: +3975 585 3657-3652-3949-3686-3688 FAX 3654
Tel: +3975 585 3605-3603-3604

UNIVERSITÀ DEGLI STUDI
DI PERUGIA

del contratto RTD-A in essere, un impegno temporale pari al 6% del tempo produttivo annuo. Di conseguenza la percentuale di tempo produttivo che sarà dedicata al progetto di ricerca oggetto del contratto RTD-A in essere è determinata in misura pari al 67,33%.

Sia il costo dell'*addendum* (corrispondente alla valorizzazione economica del tempo produttivo che verrà distolto dal progetto di ricerca originario per essere dedicato al PRIN 2017) che il costo della proroga saranno interamente finanziati a valere sulle risorse assegnate all'unità di ricerca PRIN 2017 identificata dal codice 2017X8RLFE_002.

Si indica per l'attività didattica, di didattica integrativa e di servizio agli studenti, 200 ore annue (regime a tempo definito) nell'ambito del SSD indicato o affini, di cui non più di 50 ore per attività di didattica ufficiale.

Si propone per la valutazione dell'attività didattica e di ricerca svolta dal Dott. Gabriele Discepoli la composizione della pertinente commissione di seguito indicata: Prof.ssa Linda Barelli (linda.barelli@unipg.it), Prof. Michele Battistoni (michele.battistoni@unipg.it), Prof. Francesco Di Maria (francesco.dimaria@unipg.it), tutti Professori Associati appartenenti all'Università degli Studi di Perugia, SC-09/C1, SSD ING-IND/08.

Distinti saluti.

Prof. Carlo N. Grimaldi

DIPARTIMENTO DI INGEGNERIA

Via G. Duranti, 93
06125 Perugia

Direttore
Segretario Amministrativo
Segreteria Amministrativa
Segreteria Didattica

Tel: +3975 585 3600
Tel: +3975 585 3653
Tel: +3975 585 3657-3652-3949-3686-3688 FAX 3654
Tel: +3975 585 3605-3603-3604

Allegato N. 2 al punto dell'ordine del giorno N. 15ter

DICHIARAZIONE SOSTITUTIVA DI CERTIFICAZIONE
(artt.46 e 48 del D.P.R. 28.12.2000 n. 445)
DICHIARAZIONE SOSTITUTIVA DELL'ATTO DI NOTORIETÀ
(artt.47 e 48 del D.P.R. 28.12.2000 n. 445)

DICHIARA SOTTO LA PROPRIA RESPONSABILITÀ

Il sottoscritto
DISCEPOLI Gabriele
nato a [redacted] (prov. PG) il [redacted]
residente a [redacted]

consapevole delle responsabilità penali previste dagli artt. 75 e 76 del D.P.R. 445/2000 per le ipotesi di falsità in atti e dichiarazioni mendaci

D I C H I A R A

di non avere un grado di parentela o affinità, fino al quarto grado compreso o rapporto di coniugio o rapporto di unione civile o convivenza di cui alla legge n. 76/2016 con un professore appartenente al Dipartimento o alla Struttura che effettua la chiamata, ovvero con il Rettore, il Direttore Generale o un componente del Consiglio di Amministrazione dell'Università di Perugia (art. 18 – comma 1, lett. b) e c) legge 240/2010).

Il sottoscritto prende atto, ai sensi D.Lvo 30 giugno 2003, n. 196 sul trattamento dei dati personali e del Regolamento UE 2016/679, che i dati contenuti nella presente autocertificazione verranno trattati prevalentemente con procedure informatizzate e potranno essere forniti ad altri organismi pubblici per il raggiungimento delle rispettive finalità istituzionali.

....., ...
Perugia, 4/07/2019
IL DICHIARANTE
(firma per esteso e leggibile)

La presente dichiarazione non necessita dell'autenticazione della firma e sostituisce a tutti gli effetti le normali certificazioni richieste o destinate ad una Pubblica Amministrazione nonché ai gestori di pubblici servizi e ai privati che vi consentono.
Qualora la dichiarazione non venga sottoscritta in presenza del funzionario dell'Amministrazione accettante, alla stessa va allegata fotocopia di documento di identità in corso di validità.

Gabriele Discepoli

Università degli Studi di Perugia - Dipartimento di Ingegneria

RELAZIONE ATTIVITÀ RTD-A

DESCRIZIONE GENERALE

La necessità di ridurre le emissioni inquinanti, così come di migliorare l'efficienza dei motori a combustione interna, ha spinto la ricerca nell'ambito del progetto RTDa *"Studio e definizione di sistemi innovativi per la riduzione delle emissioni inquinanti da sistemi propulsivi e di conversione dell'energia"* verso l'indagine sull'adozione di miscele ultra-magre e di percentuali di EGR particolarmente alte, richiedendo l'intervento di sistemi innovativi di accensione che migliorassero drasticamente le prestazioni delle candele convenzionali.

La linea di ricerca quindi che è stata principalmente sviluppata nel corso triennale del contratto RTDa, ha riguardato i sistemi di accensione a effetto Corona, per motori a combustione interna ad accensione comandata. Questa attività si è suddivisa in tre tronconi comprendenti:

- la misura dell'energia rilasciata dagli accenditori in un mezzo gassoso. Questa attività ha inoltre comportato lo sviluppo di un banco prova dedicato per la caratterizzazione energetica di tali sistemi di accensione (convenzionali o innovativi) in differenti condizioni operative;
- test su motore ad accesso ottico in diverse condizioni di lavoro e con diverse strategie di controllo dello stesso sistema di accensione;
- simulazione numerica degli stadi iniziali di sviluppo della fiamma innescata da accenditori a effetto Corona.

In ottica di riduzione di inquinanti e, più in generale, delle emissioni, sia per sistemi propulsivi che per conversione dell'energia, sono state condotte altre attività che hanno riguardato:

- l'analisi sperimentale di un sistema di sovralimentazione per il settore motociclistico;
- la caratterizzazione sperimentale al banco prova delle prestazioni di motori elettrici;
- le prime fasi della progettazione e sviluppo di un motore ad accesso ottico ad accensione per compressione a benzina *LTC* (combustione a basse temperature).
- Studio preliminare sul controllo di motori a combustione interna realizzato tramite implementazione in centralina di reti neurali artificiali.
- Studio numerico di strategie di *water injection* per il controllo della detonazione.
- Studio di sistemi di produzione, stoccaggio e conversione di energia (stazionario/mobile) basati su *fuel cell* (carbonati fusi e ossidi solidi) e *redox flow battery*.

CARATTERIZZAZIONE SPERIMENTALE DI SISTEMI DI ACCENSIONE CONVENZIONALE E INNOVATIVI

Il sistema di accensione basato sull'effetto Corona è una tecnologia promettente capace di produrre più centri di accensione in camera di combustione attraverso la generazione di più "streamers", canali di plasma a (relativamente) bassa temperatura. Il sistema si avvale della capacità di operare su volumi maggiori di un sistema convenzionale, oltre che sulla produzione di cascami di particelle attive (radicali), in grado di stimolare positivamente la

combustione e accelerarla notevolmente nelle sue prime fasi. Queste caratteristiche lo rendono capace di produrre una combustione stabile anche con concentrazioni di combustile molto basse, tipiche delle condizioni operative di "magro" o con alto EGR, necessarie alla riduzione delle emissioni nocive.

Nel corso di questo studio, un sistema prototipale a effetto corona (ACIS) è stato confrontato con uno convenzionale (stesso produttore con in quale esiste una convenzione) operante sia in condizioni standard che "multispark", ossia con più eventi consecutivi. Il confronto è avvenuto sulle base sia dell'energia assorbita che, soprattutto, su quella rilasciata dagli stessi sistemi d'accensione nel mezzo contenuto in un calorimetro a pressione.

L'ACIS è stato quindi sistematicamente caratterizzato misurandone l'energia assorbita e quella termica rilasciata nella finestra operativa dei propri parametri di funzionamento e al variare della pressione del gas (azoto o aria) all'interno della camera di misura a volume costante. L'intervallo della pressione applicata ha compreso valori confrontabili a quelli sperimentati nel motore ad accesso ottico i cui test hanno costituito parte sostanziale dell'attività. In particolare, in questi test è stato esplorato il campo di operatività dei parametri di funzionamento dell'ACIS attraverso l'analisi della velocità di fiamma. Inoltre, col medesimo metodo è stata valutata la capacità di estendere il limite di magro dell'ACIS in confronto ad accenditori a candela convenzionali in funzione della complessità chimica del combustibile adottato (benzina, metano, miscela metano/idrogeno).

Lo studio su ACIS ha portato anche a uno studio numerico preliminare tale da riprodurre i risultati sperimentali ottenuti per l'energia termica depositata nel calorimetro a volume costante per poi esportare i risultati nella simulazione del motore ad accesso ottico e predire quindi il comportamento in combustione.

IMPULSE DRUM CHARGER

Scopo di questa attività è lo studio di un sovralimentatore di tipo motociclistico, cosiddetto a onde di pressione, l'*Impulse Drum Charger*. Lo studio si è incentrato nel confronto delle prestazioni al banco prova di un motore motociclistico commerciale a 4 tempi (KTM 390) equipaggiato con e senza sistema di sovralimentazione. In particolare, lo studio è stato condotto sull'analisi indicata (interno motore) e sulla pressione all'aspirazione dimostrando che effettivamente il sistema di sovralimentazione è in grado di migliorare le performance del motore esaminato (fino a 1.4 kW a 9500 giri/minuto). Il lavoro ha previsto l'ottimizzazione del sistema di scarico così da garantire la corretta propagazione delle onde di pressione e contenere le temperature entro livelli accettabili.

VALUTAZIONE PERFORMANCE MOTORI ELETTRICI

In ottica della futura attività di prova sperimentale e sviluppo di motorizzazioni termiche ibride, sono stati condotti test di valutazione performance di durata di motori elettrici. Le prove, automatizzate sull'intero range operativo dell'unità elettrica, sono state finalizzate alla valutazione e omologazione della tipologia di propulsore.

SVILUPPO MOTORE AD ACCESSO OTTICO LTC

Scopo di questa attività è la modifica dell'attuale motore ad accesso ottico per ottenerne una versione *Low Temperature Combustion*, direzione fondamentale dell'attuale ricerca sui propulsori: la combustione a basse temperature permette di migliorare radicalmente

l'efficienza del propulsore riducendo drasticamente gli inquinanti prodotti. In questa fase, gran parte del motore è stato riprogettata (in particolare il volume comprendente la camera di combustione) e prodotta.

RETI NEURALI ARTIFICIALI PER LA GESTIONE ICE

In ambiente automotive un tema centrale è costituito dalla capacità di controllare ed elaborare un numero sempre maggiore di parametri sfruttando risorse di calcolo limitate. L'implementazione di reti neurali artificiali permette di correlare rapidamente un alto numero d'informazioni, la creazione di sensori virtuali e l'implementazione di un sistema di diagnostica on-board, con costi limitati e sfruttando le capacità di calcolo già presenti.

A questo proposito, si è effettuato uno studio preliminare dove, basandosi su dati sperimentali, le reti neurali sono state utilizzate per simulare il funzionamento di sensori virtuali posti all'interno di un circuito olio motore. I risultati sono stati quindi confrontati e validati con dati misurati da sensori reali.

WATER INJECTION

L'utilizzo di acqua in camera di combustione permette in linea teorica un aumento dell'efficienza, un miglioramento delle prestazioni motoristiche e una contestuale riduzione delle emissioni. In particolare, la water injection è una tecnologia che permette numerosi benefici (rapporti di compressione maggiori, riduzione dell'EGR e del rischio di detonazione), grazie alla capacità di assorbire calore sia in fase di evaporazione che per l'alto calore specifico dell'acqua. In questo studio numerico sono ottimizzati i parametri fondamentali di iniezione dell'acqua, quali posizionamento dell'iniettore, tempistica dell'iniezione e qualità dell'atomizzazione primaria, in modo da massimizzare l'efficacia delle caratteristiche dell'iniezione di acqua e, in particolare, ridurre sensibilmente la detonazione.

SISTEMI DI PRODUZIONE, STOCCAGGIO E TRASFORMAZIONE DELL'ENERGIA

Le MCFC sono sistemi energetici intrinsecamente efficienti che, in particolare configurazione, possono associare alla produzione di energia anche la cattura della CO2 prodotta da altri impianti. In questo studio è stato valutata la risposta di tali sistemi in funzione di concentrazioni catodiche variabili di anidride carbonica sia dal punto di vista delle performance che da quello elettrochimico, tramite analisi d'impedenza.

Nell'ottica della necessità di bilanciamento della rete elettrica richiesto dal crescente ricorso a sistemi di produzione di energia rinnovabile e non predicibile, è stata fatta una valutazione tecno-economica di due promettenti sistemi di trasformazione e stoccaggio di energia basati su tecnologia redox flow battery (batterie a flusso) e reversibile solide oxide fuel cell.

ALTRE ATTIVITÀ

Nel corso dell'anno sono state condotte attività di didattica (correlatore in tesi, partecipazione a commissioni d'esame e servizio agli studenti) e di aggiornamento (partecipazione ai congressi SAE Capri 2017, SAE Detroit 2018, ATI Pisa 2018 e VERIFI Argonne National Laboratory 2019), di disseminazione (pubblicazioni e presentazione orale all'ATI Pisa 2018,

coautore di presentazioni orali al SAE Capri 2017, EFC 2019, SAE Detroit 2018 e VERIFI Argonne National Laboratory 2019)

PUBBLICAZIONI

Battistoni, M., Grimaldi, C. N., Cruccolini, V., Discepoli, G., & De Cesare, M. (2017). Assessment of Port Water Injection Strategies to Control Knock in a GDI Engine through Multi-Cycle CFD Simulations. In *SAE Technical Paper*. https://doi.org/10.4271/2017-24-0034

Audasso, E., Barelli, L., Bidini, G., Bosio, B., & Discepoli, G. (2017). Molten Carbonate Fuel Cell performance analysis varying cathode operating conditions for carbon capture applications. *Journal of Power Sources, 348*, 118–129. https://doi.org/10.1016/j.jpowsour.2017.02.081

Cimarello, A., Cruccolini, V., Discepoli, G., Battistoni, M., Mariani, F., Grimaldi, C. N., & Dal Re, M. A. (2018). Combustion Behavior of an RF Corona Ignition System with Different Control Strategies. In *SAE Technical Paper* (pp. 1–19). https://doi.org/10.4271/2018-01-1132

Discepoli, G., Cruccolini, V., Dal Re, M. A., Zembi, J., Battistoni, M., Mariani, F., & Grimaldi, C. N. (2018). Experimental assessment of spark and corona igniters energy release. *Energy Procedia, 148*(Ati), 1262–1269. https://doi.org/10.1016/j.egypro.2018.08.001

Cruccolini, V., Discepoli, G., Zembi, J., Battistoni, M., Mariani, F., & Grimaldi, C. N. (2018). Experimental Assessment of a Pressure Wave Charger for Motorcycle Engines. *Energy Procedia, 148*, 1254–1261. https://doi.org/10.1016/j.egypro.2018.08.002

Baldinelli A., Barelli L., Bidini G., Discepoli G., Economic viability of tailored power-to-capacity energy storage for renewable-based micro-grids: Vanadium Redox Flow Batteries vs. Reversible Solid Oxide Cells. *Journal of Power Sources (submitted)*

Cruccolini V., Discepoli G., Cimarello A., Battistoni M., Mariani F., Grimaldi C. N., Dal Re M., Lean combustion analysis using a corona discharge igniter in an optical engine fueled with methane and a hydrogen-methane blend. *Fuel (submitted)*

Petrucci L., Ricci F., Mariani F., Grimaldi C. N., Discepoli G., Violi M., Meatteazzi N., Performance Analysis of Artificial Neural Networks for Control in Internal Combustion Engines *Energy Procedia (submitted)*

Ricci F., Zembi J., Battistoni M., Grimaldi C. N., Discepoli G., Petrucci L., Numerical Simulation of the Early Flame Development Produced by an Advanced Radio Frequency Ignition System in an Optical Access Engine. In *SAE Technical Paper (submitted).*

Discepoli G., Cruccolini V., Ricci F. Di Giuseppe A., Papi S., Grimaldi C. N., Experimental characterization of the thermal energy released by a Radio-Frequency Corona Igniter. *(in progress)*

Allegato N. ....4..... al punto dell'ordine del giorno N. 15 ter

UNIVERSITÀ DEGLI STUDI DI PERUGIA

Perugia,
28.06.2019

Al Direttore del CIRIAF
Prof. Pietro Buzzini

e al Direttore del Dipartimento di Ingegneria
Prof. Giuseppe Saccomandi

Oggetto: Proposta di proroga per due anni, mediante fondi esterni del CIRIAF, del ricercatore a tempo determinato ex art. 24, comma 3, lettera a) – SC 09/C2 - SSD ING-IND/11 Dott. Emanuele Bonamente.

Gentili Direttori,

il Dott. Emanuele Bonamente sta completando il triennio di attività da ricercatore a tempo determinato ex art. 24, comma 3, lettera a) – SC 09/C2 - SSD ING-IND/11 in regime di tempo definito, a valere sul finanziamento erogato dal Ministero dell'Ambiente e della Tutela del Territorio e del Mare (di seguito MATTM) nell'ambito del progetto "Sostenibilità ambientale, riduzione delle emissioni clima alteranti, diffusione e implementazione di metodologie per la valutazione e certificazione dell'impronta di carbonio e dell'impronta ambientale".

Il sottoscritto prof. Franco Cotana, in considerazione dell'importanza dell'attività di ricerca fin qui svolta e considerate le esigenze del progetto PRIN 2017 dal titolo "BIOmasses Circular Holistic Economy APproach to EneRgy equipments (BIO-CHEAPER)", richiede, in qualità di componente dell'unità di ricerca, una proroga di due anni del contratto da ricercatore a tempo determinato ex art. 24, comma 3, lettera a) del dott. Emanuele Bonamente a valere sui fondi del medesimo progetto BIO-CHEAPER.

Tale attività, e conseguentemente le competenze acquisite dal dott. Bonamente, infatti, risultano di particolare interesse anche per il progetto di ricerca "BIOmasses Circular Holistic Economy APproach to EneRgy equipments (BIO-CHEAPER)", approvato con Decreto Direttoriale n. 1162 del 17.06.2019. In particolare, si rendono necessarie attività di simulazione e caratterizzazione sperimentale dei processi di conversione energetica delle biomasse e l'ottimizzazione delle prestazioni, in termini di sostenibilità ambientale, di tali processi tramite un approccio di economia circolare e LCA applicato all'intera filiera, che rappresentano una naturale prosecuzione ed approfondimento delle tematiche finora affrontate. A tal fine, nonché per le esigenze didattiche del settore, è di particolare rilevanza la professionalità acquisita dal dott. Emanuele Bonamente.

Si comunica inoltre che il costo della suddetta proroga verrà coperto con il fondo di seguito indicato:

- per € 80.439,76 (ottantamilaquattrocentotrentanove/76) con i fondi derivanti dal finanziamento del progetto BIO-CHEAPER "BIOmasses Circular Holistic Economy APproach to EneRgy equipments".

CIRIAF
Centro Interuniversitario di Ricerca sull'Inquinamento e sull'Ambiente "Mauro Felli"

Polo Ingegneria
Via G. Duranti, 63
06125 Perugia - Italia

Tel.: +39 075 585 3717
Fax: +39 075 585 3697

E-mail: centro.ciriaf@unipg.it
Web: www.ciriaf.it

UNIVERSITÀ DEGLI STUDI
DI PERUGIA

L'attività didattica, didattica integrativa e servizio agli studenti sarà pari a 200 ore annue (regime a tempo definito) nell'ambito della SSD ING/IND 11 o settori affini, di cui non più di 50 ore di didattica frontale.
Ai fini della valutazione della relazione dell'attività didattica e di ricerca svolta dal dott. Emanuele Bonamente, si propone la seguente commissione di valutazione:

- Prof. Federico Rossi - Università degli Studi di Perugia - SSD ING-IND/11;
- Prof.ssa Cinzia Buratti - Università degli Studi di Perugia - SSD ING-IND/11;
- Prof.ssa Elisa Moretti - Università degli Studi di Perugia - SSD ING-IND/11;

Prego Le SS.VV. di portare in approvazione, la richiesta nei Consigli dei rispettivi Dipartimenti nella prima seduta utile.

Cordiali saluti,

Prof. Franco Cotana

CIRIAF
Centro Interuniversitario
di Ricerca sull'Inquinamento
e sull'Ambiente "Mauro Felli"

Polo Ingegneria
Via G. Duranti, 63
06125 Perugia - Italia

Tel.: +39 075 585 3717
Fax: +39 075 585 3697

E-mail: centro.ciriaf@unipg.it
Web: www.ciriaf.it

Allegato N. 5 al punto
dell'ordine del giorno N. 15 Ter

DICHIARAZIONE SOSTITUTIVA DI CERTIFICAZIONE
(artt.46 e 48 del D.P.R. 28.12.2000 n. 445)
DICHIARAZIONE SOSTITUTIVA DELL'ATTO DI NOTORIETÀ
(artt.47 e 48 del D.P.R. 28.12.2000 n. 445)

DICHIARA SOTTO LA PROPRIA RESPONSABILITÀ

Il sottoscritto
(Cognome) BONAMENTE (Nome) EMANUELE
nato a [redacted] (prov. PG) il [redacted]
residente a [redacted] Via [redacted]

consapevole delle responsabilità penali previste dagli artt. 75 e 76 del D.P.R. 445/2000 per le ipotesi di falsità in atti e dichiarazioni mendaci

D I C H I A R A

di non avere un grado di parentela o affinità, fino al quarto grado compreso o rapporto di coniugio o rapporto di unione civile o convivenza di cui alla legge n. 76/2016 con un professore appartenente al Dipartimento o alla Struttura che effettua la chiamata, ovvero con il Rettore, il Direttore Generale o un componente del Consiglio di Amministrazione dell'Università di Perugia (art. 18 – comma 1, lett. b) e c) legge 240/2010).

Il sottoscritto prende atto, ai sensi D.Lvo 30 giugno 2003, n. 196 sul trattamento dei dati personali e del Regolamento UE 2016/679, che i dati contenuti nella presente autocertificazione verranno trattati prevalentemente con procedure informatizzate e potranno essere forniti ad altri organismi pubblici per il raggiungimento delle rispettive finalità istituzionali.

Perugia, 1/7/2019
(luogo e data)
IL DICHIARANTE
Emanuele Bonamente
(firma per esteso e leggibile)

La presente dichiarazione non necessita dell'autenticazione della firma e sostituisce a tutti gli effetti le normali certificazioni richieste o destinate ad una Pubblica Amministrazione nonché ai gestori di pubblici servizi e ai privati che vi consentono.
Qualora la dichiarazione non venga sottoscritta in presenza del funzionario dell'Amministrazione accettante, alla stessa va allegata fotocopia di documento di identità in corso di validità.

Allegato N. 6 al punto dell'ordine del giorno N. 15ter

Relazione Triennale Conclusiva

Dott. Emanuele Bonamente

Ricercatore universitario a Tempo Determinato (art. 24 – comma 3, lettera a) Legge 240/10), Settore concorsuale 09/C2- Fisica Tecnica e Ingegneria Industriale - Settore scientifico-disciplinare ING-IND/11 (Fisica Tecnica Ambientale).

Progetto di ricerca: "Energia e sostenibilità ambientale della risorsa idrica".

Sede: Università degli Studi di Perugia - Dipartimento di Ingegneria, Centro Interuniversitario di Ricerca sull'Inquinamento e sull'Ambiente "M. Felli", Via G. Duranti, Perugia.

Tel: +39 075 585 3914

e-mail: emanuele.bonamente@unipg.it

Attività scientifica:

Scopus – Author ID: 23017714200, 194 documenti, 25175 citazioni, h-Index: 86

ORCID: orcid.org0000-0003-3847-0510

Research Gate – 291 documenti, RG Score: 46.99 (>97.5% dei membri di RG), h-index: 77

Google Scholar – 228 documenti, 36011 citazioni; h-index: 94; i10-index: 170

Il progetto di ricerca è incentrato su attività connesse alla sostenibilità nell'impiego dell'energia e nello sfruttamento della risorsa idrica, con particolare attenzione alla valutazione di carbon e water footprint, a sistemi innovativi per lo sfruttamento delle fonti energetiche rinnovabili e ai materiali innovativi per il miglioramento della sostenibilità ambientale di beni e servizi.

Le attività svolte nel periodo di tre anni iniziato il 7 novembre 2016 sono incentrate nel progetto "Energia e sostenibilità ambientale della risorsa Idrica" e hanno coinvolto ambiti ad esso affini e complementari anche tramite collaborazione e direzione di progetti finanziati su fondi esterni.

Progetto "Sostenibilità ambientale, riduzione delle emissioni clima alteranti, diffusione e implementazione di metodologie per la valutazione e certificazione dell'impronta di carbonio e dell'impronta ambientale"

Responsabile scientifico degli obiettivi realizzativi AP, ESSC2 e RI. Le attività svolte riguardano la ricognizione dettagliata dei database disponibili relativi alla risorsa energetica su base nazionale al fine di effettuare una raccolta e categorizzazione dei dati e creare una struttura dinamica del Database Nazionale dell'Energia. In particolare, sono stati individuati i tre settori più rilevanti del panorama energetico nazionale (energia elettrica, gas naturale, carburanti) e raccolti tutti i riferimenti necessari e i dati indispensabili per la predisposizione del Database. È stata inoltre effettuata una ricognizione del territorio nazionale, attraverso l'utilizzo di mappe topologiche georeferenziate che descrivono, con precisione sufficiente a rappresentare in modo adeguato le peculiarità del panorama italiano, lo stato attuale dell'utilizzo del suolo ed in particolare permettono una categorizzazione dei singoli elementi per finalità d'uso (e.g. agricola, industriale, etc.). Si è realizzata una valutazione dell'impronta idrica in termini di acqua verde (WFgreen), blu (WFblue) e grigia (WFgrey) con lo scopo di delineare un quadro globale che permette di valutare gli impatti sull'ambiente relativi all'uso della risorsa idrica. Sono stati elaborati ed applicati indicatori specifici con lo scopo di valutare lo stress idrico prodotto dall'utilizzo di acqua dolce in considerazione dell'effettiva disponibilità nel bacino dal quale l'acqua viene prelevata (Water Scarcity) e misurare l'inquinamento prodotto sull'acqua superficiale e di falda (Water Degradation).

Progetto SmartEnergy

L'obiettivo del progetto Smart Energy è stato quello di sviluppare e testare una modalità innovativa di utilizzo delle fonti energetiche rinnovabili per la climatizzazione di edifici, con particolare attenzione allo sfruttamento e alla conversione dell'energia geotermica per applicazioni a pompa di calore tramite un approccio innovativo che include un sistema di accumulo di calore *upstream*. In quest'ottica, la gestione dei flussi energetici all'interno dell'edificio è potenzialmente sfruttabile in modalità intelligente, ovvero il sistema di accumulo termico può essere pensato come il centro di raccolta e smistamento dell'energia proveniente anche da altre fonti oltre a quella geotermica, come quella proveniente da collettori solari, e può utilizzare in modi ottimale le varie componenti dell'impianto (e.g. la poma di calore reversibile, l'energia elettrica prelevata dalla rete o prodotta da installazioni fotovoltaiche, etc.).

Le attività principali del progetto Smart Energy si sono concentrate nella progettazione, realizzazione e caratterizzazione sperimentale del prototipo di storage termico.

Sostenibilità Ambientale

Nell'ambito della sostenibilità ambientale sono state effettuate numerose analisi di valutazione di carbon e water footprint di beni e servizi in accordo con le più recenti normative internazionali, nonché studi su indicatori innovativi per la quantificazione dell'impatto sulla risorsa idrica.

Fluidodinamica

Sono stati effettuati studi sul comportamento fluidodinamico di diversi apparati sperimentali volti alla cattura della CO2 tramite materiali porosi sostenibili, l'immagazzinamento di energia termica in sistemi di accumulo basati su calore sensibile e latente, e più approfonditamente sulle proprietà termiche dei solidi a cambiamento di fase (PCM).

Intelligenza artificiale

Si sono sviluppati modelli per la valutazione in uno scenario di ottimizzazione multiobiettivo delle caratteristiche progettuali di edifici in fase di progettazione e ristrutturazione basati su un approccio a ciclo di vita che tenga conto anche degli impatti ambientali da essi generati.

Pubblicazioni nel triennio di riferimento:

Riviste scientifiche peer-reviewed

1. A life-cycle approach for multi-objective optimization in building design: methodology and application to a case study. E. Bonamente et al. Civil Engineering and Environmental Systems, 35(1-4):158-179, 2018. doi: 10.1080/10286608.2019.1576646

2. Carbon and energy footprint of the hydrate-based biogas upgrading process integrated with CO2 valorization. B. Castellani et al. Science of the Total Environment, 615(15):404-411, 2018. doi: doi.org/10.1016/j.scitotenv.2017.09.254

3. Life-Cycle Assessment of an Innovative Ground-Source Heat Pump System with Upstream Thermal Storage. E. Bonamente and A. Aquino. Energies, 10(11):1854, 2017. doi:10.3390/en10111854

4. Experimental investigation and energy considerations on hydrate-based biogas upgrading with CO2 valorization. B. Castellani et al. Biomass and Bioenergy, 105:364-372, 2017. doi:10.1016/j.biombioe.2017.07.022

5. National water footprint: toward a comprehensive approach for the evaluation of the sustainability of water use in Italy. E. Bonamente et al. Sustainability, 9(8):1341, 2017. doi:10.3390/su9081341iviste internazionali

Convegni

1. 6th International Conference on Energy, Sustainability and Climate Change (ESCC2019), Chania, Crete, Greece, 3-7 June 2019, Experimental characterization of a PCM thermal storage for ground-source heat pumps

2. 4th International Conference on Energy and Environment: bringing together Engineering and Economics (ICEE2019), Guimaraes, Portugal, 16-17 May 2019, GHG emission reduction for ground-source heat pumps: energy storage using phase-change materials

3. 12th Italian LCA Network Conference, Messina, Italy, 11-12 June 2018, Practitioner-related effects on LCA results: a case study on Energy and Carbon Footprint of wine

4. Vinitaly, Verona, Italy, 15-18 April 2018, LCA – Life-cycle assessment of olive and wine

5. 18th CIRIAF National Congress – Sustainable Development, Environmental Protection, and Human Health, Perugia, Italy, 6-7 April 2018, Uncertainty due to choices in LCA: a case study on Energy and Carbon footprints of wine

6. 18th CIRIAF National Congress – Sustainable Development, Environmental Protection, and Human Health, Perugia, Italy, 6-7 April 2018, An innovative methodology for multi-objective optimization applied to building design

7. 17th CIRIAF National Congress – Sustainable Development, Environmental Protection, and Human Health, Marsciano (PG), Italy, 6-7 April 2017, National water footprint: toward a comprehensive approach for the evaluation of the sustainability of water use in Italy

8. 17th CIRIAF National Congress – Sustainable Development, Environmental Protection, and Human Health, Marsciano (PG), Italy, 6-7 April 2017, Life cycle assessment of a ground-source heat pump including an upstream thermal storage

9. 17th CIRIAF National Congress – Sustainable Development, Environmental Protection, and Human Health, Marsciano (PG), Italy, 6-7 April 2017, Carbon footprint of a water distribution service: comparison between product and organization approaches

10. 17th CIRIAF National Congress – Sustainable Development, Environmental Protection, and Human Health, Marsciano (PG), Italy, 6-7 April 2017, Carbon and energy footprint of the hydrate-based biogas upgrading process integrated with CO2 valorization

11. 22nd Conference of Parties (COP22), Marrakech, Morocco, November 7-18 2016, High-albedo surfaces for Urban Heat Island mitigation

Responsabilità scientifica di progetti finanziati su bandi competitivi

1. *BIOmasses Circular Holistic Economy APproach to EneRgy equipments (BIO-CHEAPER)* - PRIN: progetti di ricerca di rilevante interesse nazionale – Bando 2017, 2019-2022 (€ 1,200,000). Responsabile Scientifico di Unità.

2. *Smart Energy: design e ottimizzazione di un sistema integrato per la climatizzazione tramite energie rinnovabili ed accumulo termico con PCM* – Fondazione Cassa di Risparmio di Perugia, 2017-2019 (€ 40,000.00). Responsabile Scientifico (PI).

Attività didattica

Titolarità di corsi universitari

Elementi di Fisica (Matematica e Fisica), Corso di laurea in Produzioni Animali, Dipartimento di Medicina Veterinaria – Università di Perugia, AA 2018-19.

Fisica Tecnica Ambientale (Prevenzione e Sicurezza sul Lavoro 1), Corso di laurea in Tecniche della prevenzione nell'ambiente e nei luoghi di lavoro, Dipartimento di Medicina Sperimentale – Università degli Studi di Perugia, A.A. 2017-18 e 2018-19.

Fisica Tecnica Industriale (Scienze applicate per il Design), Corso di laurea in Design, Dipartimento di Ingegneria Civile e Ambientale – Università degli Studi di Perugia, A.A. 2017-18.

Superficial optical properties: theory and practice, Corso di Dottorato in Ingegneria Energetica e Sviluppo Sostenibile – Università degli Studi di Perugia, 2016-17.

Attività di coordinamento

Responsabile tecnico operativo del laboratorio di fisica tecnica industriale.

Organizzazione dei seguenti congressi:

19° congresso nazionale CIRIAF – Energia e Sviluppo Sostenibile. Perugia, Italy, 12 Aprile 2019.

18° congresso nazionale CIRIAF – Sostenibilità Energetico-Ambientale e consolidamento sismico del patrimonio costruito. Perugia, Italy, 5-6 Aprile 2018.

17° congresso nazionale CIRIAF – Sostenibilità Energetico-Ambientale e consolidamento sismico del patrimonio costruito. Rocca di Sant'Apollinare, Marsciano (PG), Italy, 6-7 Aprile 2017.

Attività di revisione per riviste scientifiche peer-reviewed

Buildings – MDPI (ISSN 2075-5309)

Carbon Management – Taylor & Francis (ISSN 1758-3004/1758-3012)

Energies – MDPI (ISSN 1996-1073)

Energy and Buildings – Elsevier (ISSN: 0378-7788)

Journal of Cleaner Production – Elsevier (ISSN: 0959-6526)

Journal of Solar Energy Engineering – ASME (ISSN: 0199-6231)

Sustainability – MDPI (ISSN 2071-1050)

Science of the Total Environment – Elsevier (ISSN: 0048-9697)

Applied Energy – Elsevier (ISSN: 0306-2619)

Environmental Engineering Research – KSEE (eISSN: 2005-968X)

Dott. Emanuele Bonamente